Spectroscopy of fulminic acid HCNO with VUV- and soft X-ray radiation

Marius David Gerlach

Spectroscopy of fulminic acid HCNO with VUV- and soft X-ray radiation

Dissertation zur Erlangung des
naturwissenschaftlichen Doktorgrades der
Julius-Maximilians-Universität Würzburg

vorgelegt von

Marius David Gerlach

aus Hattersheim

Würzburg, Juli 2023

Eingereicht bei der Fakultät für Chemie und Pharmazie am ....

Gutachter der schriftlichen Arbeit:

1. Gutachter: ....

2. Gutachter: ....

Prüfer des öffentlichen Promotionskolloquiums:

1. Prüfer: ....

2. Prüfer: ....

3. Prüfer: ....

Datum des öffentlichen Promotionskolloquiums:

....

Doktorurkunde ausgehändigt am:

....

Science isn't about why, it's about why not!

-Cave Johnson, Portal 2

Contents

Abbreviations

AE	Appearance energy
AEPICO	Auger-electron-photoion coincindence
AEPIPICO	Auger-electron-photoion-photoion coincidence
AES	Auger electron spectroscopy
ATcT	Active thermochemical tables
DPI	Dissociative photoionisation
DTA	Double toroidal analyzer
EPSD	Electron position sensitive detector
es	energy-selective
Eq.	Equation
EXAFS	Extended X-ray absorption fine structure
Fig.	Figure
HOMO	Highest occupied molecular orbital
IE	Ionization energy
IR	Infrared radiation
LUMO	Lowest unoccupied molecular orbital
MCP	Micro channel plate
MO	Molecular orbital
ms	mass-selective
NEXAFS	Near edge x-ray absorption fine structure
NMR	Nuclear magnetic resonance
PIPICO	Photoion-photoion-coincidence
PLEIADES	Polarized Light source for Electron and Ion Analysis from Diluted Excited Species
PSD	Position sensitive detector
RAES	Resonant Auger electron spectroscopy
SLS	Swiss Light Source
SOLEIL	Source Optimisée de Lumière d'Energie Intermédiaire du LURE

Tab.	Table
TOF	Time-of-flight
UV/VIS	Ultraviolet and visible spectral range
VUV	Vacuum ultraviolet
XANES	X-ray absorption near-edge structure
XPS	X-ray photoelectron spectroscopy
XRF	X-ray fluorescence

List of Publications

The Chapters 3 and 4 are adapted versions of peer-reviewed and published articles. Chapter 5 is an adapted version of a submitted manuscript. The contribution of each author to these chapters is stated in *Erklärungen zu Autorenschaften.* The articles are:

- Auger electron spectroscopy of fulminic acid, HCNO: An experimental and theoretical study

  Marius Gerlach, Tobias Preitschopf, Emil Karaev, Heidy M. Quitián-Lara, Dennis Mayer, John Bozek, Ingo Fischer and Reinhold F. Fink

  Phys. Chem. Chem. Phys. **2022**, *24*, 15217-15229

- Photoelectron spectroscopy and dissociative photoionization of fulminic acid, HCNO

  Marius Gerlach, Barry Mant, Tobias Preitschopf, Emil Karaev, Dennis Mayer, Heidy M. Quitián-Lara, Patrick Hemberger, John Bozek, Graham Worth and Ingo Fischer

  J. Chem. Phys. **2023**, *158*, 134303.

- X-ray induced fragmentation of fulminic acid, HCNO

  Marius Gerlach, Dorothee Schaffner, Tobias Preitschopf, Emil Karaev, John Bozek, Fabian Holzmeier and Ingo Fischer

  Submitted to *J. Chem. Phys.*

Furthermore during my Phd thesis, the following articles were published, which are not discussed in this thesis:

- Kinetics of 1- and 2-methylallyl + O_2 reaction, investigated by photoionisation using synchrotron radiation

  Domenik Schleier, Engelbert Reusch, Marius Gerlach, Tobias Preitschopf, Deb Pratim Mukhopadhyay, Nancy Faßheber, Gernot Friedrichs, Patrick Hemberger and Ingo Fischer

  Phys. Chem. Chem. Phys., **2021**, *23*, 1539

- Fragmentation of isocyanic acid, HNCO, following core excitation and ionization

  Marius Gerlach, Felipe Fantuzzi, Lilith Wohlfart, Karina Kopp, Bernd Engels, John Bozek, Christophe Nicolas, Dennis Mayer, Markus Gühr, Fabian Holzmeier and Ingo Fischer

  J. Chem. Phys. **2021**, *154*, 114302

- Femtosecond dynamics of diphenylpropynylidene in ethanol and dichloromethane

  Lea Ress, Dennis Kaiser, Janine Grüne, Marius Gerlach, Engelbert Reusch, Tobias Brixner, Andreas Sperlich, Bernd Engels and Ingo Fischer

  Spectrochim. Acta, Part A **2021**, *254*, 119606.

- Threshold Photoelectron Spectrum of Cyclobutadiene: Comparison with Time-Dependent Wavepacket Simulations

  Lea Bosse, Barry Mant, Domenik Schleier, Marius Gerlach, Ingo Fischer, Anke Krueger, Patrick Hemberger and Graham Worth

  J. Phys. Chem. Lett. **2021**, *12*, 6901-6906.

- Photoelectron Photoion Coincidence Spectroscopy of NCl_3 and NCl_2

  Marius Gerlach, Sophie Monninger, Domenik Schleier, Patrick Hemberger, Jamie Goettel, Holger Braunschweig and Ingo Fischer

  Chemphyschem **2021**, *22*, 2164-2167.

- Threshold photoelectron spectroscopy of iminoborane, HBNH

  Domenik Schleier, Dorothee Schaffner, Marius Gerlach, Patrick Hemberger and Ingo Fischer

  Phys. Chem. Chem. Phys. **2022**, *24*, 20-24.

- Photoelectron spectroscopy of low valent organophosphorus compounds, P–CH_3, H–P=CH_2 and P=CH_2

  Deb Pratim Mukhopadhyay, Marius Gerlach, Sebastian Hartweg, Ingo Fischer and Jean-Christophe Loison

  Phys. Chem. Chem. Phys. **2022**, *24*, 10993-10999.

- Ammonia Borane, NH_3-BH_3 : A Threshold Photoelectron-Photoion Coincidence Study of a Potential Hydrogen-Storage Material

  Domenik Schleier, Marius Gerlach, Deb Pratim Mukhopadhyay, Emil Karaev, Dorothee Schaffner, Patrick Hemberger and Ingo Fischer

  Chem. Eur. J **2022**, *28*, e202201378.

- Threshold photoelectron spectroscopy of trimethylborane and its pyrolysis products

  Domenik Schleier, Marius Gerlach, Dorothee Schaffner, Deb Pratim Mukhopadhyay, Patrick Hemberger and Ingo Fischer

  Phys. Chem. Chem. Phys. **2023**, *25*, 4511-4518.

- Threshold Photoelectron Spectrum of *m*-Benzyne

  Marius Gerlach, Emil Karaev, Dorothee Schaffner, Patrick Hemberger and Ingo Fischer

  J. Phys. Chem. Lett. **2022**, *13*, 11295-11299.

- Bonding in Low-Coordinated Organoarsenic and Organoantimony Compounds: A Threshold Photoelectron Spectroscopic Investigation

  Emil Karaev, Marius Gerlach, Lukas Faschingbauer, Jacqueline Ramler, Ivo Krummenacher, Crispin Lichtenberg, Patrick Hemberger and Ingo Fischer

  J. Chem. Phys. **2023**, *29*, e202300637.

CHAPTER 1

Introduction

1.1 The history of fulminic acid

Fulminic acid, HCNO, has fascinated chemists since 1800, when it was first discovered by Edward Howard.[1] In those times, chemists still believed that the element "murium" existed, which together with hydrogen and oxygen formed hydrochloric acid, HCl.[2] Howard's goal was to synthesize muriate salts, so he combined ethanol, nitric acid and mercury oxide. Ethanol and nitric acid were meant to be the sources of hydrogen and oxygen, respectively, while the mercury served as a metal base for the salt. The product was a white solid. The common test for murium was the addition of sulfuric acid, producing gaseous HCl. However, when Howard added sulfuric acid to this compound a violent explosion ensued instead. Howard now knew that he had not produced a muriate salt and instead named this new substance, after its explosive properties, "fulminating mercury".[1]

Howard had produced mercury fulminate $Hg(CNO)_2$. Adding sulfuric acid led to the highly exothermic formation of fulminic acid, HCNO. It has to be noted here, that the free acid is nonexplosive, instead the released heat of the reaction caused the explosion of unreacted mercury fulminate. Mercury fulminate itself has a captivating history; due to its high explosive power, it was used as an initiating explosive to set off more tame explosives like gunpowder.[3] It was also the initiating explosive used by Alfred Nobel to detonate his dynamite explosive.[4,5]

The composition and structure of fulminic acid and fulminate puzzled chemists for close to 150 years. In 1824, Justus Liebig published the quantitative analysis of silver and mercury fulminate[6] and found that they were identical to the composition of the seemingly unrelated compound silver cyanate (AgNCO) published in the same year by Friedrich Wöhler.[7] This led to a disagreement and Liebig accused Wöhler of making a mistake.[8,9] Only after a personal meeting and another round of experiments, Liebig was convinced that both results were correct.[10] These findings conflicted with the contemporary idea that the properties of a substance were solely dependent on its composition. Thus, Jöns Jakob Berzelius suggested that the way that these atoms are connected with each other, i.e., the chemical structure is also important. He introduced the concept of isomerism to explain these and other observations.[8,11]

The structure of fulminic acid, HCNO, and its isomer isocyanic acid, HNCO, as well as their salts turned out to be challenging questions. In the beginning, it was believed that fulminic acid contained two carbon atoms since the still employed synthesis by Howard was based on ethanol.[1] This led to several erroneous suggestions. Of note are those by August Kekulé who gained fame for coming up with the correct structure of benzene in 1865.[18,19] He proposed the structure $H_2C(NO_2)CN$ (**3**, Figure 1.1).[14,15] Others also put forward structures based on two carbon atoms[16,17,20], some of which are shown in Figure 1.1.

In 1892, Nef first proposed a structure containing only one of each atom.[13] His structure (**2** in Figure 1.1) contained a divalent carbon atom, a novel concept at the time. Today we know that his structure is that of the isofulminic acid. The correct structure was first suggested by Ley and Kissel, two researchers from the Universität Würzburg in 1899.[12] Lothar Wöhler could show in 1905 that indeed

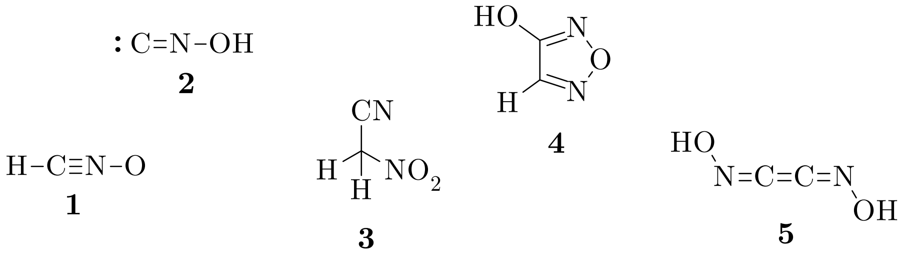

Figure 1.1: Proposed structures of fulminic acid throughout the years. **1** was first suggested by Ley and Kiesel[12], while Nef suggested **2**[13]. The two-carbon variants **3**, **4** and **5** were introduced by Kekulé,[14,15] Divers[16] and Steiner[17], respectively.

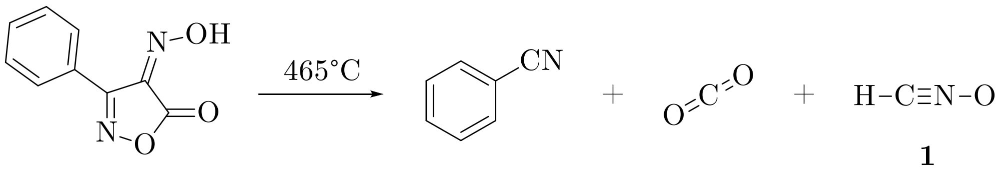

1

Figure 1.2: Pyrolytic route to fulminic acid, HCNO, developed by Wentrup *et al.*.[26]

fulminic acid was of the monomeric variety by determining the freezing-point depression in water.[21] In 1926, Linus Pauling provided a powerful argument against **2** and in favor of **1**.[22] He calculated the free energies of HONC and HCNO and concluded that HCNO is the correct structure of fulminic acid.[22] This constitutes one of the earliest examples where calculations were conducted to enhance the chemical understanding. Finally, the first convincing experimental evidence for **1** was provided in 1961 by Huisgen. In his work to elucidate the 1,3-dipolar cycloadditions he found that fulminic acid reacted with dipolarophiles and formed products consistent with structure **1**.[23] With the advent of molecular spectroscopy the final piece of evidence was obtained in the form of infrared and microwave spectroscopy. In 1966, Beck and Feldl measured its IR spectrum[24] and observed a C-H stretching mode (3335 cm^{-1}) and no O-H stretching mode. The observed spectrum was similar to that of nitrous oxide, NNO. The microwave spectra[25] supported these findings and found a linear structure with the bond lengths r(C-H) = 1.027 Å, r(C-N) = 1.161 Å and r(N-O) = 1.207 Å. Finally, the doubts surrounding the composition and structure and fulminic acid had been removed.

As discussed, the synthesis of fulminic acid involved the highly explosive fulminate salts of mercury and sodium and was still more or less based on the procedure provided by Edward Howard in 1800. In 1979, Curt Wentrup introduced a much safer synthesis, albeit with a more complex setup. His route went *via* the gas-phase pyrolysis of the phenyl-substituted isoxazol-5(4H)-ones, which produces carbon dioxide, benzonitrile and fulminic acid (see Figure 1.2).[26] All experimental studies after this publication used the new gas-phase pyrolysis route.

Further detailed studies have been conducted by IR[27–29] and microwave spectroscopy.[30,31] The VUV absorption spectrum,[32] photoelectron spectrum[33] and penning ionization spectrum[34] have also been measured. Bondybey and English measured the IR spectrum of HOCN after irradiation of HCNO with a Xe arc lamp in a Ne matrix.[35] The mass spectrometry of HCNO[36] and the gas-phase reactions of HCNO with small radicals were also studied.[37–44] Due to its small size and unusual properties, HCNO has also been the subject of numerous in-depth computational studies.[44–53] Particular interest is given to the "floppy" nature of the molecule owed to the HCN bending mode with a wavenumber of 225 cm^{-1} and a remarkably flat potential energy surface. For this reason, HCNO is considered a quasilinear molecule. These properties even inspired two limericks, which are included in a review on quasilinear and quasiplanar molecules.[48] Monda *et al.* examined the occurrence of Jahn-Teller and Renner-Teller interactions in the $HCNO^+$ cation,[53] while Luna *et al.* computed the potential energy surface of $HCNO^+$ and its isomers.[50]

In summary, fulminic acid and its isomers have been used as model systems to better understand chemical theory and also to test new ideas and methods. This can be attributed to its small size limiting the degrees of freedom, thus decreasing the complexity, and allowing for more detailed analysis. Research on fulminic acid was for a long time at the cutting edge of chemistry and, in some sense, its history reflected the current state-of-the art. In the span of 200 years chemists evolved from believing in the fictional element murium to introducing isomerism and chemical structures and finally towards investigating these molecules with complex experiments and high-level quantum chemical theories. Looking back, it is intriguing to ponder what chemists will think of the science conducted today, for example the research presented in this thesis.

1.2 HCNO in interstellar space

Hydrogen, carbon, nitrogen, and oxygen are the essential elements of organic life. They make up more than 90% of biomass on planet earth.[54] fulminic acid and its isomers isofulminic acid, HONC, cyanic acid, HOCN, and isocyanic acid, HNCO, form a tetrad of species called CHON. Their relative stability is pictured in

Figure 1.3, showing that HNCO is the most stable isomer.[51] A prebiotic role has been suggested for the molecules of the CHNO tetrad, meaning that they may be intermediates in the formation of larger biochemical compounds. Isocyanic acid, HNCO, has been discussed in particular as it may react with H_2 to produce formamide,[55] a key prebiotic precursor.[56]

HCNO was first detected in interstellar space by Marcelino *et al.* *via* its microwave spectrum using the 3 mm band of the IRAM 30m radio telescope.[57] It was observed towards the dark molecular clouds B1, L1544 and L183, and in the low-mass protostar L1527. It has now been detected in numerous interstellar objects such as L1157-mm, NGC1333 IRAS4a, L1157-B1 and the dense core L483.[58–61] Fulminic acid is most likely formed in interstellar space through the neutral-neutral reaction $CH_2 + NO \rightarrow HCNO + H$.[57] Both experimental and theoretical evidence has been provided for this reaction,[62–64] while Zhang *et al.* computed that the main product of this reaction should be HNCO + H.[65] On grain surfaces HCNO is believed to be formed by the reaction of CNO and H adsorbed on the grain.[66] Isofulminic acid, HONC, is the only isomer in the tetrad that has not yet been detected in interstellar space, although its laboratory microwave spectrum is known.[67]

Isocyanic acid is the most abundant isomer in interstellar space with HNCO/HCNO ratios of 40 to 70 in the protostar L1527.[57] HNCO was first de-

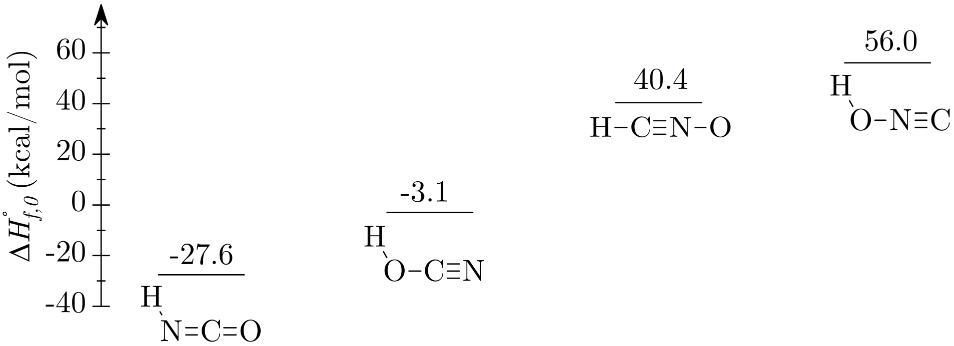

Figure 1.3: Relative heats of formation of the isomers of the CHON tetrad calculated by Schuurman *et al.*.[51] Values are given in kcal/mol.

tected in 1972 in Sagittarius B2, a giant molecular cloud close to the center of the milky way.[68] Since then, isocyanic acid has been detected in massive star forming regions,[69–71], in galactic and extragalactic interstellar media,[72] and in over 50 other sources.[58,73–79] Cyanic acid, HOCN, has so far been identified in Sagittarius B2 and few other sources.[61,80,81] In cold sources the abundance of cyanic and fulminic acid are roughly equal, while in hot sources cyanic acid is at least 10 to 100 times more abundant. In a 2010 publication Marcelino *et al.* attempted to explain these observations with two gas-phase models and one gas-grain model.[61] They were not able to reproduce the results and concluded that the chemistry of the CHNO isomers is still "poorly understood" and that in particular for HCNO the model may be missing an important destruction mechanism.

1.3 Interstellar VUV and X-ray radiation

One possible destruction mechanism of molecules in interstellar space is the interaction with highly energetic photons, such as vacuum ultraviolet (VUV) and X-ray radiation.

Interstellar VUV radiation is produced by early type stars in the galaxy, also called the diffuse radiation field.[82] It is a combination of diffuse galactic and extragalactic light.[83] Diffuse galactic light originates from stars in the galactic plane scattered by interstellar dust,[84] while extragalactic light has several sources, the biggest of which are other galaxies.[85] VUV radiation influences the chemistry in interstellar space and on grains.[86] It could be shown, for example, that VUV photolysis of interstellar ice analogues could produce amino acids.[87,88] Irradiating ice mixtures containing H_2O, CO, CO_2, CH_3OH and NH_3 with light from a hydrogen flow discharge lamp produced a vast catalog of species including glycine, alanine, valine and serine.[88] These measurements support the hypothesis that the first amino acids were not formed on earth, but rather transported here by cometary dust, meteorites or dust particles.

Dark clouds or dense clouds are considered opaque to VUV photons. The photons are absorbed by the outermost layer of the cloud and do not penetrate deeper. In these dense clouds, Philips *et al.* measured an unexpectedly high ratio of carbon to carbon monoxide,[89] indicating that their model was missing an efficient destruction mechanism from CO to C. Prasad and Tarafdar then proposed a new mechanism that can produce VUV photons in these dark clouds. Cosmic rays with energies from 10 to 100 MeV may ionize molecular hydrogen producing electrons. These electrons in turn electronically excite molecular hydrogen deep in the dense cloud. The excited hydrogen molecules can then emit either a Lyman line producing photons in the range of around 8 to 15 eV.[90] This mechanism is called the Prasad-Tarafdar mechanism and explained discrepancies between the composition of dense clouds measured in experiments and those determined by theoretical models.[90] For the C/CO example above, the model could be corrected by including the photodissociation of CO:[91]

$$\mathrm{CO} + h\nu \rightarrow \mathrm{C} + \mathrm{O} \tag{1.1}$$

Other than photodissociation, VUV photons may also induce photoionization leading to the creation of a photoelectron and a photoion. In certain cases, the produced photoion can have enough energy that it dissociates into a positively charged and a neutral fragment. For some small and well-studied molecules like methanol all pathways, i.e., photodissociation, photoionization and dissociative photoionization are considered in the models.[92] For the CHNO tetrad only the

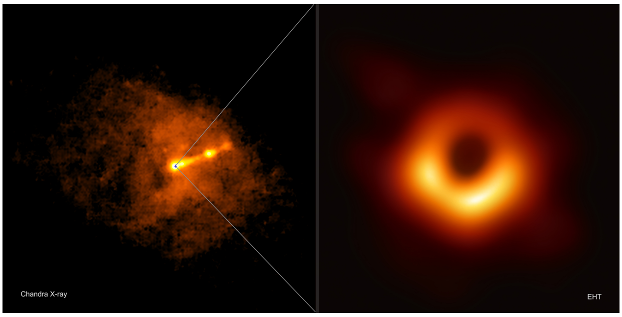

Figure 1.4: Images of Messier 87, the black hole at the center of our galaxy. Shown on the right is the famous picture of M87 captured by the Event Horizon telescope. The picture on the left is an X-ray observation of M87 conducted by the Chandra X-ray observatory. Chandra has a significantly wider field of view. Image credit to NASA/CX-C/Villanova University/J. Neilsen (left) and Event Horizon Telescope collaboration (right).

photodissociation is included in models, while the (dissociative) photoionization is not considered, possibly due to the lack of reliable data.

X-ray radiation is ubiquitous in interstellar space. There exists a cosmic background of X-rays arising from *bremsstrahlung*, black-body radiation and inverse Compton scattering.[93] But X-ray radiation is also produced by discrete objects. Our own sun for example is a source for X-rays.[93] In general, they can be produced by X-ray binary systems,[94], bullet clusters,[95] black holes (see Figure 1.4) and supernova remnants.[96]

An additional class of systems are the super soft X-ray sources (SSXS). They have effective temperatures of 20 to 100 eV or $2 \cdot 10^5$ to $1 \cdot 10^6$ K. A source with an effective temperature of 70 eV has its maximum emissivity at around 300 eV. They were first recognized as a new class of interstellar sources in 1991 by the Röntgen Observatory Satellite (ROSAT) conducting measurements in the central region of the Large Magellanic Cloud.[97] The most luminous sources can be explained by white dwarfs, which are undergoing stable nuclear burning by accreting H-rich matter from a companion star.[98] White dwarf are remnants of stars, which ended their hydrogen-fusing period and expanded into red giants, which fuse helium to carbon and oxygen. If these red giants are too small to fuse carbon, an inert core of carbon and oxygen will build up. When this red giant sheds its outer-most layer it turns into a white dwarf. In a super soft X-ray source, a white dwarf steadily pulls material, i.e., accretes, from a binary companion star.[99]

X-ray radiation is about an order of magnitude more energetic than VUV photons and the induced processes differ. X-ray radiation is energetic enough to excite or ionize the core electrons of atoms and molecules, i.e., those electrons that do not participate in the formation of chemical bonds. This leads to a “hole” in the core orbital. This core vacancy can be filled by an Auger-Meitner process. Here, a valence electron fills the hole. This released energy is transferred to another valence electron, which gets ejected from the molecule. This effect was discovered by Lise Meitner in 1922[100] and independently by Pierre Auger in 1923.[101] At first, Meitner’s discovery was overlooked, and the process was named after Auger only. In 2019, it was proposed to rename the effect to recognize Meitner’s contribution.[102]

1.4 Outline of this thesis

The goal of this thesis is two-fold. First, investigating how HCNO interacts with ionizing interstellar radiation leads to a better understanding of its fate in interstellar space. We want to find out which cationic states are produced, when HCNO interacts with VUV- or Soft X-ray radiation, but also to which fragments the produced ion dissociates. The other goal of this thesis is to use HCNO as a small, computationally tractable molecule to better understand complicated effects, such as the Renner-Teller distortion or the Auger-Meitner decay. Here, high-level quantum chemical theory will be of integral importance. Before the results are shown in Chapter 3, Chapter 4 and Chapter 5, some required fundamentals are provided. In Chapter 2 the theoretical background of the observed processes is given. In particular, the Auger-Meitner process is explained in more detail. Also details regarding the experiments are provided. Here, focus is given to the EPICEA setup, which was used for the first time in our group. The data is analyzed using a home-written Python program.

In Chapter 3 the photoelectron spectroscopy and subsequent dissociation is investigated. The data sets for this study were collected during two beamtimes, one at the PLÉIADES beamline of the SOLEIL Synchrotron and the other at the VUV beamline of the Swiss Light Source. At the PLÉIADES beamline the high-resolution photoelectron spectrum was recorded using a hemispherical analyzer. At the VUV beamline we used the photoelectron-photoion coincidence setup to elucidate the dissociative photoionization mechanism of the fulminic acid cation. The experimental spectra are compared to quantum chemical calculations.

Our investigation of the interaction soft X-ray photons with fulminic acid, HCNO is shown in Chapter 4. These experiments were conducted at the PLÉIADES beamline. The ionization and excitation of the carbon, oxygen, and nitrogen 1s electron is measured *via* X-ray photoelectron spectra (XPS) and Near-edge X-ray absorption fine structure (NEXAFS) spectra. We then observed the subsequent Auger-Meitner processes by measuring the normal and resonant Auger electron spectra. To extract further information on the observed signals, the Auger-Meitner transition rates were also computed theoretically.

In Chapter 5 of this thesis, we conducted Auger-electron-photoion-coincidence spectroscopy of HCNO. Here, the photoions following the 1s ionization or 1s excitation are measured. The spectra are then examined for site-selective effects, i.e., whether the ionization or excitation of different atomic sites lead to different product distributions.

References

[1] E. Howard, *Philos. Trans. R. Soc.* **1800**, *90*, 204–238.

[2] H. E. Le Grand, *Ann. Sci* **1974**, *31*, 213–225.

[3] E. G. Wright, *Tilloch's Philos. Mag.* **1823**, *62*, 203–204.

[4] J. Thompson, A. F., *J. Chem. Educ.* **1943**, *20*, 151.

[5] A. Nobel, *J. Soc. Arts* **1875**, *23*, 611–630.

[6] J. Liebig, *Ann. Chim.* **1824**, *24*, 294–318.

[7] F. Wöhler, *Ann. Phys.* **1824**, *77*, 117–124.

[8] S. Esteban, *J. Chem. Educ.* **2008**, *85*, 1201.

[9] F. Kurzer, *J. Chem. Educ.* **2000**, *77*, 851.

[10] J. Liebig, *Schweiggers Jahrbuch der Chemie und Physik* **1826**, *18*.

[11] J. J. Berzelius, *Jahresberichte über die Fortschritte der Physischen Wissenschaften* **1832**, *11*, 44–48.

[12] H. Ley, H. Kissel, *Ber. Dtsch. Chem. Ges.* **1899**, *32*, 1357–1368.

[13] J. U. Nef, *Justus Liebigs Ann. Chem.* **1894**, *280*, 291–342.

[14] A. Kekulé, *Justus Liebigs Ann. Chem.* **1857**, *101*, 200–213.

[15] A. Kekulé, *Justus Liebigs Ann. Chem.* **1858**, *105*, 279–286.

[16] E. Divers, *J. Chem. Soc. Trans.* **1884**, *45*, 18–24.

[17] A. Steiner, *Ber. Dtsch. Chem. Ges.* **1883**, *16*, 1484–1486.

[18] A. Kekulé, *Justus Liebigs Ann. Chem.* **1866**, *137*, 129–196.

[19] A. Kekulé, *Justus Liebigs Ann. Chem.* **1872**, *162*, 77–124.

[20] H. E. Armstrong, *J. Chem. Soc. Trans.* **1884**, *45*, 25–27.

[21] L. Wöhler, *Ber. Dtsch. Chem. Ges.* **1905**, *38*, 1351–1359.

[22] L. Pauling, S. B. Hendricks, *J. Am. Chem. Soc.* **1926**, *48*, 641–651.

[23] R. Huisgen, *Proc. Chem. Soc.* **1961**, 357–396.

[24] W. Beck, K. Feldl, *Angew. Chem.* **1966**, *78*, 746–746.

[25] M. Winnewisser, H. K. Bodenseh, *Z. Naturforsch. A* **1967**, *22*, 1724.

[26] C. Wentrup, B. Gerecht, H. Briehl, *Angew. Chem. Int. Ed.* **1979**, *18*, 467–468.

[27] B. P. Winnewisser, M. Winnewisser, *J. Mol. Spectrosc.* **1969**, *29*, 505–507.

[28] W. Beck, P. Swoboda, K. Feldl, R. S. Tobias, *Chem. Ber.* **1971**, *104*, 533–543.

[29] B. P. Winnewisser, P. Jensen, *J. Mol. Spectrosc.* **1983**, *101*, 408–421.

[30] B. P. Winnewisser, M. Winnewisser, F. Winther, *J. Mol. Spectrosc.* **1974**, *51*, 65–96.

[31] B. P. Winnewisser, M. Winnewisser, G. Wagner, J. Preusser, *J. Mol. Spectrosc.* **1990**, *142*, 29–56.

[32] W. D. Sheasley, C. W. Mathews, *J. Mol. Spectrosc.* **1972**, *43*, 467–471.

[33] J. Bastide, J. P. Maier, *Chem. Phys.* **1976**, *12*, 177–190.

[34] T. Pasinszki, N. Kishimoto, K. Ohno, *J. Phys. Chem. A* **1999**, *103*, 6746–6756.

[35] V. E. Bondybey, J. H. English, C. W. Mathews, R. J. Contolini, *J. Mol. Spectrosc.* **1982**, *92*, 431–442.

[36] C. E. C. A. Hop, K. J. Van den Berg, J. L. Holmes, J. K. Terlouw, *J. Am. Chem. Soc.* **1989**, *111*, 72–75.

[37] W. Feng, J. P. Meyer, J. F. Hershberger, *J. Phys. Chem. A* **2006**, *110*, 4458–4464.

[38] W. Feng, J. F. Hershberger, *J. Phys. Chem. A* **2006**, *110*, 12184–12190.

[39] W. Feng, J. F. Hershberger, *J. Phys. Chem. A* **2007**, *111*, 3831–3835.

[40] W. Feng, J. F. Hershberger, *J. Phys. Chem. A* **2007**, *111*, 10654–10659.

[41] W. Feng, J. F. Hershberger, *J. Phys. Chem. A* **2012**, *116*, 10285–10292.

[42] W. Feng, J. F. Hershberger, *J. Phys. Chem. A* **2014**, *118*, 829–837.

[43] W. Feng, J. F. Hershberger, *Chem. Phys.* **2016**, *472*, 18–23.

[44] H. M. T. Nguyen, T. N. Nguyen, L. Vereecken, *Combust. Flame* **2018**, *190*, 317–326.

[45] G. H. Kirby, *J Mol Struct* **1975**, *26*, 77–83.

[46] A. Rey Planells, A. Espinosa Ferao, *New J. Chem.* **2022**, *46*, 5771–5778.

[47] P. R. Bunker, B. M. Landsberg, B. P. Winnewisser, *J. Mol. Spectrosc.* **1979**, *74*, 9–25.

[48] P. R. Bunker, *Annu. Rev. Phys. Chem.* **1983**, *34*, 59–75.

[49] J. Koput, B. P. Winnewisser, M. Winnewisser, *Chem. Phys. Lett.* **1996**, *255*, 357–362.

[50] A. Luna, A. M. Mebel, K. Morokuma, *J. Chem. Phys.* **1996**, *105*, 3187–3205.

[51] M. S. Schuurman, S. R. Muir, W. D. Allen, H. F. S. III, *J. Chem. Phys.* **2004**, *120*, 11586–11599.

[52] M. Mladenović, M. Lewerenz, *Chem. Phys.* **2008**, *343*, 129–140.

[53] R. Mondal, D. Mukhopadhyay, *Int. J. Quantum. Chem.* **2020**, *120*, e26195.

[54] S. V. Vassilev, D. Baxter, L. K. Andersen, C. G. Vassileva, *Fuel* **2010**, *89*, 913–933.

[55] M. Ferus, V. Laitl, A. Knizek, P. Kubelík, J. Sponer, J. Kára, J. E. Sponer, B. Lefloch, G. Cassone, S. Civiš, *Astron. Astrophys.* **2018**, *616*, A150.

[56] A. López-Sepulcre, N. Balucani, C. Ceccarelli, C. Codella, F. Dulieu, P. Theulé, *ACS Earth Space Chem.* **2019**, *3*, 2122–2137.

[57] N. Marcelino, J. Cernicharo, B. Tercero, E. Roueff, *Astrophys. J.* **2009**, *690*, L27–L30.

[58] E. Mendoza, B. Lefloch, A. López-Sepulcre, C. Ceccarelli, C. Codella, H. M. Boechat-Roberty, R. Bachiller, *Mon. Not. R. Astron. Soc.* **2014**, *445*, 151–161.

[59] B. Lefloch, R. Bachiller, C. Ceccarelli, J. Cernicharo, C. Codella, A. Fuente, C. Kahane, A. López-Sepulcre, M. Tafalla, C. Vastel, E. Caux, M. González-García, E. Bianchi, A. Gómez-Ruiz, J. Holdship, E. Mendoza, J. Ospina-Zamudio, L. Podio, D. Quénard, E. Roueff, N. Sakai, S. Viti, S. Yamamoto, K. Yoshida, C. Favre, T. Monfredini, H. M. Quitián-Lara, N. Marcelino, H. M. Boechat-Roberty, S. Cabrit, *Mon. Not. R. Astron Soc.* **2018**, *477*, 4792–4809.

[60] N. Marcelino, M. Agúndez, J. Cernicharo, E. Roueff, M. Tafalla, *Astron. Astrophys.* **2018**, *612*, L10.

[61] N. Marcelino, S. Brünken, J. Cernicharo, D. Quan, E. Roueff, E. Herbst, P. Thaddeus, *Astron. Astrophys.* **2010**, *516*, A105.

[62] J. Roggenbuck, F. Temps, *Chem. Phys. Lett.* **1998**, *285*, 422–428.

[63] G. Eshchenko, T. Köcher, C. Kerst, F. Temps, *Chem. Phys. Lett.* **2002**, *356*, 181–187.

[64] M. Fikri, S. Meyer, J. Roggenbuck, F. Temps, *Faraday Discuss.* **2002**, *119*, 223–242.

[65] W. Zhang, B. Du, C. Feng, *J. Mol. Struct.: THEOCHEM* **2004**, *679*, 121–125.

[66] D. H. Quan, E. Herbst, Y. Osamura, E. Roueff, *Astrophys. J.* **2010**, *725*, 2101–2109.

[67] M. Mladenović, M. Lewerenz, M. C. McCarthy, P. Thaddeus, *J. Chem. Phys.* **2009**, *131*, 174308.

[68] L. E. Snyder, D. Buhl, *Astrophys. J.* **1972**, *177*, 619.

[69] E. Churchwell, D. Wood, P. C. Myers, R. V. Myers, *Astrophys. J.* **1986**, *305*, 405–416.

[70] G. A. Blake, E. C. Sutton, C. R. Masson, T. G. Phillips, *Astrophys. J.* **1987**, *315*, 621–645.

[71] S. E. Bisschop, J. K. Jorgensen, E. F. van Dishoeck, E. B. M. de Wachter, *Astron. Astrophys.* **2007**, *465*, 913–U123.

[72] Nguyen-Q-Rieu, C. Henkel, J. M. Jackson, R. Mauersberger, *Astron. Astrophys.* **1991**, *241*, L33.

[73] J. M. Jackson, J. T. Armstrong, A. H. Barrett, *Astrophys. J.* **1984**, *280*, 608–614.

[74] I. Zinchenko, C. Henkel, R. Q. Mao, *Astron. Astrophys.* **2000**, *361*, 1079–1094.

[75] M. Wang, C. Henkel, Y.-N. Chin, J. B. Whiteoak, M. Hunt Cunningham, R. Mauersberger, D. Muders, *Astron. Astrophys.* **2004**, *422*, 883–905.

[76] S. Martín, M. A. Requena-Torres, J. Martín-Pintado, R. Mauersberger, *Astrophys. J.* **2008**, *678*, 245.

[77] S. Martín, J. Martín-Pintado, R. Mauersberger, *Astrophys. J.* **2009**, *694*, 610.

[78] Y.-J. Kuan, L. E. Snyder, *Astrophys. J.* **1996**, *470*, 981.

[79] B. E. Turner, R. Terzieva, E. Herbst, *Astrophys. J.* **1999**, *518*, 699–732.

[80] S. Brünken, C. A. Gottlieb, M. C. McCarthy, P. Thaddeus, *Astrophys. J.* **2009**, *697*, 880.

[81] S. Brünken, A. Belloche, S. Martín, L. Verheyen, K. M. Menten, *Astron. Astrophys.* **2010**, *516*, A109.

[82] P. M. Gondhalekar, R. Wilson, *Philos. Trans. R. Soc. London A* **1975**, *279*, 331–336.

[83] M. S. Akshaya, J. Murthy, S. Ravichandran, R. C. Henry, J. Overduin, *Astrophys. J.* **2018**, *858*, 101.

[84] M. Jura, *Astrophys. J.* **1979**, *227*, 798–800.

[85] S. P. Driver, S. K. Andrews, L. J. Davies, A. S. G. Robotham, A. H. Wright, R. A. Windhorst, S. Cohen, K. Emig, R. A. Jansen, L. Dunne, *Astrophys. J.* **2016**, *827*, 108.

[86] C. Cecchi-Pestellini, R. Saija, M. A. Iatì, A. Giusto, F. Borghese, P. Denti, S. Aiello, *Astrophys. J.* **2005**, *624*, 223.

[87] M. P. Bernstein, J. P. Dworkin, S. A. Sandford, G. W. Cooper, L. J. Allamandola, *Nature* **2002**, *416*, 401–403.

[88] G. M. Muñoz Caro, U. J. Meierhenrich, W. A. Schutte, B. Barbier, A. Arcones Segovia, H. Rosenbauer, W. H. P. Thiemann, A. Brack, J. M. Greenberg, *Nature* **2002**, *416*, 403–406.

[89] T. G. Phillips, P. J. Huggins, T. B. H. Kuiper, R. E. Miller, *Astrophys. J.* **1980**, *238*, L103–L106.

[90] S. S. Prasad, S. P. Tarafdar, *Astrophys. J.* **1983**, *267*, 603–609.

[91] R. Gredel, S. Lepp, A. Dalgarno, *Astrophys. J.* **1987**, *323*, L137.

[92] R. Gredel, S. Lepp, A. Dalgarno, E. Herbst, *Astrophys. J.* **1989**, *347*, 289.

[93] P. Morrison, *Annu. Rev. Astron. Astrophys.* **1967**, *5*, 325–350.

[94] C. F. Bradshaw, E. B. Fomalont, B. J. Geldzahler, *Astrophys. J.* **1999**, *512*, L121.

[95] D. Clowe, M. Bradač, A. H. Gonzalez, M. Markevitch, S. W. Randall, C. Jones, D. Zaritsky, *Astrophys. J.* **2006**, *648*, L109.

[96] J. Vink, *Astron. Astrophys. Rev.* **2012**, *20.*

[97] J. Trümper, G. Hasinger, B. Aschenbach, H. Bräuninger, U. G. Briel, W. Burkert, H. Fink, E. Pfeffermann, W. Pietsch, P. Predehl, J. H. M. M. Schmitt, W. Voges, U. Zimmermann, K. Beuermann, *Nature* **1991**, *349*, 579–583.

[98] C. Maitra, F. Haberl, *Astron. Astrochem.* **2022**, *657*, A26.

[99] P. Kahabka, E. P. J. van den Heuvel, *Annu. Rev. Astron. Astrophys.* **1997**, *35*, 69–100.

[100] L. Meitner, *Z. Phys.* **1922**, *11*, 35–54.

[101] P. Auger, *Comptes rendus hebdomadaires des séances de l'Académie des sciences* **1923**, *177*, 169–171.

[102] D. Matsakis, A. Coster, B. Laster, R. Sime, *Phys. Today* **2019**, *72*, 10–11.

CHAPTER 2

Methods

This chapter summarizes the methods that are investigated in the presented publications. In this thesis, synchrotron radiation, specifically VUV- and soft X-ray radiation, is used. The production and properties of synchrotron radiation are well described in numerous textbooks.[1,2] Here I will focus on the processes initiated by soft X-ray ionization. Extensive literature is available on photoelectron spectroscopy[3,4], dissociative photoionization[5] and threshold photoelectron photoion coincidence spectroscopy[6–8] and will also not be expanded on here. Further literature is also cited in the respective chapters.

Soft X-ray photons have energies of roughly 100 eV to a few keV. In this energy range it is possible to excite or ionize the core electrons in molecules and atoms. The processes of core ionization will be covered in Section 2.1 and the normal Auger-Meitner process in Section 2.2. The sections 2.3 and 2.4 will expand on the X-ray absorption spectroscopy and the resonant Auger-Meitner process and the fragmentation following the Auger-Meitner decay will be outlined in Section 2.5.

The hemispherical analyzer used in Chapter 3 and Chapter 4 is also elaborated on briefly in Section 2.6. Then, details are given on the setup and data treatment of the EPICEA setup (Section 2.7). For the threshold electron photoion coincidence setup, used in Chapter 3, detailed procedures on the data treatment are already available in the literature.[6,9–11] The fundamentals of dissociative photoionization and the modeling using the minimalPEPICO program are described in Ref. [5].

2.1 X-ray photoelectron spectroscopy

In X-ray photoelectron spectroscopy a molecule M absorbs the energy of an X-ray photon $h\nu$, this produces a molecular cation M^+ and a photoelectron e^-. This process is in principle identical to that of conventional photoelectron spectroscopy using vacuum ultraviolet (VUV) radiation. The difference lies in the energy of the incident photon and consequently in the electron that gets ejected. Soft X-ray radiation is energetic enough to affect the core electrons in atoms and molecules, while VUV radiation interacts with the valence electron,[3] these processes are depicted in Figure 2.1. Thus, ionization *via* soft X-ray photons produces a molecular cation, where an electron from a core orbital is removed:

$$M + h\nu \rightarrow M^+(Core^{-1}) + e^-_{ph} \tag{2.1}$$

By invoking Koopmans' theorem, the ionization energy IE(Core) of an electron in the core orbital is equal to the negative orbital energy E(Core)[12]:

$$-E(Core) = IE(Core). \tag{2.2}$$

Typically, the photon energy is chosen to be far above the core orbital ionization energy. Due to its much smaller mass, the excess energy of this process is transferred almost entirely to the photoelectron as kinetic energy eKE,[13] which is given by

$$eKE = h\nu - IE(Core). \tag{2.3}$$

The kinetic energy eKE is measured during X-ray photoelectron spectroscopy. With the photon energy, the core electron ionization energies in atoms and molecules can be calculated. In this context, it is useful to introduce the binding energy E_B, which is defined as the difference between the energy deposited in the molecule by the photon and the energy that was removed again by the photoelectron. It represents the energy that remains in the molecule relative to the neutral ground state:

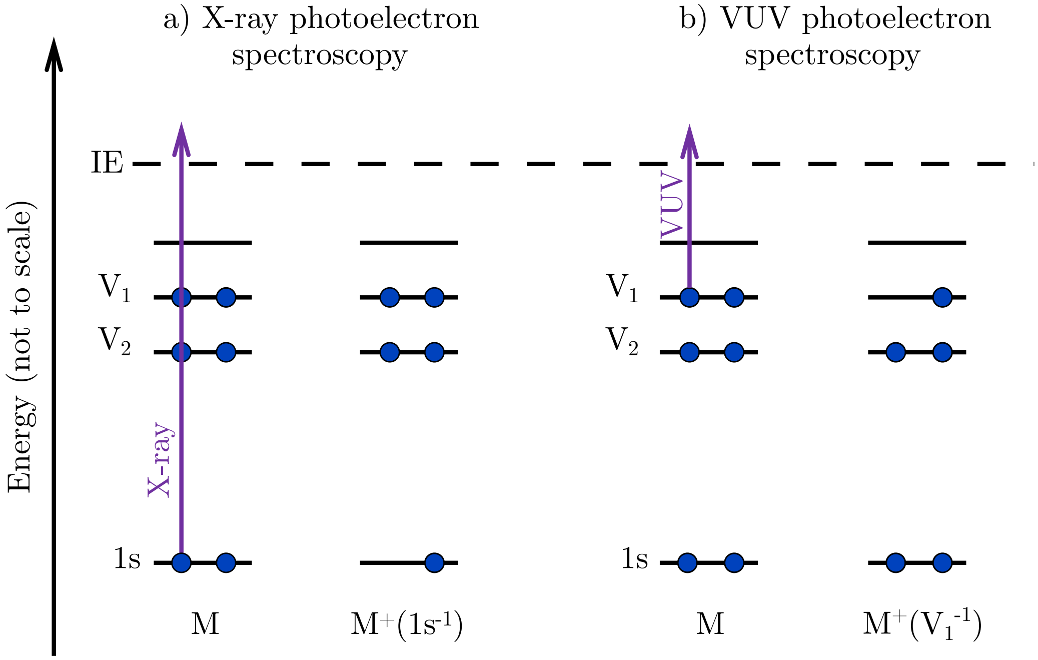

Figure 2.1: Schematic representation of a) X-ray photoelectron spectroscopy and b) VUV photoelectron spectroscopy. In this case, the core orbital is a 1s orbital, but the concept applies to any type of core orbital.

$$\begin{aligned} E_B &= h\nu - eKE \\ &\text{with Equation 2.3} \\ E_B &= IE(Core). \end{aligned} \tag{2.4}$$

On the binding energy scale, the core ionization energy can be easily extracted from the maximum of the signal in the X-ray photoelectron spectrum. In this context, the term binding energy and ionization energy are used interchangeably.

Since the core orbitals do not participate in the formation of valence bonds in molecules, they remain highly localized at the atom. This also means that the corresponding orbital energies (and ionization energies) are mostly unchanged, which leads to characteristic core orbital binding energies for each element. For example, the 1s ionization energies in carbon, nitrogen and oxygen are around 290 eV, 410 eV and 540 eV, respectively. In the third period of the periodic table, the 2s and 2p orbitals are also formally core orbitals. Sulfur for example has binding energies of around 2470, 230 and 160 eV for the 1s, 2s and 2p orbitals, respectively.

As mentioned, these binding energies change slightly when the atoms are involved in molecular bonds. They are mostly affected by the electronegativity of the neighboring elements.[3] Electronegative substituents will remove electron density from an atomic site and the remaining electrons are subjected to a higher effective atomic charge. This increases their binding energy. The inverse is true for electropositive substituents leading to lower binding energies. This effect is illustrated by the molecule ethyl-trifluoroethylacetat $CF_3COOCH_2CH_3$. The four carbon atoms have substituents with significantly different electronegativities. This leads to binding energies of 299.6, 297.1, 293.0, 291.2 eV going from CF_3 to CH_3, i.e., a maximum separation of roughly 8 eV.[3] This shows that in general this shift will be small compared to the absolute binding energy.

Since the binding energies of different elements are well separated, it is possible to selectively ionize only the 1s electrons of a particular element in a molecule. So, with HCNO we can ionize for example only the O1s electron. This is true although the O1s ionization energy is higher than, for example, the N1s ionization energy, meaning that technically the N1s electron could also be ejected from the molecule. The core orbital ionization cross section in atoms scales roughly as $\Delta E^{-2.7}$, where ΔE is the excess energy relative to the respective ionization energy.[14,15] Assuming that the core orbital cross section in molecules are similar to those of the free atoms the ionization edge closest in energy has a substantially larger cross section.

There are a number of different detectors that can measure high kinetic energy photoelectrons. An overview over these detectors can be found in textbooks.[3,16,17] The detectors used in this thesis are described in Section 2.6 and Section 2.7.

2.2 Normal Auger-Meitner processes

The molecular cation $M^+(CO^{-1})$, which is created by core orbital ionization, is highly excited. These excited molecules can then relax electronically *via* two competing processes. When a valence electron fills the vacancy, this energy can be converted to a photon through X-ray fluorescence (Figure 2.2 b)). The other possibility is the Auger-Meitner decay. For low-Z elements like carbon, nitrogen and oxygen the Auger electron yield is around 99%.[4,16] With rising atomic number fluorescence becomes more likely and at Z = 30 both transitions are roughly equally likely.[4,16] Both of these processes occur on timescales below 10 fs and are typically faster than molecular dissociation.[13]

In the Auger-Meitner decay, a valence electron also fills the vacancy in the core orbital. This releases energy equal to the orbital energy difference $E(V_1) - E(Core)$. Note that the orbital energies are formally negative. This energy is transferred to another valence electron which gets ejected from the molecule. The excess energy of this process is transferred to the kinetic energy of the ejected electron, which is called the Auger electron. The kinetic energy of the Auger electron E^A_{kin} is the difference of the excess energy and the orbital energy of the ionized valence electron.

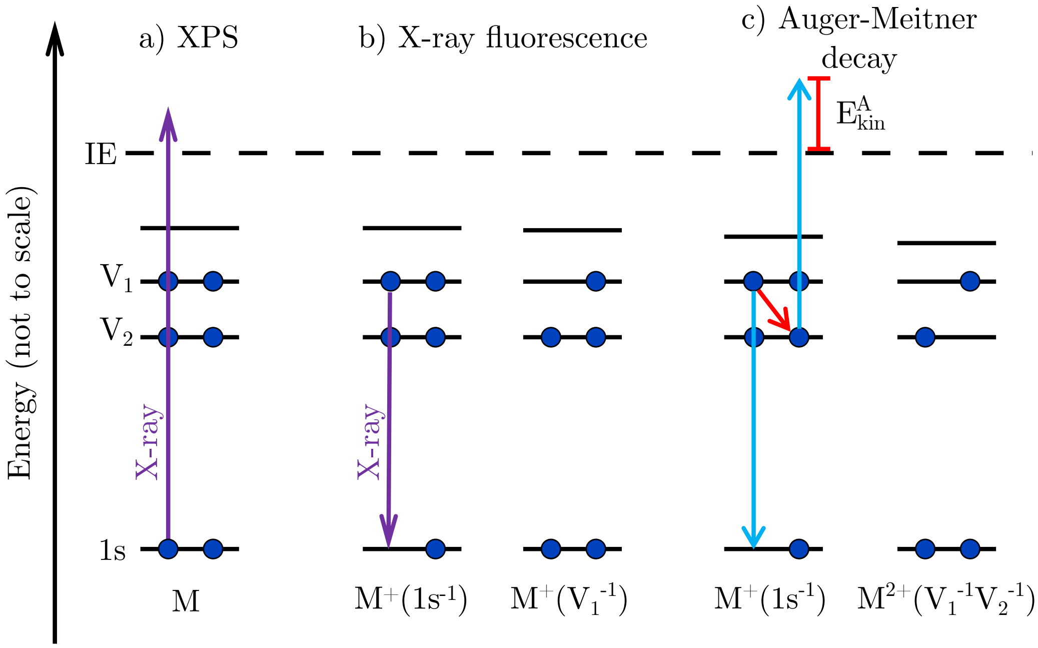

Figure 2.2: Schematic representations of the processes following 1s ionization. a) shows X-ray fluorescence and b) the Auger-Meitner decay. The core orbital is represented by a 1s orbital.

$$E^A_{kin} = E(V_1) - E(Core) + E(V_2) \tag{2.5}$$

In Auger electron spectroscopy the kinetic energy of this Auger electron is measured. Auger-Meitner processes lead to two-hole final states. The depopulated orbitals V_1 and V_2 can be any combination of two valence orbitals in a molecule, or even the same orbital. However, different combinations of orbitals may have different Auger transition rates, and as a result have different intensities in the Auger electron spectra. Like in X-ray photoelectron spectroscopy, we can define a binding energy. Here, the energy that is present in the molecule after 1s ionization is the core orbital energy or, using Equation 2.2, the core ionization energy. Thus, in normal Auger electron spectroscopy the binding energy E_B is defined as:

$$\begin{gathered} E_B = IE(Core) - E^A_{kin} \\ \text{with Equation 2.5 and Equation 2.2} \\ E_B = -(E(V_1) - E(V_2)). \end{gathered} \tag{2.6}$$

The binding energy can be seen as the excess energy of the formed dicationic state relative to the neutral ground state. It also useful to compare the Auger electron spectra on the same energy scale, as the final states have fixed binding energies. Note that both E^A_{kin} and E_B are independent of the incident photon energy.

2.3 X-ray absorption spectroscopy

Instead of ionizing the core electron, it can also be resonantly excited into an unoccupied valence orbital:

$$M + h\nu \rightarrow M^*(CO^{-1}V_1^1) \tag{2.7}$$

These transitions are investigated as part of X-ray absorption spectroscopy. These spectra can be recorded by measuring the incident and transmitted light intensity and calculating the absorption using the Lambert-Beer law.[3] This is however challenging for low sample concentrations, for example in the gas phase.

In this thesis, we determined these resonances using an ion yield detector. As will be shown in Section 2.4, resonantly exciting a core electron leads to the formation of an Auger electron and a cation. The photon energy is then scanned from low to high energies. Whenever the energy is equal to a resonance an increase in total ion yield is observed.

The resulting spectra are split into two energetic regions, the near-edge X-ray absorption fine structure (NEXAFS) region and the extended X-ray absorption fine structure (EXAFS) region. Occasionally, the NEXAFS region is also called X-ray absorption near-edge structure (XANES).[18] NEXAFS is the structure observed just below the core electron ionization energy and it is this region, where the excitation of the core electron into unoccupied orbitals is observed. This transition is pictured in Figure 2.3 a). Similar to the shift in XPS, the energetic position of these signals is also dependent on the electron density at the atom and can be influence by the substituents. This is particularly relevant for the X-ray absorption spectroscopy of metal complexes as these shifts provide information on the oxidation state of the metal.[18] In this thesis, the observed signals are either excitations into the unoccupied 3π orbital of HCNO or into diffuse Rydberg states.

EXAFS occurs at energies equal or higher than the core electron ionization. The interaction of the ejected photoelectron with nearby atoms causes scattering effects, which lead to modulations in the spectra. These signals start immediately after the absorption edge and appear up to 1 keV above the edge.[18] Fourier transforming these modulations provides distance information between the excitation site and neighboring atoms.

2.4 Resonant Auger-Meitner processes

An Auger-Meitner process may also take place after core electron excitation. This process is pictured in Figure 2.3 b) and c) and is called the resonant Auger-Meitner decay. Like before, a valence electron fills the core vacancy, and another valence electron picks up the energy and gets ejected from the molecule. This produces an Auger electron and a singly charged cation. As mentioned above, this process takes less than 10 fs and is usually much faster than nuclear motion. This is not the

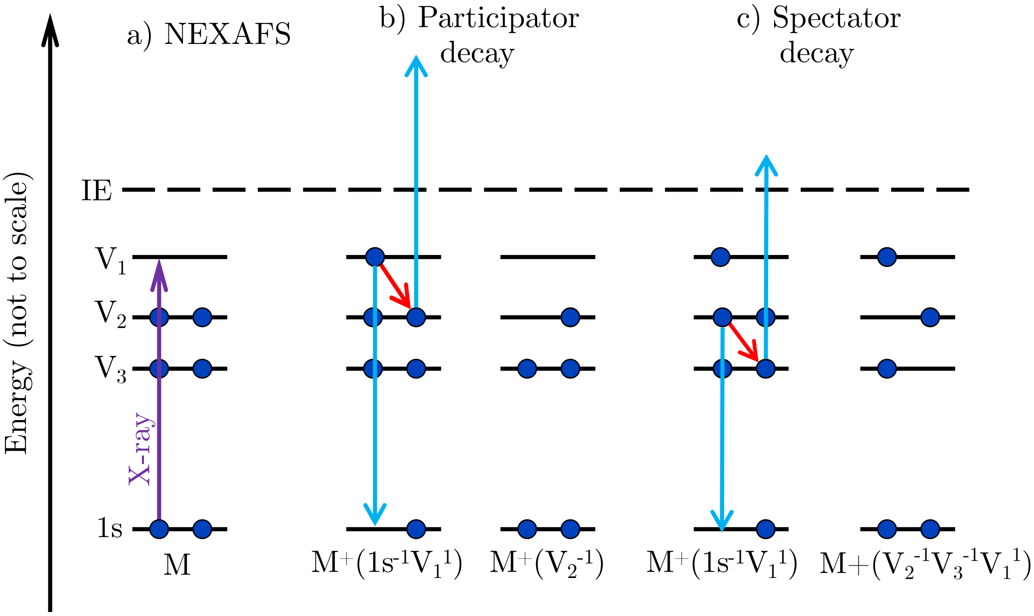

Figure 2.3: Schematic representation of the process of a) near-edge X-ray absorption fine structure, b) Auger-Meitner participator decay and c) Auger-Meitner spectator decay. The core orbital is represented here by a 1s orbital, the concept however applies to any type of core orbital.

case however, when the core-excited state has a repulsive potential energy surface along one internuclear coordinate. This dissociation that can precede the Auger-Meitner decay is called ultrafast dissociation.[13] For example, it is observed for the core-excited HBr (Br $3d^{-1}\sigma^*$).[19] Ultrafast dissociation in this state leads to ground state atomic hydrogen and core-excited atomic Br*, which then undergoes the Auger-Meitner decay. This leads to a resonant Auger electron spectrum of HBr, which includes the signals of atomic Br.

The kinetic energy of the Auger electron is dependent on the involved orbitals and also given by Equation 2.5. It is possible to distinguish between two different types of decays. In participator decays the electron that was excited in the initial step is involved in the decay and the released energy $E(V_1) - E(Core)$ is equal to the energy of the photon. In this case Equation 2.5 becomes

$$E_{kin}^{RA,P} = h\nu + E(V_2), \tag{2.8}$$

meaning that the kinetic energy of an Auger electron produced by participator decay $E_{kin}^{RA,P}$ depends on the photon energy. The other type of decay is called a spectator decay, where the initially excited electron does not participate in the Auger-Meitner process. The kinetic energy of the Auger electron $E_{kin}^{RA,S}$ is then unchanged from Equation 2.5:

$$E_{kin}^{RA,S} = E(V_2) - E(Core) + E(V_3) \tag{2.9}$$

Thus, $E_{kin}^{RA,S}$ is independent of the photon energy. This makes it possible to differentiate between participator and spectator decays by changing the photon energy and observing which signals shift in kinetic energy and which do not.

The binding energy is defined as the difference between the photon energy $h\nu$ and the kinetic energy of the Auger electron. This leads to the following expressions for spectator and participator decay, respectively:

$$E_{Bin}^{RA,P} = -E(V_2) \tag{2.10}$$

$$E_{Bin}^{RA,S} = h\nu + E(Core) - E(V_2) - E(V_3) \tag{2.11}$$

The binding energy of participator states is thus not dependent on the photon energy, while the binding energy of the spectator states is. The final states produced by participator decay are so-called one-hole states, while the final states of the spectator decay are called two-hole-one-particle states, since there are two holes in the valence orbitals and the spectator electron in the previously unoccupied orbital. The participator final states (one-hole states) are equivalent to the final states produced by VUV photoelectron spectroscopy. The two-hole one particle final states of the spectator decay are comparable to the final states produced by the normal Auger-Meitner decay (Figure 2.2). Thus, the resonant Auger electron spectra can be seen as the sum of the valence photoelectron spectrum and the normal Auger electron spectrum.

2.5 Fragmentation after Auger-Meitner processes

In Chapter 5 the fragmentation of the dications and cations formed by normal and resonant Auger-Meitner decays will be described. The EPICEA setup (see Section 2.7) allows the detection of Auger electron and photoions in coincidence. It couples a double toroidal electron analyzer with a time-of-flight mass spectrometer, which provides insights into the mechanisms of the fragmentation.

The molecular dication M^{2+} can fragment in the following patterns:

$$M^{2+} \rightarrow A^{+} + B^{+} \tag{2.12}$$

$$M^{2+} \rightarrow A^{+} + B^{+} + N \tag{2.13}$$

$$M^{2+} \rightarrow A^{2+} + N \tag{2.14}$$

Equation 2.12 corresponds to a simple bond cleavage and the formation of two ions A^{+} and B^{+}, while Equation 2.13 involves the cleavage of several bonds and the formation of two ions and any number of neutral fragments N, which are not

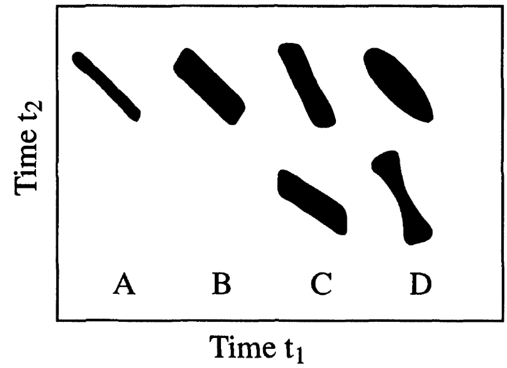

Figure 2.4: Simulations of the standard peak shapes observed in photoion-photoion coincidence maps. A) two-body dissociation, B) three-body dissociation, where the neutral fragment is ejected first, C) three-body dissociation, where charge separation occurs first, D) ultrafast three-body dissociation. Taken from Ref. [20] under the Creative Commons license.

detected. M^{2+} may also fragment into a dicationic daughter ion (Equation 2.14) and a neutral fragment. This pathway can be identified by the appearance of doubly charged fragments in the time-of-flight mass spectrum. The channels Equation 2.12 and Equation 2.13 are not so easily identified in the one-dimensional TOF mass spectra. The coincidence information of the EPICEA setup enables the creation of two-dimensional photoion-photoion coincidence (PIPICO) maps. In these maps the different mechanisms produce unique peak shapes, which are summarized in Figure 2.4. When the molecular dication fragments, the produced fragments are ejected in opposite directions. Linear momentum is conserved leading to $\vec{p}_1 = -\vec{p}_2$.[21] The time-of-flight t scales linearly with the momentum component along the spectrometer axis[21]

$$t = t_0 + |\vec{p}|\ cos(\theta), \tag{2.15}$$

where θ is the angle between the momentum vector and the spectrometer axis. t_0 is the time-of-flight of the ion without additional momentum.

Due to the conservation of momentum the time of flight of A^+ is reduced by the same amount as the time of flight of B^+ is increased and vice versa. This leads to peaks in the PIPICO maps with slopes of -1 in time-of-flight units, corresponding to case A) in Figure 2.4. In case of charge separation and formation of a neutral fragment (Equation 2.13), there are two possible mechanisms, depending on the order of the two fragmentation steps. If the neutral fragment is formed before the charge separation, i.e., $M^{2+} \rightarrow AB^{2+} + N \rightarrow A^+ + B^+ + N$, peak shape B) would be observed. This is due to the additional random momentum applied to the dicationic fragment, so the slope is still -1 but the peak is broadened by the additional momentum. If charge separation occurs first peak shape C) is observed and the slope depends on the mass relation of the ionic and neutral fragments.[20] Peak shape D) is observed after ultrafast three body dissociation, where the momentum component of the neutral fragment is no longer randomly distributed leading to more complex peak shapes.

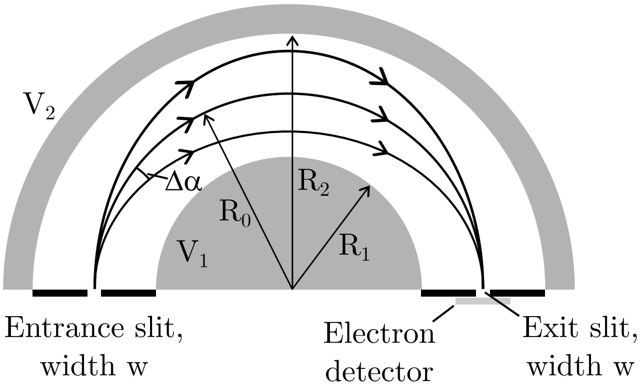

Figure 2.5: Schematic figure of a hemispherical analyzer. The parameters and components are explained in the text.

2.6 The hemispherical electron analyzer

The VUV photoelectron spectrum, X-ray photoelectron spectra and Auger electron spectra in Chapter 3 and Chapter 4 were recorded using a hemispherical electron analyzer (Figure 2.5). It consists of two concentric hemispherical electrodes with radii R_1 and R_2, with $R_1 < R_2$. On these electrodes the potentials V_1 and V_2 are applied, with $V_1 > V_2$. The electrons enter the analyzer through an entrance slit with width w. Under these parameters only electrons with a certain kinetic energy E$_p$ will pass through the dispersive field and the exit slit and arrive on the detector. The pass energy E$_p$ is given by[16]

$$E_p = e\Delta V \left(\frac{R_1 R_2}{R_2^2 - R_1^2} \right). \tag{2.16}$$

e is the elementary charge and ΔV is $V_1 - V_2$. The resolution ΔE of this kind of spectrometer is given by[16]

$$\frac{\Delta E}{E_p} = \frac{w}{2R_0} + \frac{1}{4}(\Delta a)^2, \tag{2.17}$$

where R$_0$ is the mean radius between R$_1$ and R$_2$ and Δa is the angular range of the electrons entering the analyzer. Typically, $\Delta E/E_p$ is on the order of 0.02.[16,17] For Auger electron spectroscopy with electrons on the order of a few hundred eV this resolution is not sufficient. To overcome this, the Auger electrons are retarded to a lower pass energy in an electrostatic lens by a retardation voltage V_{ret}.

$$E_p = E_{kin} - V_{ret} \tag{2.18}$$

ΔV is then adjusted to account for the lower kinetic energy. Since the ratio $\Delta E/E_p$ (Equation 2.17) must remain constant, the resolution will improve accordingly. In order to then measure a larger range of energies the pass energy (and ΔV) is fixed and the retardation voltage V_{ret} is scanned or "swept" over the desired range.

2.7 EPICEA Setup

The experimental setup EPICEA of the PLÉIADES beamline[22] is used to record Auger-electron-photoion-coincidence (AEPICO) spectra. This means that the Auger electrons and the photoions are measured simultaneously and electrons and ions produced by the same event are correlated with each other. The setup consists of a double toroidal analyzer (DTA), which measures the kinetic energy of electrons and a time-of-flight mass spectrometer (TOF-MS), which measures the ions. This setup uses a double toroidal analyzer instead of a hemispherical analyzer due to its higher collection efficiency.[23] A high collection efficiency is critical for coincidence experiments in order to increase the contribution of true coincidences relative to false coincidences (*vide infra*). The trade-off is a lower kinetic energy resolution.

2.7.1 Double toroidal analyzer

The schematic setup of the DTA is shown in Figure 2.6. The DTA collects all electrons that are emitted in a polar angle of 54.7±3° relative to the symmetry axis of the DTA. Due to the cylinder symmetry of the DTA the full circle of azimuthal angles (0° to 360°) is collected.[24,25] This leads to a collection efficiency of around 5% of the total emission sphere 4π sr.

The electrons travel from the ionization region (a) through a collimator (b) consisting of two grounded elements. A four-element conical electron lens (c),[26]

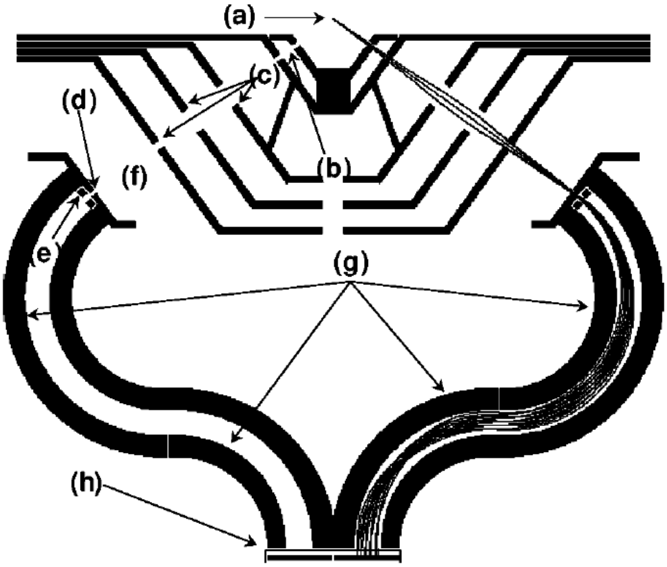

Figure 2.6: Schematic drawing of the double toroidal analyzer and its components. A description of the components is given in the text. The electrostatic lens system had four elements during the measurements of this thesis and not three as it is pictured. Figure taken from Ref. [23] with permission from AIP publishing.

focuses the Auger electrons through the field-free region (f) onto the entrance slit (d) of the analyzer. This lens also retards the Auger electrons to the pass energy E_p. Like with the hemispherical analyzer E_p is the energy of the Auger electrons that can pass the DTA. (e) are correction rings which optimize the incident angle of the electrons entering the analyzer.[23] The electron then passes through the toroidal deflection plates (g) and onto the detector (h). The detector is a delay-line position sensitive detector.[27] The geometries of the analyzer and the electrostatic lens were found by simulating and optimizing the electron trajectories.[23,26]

The pass energy E_p is an essential parameter of the experiment. It determines the resolution of the experiment, which was empirically found to be 0.8% of E_p.[24] It also governs the range of kinetic energies that are detected simultaneously as 14% of E_p.[24] In this thesis a pass energy of 250 eV was used, leading to a resolution of 2 eV and a detection window of roughly 35 eV. The kinetic energy of the Auger electrons after the retardation E_{kin}^{ret} can then be determined by their distance r from the center of the detector:[24]

$$E_{kin}^{ret} = E_p + a(r - r_p) + b\left(\frac{1}{r} - \frac{1}{r_p}\right) \tag{2.19}$$

r_p is the radial position of electrons that hit the detector with kinetic energy E_p. E_{kin}^{ret} is converted to the actual kinetic energy by adding the retardation voltage. The dispersive coefficients a and b are determined by fitting Equation 2.19 to calibration measurements on the $3d_{3/2}$ and $3d_{5/2}$ photoelectron lines of Krypton.[28]

2.7.2 Auger-electron-photoion-coincidence (AEPICO) experiment

The DTA is mounted opposite of a time-of-flight mass spectrometer, together they form the EPICEA setup. It was first described by Morin *et al.* in 1998.[29] The goal of coincidence experiments is to simultaneously measure the particles (electron and ions) that are created in the same event. In the case of EPICEA this is achieved using a single-start-multiple-stop acquisition scheme: Detection of an electron applies a pulsed field which extracts the photoions in the chamber. A pulsed extraction field is used since a continuous field would interfere with the electron detection and decrease the energy resolution.[29] All ions detected by this pulse are detected in coincidence with the Auger electron which triggered the extraction. The pulsed field also provides a start time for the time-of-flight detection of the ions. The ions are detected on a hexagonal delay line imaging detector.[27]

This coincidence scheme will inevitably lead to undesired signals of false coincidences, i.e., the coincidence of two particles that were not created in the same event. To quantify and reduce the contribution of these signals a random trigger is employed alongside the actual trigger of real electrons.[30] Here, a random pulse generator also extracts ions out of the experimental chamber at a rate of 150 pulses/s and creates events without electrons. In general, the ionization rate has to be kept low to decrease the false coincidence background, so a total rate of up to 250 events/s was chosen. The procedures using these random events is expanded in the appendix of Chapter 5.

2.7.3 Data format

The data is recorded as events, where events caused by the detection of an electron are called electron events, while events caused by the random pulse are called random events. An electron event consists of a single electron and all ions that are detected by the pulsed field triggered by the electron detection. A random event contains no electron and all detected ions. All of these events are collected in a table, an exemplary table is shown in Table 2.1.

Table 2.1: Example of an event table produced by the EPICEA setup.

Event id	Number of electrons	Electrons wave index	Number of ions	Ions wave index	Coincidence order
1	1	0	0		0
2	1	1	2	0	2
3	0		1	2	1

The event id serves as a unique identifier for each event, the columns “electrons wave index” and “ions wave index” show the index of the electron or ion in the electron or ion table, respectively. If there are multiple ions detected in the event, the index of the first ion is given. The column “coincidence order” states how many ions are detected in the event, so it is practically equivalent to the fourth column. Events are formally split into different categories according to the coincidence order. They are described as xn-events, where n is the number of ions. An event with two detected ions for example is called an x2 event. Row 3 shows an event caused by a random pulse, since no electron was detected, while the other two events are due to electrons.

The information of the electron and the ions are then given in separate tables, examples are shown in Table 2.2 and Table 2.3.

Table 2.2 contains the relevant information of the measured real electrons. The first column shows which event they are associated with, while columns 2 and 3 show the cartesian coordinates of the electron on the detector. Columns 4 and 5 encode the same information expressed in polar coordinates. The third row shows

Table 2.2: Example of an electron table produced by the EPICEA setup.

Event id	X-coordinate	Y-coordinate	Distance from the center r	Polar angle θ
1	-9.6363	13.196	15.061	345.232
2	-7.62333	11.212	14.358	60.232
4				

an electron that was detected, but due to missing information from the delay-line detector no position could be determined.

Column 1 of the ion table (Table 2.3) also contains which event they belong to. Table 2.1 showed that the event with id 3 was a random event with one ion. Row 3 of the ion table contains the information of that ion, since it is associated with event id 3. The second column contains the time-of-flight in picoseconds. The position of the ion on the detector is also available in the data but was not used in the analysis of this thesis.

Table 2.3: Example of an ion table produced by the EPICEA setup.

Event id	Time-of-flight [ps]
2	$9.6914 \cdot 10^6$
2	$5.87883 \cdot 10^6$
3	$6.14528 \cdot 10^6$

2.8 Layout of the python program

The python program basically has to perform two tasks. First it has to read the raw data in the form shown in the previous section and convert this into a format that the program can work with. The second task is using the data, i.e., calibrating, filtering, preliminary plotting and saving it, so that the spectra can be plotted using programs like Origin.

The data is saved in the hdf5 file format, which is a collection of tables. The required tables and the relevant information in those tables can then readily be extracted. The python program is based on an object-oriented approach to analyze the data. The data of the events triggered by the detection of an electron is saved in an object called `Electron_obj`. This object contains the following properties:

- Event id
- x and y: Cartesian coordinates of the position on the detector
- r and θ: Polar coordinates of the position on the detector
- ions: The number of ions that are in coincidence to this electron
- ionlist: List of the coincident `Ion_obj` objects
- tof: List of the times-of-flight of the coincident ions

The object `Ion_obj` has these attributes:

- tof: Its time-of-flight
- Information on its position on the ion detector, since this information is not used in the present thesis, it will not be elaborated on further

All `Electron_obj` are then saved in the list `electronList`. The ion signals due to the random trigger are saved in `random_tof_lists`.

The second step of filtering the data is now fairly straightforward. For example, filtering for a specific mass range (tof1 to tof2) is achieved by:

```
mass_sel_electrons = []
# list that will be returned
# contains the selected events
ion_obj_list = []
# list that will be returned
# contains the selected ions
for el in electron_obj:
#iterate over all electron objects
        k = 0
        for index,i in enumerate(el.tof):
        #iterate over all ions in
        #coincidence to the electron
            if (i >= tof1 and i <= tof2):
```

```
            #check whether the ion is
            #within the specified tof range[tof1,tof2]
                k +=1
                ion_obj_list.append((el.ionlist[index]))
                #append the found ion
                break
        if k >= 1:
            mass_sel_electrons.append(el)
            #append the selected electron
return mass_sel_electrons,ion_obj_list
```

We can then use these selected electrons to plot the corresponding mass-selected Auger electron spectrum:

```
r_list = [el.r for el in mass_sel_electrons]
#Extracts the radii of all electrons in the filtered list
counts, x_axis = np.histogram(r_list, bins=augerbin)
#converts the list into a histogram
#augerbin specifies the number of bins used in the histogram
plt.figure(fig)
plt.plot(x_axis[0:augerbin], counts)
#Generates a plot using the x-axis
#and the counts of the histogram
plt.title('Mass-selected␣Auger␣spectrum')
#defines the title of the plot
plt.xlabel('radius')
plt.ylabel('␣[counts]')
#Defines the label of the axes
plt.xlim(8,25)
#Defines the range of the x-axis
#The units here are pixel positions
#Which are converted to kinetic energies
#using calibration measurements
```

References

[1] S. Mobilio, F. Boscherini, C. Meneghini, *Synchrotron Radiation : Basics, Methods and Applications*, Springer, Berlin, Heidelberg, **2014**.

[2] T. M. Jens Falta, *Forschung mit Synchrotronstrahlung*, Vieweg+Teubner Verlag, Wiesbaden, **2010**.

[3] J. M. Hollas, *Moderne Methoden in der Spektroskopie*, 1st ed., John Wiley and Sons Ltd., Chichester, **1995**.

[4] T. A. Carlson, *Annu. Rev. Phys. Chem.* **1975**, *26*, 211–234.

[5] B. Sztáray, A. Bodi, T. Baer, *J. Mass. Spectrom.* **2010**, *45*, 1233–1245.

[6] B. Sztaray, K. Voronova, K. G. Torma, K. J. Covert, A. Bodi, P. Hemberger, T. Gerber, D. L. Osborn, *J. Chem. Phys.* **2017**, *147*, 013944.

[7] D. L. Osborn, C. C. Hayden, P. Hemberger, A. Bodi, K. Voronova, B. Sztáray, *J. Chem. Phys.* **2016**, *145*.

[8] I. Fischer, P. Hemberger, *Chemphyschem* **2023**, *n/a*, e202300334.

[9] B. Sztáray, T. Baer, *Rev. Sci. Instrum.* **2003**, *74*, 3763–3768.

[10] A. Bodi, B. Sztáray, T. Baer, M. Johnson, T. Gerber, *Rev. Sci. Instrum.* **2007**, *78*, 084102.

[11] T. Baer, R. P. Tuckett, *Phys. Chem. Chem. Phys.* **2017**, *19*, 9698–9723.

[12] T. Koopmans, *Physica* **1934**, *1*, 104–113.

[13] C. Miron, P. Morin in *Handbook of High-resolution Spectroscopy*, American Cancer Society, **2011**.

[14] M. Gryziński, *Phys. Rev.* **1965**, *138*, A336–A358.

[15] A. M. Juett, N. S. Schulz, D. Chakrabarty, *Astrophys. J.* **2004**, *612*, 308–318.

[16] J. Wolstenholme, *Auger Electron Spectroscopy: Practical Application to Materials Analysis and Characterization of Surfaces, Interfaces, and Thin Films*, Momentum Press, New York, **2015**.

[17] S. Hofmann, *Auger- and X-Ray Photoelectron Spectroscopy in Materials Science: A User-Oriented Guide*, Springer Berlin Heidelberg, **2014**.

[18] J. Yano, V. K. Yachandra, *Photosynth. Res.* **2009**, *102*, 241–254.

[19] P. Morin, I. Nenner, *Physical Review Letters* **1986**, *56*, 1913–1916.

[20] J. H. D. Eland, *Laser Chem.* **1991**, *11*, 259–263.

[21] J. H. D. Eland, *Mol. Phys.* **1987**, *61*, 725–745.

[22] Pleiades, `https://www.synchrotron-soleil.fr/fr/lignes-de-lumiere/pleiades` (visited on 09/16/2019, 15:43).

[23] C. Miron, M. Simon, N. Leclercq, P. Morin, *Rev. Sci. Instrum.* **1997**, *68*, 3728–3737.

[24] X.-J. Liu, C. Nicolas, C. Miron, *Rev. Sci. Instrum.* **2013**, *84*, 033105.

[25] D. Céolin, C. Miron, M. Simon, P. Morin, *J. Electron Spectrosc. Relat. Phenom.* **2004**, *141*, 171–181.

[26] K. Le Guen, D. Céolin, R. Guillemin, C. Miron, N. Leclercq, M. Bougeard, M. Simon, P. Morin, A. Mocellin, F. Burmeister, A. Naves de Brito, S. L. Sorensen, *Rev. Sci. Instrum.* **2002**, *73*, 3885–3894.

[27] X.-J. Liu, C. Nicolas, M. Patanen, C. Miron, *Sci. Rep.* **2017**, *7*, 2898.

[28] G. Johansson, J. Hedman, A. Berndtsson, M. Klasson, R. Nilsson, *J. Electron Spectrosc. Relat. Phenom.* **1973**, *2*, 295–317.

[29] P. Morin, M. Simon, C. Miron, N. Leclercq, D. L. Hansen, *J. Electron Spectrosc. Relat. Phenom.* **1998**, *93*, 49–60.

[30] G. Prümper, K. Ueda, *Nucl. Instrum. Meth. A* **2007**, *574*, 350–362.

CHAPTER 3

Photoelectron spectroscopy and dissociative photoionization of fulminic acid, HCNO

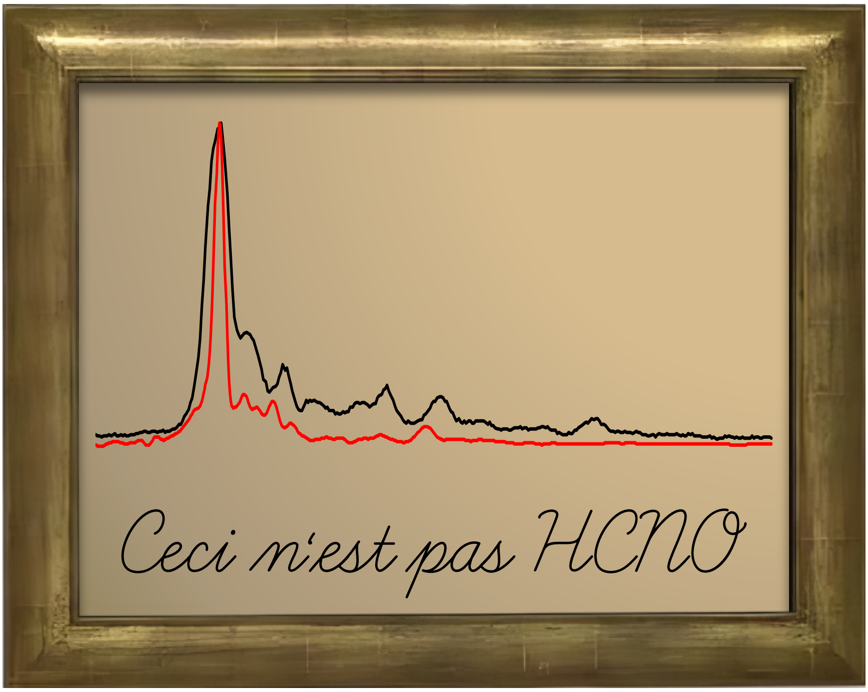

This chapter is reproduced and partly adapted from

Phys. Chem. Chem. Phys., **2022**, *24*, 15217-15229
Marius Gerlach, Tobias Preitschopf, Emil Karaev,
Heidy M. Quitián-Lara, Dennis Mayer, John Bozek,
Ingo Fischer and Reinhold F. Fink

with the permission of AIP Publishing.

Abstract

We report a joint experimental and computational study of the photoelectron spectroscopy and the dissociative photoionization of fulminic acid, HCNO. The molecule is of interest to astrochemistry and astrobiology as a potential precursor of prebiotic molecules. Synchrotron radiation was used as the photon source. Dispersive photoelectron spectra were recorded from 10 eV to 22 eV, covering four band systems in the HCNO cation and an ionization energy of 10.83 eV was determined. Transitions into the Renner-Teller distorted $X^{+2}\Pi$ state of the cation were simulated using wavepacket dynamics based on a vibronic coupling Hamiltonian. Very good agreement between experiment and theory is obtained. While the first excited state of the cation shows only a broad and unstructured spectrum, the next two higher states exhibit a well-resolved vibrational progression. Transitions into the excited electronic states of $HCNO^+$ were not simulated, due to the large number of electronic states that contribute to these transitions. Nevertheless, a qualitative assignment is given, based on the character of the orbitals involved in the transitions. The dissociative photoionization was investigated by photoelectron-photoion coincidence spectroscopy. The breakdown diagram shows evidence for isomerization from $HCNO^+$ to $HNCO^+$ on the cationic potential energy surface. Zero Kelvin appearance energies for the daughter ions HCO^+ and NCO^+ have been derived.

3.1 Introduction

Fulminic acid, HCNO has been and still is a molecule of considerable interest in organic chemistry.[1,2] At present, the astrochemical relevance drives spectroscopic and theoretical work on the molecule, because HCNO contains the basic atoms of organic chemistry. It has been detected in numerous astrophysical objects, including molecular clouds, protostars, starless cores such as B1, L1544, and L183, as well as the low-mass star-forming region L1527.[3–8] It is most likely formed from $CH_2 + NO \rightarrow HCNO + H$ in the gas phase or $H + CNO \rightarrow HCNO$ on grains.[9,10] HCNO has three additional stable isomers; isocyanic acid (HNCO), cyanic acid (HOCN) and isofulminic acid (HONC). The relative stability is HNCO > HOCN >

HCNO > HONC with HNCO being the most stable isomer.[11] Of these molecules, only isofulminic acid has not yet been detected in interstellar space,[4] although its microwave spectrum is known.[12] Recent computational studies have also shown that HCNO and its isomers can be formed in (exo)planetary atmospheres[13] and become the simplest conceivable quaternary compounds in the high-pressure interior of Neptune-like giant icy (exo)planets.[14] Like its isomers, fulminic acid is considered to be a potential precursor in the interstellar synthesis of prebiotic molecules and might be chemically linked to small amides.[15] Laboratory astrophysics is dominated by spectroscopy in the radiofrequency, microwave and infrared. However, the availability of instruments such as Chandra X-Ray Observatory and XMM-Newton triggered interest in the interaction of molecules with high energy VUV and soft X-ray radiation. For example, Juell *et al.* analyzed the K-shell absorption spectra of neutral and ionized atomic oxygen with Chandra.[16] Interestingly, UV and VUV radiation could also appear within dense clouds, due to the so-called Prasad-Tarafdar mechanism.[17] Hydrogen molecules excited by the impact of electrons produced by cosmic-ray ionization, can emit UV and VUV photons that initiate photochemistry and (dissociative) photoionization. These photons can have energies up to roughly 13.7 eV (90 nm) and influence the chemistry in dense interstellar clouds, where external UV photons may not enter. For example, the dissociation of CO to C + O and of H_2O to OH + H is initiated in this way.[18,19] Accurate estimation of photodissociation and dissociative photoionization is therefore relevant for astrochemical gas-grain models, where the photodissociation of HCNO has so far only been estimated.[9]

Given the importance of HCNO in astrochemistry, it is not surprising that significant work has been dedicated to this molecule. Due to its small size HCNO and its isomers have been investigated by various high-level quantum chemical approaches.[11,20–25] Bunker *et al.* used the semirigid bender Hamiltonian to fit the remarkably flat potential of the HCN bending mode,[26] which even inspired two limericks which are included in a review on quaslinear and quasiplanar molecules by Bunker.[27] Particularly relevant for the present work are studies by Mondal *et al.*[28] on the appearance of Jahn-Teller and Renner-Teller interactions in $HCNO^+$ as well as the work by Luna *et al.* who published the global potential energy surface of the $[H,C,N,O]^+$ system using density functional theory.[29] Experimentally the microwave[30–32] and IR-spectra[32–40] have been reported, the photodissociation has been investigated at 248 nm[41] and 193 nm[42] and the kinetics of the HCNO + OH reaction has been studied[43]. In the soft X-ray regime, we recently reported normal and resonant Auger spectra of HCNO at all three K-edges (Chapter 4 of this thesis).[44] In contrast, valence photoelectron spectra have only been reported using He I and II ionization.[45] An adiabatic ionization energy IE_{ad}=10.83 eV has been derived and transitions into electronically excited states of the ion have been observed. However, band assignments were based on rather simple computations and the Renner-Teller effect in the $X^{+2}\Pi$ ground state of $HCNO^+$ was not considered. Hop *et al.* investigated the products formed through electron impact ionization.[46] The main dissociation products were m/z 30 and m/z 27 as well as a large number of other products with smaller intensities. Due to the limitations of their setup they were not able to provide energy selective data or provide insights into the mechanism of the dissociation. In this joint experimental and computational study we therefore reinvestigate the photoionization and dissociative photoionization of HCNO by photoelectron spectroscopy using synchrotron radiation and coupled-cluster calculations. When combined with high-level computations, photoelectron spectroscopy has shown to be an excellent tool to characterize the electronic structure of reactive molecules,[47] as shown for example in recent work on C_4H_4, the paradigm for antiaromaticity.[48] Note that the photoionization of the isomer isocyanic acid, HNCO has already been extensively investigated by our group.[49,50]

3.2 Experimental and Computational Methods

3.2.1 Experimental

The photoelectron spectrum was recorded at the soft X-ray beamline PLEIADES[51] of Synchrotron SOLEIL, while the breakdown diagram for the analysis of dissociative photoionization was obtained at the VUV beamline of the Swiss Light Source (SLS) in Villigen.[52] Fulminic acid was prepared according to the procedure by Wentrup *et al.*[53] Details on the synthesis are given in the appendix at the end of the chapter.

At the PLEAIDES beamline the HCNO sample enters a gas cell through an effusive inlet. Here, it interacts with the synchrotron light, which is produced by an Apple II HU256 undulator and monochromatized by 400 lines mm^{-1} grating. The photon energy was fixed at 30 eV and the light was circularly polarized. Since the undulator cannot produce light oriented at the magic angle relative to the detector at this low energy, circularly polarized light was used to avoid anisotropy of the emitted electrons. Electrons entered a VG Scienta R4000 hemispherical electron analyzer through an entrance slit of 300 micrometers. A pass energy of 5 eV was adjusted, leading to a spectral resolution of 6 meV. Electron binding energies E_B are obtained by subtracting the photoelectron kinetic energy from the photon energy $h\nu$:

$$E_B = h\nu - E_{kin}. \tag{3.1}$$

Error bars in the photoelectron spectra are derived from the full width half maximum of the peak.

At the VUV beamline[52] the sample also enters the experimental chamber through an effusive inlet. A bending magnet delivers the synchrotron radiation, which is monochromatized using a 150 lines mm^{-1} grating. Electrons and ions were detected in coincidence by a multi-start/multi-stop scheme by a pair of position sensitive Roentdeck DL40 detectors with a delay line anode.[54] Threshold electrons were collected with a resolution of 5 meV, the contributions of hot electrons were subtracted according to the procedure of Sztaray and Baer.[55] The breakdown diagram is produced by dividing the threshold electron signal of each relevant mass channel by the sum of all relevant mass channels. It was recorded from 11.5 to 13.5 eV with 25 meV step size and from 13.5 to 15.3 eV with 20 meV step size.

3.2.2 Computational

The equilibrium structures of neutral fulminic acid and the fulminic acid cation were calculated using Molpro[56–58] at the CCSD(T)/cc-pVTZ and RCCSD(T)/cc-pVTZ levels of theory[59–61], respectively. Both molecules were restricted to be linear. Harmonic vibrational normal modes and frequencies were calculated at optimized geometries using the same methods.

We initially intended to simulate the full experimental photoelectron spectra of fulminic acid, however, it was found that at least 12 electronic states of the molecule spanned the energy range of experiments (see discussion in the appendix). The excited state potential energy surfaces were also found to vary in a complicated way along the normal mode coordinates such that they could not be described using a vibronic coupling model. Here we restrict simulation of the photoelectron spectra to the first two electronic states of the fulminic acid cation.

Ab initio energies for the fulminic acid cation were calculated using OpenMolcas[62] along 1D and 2D cuts of each (neutral) normal mode from the equilbrium geometry outwards using a two state-averaged restricted active space self consistent field[63] (RASSCF) method followed by second order multiconfigurational perturbation theory[64,65] (CASPT2). The active space comprised of 11 electrons in 10 orbitals (11,10). For the neutral molecule a cc-pVDZ basis was used while for the cation a cc-pVTZ basis was employed. These calculations were based on an initial unrestricted Hartree-Fock treatment at the equilibrium geometry and RASSCF orbitals from the previous geometry were used as starting orbitals for each subsequent geometry. Symmetry was turned off for all calculations and a level shift of 0.2 hartree was used for CASPT2 calculations.

To obtain coupled potential energy surfaces for dynamics calculations and spectra simulations, a vibronic coupling Hamiltonian model[66] was employed. The diabatic potentials are expressed as a Taylor series, in dimensionless (mass-frequency scaled) normal modes around a particular point, $\mathbf{Q}_0$, here taken as the equilibrium geometry. The Hamiltonian can be written in matrix form as

$$\mathbf{H} \;=\; \mathbf{H}^{(0)} + \mathbf{W}^{(0)} + \mathbf{W}^{(1)} + \dots \tag{3.2}$$

with the zeroth-order diagonal Hamiltonian $\mathbf{H}^{(0)}$ often expressed in the harmonic approximation

$$H_{ii}^{(0)} \;=\; \sum_{\alpha} \frac{\omega_\alpha}{2} \left(\frac{\partial}{\partial Q_\alpha^2} + Q_\alpha^2 \right). \tag{3.3}$$

The subsequent matrices include the effects of electronic excitation and vibronic coupling as a Taylor expansion around $\mathbf{Q}_0$. The zero order term $\mathbf{W}^{(0)}$ is a diagonal matrix of excitation energies. The first order term $\mathbf{W}^{(1)}$ usually contains on-diagonal linear terms for each electronic state and off-diagonal linear terms coupling states along a particular mode, however, for fulminic acid these terms are absent due to symmetry.

As discussed in the appendix, for all modes the basic harmonic potential was replaced by polynomial or Morse functions which provide more accurate fits to the *ab initio* energies and give better agreement between the calculated and experimetal photoelectron spectra.

As the fulminic acid cation is a tetra-atomic linear molecule with $\mathrm{C}_{\infty v}$ symmetry and degenerate electronic states at equilibrium, it displays the Renner-Teller (RT) effect for the pairs of degenerate vibrations $Q_{1/2}$ and $Q_{3/4}$. These modes do not have the correct symmetry to provide linear coupling ($\mathbf{W}^{(1)}$) between the electronic states and coupling is provided through second order terms. This causes the potential energy surfaces to meet at a glancing intersection rather than at the peak of a cone. Of the five possible Renner-Teller cases, HCNO^+ is an example of case (b) as defined by Lee *et al.*[67]: both curves are repulsive as a function of bending but the two harmonic bending frequencies have the same value.

Following Worth and Cederbaum[68], for the two pairs of degenerate vibrational modes ($Q_{1/2}$ and $Q_{3/4}$), the vibronic coupling Renner-Teller Hamiltoniann can be expressed as

$$\mathbf{H} \;=\; \frac{\omega}{2}\left(Q_i^2 + Q_j^2\right) + \begin{pmatrix} -\frac{1}{2}\gamma(Q_j^2 - Q_i^2) & \gamma Q_i Q_j \\ \gamma Q_i Q_j & \frac{1}{2}\gamma(Q_j^2 - Q_i^2) \end{pmatrix} \tag{3.4}$$

where ω is the degenerate vibrational frequency for the pair of modes i and j and γ is the parameter which causes splitting of the degenerate electronic surfaces. In this work the harmonic potential was replaced by polynomial functions but the RT γ parameters were retained.

The RT parameter ϵ can be used to describe the splitting and is defined as $V^{\pm} \;=\; V_m(1 \pm \epsilon)$ where V_m is the mean potential of the split surfaces V^+ and

V^-.[69] The RT parameter can be calculated as

$$\epsilon = \frac{V^+ - V^-}{V^+ + V^-}. \tag{3.5}$$

Usually only quadratic terms are considered, which for the fitting functions used here gives $\epsilon = 2\gamma/\beta$ where β is the quadratic term parameter (see appendix).

All parameters of the vibronic coupling Hamiltonian were obtained by least-squares fitting to the CASPT2 *ab initio* energies using the VCHAM package[70] as implemented within the Quantics program suite[71]. Fits were constrained so that the degenerate electronic energies and parameters for degenerate vibrational modes remained equal. Fitted parameters and plots comparing the *ab initio* energies to the vibronic coupling model are provided in the appendix.

The photoelectron spectrum of fulminic acid was simulated in a similar manner to that described previously for both cyclobutadiene[48,72] and phenol[73] from wavepacket dynamics simulations using the MCTDH method[74] implemented in Quantics[71]. In this case, however, thermal effects were found to be important and a thermalised density operator was propagated in place of the usual 0 K wavepacket (see appendix for 0 K spectra and assignments). Propagation was done including all 7 modes using a new multilayer implementation[75] of the ρ-MCTDH algorithm of Raab *et al*[76].

The ground state nuclear density operator of neutral fulminic acid was obtained using energy relaxation[74] of an initial density operator built from harmonic oscillator eigenfunctions, thermalised to infinite temperature and propagated in imaginary time until the temperature was 300 K, the temperature of the experimental sample. A vertical excitation was then performed by placing the ground state neutral density operator on one of the two lowest electronic states of the fulminic acid cation and then propagating on these coupled states for 200 fs. The photoelectron spectrum was obtained from the Fourier transform of the autocorrelation function as

$$I(\omega) \propto \omega \int_{-\infty}^{\infty} \mathrm{d}t\, C(t) e^{i\omega t} e^{(-t/\tau)}, \tag{3.6}$$

where the last factor is an exponential dampening term to simulate experimental broadening in the photoelectron spectra This phenomenological damping term accounts for missing terms in the model and experimental line broadening by convoluting the spectral lines with a Lorentzian function. The autocorrelation function C(t) is defined as

$$C(t) \;=\; Re\,\{\mathrm{Tr}\rho_{\mathrm{s0}}\} \tag{3.7}$$

where ρ_{s0} is the off-diagonal density matrix connecting the neutral ground-state with the initially excited cation state s. All seven vibrational modes were included in the calculation in a 3-layer multi-layer scheme,[77] adding basis functions until convergence with respect to the autocorrelation function was obtained. For all modes, the primitive basis functions were harmonic oscillator DVRs with 21 points used. Assignments in the photoelectron spectra to specific vibrational modes were determined by including/excluding modes from the simulation and observing the effect on the simulated spectrum.

The mechanism of the dissociation of the fulminic acid cation was calculated using the Gaussian-4 composite method[78] contained in the Gaussian09 program.[79] The evaluated intermediates and transition states are based on the previous DFT calculations by Luna *et al.*.[29] Transition states were located by using the berny algorithm.[80] They were identified by the presence of a vibration with an imaginary frequency, which corresponded to the respective reaction coordinate. The coordinates of all the intermediates and transition states are given in the appendix (Tables A3.8 and A3.9). With these transition states the breakdown diagram is modeled using the minimalPEPICO program.[81]

3.3 Results and Discussion

3.3.1 Equilibrium Geometry and Harmonic Frequencies

Equilibrium bond lengths of $r_{\mathrm{HC}} = 1.06$ (1.08), $r_{\mathrm{CN}} = 1.17$ (1.17) and $r_{\mathrm{NO}} = 1.21$ (1.21) Å were calculated for HCNO (HCNO^+), in good agreement with more elaborate calculations for the neutral molecule.[25] Harmonic vibrational frequencies are given in Table 3.1 along with their symmetry labels (in $\mathrm{C}_{2\mathrm{v}}$). Values obtained by Mladenović and Lewerenz[25] are also given for comparison. The force vectors of the normal modes are shown in the appendix.

Table 3.1: Comparison of harmonic vibrational frequencies with previous theoretical values of Mladenović and Lewerenz,[25] "all" denotes that all electrons were correlated in the calculation. Units of cm^{-1} are employed.

Mode	CCSD(T)/ cc-pVTZ (this work)	CCSD(T)/ cc-pVQZ[25]	CCSD(T)/ cc-pVQZ[25] (all)	RCCSD(T)/ cc-PVTZ (cation)	Description
$\omega_{1/2}(B_{1/2})$	206i	128i	33	677/512	H-C-N bend
$\omega_{3/4}(B_{1/2})$	555	555	565	402/368	C-N-O bend
$\omega_5(A_1)$	1266	1269	1279	1140	C-N-O sym. stretch
$\omega_6(A_1)$	2276	2280	2296	1992	C-N-O asym. stretch
$\omega_7(A_1)$	3500	3493	3505	3296	C-H stretch

For the doubly degenerate H-C-N bend, lower levels of theory give imaginary frequencies, indicating that this geometry is not the global minimum. Many experimental[26,31,36,38,39] and theoretical[11,20–23] studies have been carried out to determine whether the equilibrium structure of fulminic acid is linear or bent. As shown by Mladenović and Lewerenz[25] and Bunker *et al.*,[26] fulminic acid is a very floppy molecule with an almost flat region of the potential energy surface for hydrogen bending motions. Very large basis sets are required to converge to a linear equilibrium structure. Since we obtain cuts through the potential energy surface along the calculated normal modes, the precise determination of the equilibrium structure is not important here. As an aside, we note that in practical applications, fulminic acid is usually taken to have a linear structure, for example in determining its electronic and magnetic properties[82] or for describing collisions with other species.[83]

For the cation, the harmonic stretching frequencies are broadly similar to the neutral. Values for the bending modes are seen not to be degenerate, only approximately so. Although as discussed above, the fulminic acid cation displays the Renner-Teller effect for the bending modes and thus a simple harmonic description is not sufficient, we retain harmonic frequencies for reference purposes. From least squares fits to the CASPT2 *ab initio* energies, we obtain γ parameter values (see Eq. 3.4) of 0.062959 and 0.0054112 eV for modes $\omega_{1/2}$ and $\omega_{3/4}$ respectively. Using Eq. 3.5 this gives RT parameters $|\epsilon|$ of 0.48 and 0.41 respectively, indicating a somewhat intermediate coupling strength compared to other RT systems[69].

3.3.2 Photoelectron spectrum

Figure 3.1 shows the complete photoelectron spectrum. Four bands are observed at around 10.83 eV, 16.0 eV, 17.81 eV and 19.08 eV. The first, third and fourth band show well separated vibrational structure, while the second band is broad and unstructured. The spectrum agrees overall well with the previous dispersive

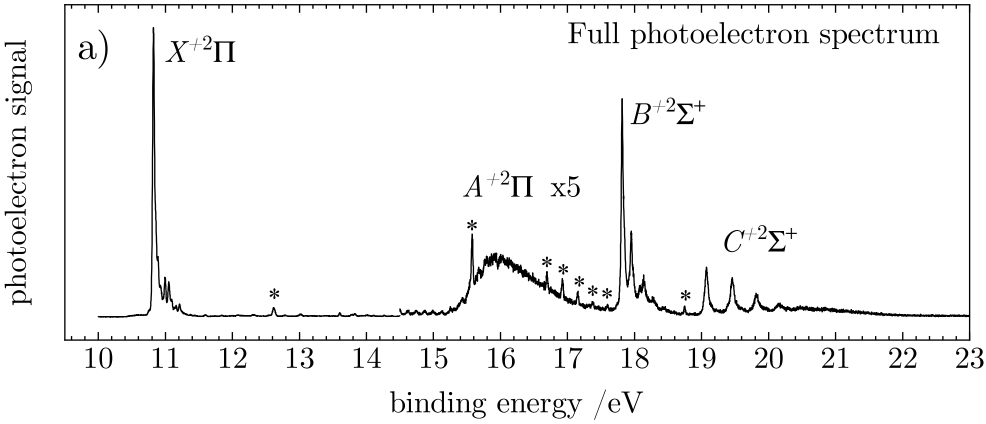

Figure 3.1: Photoelectron spectrum of HCNO from 9 to 23 eV recorded at 30 eV photon energy. The signal upwards from 14.5 eV was multiplied by 5 for ease of viewing. Signals marked by asterisk are due to contamination from water (peak at 12.6 eV)[84] or molecular nitrogen (peaks at 15.6, 16.7, 16.9, 17.2 and 18.8 eV)[85].

photoelectron spectrum by Bastide *et al.*,[45] however due to the higher resolution additional bands are observed. Several narrow transitions appear that are assigned to ionization of H_2O and N_2. They are indicated by asterisks in Figure 3.1.

Figure 3.2 shows the experimentally observed first band in more detail (black line), partial vibrational resolution is visible. From the first band an IE_{ad}= 10.83± 0.02 eV is derived. The error bars are based on the full width of the band at half maximum. The value is in very good agreement with the previous one of 10.83 eV.[45] The main peak shows a shoulder on the high energy side and an irregular progression of multiple peaks is observed.

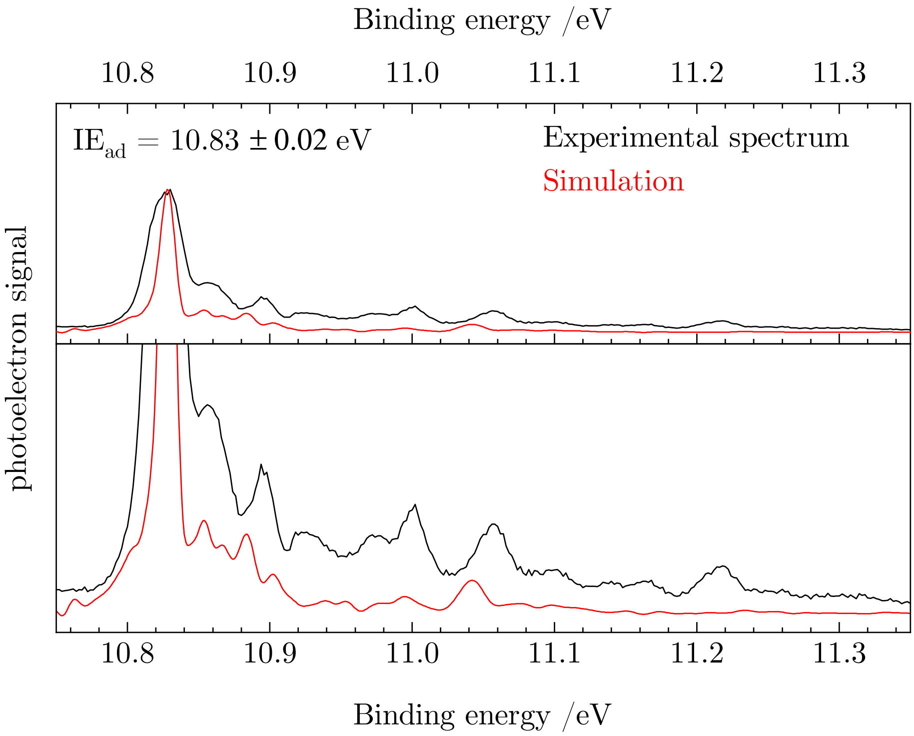

Figure 3.2: Experimental photoelectron spectrum (black line) compared to the calculated spectrum (red). The simulated spectra has been normalised and shifted to match the main peak with experiment.

The red line in Figure 3.2 show the simulated photoelectron spectra obtained from MCTDH density operator dynamics run on the first two electronic states of the cation. The simulated spectrum has been normalised and shifted for best agreement with experiment. To represent the experimental broadening, an exponential damping term (see Eq. 3.6) was included in the computations, with a time constant of 100 fs. While the relative intensities are not fully accounted for in the simulated spectra, the peak positions in the experimental spectrum are well reproduced. To assign the spectrum, repeated runs starting at 0 K were made including different modes. Figure A3.12 in the appendix shows the full and assigned 0 K spectrum compared to the one calculated at 300 K and the experimental spectrum. The simulations show that the first peak on the main band at 10.9 eV is caused by the CNO bending modes ω_3 and ω_4. There is a small peak just below 11 eV which is due to the CNO symmetric stretching mode ω_5. The two peaks at 11 and 11.05 eV are due to the RT modes ω_1 and ω_2 (approximate HCN bending). At higher energies there are some smaller peaks caused by stretching modes ω_6 and ω_7 (asymmetric CNO stretch and C-H stretch, respectively). A comparison between the 0 K and 300 K spectra shows that the shoulder on the high energy side of the main band is due to temperature allowing extra transitions in the ω_1 - ω_4 vibrations.

The second band, corresponding to the A^+ state of $HCNO^+$ ranges from 15.2 to 17.6 eV and is unstructured. A close-up is shown in the appendix (Figure A3.2). The third band is shown in Figure 3.3 a). It features the intense origin band of the B^+ state at 17.81 eV and two further bands at +1130 and +2100 cm^{-1} above the origin. Additionally, a shoulder of around 240 cm^{-1} is visible for each band. The origin of the fourth band system (C^+ state, Figure 3.3 b)) lies at 19.08 eV. A well-resolved progression with a spacing of around 3000 cm^{-1} is apparent.

As mentioned above, a simulation of these progressions was not possible using the vibronic coupling model. However, a tentative assignment of the progressions is provided by investigating the involved orbitals. In Figure A3.4 the calculated MOs of $HCNO^+$ are shown. According to Bastide *et al.* the configuration of the neutral HCNO is $...6\sigma^2 7\sigma^2 1\pi^4 2\pi^4$.[45] For the B^+ state they assigned two vibrational bands with 1070 cm^{-1} and 2420 cm^{-1} to ω_s(CNO) and ω_{as}(CNO). In our spectrum a progression better described by a single mode is observed, so we

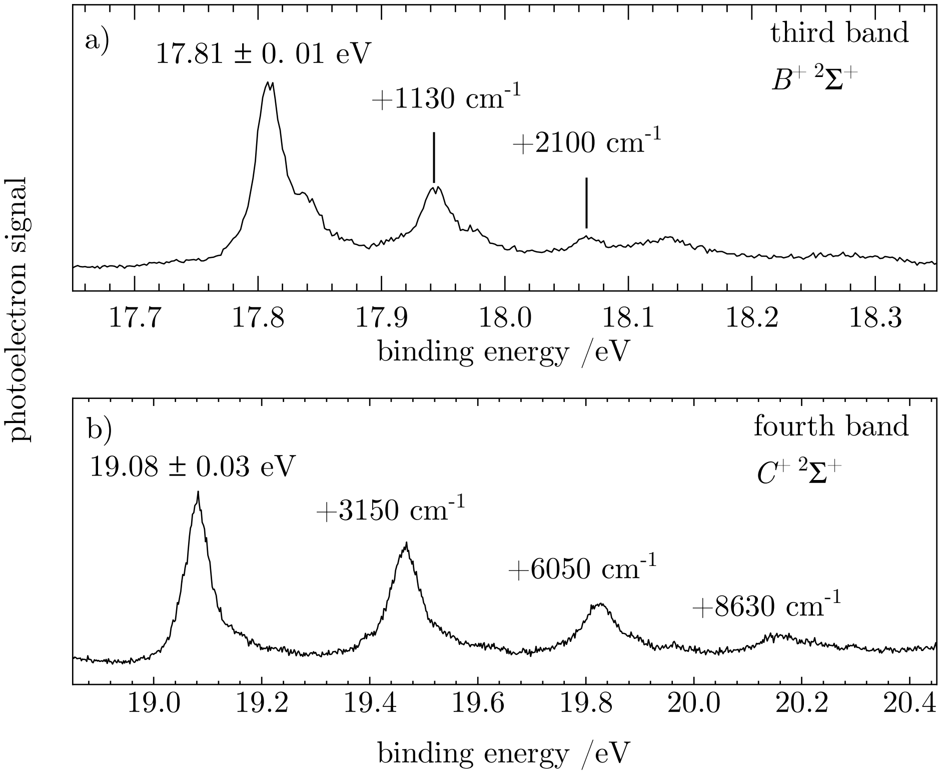

Figure 3.3: High resolution spectra of the two excited states of HCNO with vibrational progression. a) shows in black the spectrum corresponding to the third band, b) shows the spectrum of the fourth band. The observed peaks are labeled with wavenumbers relative to the most intense peak.

assign it to the symmetric CNO stretch ω_5, with a wavenumber of 1130 cm^{-1} in the excited state. This assignment is substantiated by the $2\sigma^*$ orbital (Figure A3.4), corresponding to the 7σ orbital in the notation of Bastide *et al.*, which has strong CNO antibonding character. Thus removal of an electron from this MO is expected to lead to vibrational activity in a CNO mode.

The C^+ state shows a vibrational progression with 3150 cm^{-1} for the $\text{v}^+ = 1 \leftarrow \text{v} = 0$ fundamental. Transitions into the first and second overtone at 6050 cm^{-1} and 8630 cm^{-1} are visible. Due to anharmonicity the energy dif-

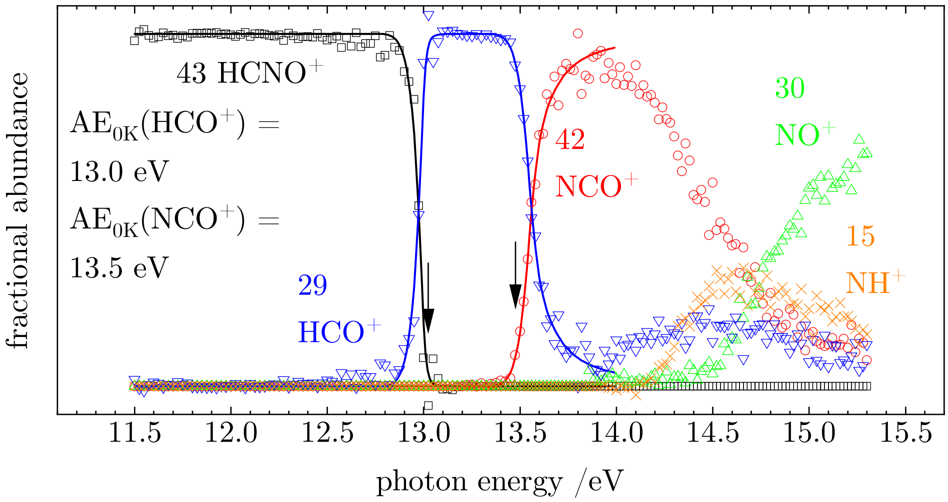

Figure 3.4: Breakdown diagram of HCNO from 11.5 to 15.3 eV. The open symbols corresponds to the experimental data, while the solid lines are the fit produced by the minimalPEPICO program. The labeling of the curves show the m/z value as well as the assigned structure. The arrows show the appearance energies produced by the fit, which are also shown on the left.

ference between the peaks decreases. The high vibrational wavenumber indicates that the bands have to be assigned to a progression in the C-H-stretch mode ω_7(CH). The 2σ MO (Figure A3.4, 6σ in Bastides notation[45]) has C-H bonding character so a removal of that electron may destabilize the C-H bond and lead to vibrational activity in ω(CH). Nevertheless, it should be kept in mind that a simple Koopmans-type picture provides only a rather approximate description of the electronic structure that is not fully appropriate for HCNO.

3.3.3 Dissociative photoionization

The breakdown diagram for the dissociative photoionization of HCNO, recorded between 11.5 and 15.3 eV, is shown in Figure 3.4. The fractional abundances of the parent and daughter ion's TPE signal are plotted as a function of the photon energy. The open symbols represent experimental data. The simultaneously

Table 3.2: Heats of reaction, $\Delta_R H^\circ$ for the dissociation HCNO → products. A more extensive table is available in the appendix. The energies are taken from the Active thermochemical tables.[86] Ground state multiplicites are taken from ref. [29].

Products	$\Delta_R H^\circ$ /eV
^{1}HCO$^+$ + ^{4}N	11.68
^{3}NCO$^+$ + ^{2}H	13.54
^{2}NH$^+$ + ^{1}CO	14.24
^{1}NO$^+$ + ^{2}CH	14.57
^{3}CNO$^+$ + ^{2}H	16.11

recorded TOF distribution show a small asymmetry for the daughter ion peaks, which indicates the presence of a kinetic shift (see Figure A3.3). As we consider the effect of the kinetic shift on the thermochemcial quantities determined in the present work to be small, we did not include it in the data analysis.

The breakdown diagram shows several unusual features that are in contrast with a simple sequential dissociation in the ion. Until around 12.7 eV no fragmentation is visible, then the signal of m/z = 29 (▽) increases, which corresponds to HCO$^+$, while the parent signal (□) drops to zero. At 13.45 eV, m/z = 42 (○) starts to rise, maximizes at around 14 eV and decreases again. Interestingly the rise and decrease of m/z = 42 are rather slow compared to HCO$^+$. At this point, it is important to realize that the structure of m/z = 42 is ambiguous and could correspond to CNO$^+$ or NCO$^+$. Table 3.2 shows the heats of reaction $\Delta_R H^\circ$ of the most relevant fragment channels. They are calculated using the heats of formation provided by the Active Thermochemical Tables (ATcT).[87] Assuming a barrierless mechanism, these reaction enthalpies are equivalent to appearance energies. In any case $\Delta_R H^\circ$ represent the minimum energy that is required to produce these ions. In fact, HCO$^+$ appears above the computed value of 11.68 eV. The heat of reaction for formation of CNO$^+$ + H, the presumed carrier of m/z = 42, is $\Delta_R H^\circ = 16.11$ eV, outside the energy range monitored in Figure 3.4. However, for the product channel ^{3}NCO$^+$ + ^{2}H $\Delta_R H^\circ = 13.54$ eV is computed, a thermochemical value that agrees well with the observed onset. We therefore conclude an isomerization on the ionic potential energy surface. The second unusual feature corresponds to the HCO$^+$ curve (▽), which drops to almost zero at 13.9 eV, but rises again to a value of around 12% of its maximum at 14.5 eV. This suggest two different channels for the formation of this fragment. Two further fragments are visible, the formation of m/z = 15 (×), corresponding to NH$^+$ at 14.1 eV, and the onset of m/z = 30 NO$^+$ (△) around 14.5 eV. Both fragment ion curves are in accordance with the values in Table 3.2.

The minimalPEPICO programm allows the modeling of these breakdown diagrams to extract thermochemical data.[81] This requires detailed knowledge of the reaction mechanism that form the products and the vibrational frequencies of the stationary points of the potential energy surface. Luna *et al.* published the global potential energy surface of the [H,N,C,O]$^+$ system in doublet and quartet multiplicity, including transition states. Their findings yield the mechanism shown in Figure 3.5, which was confirmed by our own calculations that yielded the necessary frequencies. The appearance of HCO$^+$ requires the formation of a C-O bond which is not present in the parent HCNO$^+$. This bond can form via **TS1** where the C-N-O angle is decreased to 97.6°, which leads to the structure **I**. Formation of HCO$^+$ also produces atomic nitrogen. The ground state of N is ${}^4S^{\circ}_{3/2}$.[88] Since the parent ion is of doublet multiplicity, the direct formation of HCO$^+$ + ^{4}N is not possible and the cation has to switch to the quartet surface since the product channel HCO$^+$ + ^{2}N lies at 14.1 eV. We propose that that this happens either at **I** or between **I** and the products. On the quartet surface **I** may dissociate over **TS2** and molecule-ion complex **II**.[29] Note that in the experiment we only measure the highest barrier along the reaction coordinate. This mechanism can also explain the revival of HCO$^+$ at around 14.0 eV. At this energy the reaction along the doublet surface is possible to form HCO$^+$ + ^{2}N (Figure 3.5) via **TS3** and the HCON$^+$ intermediate.[29] The formation of NCO$^+$ requires the formation of the isocyanic acid cation HNCO$^+$. This mechanism involves a 1,2-H-shift (**TS4**) to **III** and an N-O bond cleavage (**TS5**). The solid lines in Figure 3.4 represent the fit obtained using the MinimalPEPICO program employing the highest barriers (TS1 to HCO$^+$ + ^{2}N, TS4 to NCO$^+$ + ^{2}H) of the above mechanism. As visible, the behavior of m/z = 29 and the onset of m/z = 42 are well represented.

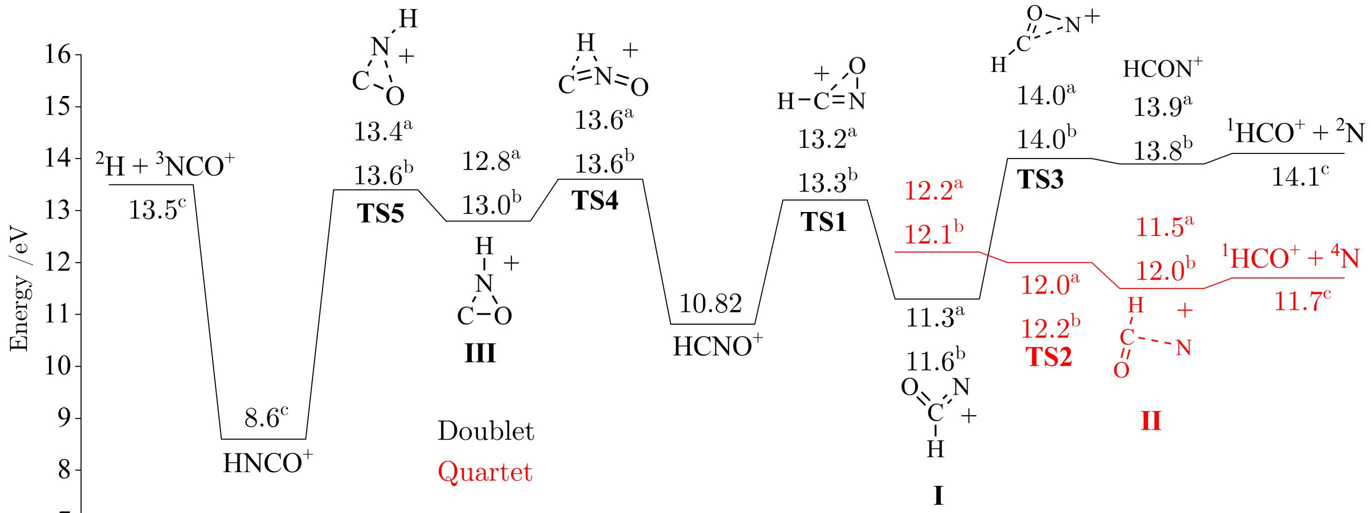

Figure 3.5: Mechanism of the isomerization of the HCNO cation to form ^{3}NCO$^+$ and ^{1}HCO$^+$. Energies are given in eV relative to the neutral HCNO molecule. Values marked with ^{a} were calculated using the G4 composite method. Values marked with ^{b} and ^{c} were taken from Ref. [29] and from the Active Thermochemical Tables[86], respectively. Lines shown in black are on the doublet surface and lines in red are on the quartet surface.

Zero Kelvin appearance energies for both fragments are derived from the model, AE_{0K}(HCNO, HCO^+) = 13.0 ± 0.1 eV and AE_{0K}(HCNO, NCO^+) = 13.5 ± 0.1 eV. The reaction coordinate for formation of NO^+ and NH^+ has not been investigated, consequently their appearance energies are not modeled in this work. The observed onset of NCO^+ agrees very well with the ATcT value, while the AE_{0K}(HCNO, HCO^+) is associated with a complex doublet-quartet intersystem crossing. This ISC may be close to **TS1** or **I** (Figure 3.5) and does not allow an extraction of the $\Delta_R H°$.

3.4 Conclusion

The VUV spectroscopy of fulminic acid, HCNO, has been investigated using synchrotron radiation and dispersive as well as threshold photoelectron detection. Compared to a previous spectrum[45] the present spectra are better resolved and show more information. Four bands are observed, three of them exhibit a vibrational progession. The band origins are identified at at 10.83 ± 0.02 eV ($X^{+2}\Pi$) 17.81 ± 0.01 eV (B^+) and 19.08 ± 0.03 eV (C^+), respectively. A simulation of the transition into the Renner-Teller distorted $X^{+2}\Pi$ ground state of the cation using wavepacket dynamics that rely on a vibronic coupling Hamiltonian yielded very good agreement with the experiment. Several bending mode transitions are identified in the simulations. In addition, hot and sequence band transitions from low energy bending modes of neutral HCNO are essential to achieve agreement between experiment and simulation. No simple description of the transitions into excited electronic states of cation is possible, because twelve electronic states contribute to the transitions and the excited state potential energy surfaces depend in a complicated way on the normal mode coordinates. Therefore only an approximate character was assigned to the transitions, which can nevertheless qualitatively explain the observed vibronic transitions.

Furthermore, a breakdown diagram of HCNO up to 15.3 eV was recorded to investigate its dissociative photoionization. The spectrum was then modelled to extract thermochemical data and the mechanism has been investigated computationally. Dissociative ionization to $^1HCO^+$ + ^4N was found to be the lowest energy dissociation pathway with an appearance energy of AE_{0K}(HCNO, HCO^+) = 13.0

± 0.1 eV. The reaction requires a switch to the quartet potential energy surface in the cation. Next, dissociation to ^{3}NCO$^+$ + ^{2}H sets in at AE_{0K}(HCNO, NCO$^+$) = 13.5 ± 0.1 eV. This dissociation is preceded by an isomerization from HCNO$^+$ to HNCO$^+$, which proceeds via a tricyclic intermediate. The confirmation of isomerization from HCNO$^+$ to HNCO$^+$ might be relevant for explaining the relative abundance of the various CHNO isomers and their fragments, which is not well understood.[89]

Appendix

Additional Experimental Details

Synthesis of Fulminic Acid

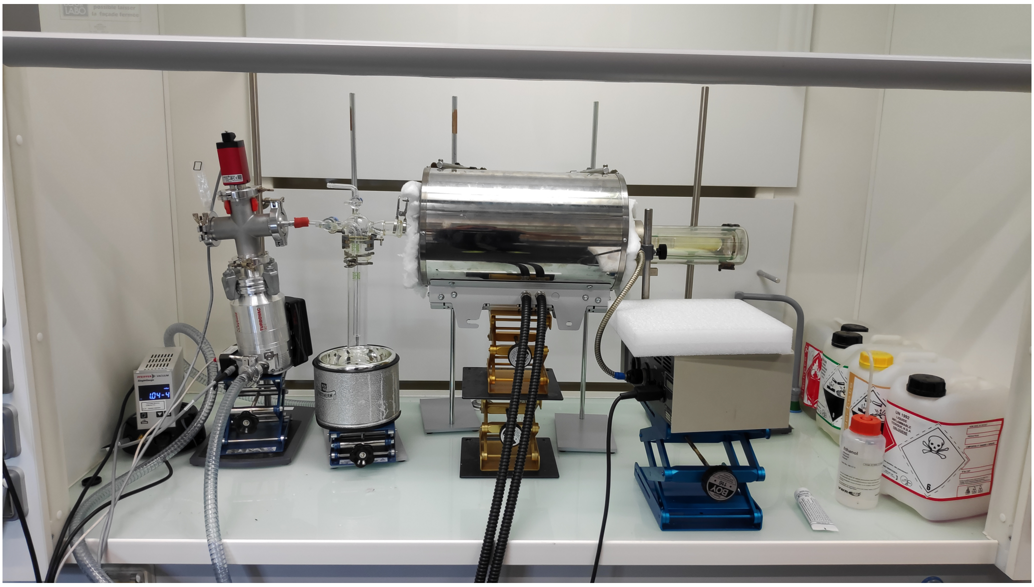

Figure A3.1: Setup of the preparative pyrolysis of fulminic Acid, HCNO. The Kugelrohr furnance which heats up the solid precursor is on the right. The vapor then enters a 3 cm diameter quartz tube which is inside the tube oven, set to 465°C. The pyrolytic products then enter the cooling trap. The Leybold turbomolecular pump which produces the high vacuum is pictured on the left. The roughing pump, a Pfeiffer rotary vane pump, is set up below the fume hood.

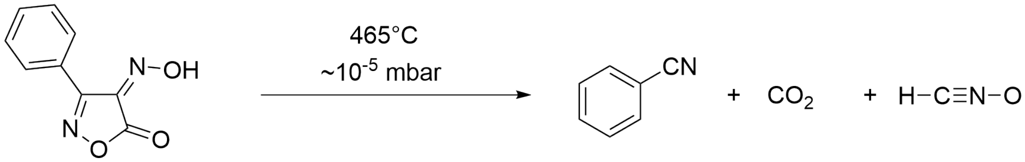

The precursor 3-phenyl-4-oximino-isoxazol-5(4H)-one was prepared in a two step synthesis according to the procedure by Wilmes and Winnewisser.[90] The setup (Figure A3.1) of the preparative pyrolysis is similiar to that shown in a review article by Wentrup[91], the preparative pyrolysis of fulminic acid was first published by Wentrup *et al.* in 1979.[53] The setup consists of several parts. The solid precursor needs to be heated to around 100°C at high vacuum to yield sufficient vapor pressure. The vapor is then heated to 465°C to induce pyrolysis. The products are collected in a liquid nitrogen cooling trap.

To heat up the precursor we used a Büchi Kugelrohr furnace. The pyrolysis is initiated in a Carbolite EVA12/300B tube furnace. The high vacuum is produced by Leybold TURBOVAC 90i turbomolecular pump (78 l/s for H_2) combined with a rotary vane roughing pump. It is integral that the entire setup is built as compact as possible so that the pressure at the precursor is sufficiently low. This means that all lines should be as short as possible and that the diameter of the glassware is as big as possible. Long tubes connecting different parts of the setup should be avoided. The tube furnace and the turbomolecular pump must be secured to the fume hood to provide stability.

The sample holder is a glass tube closed on one end and with a NS29/32 glass joint on the other end. The pyrolysis tube is a 50 cm long quartz glass tube with a 3 cm diameter and NS29/32 glass joints on each end. The cooling trap has three connections, on the right side a glass joint that connects to the pyrolysis tube. On the left is a glass valve that is connected to the turbomolecular pump by a short piece of rubber tube. This valve is also connected to the glass tube that reaches down into the cooling trap. If this tube would lead instead to the pyrolysis tube the product may freeze inside the tube and clog the setup. The cooling trap has a second valve on top which is used to introduce inert gas into the setup.

Around 500 mg of the precursor are used in each run of the synthesis. First the setup is evacuated to about 10^{-5} mbar and the cooling trap is cooled with liquid nitrogen. Once the tube oven is at 465°C the Kugelrohr furnace is turned on. After around 2 to 3 hours most of the precursor was used up and a white solid is visible in the cooling trap. In the next step the side product CO_2 and possible contaminations are removed by roughing pump pressure. First the turbomolecular pump is turned off and the pressure rises. When the pressure has stabilized again the liquid nitrogen is replaced by a ethanol/dry ice bath at around -45°C. The pressure will rise due to the outgasing of CO_2 and returns to 10^{-2} mbar, once most of the CO_2 is removed. Inert gas is introduced over the top valve and under inert gas flow the cooling trap is disconnected from the pyrolysis tube and closed by a glass stopper. Finally the sample is again evacuated using the roughing pump and transported to the beamline at -45°C.

Additonal photoelectron spectra

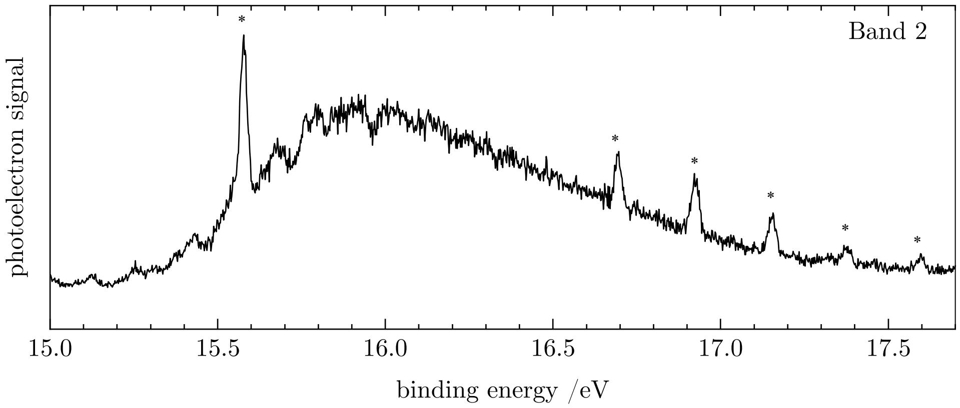

Figure A3.2: Photoelectron spectrum of the broad band of HCNO around 16 eV. The asterisks mark contaminations by molecular nitrogen.[85]

HCNO Reaction enthalpies to for dissociative photoionization

Table A3.1: Heats of reaction, $\Delta_R H^\circ$ for the dissociation HCNO → products. The energies are taken from the Active thermochemical tables and given in eV.[86] Only the ten most favored reactions are shown. Spin multiplicites of the fragments are taken from Ref. [29].

Products	$\Delta_R H^\circ$, /eV
$^1HCO^+ + {}^4N$	11.68
$^3NCO^+ + {}^2H$	13.54
$^2NH^+ + {}^1CO$	14.24
$^1NO^+ + {}^2CH$	14.57
$^2CO^+ + {}^3NH$	14.78
$^2HNC^+ + {}^3O$	14.79
$^2HCN^+ + {}^3O$	15.73
$^4O^+ + {}^1HCN$	15.74
$^1HC^+ + {}^2NO$	15.95
$^3CNO^+ + {}^2H$	16.11

Time-of-flight mass spectra

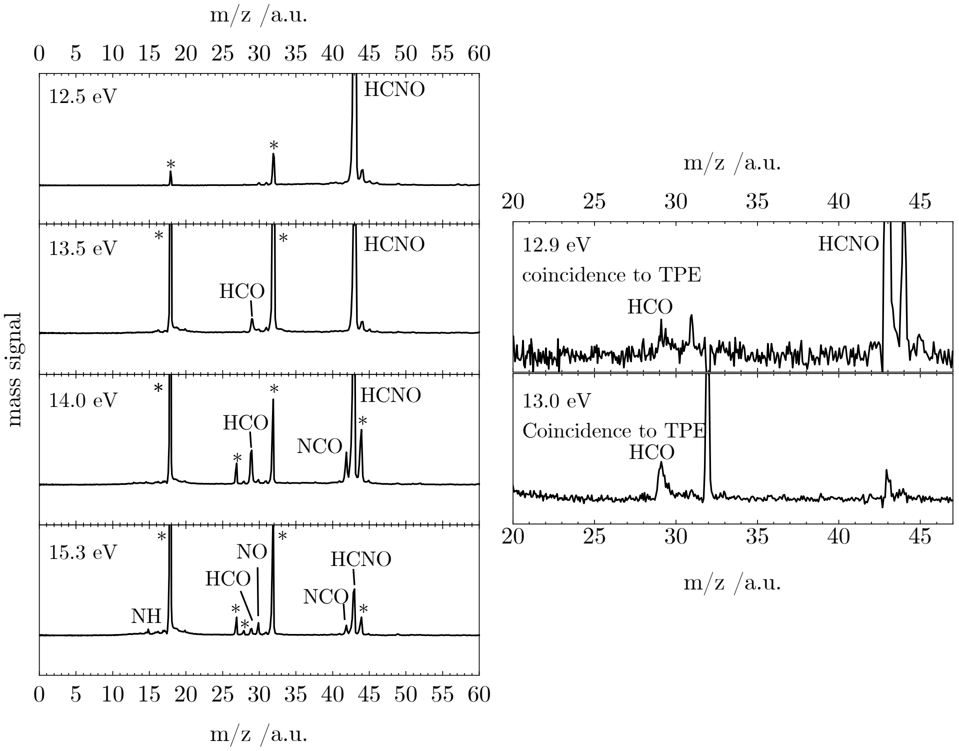

Figure A3.3: Time-of-flight mass spectra of HCNO at different photon energies. Left: Time-of-flight mass spectra (TOF-MS) without selection of electrons. All y-axes have the same scaling. Peaks marked with asterisks are due to contamination in the sample or the experimental chamber. m/z = 18 corresponds to water and m/z = 32 to O_2. Starting at 14.0 eV molecular HCN and CO_2 are observed at m/z = 27 and m/z = 44. In the spectrum at 15.3 eV CO with m/z = 28 is observed. Peaks associated with the DPI from HCNO are marked with their molecular formula. Right: TOF-MS 12.9 and 13.0 eV of the ions that are in coincidence with threshold photoelectrons (TPE). The chosen energies are at the threshold of the dissociation to HCO^+. Some asymmetry can be observed in the peak corresponding to HCO^+.

Additional Computational Details

Fulminic Acid Cation Electronic States

The energy range covered by the experimental photoelectron spectrum of 10-22 eV spans many electronic states of the fulminic acid cation. We attempted to calculate these states using a similar *ab initio* procedure to that described in the main manuscript. Energies for the fulminic acid cation were calculated with OpenMolcas[62] using a 30 state-averaged RASSCF method followed by CASPT2 (with a level shift of 0.2 hartree) using an (11,10) active space with a cc-pVDZ basis set. It was found that a large number of states had to be included in the calculation to obtain the correct ordering of lower energy states. The obtained molecular orbitals are shown in Figure A3.4. Table A3.2 shows the occupations in increasing energy with respect to the neutral molecule, of the cation's first 12 electronic states. Note that the orbital occupation order obtained from OpenMolcas does not follow the orbital energies.

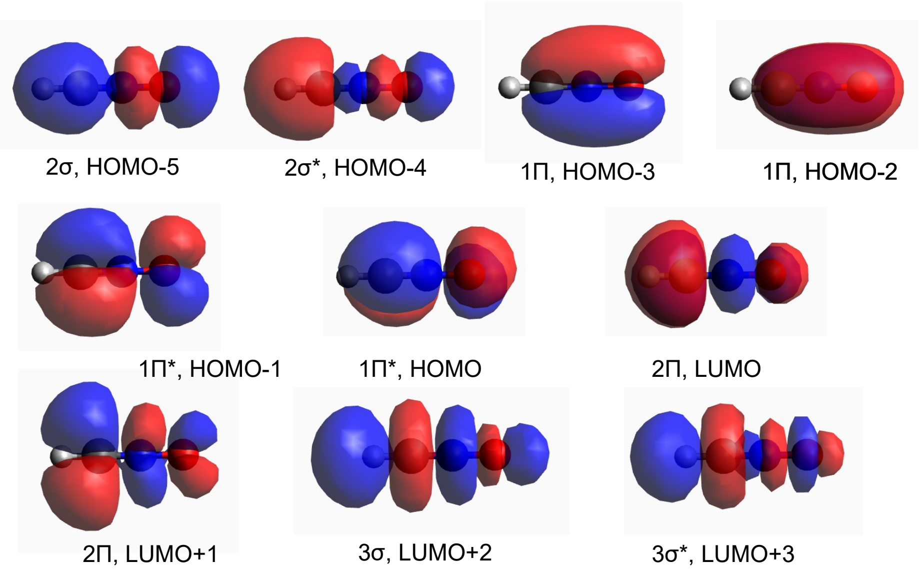

Figure A3.4: $HCNO^+$ molecular orbitals at (neutral) equilibrium geometry using CASPT2/cc-pVDZ.

Table A3.2: Electronic states of fulminic acid cation using (11,10) CASPT2/cc-pVDZ method.

Electronic State	Occupation	|CI coefficient|	Energy / eV
1	222u220000	0.89	10.33
2	22222u0000	0.89	10.33
3	u222220000	0.73	15.64
4	2222u20000	0.73	15.64
5	222u2ud000	0.67	16.64
6	222u2u0d00	0.67	16.64
7	222u2du000	0.59	17.22
8	222u2d0u00	0.59	17.22
9	22u2220000	0.70	18.08
10	222022u000	0.54	18.19
11	2222200u00	0.54	18.19
12	2u22220000	0.62	19.41

As noted by Mondal and Mukhopadhyay[28], at equilibrium $HCNO^+$ has consecutive low-lying doubly degenerate $^2\Pi$ states with deviations from linearity lifting this degeneracy and leading to the generation of $^2A'$ and $2A''$ states. States 1 and 2 are the expected states resulting from removal of an electron from the neutral's HOMO and HOMO−1 degenerate π^* orbitals (see Figure A3.4). Similarly, states 3 and 4 result from the removal of an electron from the neutral's HOMO−2 and HOMO−3 degenerate π orbitals. States 5/6 and 7/8 are of mixed π character and cannot be attributed in a Koopman's theorem manner to removal of an electron from orbtials of the neutral. State 9 is obtained by removal of an electron from the HOMO−4 σ^* orbital. States 10/11 are again of mixed character resulting from promotion of an electron from lower to higher energy π orbitals. Finally, state 12 is again describable in terms of removal of an electron from a neutral orbital, in this case the HOMO-5 σ^* orbital.

In passing we note that we also tried other electronic structure methods to obtain the excited states of the fulminic acid cation. These included electron propagator theory (EPT) with renormalized partial third order approximation P3+[92] as implemented in Gaussian[79], algebraic diagrammatic construction (ADC(2)[93] and ADC(3)[94]) as implemented in Q-Chem[95] and equation-of-motion (EOM)-CCSD-IP[96], also implemented in Q-Chem. These methods gave electronic states in reasonable agreement with each other and with those of the CASPT2 calculations for states 1-4, the two sets of lowest energy degenerate states. However, these methods did not appear to be able to obtain the states of mixed character (states 5-8) described above and it seems a multi-reference method is required to obtain these states.

To give an example of the difficulty of going beyond a two-state vibronic coupling model for the fulminic acid cation, Figure A3.5 shows the *ab initio* energies of the first 12 states of $HCNO^+$ molecular orbitals along either of the $Q_{1/2}$ modes obtained from the 30 state averaged CASPT2/cc-pVDZ calculations described previously. It can be seen that between 16 and 20 eV there are ten electronic states which overlap at multiple points. The variation in energy of these states along these bending modes also shows complicated behaviour for which harmonic, Morse or polynomials would not be suitable fitting functions. It seems likely that a theoretical description of the experimental photoelectron spectra up to 20 eV will require going beyond a normal-mode vibronic coupling Hamiltonian treatment.

As a final point, we note that for other modes it was very difficult to retain electronic states 9 and 12 at geometries away from equilibrium where these states go to higher energies and the state ordering changes rapidly with geometry. A full theoretical treatment will also need a carefully chosen active space and basis set to account for this.

Vibronic Coupling Hamiltonian Parameters

As discussed in the main text, a vibronic coupling Hamiltonian model[66] was used to obtain potential energy surfaces for both the ground state of the neutral

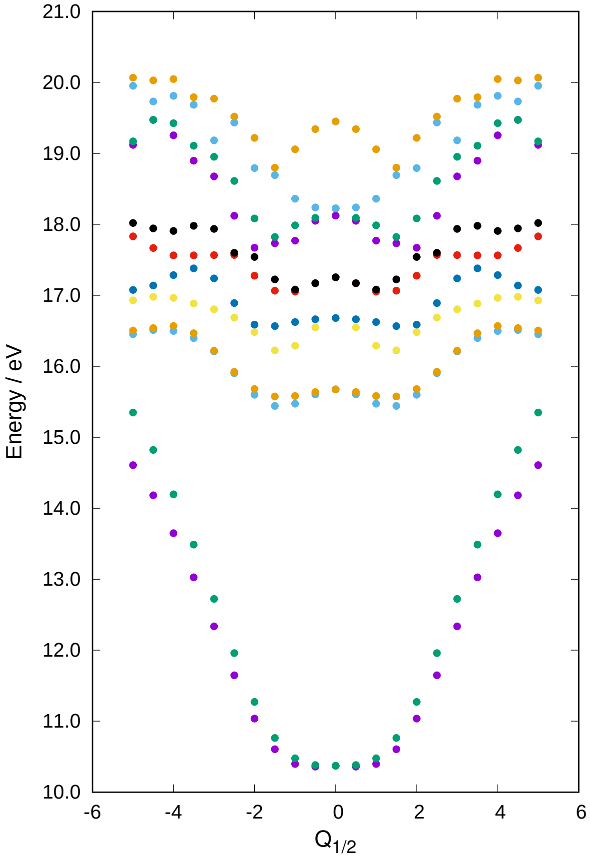

Figure A3.5: First 12 HCNO$^+$ electronic states $Q_{1/2}$ modes using 30 state averaged CASPT2/cc-pVDZ.

fulminic acid molecule and the two lowest electronic states of HCNO$^+$. The diabatic potentials are expressed as a Taylor series, in dimensionless (mass-frequency scaled) normal modes around a point, $\mathbf{Q}_0$, here taken as the equilibrium geometry. At this point, the diabatic and adiabatic electronic wavefunction are assumed to be equal.

The Hamiltonian can be written in matrix form as

$$\mathbf{H} = \mathbf{H}^{(0)} + \mathbf{W}^{(0)} + \mathbf{W}^{(1)} + \dots \tag{3.8}$$

with the zeroth-order diagonal Hamiltonian $\mathbf{H}^{(0)}$ is expressed in the harmonic approximation

$$H_{ii}^{(0)} = \sum_{\alpha} \frac{\omega_\alpha}{2} \left(\frac{\partial}{\partial Q_\alpha^2} + Q_\alpha^2 \right). \quad (3.9)$$

The subsequent matrices include the effects of electronic excitation and vibronic coupling as a Taylor expansion around $\mathbf{Q}_0$. To obtain better fits to the *ab initio* calculated energies, higher order polynomial terms are also added to the model as

$$\mathbf{W}_{ii} = \alpha Q_\alpha + \frac{\beta}{2!} Q_\alpha^2 + \frac{\delta}{3!} Q_\alpha^3 + \frac{\epsilon}{4!} Q_\alpha^4 + \frac{\zeta}{6!} Q_\alpha^6 + \frac{\eta}{8!} Q_\alpha^8 \quad (3.10)$$

while for certain stretching modes a Morse potential was used of form

$$\mathbf{W}_{ii} = D_0 \left[\exp(\alpha_m (Q_\alpha - X_0) - 1) \right]^2 . \quad (3.11)$$

All parameters of the vibronic coupling Hamiltonians were obtained by least-squares fitting to the CASPT2 *ab initio* energies using the VCHAM package[70] as implemented within the Quantics program suite[71]. Fits were constrained so that parameters for degenerate electronic energies and vibrational modes remained equal.

For neutral fulminc acid only the ground electronic state was required and so the model does not contain any coupling to higher energy electronic states. The ω parameters for the underlying harmonic approximation for both the neutral molecule and cation were obtained at the CCSD(T)/cc-pVTZ level of theory at the corresponding optimised geometry as discussed in the main text. The parameters are the same as those of Table 1 in the main text but are repeated here in Table A3.3 for the sake of completeness (in eV units). For modes $\omega_{1/2}$, the absolute value of the imaginary frequencies are used in the vibronic coupling Hamiltonian. Force vectors of the harmonic normal modes are displayed in Figure A3.6.

For neutral HCNO the underlying harmonic approximation to the potential was replaced with polynomials and Morse functions to obtain better fits to the *ab initio* energies. For the degenerate bending modes $\omega_{1/2}$, expansion terms up to eighth order were required in order to fit the very shallow potential energy curve along these modes (see discussion in main text). For the other degenerate bending modes $\omega_{3/4}$, further second and fourth order terms were added. For both modes

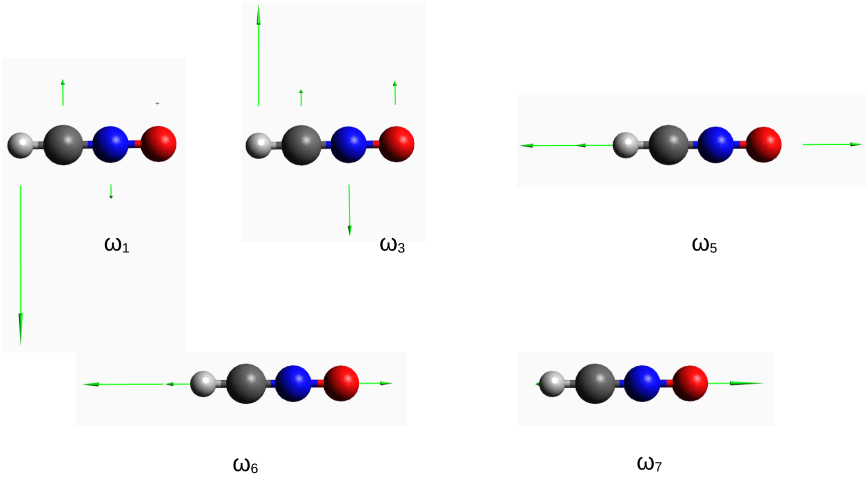

Figure A3.6: Force vectors (green) of HCNO normal modes obtained from CCSD(T)/cc-pVTZ calculations. Modes ω_2 and ω_4 are perpendicular to those of ω_1 and ω_3.

Table A3.3: Vibrational frequencies used for fulminic acid neutral and cation for harmonic terms (Eq. 3.9).

Mode	$\lvert\omega\rvert$ / eV	Normal Mode
$\omega_{1/2}(B_{1/2})$	0.026	H-C-N bend
$\omega_{3/4}(B_{1/2})$	0.069	C-N-O bend
$\omega_5(A_1)$	0.157	C-N-O sym. stretch
$\omega_6(A_1)$	0.282	C-N-O asym. stretch
$\omega_7(A_1)$	0.434	C-H stretch

$\omega_{1/2}$ and $\omega_{3/4}$, only even polynomial terms are required due to the symmetry of the bending modes around equilibrium. For the neutral molecule's stretching modes, a general quartic polynomial was used for ω_6 while for ω_5 and ω_7, a Morse potential function was used. All fitting parameters are shown in Tables A3.4 and A3.5.

Figure A3.7 shows the *ab initio* energies and fits for the degenerate bending modes of HCNO. Of note is the flatness of the potential energy surface for modes $Q_{1/2}$ around equilibrium and how little the energy varies (< 1 eV) for modes $Q_{3/4}$. Both features contribute to the floppyness of HCNO. Corresponding plots for the stretching modes are given in Figure A3.8.

Table A3.4: Parameters for polynomial fits (Eq. 3.10) to neutral HCNO modes. All values in eV.

Mode	α	β	δ	ϵ	ζ	η
$Q_{1/2}$	-	-0.053	-	1.318	-2.683	2.917
$Q_{3/4}$	-	-0.004	-	-0.004	-	-
Q_6	-0.076	0.035	-0.046	0.012	-	-

Table A3.5: Morse function parameters (Eq. 3.11) used for HCNO stretching modes ω_5 and ω_7.

Mode	D_0 / eV	α	X_0 / Å
Q_5	6.153	0.112	0.218
Q_7	6.302	-0.193	-0.0537

For the fulminic acid cation, the zero order term $\mathbf{W}^{(0)}$ is a diagonal matrix of excitation energies. These are obtained as the difference in energy between the neutral and cation calculated at the same level of theory and $\mathbf{W}^{(0)}_{11} = \mathbf{W}^{(0)}_{22} = 10.59290$ eV.

The first order term $\mathbf{W}^{(1)}$ usually contains on-diagonal linear terms for each electronic state and off-diagonal linear terms coupling states along a particular mode, however, for fulminic acid these terms are absent and coupling is provided through second order Renner-Teller (RT) terms. Following Worth and Cederbaum[68], for the two pairs of degenerate vibrational modes ($Q_{1/2}$ and $Q_{3/4}$), the

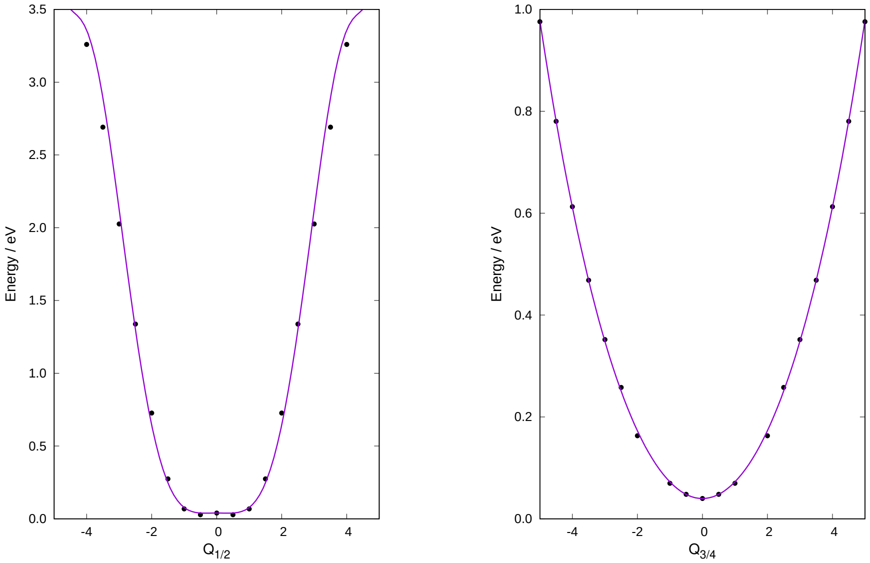

Figure A3.7: Vibronic coupling Hamiltonian fits (lines) and CASPT2 (11,10)/cc-pVDZ *ab initio* energies for $Q_{1/2}$ and $Q_{3/4}$ degenerate bending modes of HCNO ground electronic state.

vibronic coupling Renner-Teller Hamiltonain can be expressed as

$$\mathbf{H} \;=\; \frac{\omega}{2}\left(Q_i^2+Q_j^2\right)+\begin{vmatrix} -\frac{1}{2}\gamma(Q_j^2-Q_i^2) & \gamma Q_iQ_j \\ \gamma Q_iQ_j & \frac{1}{2}\gamma(Q_j^2-Q_i^2) \end{vmatrix} \tag{3.12}$$

where ω is the degenerate vibrational frequency for the pair of modes i and j and γ is the parameter which causes the splitting of the degenerate electronic surfaces. To obtain photoelectron spectra in agreement with experiment, the harmonic terms in the RT model of Eq. 3.12 had to be replaced polynomial terms. The second order γ parameters which split the degenerate modes away from equilibrium were retained as were the off-diagonal products of γQ_iQ_j.

For the fulminc acid cation, the harmonic approximation was replaced for all modes with polynomial expansions given by Eq. 3.10. As with the neutral, for modes $\omega_{1/2}$ large expansions were required and for bending modes, only even terms are required. These parameters are given in Table A3.6 along with the RT γ parameters for $Q_{1/2}$ and $Q_{3/4}$. For the HCNO$^+$ cation bi-linear terms were also

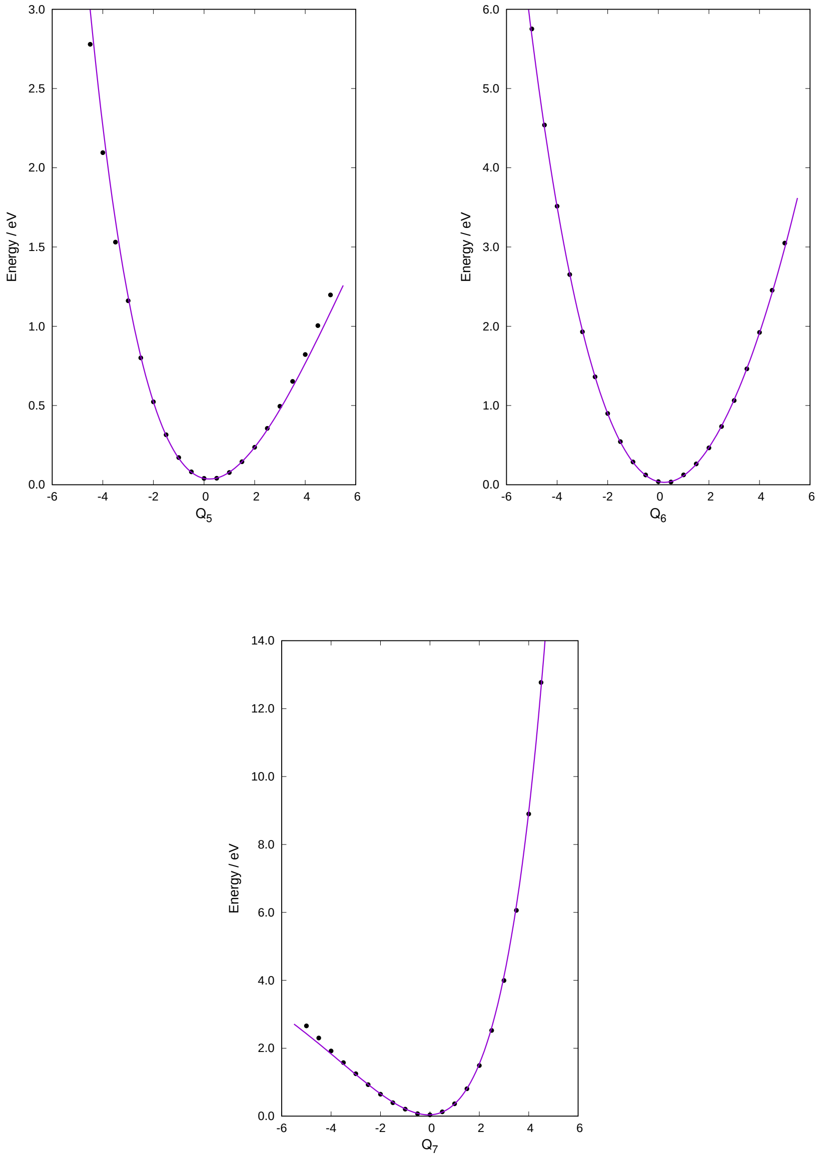

Figure A3.8: Vibronic coupling Hamiltonian fits (lines) and CASPT2 (11,10)/cc-pVDZ *ab initio* energies for Q_5, Q_6 and Q_7 stretching modes of HCNO ground electronic state.

introduced to the model of form

$$W_{ii}^{(2)} = \sum_{\alpha<\beta} \gamma_{\alpha\beta}^{(i)} Q_\alpha Q_\beta, \tag{3.13}$$

which take into account for coupling of vibrational modes. Parameters for these terms are given in Table A3.7.

Table A3.6: Parameters for polynomial fits to $HCNO^+$ modes and RT γ parameters for modes $\omega_{1/2}$ and $\omega_{3/4}$ All values in eV.

Mode	α	β	δ	ϵ	ζ	η	γ
$Q_{1/2}$	-	0.264	-	0.579	-0.974	0.799	0.063
$Q_{3/4}$	-	-0.027	-	0.006	-	-	0.005
Q_5	-0.017	0.001	-0.040	0.001	-	-	-
Q_6	-0.030	-0.051	-0.046	0.016	-	-	-
Q_7	0.040	0.023	0.280	0.104	-	-	-

Table A3.7: Bi-linear second-order coupling constant (Eq. 3.13) parameters for $HCNO^+$. All values in eV.

Modes	$\gamma^1_{i,j}$	$\gamma^2_{i,j}$
Q_1/Q_3	-0.084	-0.072
Q_2/Q_4	0.000	0.000
Q_5/Q_6	0.023	0.023
Q_5/Q_7	0.010	0.010
Q_6/Q_7	0.008	0.008

Figure A3.9 shows the *ab initio* energies and fits for the degenerate bending modes $Q_{1/2}$ and $Q_{3/4}$. To show the appearance of the Renner-Teller intersection, Figure A3.10 shows 3D and contour plots to fits for the degenerate bending modes $Q_{1/2}$ with contours again emphasising the flatness of the potential energy surface for modes $Q_{1/2}$ around equilibrium. Figure A3.11 shows the *ab initio* energies and fits for the stretching modes Q_5, Q_6 and Q_7.

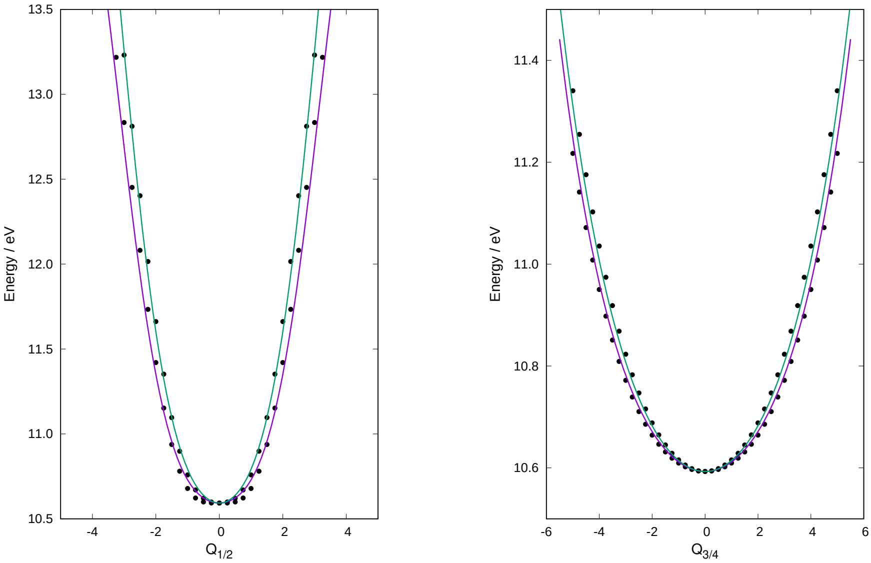

Figure A3.9: Vibronic coupling Hamiltonian fits (lines) and CASPT2 (11,10)/cc-pVTZ *ab initio* energies for $Q_{1/2}$ and $Q_{3/4}$ degenerate bending Renner-Teller modes of HCNO$^+$.

Zero kelvin photoelectron spectrum

Figure A3.12 shows the simulated photoelectron spectrmum of fulminic acid obtained from both conventional (0 K) MCTDH wavepacket calculations and those at 300 K obtained from the density matrix method. The experimental spectrum is also shown. For both simulations, wavepackets were relaxed on the neutral molecule potential energy surface and then promoted to the degenerate ground states of the cation. Assignments for the 0 K spectrum were determined by including and excluding modes from the simulation and observing the effect on the simulated spectrum. See main text for more details and a discussion of the spectrum's features.

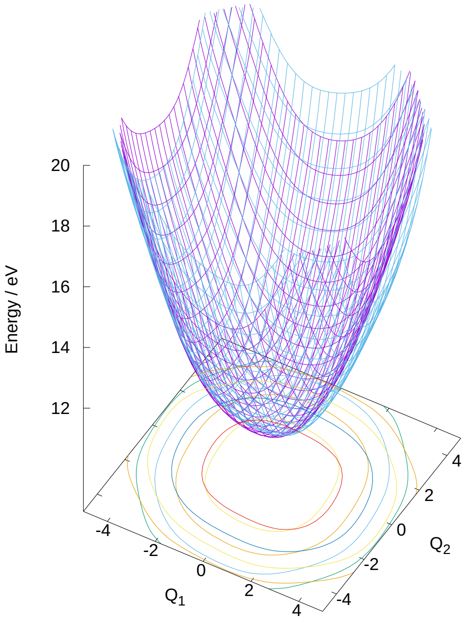

Figure A3.10: Vibronic coupling Hamiltonian fit for $Q_{1/2}$ Renner-Teller mode of HCNO$^+$ showing glancing intersection of electronic states at equilibrium geometry.

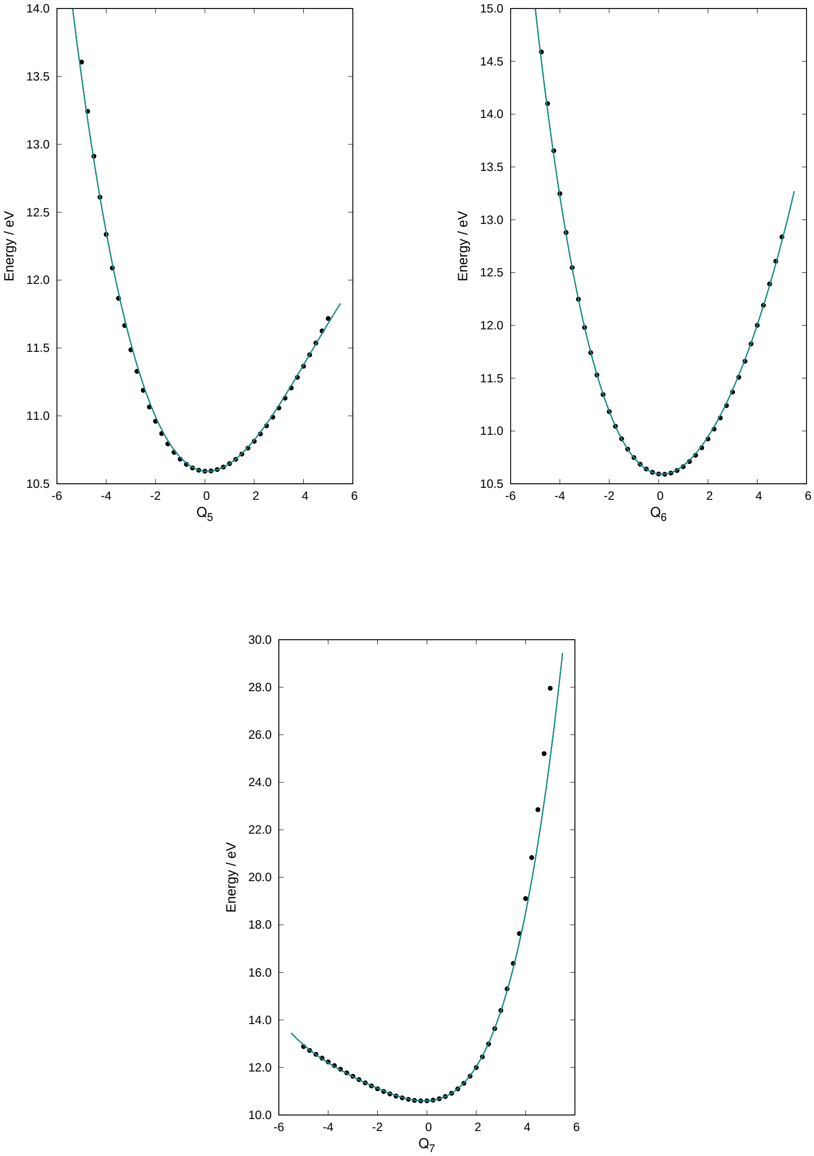

Figure A3.11: Vibronic coupling Hamiltonian fits (lines) and CASPT2 (11,10)/cc-pVTZ *ab initio* energies for Q_5, Q_6 and Q_7 stretching modes of HCNO$^+$.

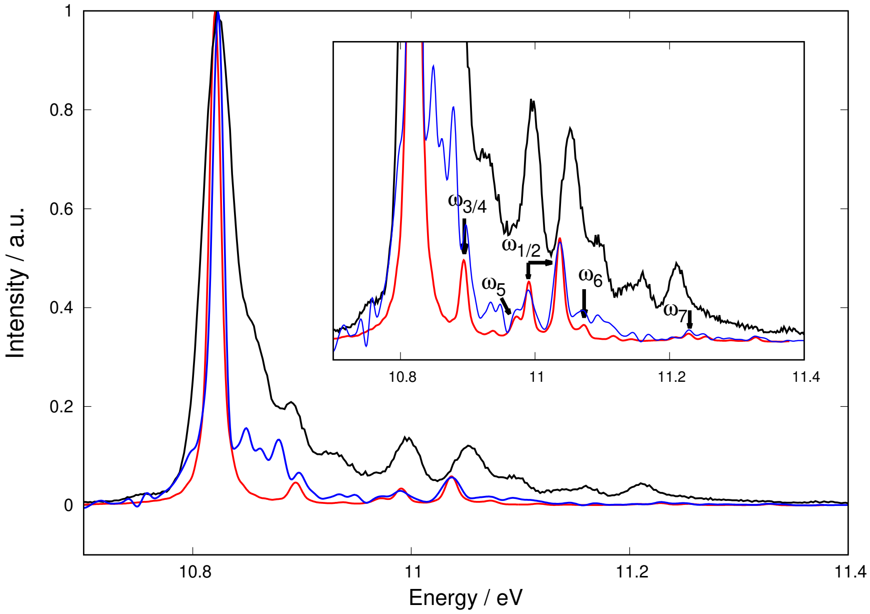

Figure A3.12: Experimental (black line), density matrix 300 K calculated (blue line) and 0 K calculated (red line) fulminic acid photoelectron spectrum. Inset shows labelling of bands from 0 K calculation.

Additional information about the dissociative photoionization

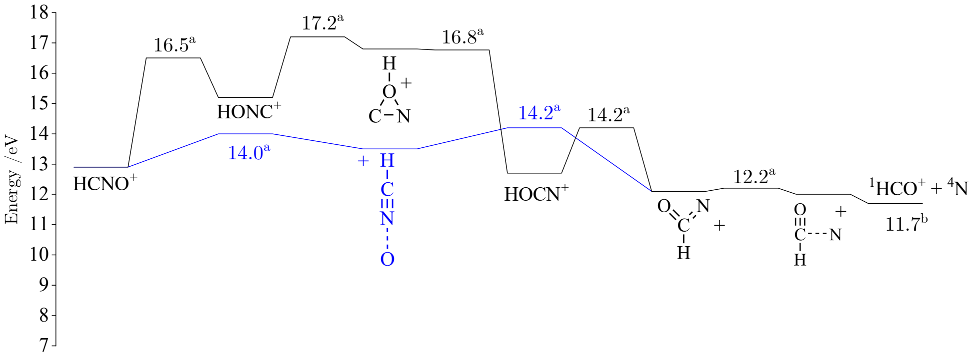

Figure A3.13: Mechanism of the ^{1}HCO$^+$ + ^{4}N formation on the quartet surface starting from HCNO$^+$ in the quartet ground state. Energies are given in eV relative to the neutral HCNO. Energies and structures marked with ^{a} were taken from Ref. [29]. Energies marked with ^{b} are taken from Ref. [86].

Table A3.8: Cartesian Coordinates of the calculated transition states using the G4 theory.[78]

TS1	X	Y	Z
C	-0.97	-0.19	0.00
H	-1.83	-0.86	0.00
N	-0.08	0.62	-0.00
O	1.02	-0.29	-0.00

TS2	X	Y	Z
C	0.00	0.52	0.00
H	0.71	1.36	0.00
O	-1.10	0.22	0.00
N	1.15	-0.89	0.00

TS3	X	Y	Z
C	-0.93	-0.36	0.00
O	-0.09	0.53	0.00
H	-2.03	-0.28	0.00
N	1.19	-0.26	0.00

TS4	X	Y	Z
C	1.12	0.73	0.00
H	-0.35	1.23	0.00
N	0.00	0.12	0.00
O	-0.80	-0.81	0.00

TS5	X	Y	Z
C	-0.17	0.80	0.04
H	1.45	-0.52	0.53
N	0.74	-0.14	-0.13
O	-0.70	-0.41	0.013

Table A3.9: Cartesian Coordinates of the calculated intermediate states using the G4 theory.[78]

I (Doublet)	X	Y	Z
C	0.02	0.67	0.00
H	-0.14	1.75	0.00
N	0.82	-0.37	-0.00
O	-0.71	-0.40	-0.00

I (Quartet)	X	Y	Z
C	-0.05	0.38	0.00
H	-0.04	1.50	-0.00
N	1.26	-0.24	-0.00
O	-1.06	-0.27	-0.00

HCON	X	Y	Z
H	1.98	0.55	0.00
C	1.17	-0.21	0.00
O	-0.01	0.12	-0.00
N	-1.27	-0.04	0.00

II	X	Y	Z
C	0.00	0.77	0.00
H	1.06	1.045	0.00
O	-1.10	0.62	0.00
N	1.11	-1.52	0.00

III	X	Y	Z
C	0.94	-0.29	-0.00
H	-0.38	1.58	0.00
N	0.00	0.62	-0.00
O	-0.66	-0.52	0.00

References

[1] F. Kurzer, *J. Chem. Educ.* **2000**, *77*, 851.

[2] C. Wentrup, *Angew. Chem. Int. Ed.* **2019**, *58*, 14800–14808.

[3] N. Marcelino, J. Cernicharo, B. Tercero, E. Roueff, *Astrophys. J.* **2009**, *690*, L27–L30.

[4] N. Marcelino, S. Brünken, J. Cernicharo, D. Quan, E. Roueff, E. Herbst, P. Thaddeus, *Astron. Astrophys.* **2010**, *516*, A105.

[5] E. Mendoza, B. Lefloch, A. López-Sepulcre, C. Ceccarelli, C. Codella, H. M. Boechat-Roberty, R. Bachiller, *Mon. Not. R. Astron. Soc.* **2014**, *445*, 151–161.

[6] B. Lefloch, R. Bachiller, C. Ceccarelli, J. Cernicharo, C. Codella, A. Fuente, C. Kahane, A. López-Sepulcre, M. Tafalla, C. Vastel, E. Caux, M. González-García, E. Bianchi, A. Gómez-Ruiz, J. Holdship, E. Mendoza, J. Ospina-Zamudio, L. Podio, D. Quénard, E. Roueff, N. Sakai, S. Viti, S. Yamamoto, K. Yoshida, C. Favre, T. Monfredini, H. M. Quitián-Lara, N. Marcelino, H. M. Boechat-Roberty, S. Cabrit, *Mon. Not. R. Astron. Soc.* **2018**, *477*, 4792–4809.

[7] N. Marcelino, M. Agúndez, J. Cernicharo, E. Roueff, M. Tafalla, *Astron. Astrophys.* **2018**, *612*, L10.

[8] M. Agúndez, N. Marcelino, J. Cernicharo, E. Roueff, M. Tafalla, *Astron. Astrophys.* **2019**, *625*, A147.

[9] D. H. Quan, E. Herbst, Y. Osamura, E. Roueff, *Astrophys. J.* **2010**, *725*, 2101–2109.

[10] S. Brünken, A. Belloche, S. Martín, L. Verheyen, K. M. Menten, *Astron. Astrophys.* **2010**, *516*, A109.

[11] M. S. Schuurman, S. R. Muir, W. D. Allen, H. F. S. III, *J. Chem. Phys.* **2004**, *120*, 11586–11599.

[12] M. Mladenović, M. Lewerenz, M. C. McCarthy, P. Thaddeus, *J. Chem. Phys.* **2009**, *131*, 174308.

[13] K. Molaverdikhani, T. Henning, P. Mollière, *Astrophys. J.* **2019**, *883*, 194.

[14] L. J. Conway, C. J. Pickard, A. Hermann, *Proc. Natl. Acad. Sci.* **2021**, *118*, e2026360118.

[15] P. Gorai, B. Bhat, M. Sil, S. K. Mondal, R. Ghosh, S. K. Chakrabarti, A. Das, *Astrophys. J.* **2020**, *895*, 86.

[16] A. M. Juett, N. S. Schulz, D. Chakrabarty, *Astrophys. J.* **2004**, *612*, 308–318.

[17] S. S. Prasad, S. P. Tarafdar, *Astrophys. J.* **1983**, *267*, 603–609.

[18] R. Gredel, S. Lepp, A. Dalgarno, E. Herbst, *Astrophys. J.* **1989**, *347*, 289.

[19] A. Sternberg, A. Dalgarno, S. Lepp, *Astrophys. J.* **1987**, *320*, 676.

[20] M. T. Nguyen, K. Pierloot, L. G. Vanquickenborne, *Chem. Phys. Lett.* **1991**, *181*, 83–87.

[21] A. P. Rendell, T. J. Lee, R. Lindh, *Chem. Phys. Lett.* **1992**, *194*, 84–94.

[22] N. Pinnavaia, M. J. Bramley, M.-D. Su, W. H. Green, N. C. Handy, *Mol. Phys.* **1993**, *78*, 319.

[23] J. Koput, B. P. Winnewisser, M. Winnewisser, *Chem. Phys. Lett.* **1996**, *255*, 357–362.

[24] A. M. Mebel, A. Luna, M. C. Lin, K. Morokuma, *J. Chem. Phys.* **1996**, *105*, 6439–6454.

[25] M. Mladenović, M. Lewerenz, *Chem. Phys.* **2008**, *343*, 129–140.

[26] P. R. Bunker, B. M. Landsberg, B. P. Winnewisser, *J. Mol. Spectrosc.* **1979**, *74*, 9–25.

[27] P. R. Bunker, *Annu. Rev. Phys. Chem.* **1983**, *34*, 59–75.

[28] R. Mondal, D. Mukhopadhyay, *Int. J. Quantum. Chem.* **2020**, *120*, e26195.

[29] A. Luna, A. M. Mebel, K. Morokuma, *J. Chem. Phys.* **1996**, *105*, 3187–3205.

[30] M. Winnewisser, H. K. Bodenseh, *Z. Naturforsch. A* **1967**, *22*, 1724.

[31] B. P. Winnewisser, M. Winnewisser, F. Winther, *J. Mol. Spectrosc.* **1974**, *51*, 65–96.

[32] B. P. Winnewisser, M. Winnewisser, G. Wagner, J. Preusser, *J. Mol. Spectrosc.* **1990**, *142*, 29–56.

[33] W. Beck, K. Feldl, *Angew. Chem.* **1966**, *78*, 746–746.

[34] B. P. Winnewisser, M. Winnewisser, *J. Mol. Spectrosc.* **1969**, *29*, 505–507.

[35] W. Beck, P. Swoboda, K. Feldl, R. S. Tobias, *Chem. Ber.* **1971**, *104*, 533–543.

[36] E. L. Ferretti, K. Narahari Rao, *J. Mol. Struc.* **1974**, *51*, 97–106.

[37] V. E. Bondybey, J. H. English, C. W. Mathews, R. J. Contolini, *J. Mol. Spectrosc.* **1982**, *92*, 431–442.

[38] B. P. Winnewisser, P. Jensen, *J. Mol. Spectrosc.* **1983**, *101*, 408–421.

[39] S. Albert, M. Winnewisser, B. P. Winnewisser, *Ber. Bunsenges.* **1996**, *100*, 1876.

[40] S. Albert, K. K. Albert, M. Winnewisser, B. P. Winnewisser, *J. Mol. Struc.* **2001**, *599*, 347–369.

[41] W. Feng, J. F. Hershberger, *J. Phys. Chem. A* **2014**, *118*, 829–837.

[42] W. Feng, J. F. Hershberger, *Chem. Phys.* **2016**, *472*, 18–23.

[43] W. Feng, J. P. Meyer, J. F. Hershberger, *J. Phys. Chem. A* **2006**, *110*, 4458–4464.

[44] M. Gerlach, T. Preitschopf, E. Karaev, H. M. Quitián-Lara, D. Mayer, J. Bozek, I. Fischer, R. F. Fink, *Phys. Chem. Chem. Phys.* **2022**, *24*, 15217–15229.

[45] J. Bastide, J. P. Maier, *Chem. Phys.* **1976**, *12*, 177–190.

[46] C. E. C. A. Hop, K. J. Van den Berg, J. L. Holmes, J. K. Terlouw, *J. Am. Chem. Soc.* **1989**, *111*, 72–75.

[47] I. Fischer, S. T. Pratt, *Phys. Chem. Chem. Phys.* **2022**, *24*, 1944–1959.

[48] L. Bosse, B. P. Mant, D. Schleier, M. Gerlach, I. Fischer, A. Krueger, P. Hemberger, G. Worth, *J. Phys. Chem. Lett.* **2021**, *12*, 6901–6906.

[49] F. Holzmeier, M. Lang, I. Fischer, X. Tang, B. Cunha de Miranda, C. Romanzin, C. Alcaraz, P. Hemberger, *J. Chem. Phys.* **2015**, *142*, 184306.

[50] F. Holzmeier, T. J. A. Wolf, C. Gienger, I. Wagner, J. Bozek, S. Nandi, C. Nicolas, I. Fischer, M. Gühr, R. F. Fink, *J. Chem. Phys.* **2018**, *149*, 034308.

[51] Pleiades, `https://www.synchrotron-soleil.fr/fr/lignes-de-lumiere/pleiades` (visited on 09/16/2019, 15:43).

[52] M. Johnson, A. Bodi, L. Schulz, T. Gerber, *Nucl. Instrum. Methods Phys. Res. Sect. A* **2009**, *610*, 597–603.

[53] C. Wentrup, B. Gerecht, H. Briehl, *Angew. Chem. Int. Ed.* **1979**, *18*, 467–468.

[54] B. Sztaray, K. Voronova, K. G. Torma, K. J. Covert, A. Bodi, P. Hemberger, T. Gerber, D. L. Osborn, *J. Chem. Phys.* **2017**, *147*, 013944.

[55] B. Sztáray, T. Baer, *Rev. Sci. Instrum.* **2003**, *74*, 3763–3768.

[56] H.-J. Werner, P. J. Knowles, G. Knizia, F. R. Manby, M. Schütz, *WIREs Comput. Mol. Sci.* **2012**, *2*, 242–253.

[57] H.-J. Werner, P. J. Knowles, G. Knizia, F. R. Manby, M. Schütz, et al., MOLPRO, version 2019.2, a package of ab initio programs, see https://www.molpro.net, **2019**.

[58] H.-J. Werner, P. J. Knowles, F. R. Manby, J. A. Black, K. Doll, A. Heßelmann, A. Kats, T. Köhn, A Korona, D. A. Kreplin, Q. Ma, T. F. Miller III, A. Mitrushchenkov, K. A. Peterson, I. Polyak, G. Rauhut, M. Sibaev, *J. Chem. Phys.* **2020**, *152*, 144107.

[59] M. J. O. Deegan, P. J. Knowles, *Chem. Phys. Lett.* **1994**, *227*, 321–326.

[60] T. H. Dunning Jr, *J. Chem. Phys.* **1989**, *90*, 1007.

[61] J. D. Watts, J. Gauss, R. J. Bartlett, *J. Chem. Phys* **1993**, *98*, 8718.

[62] I. F. Galván, M. Vacher, A. Alavi, C. Angeli, F. Aquilante, J. Autschbach, J. J. Bao, S. I. Bokarev, N. A. Bogdanov, R. K. Carlson, L. F. Chibotaru, J. Creutzberg, N. Dattani, M. G. Delcey, S. S. Dong, A. Dreuw, L. Freitag, L. M. Frutos, L. Gagliardi, F. Gendron, A. Giussani, L. González, G. Grell, M. Guo, C. E. Hoyer, M. Johansson, S. Keller, S. Knecht, G. Kovačević, E. Källman, G. Li Manni, M. Lundberg, Y. Ma, S. Mai, J. P. Malhado, P. Å. Malmqvist, P. Marquetand, S. A. Mewes, J. Norell, M. Olivucci, M. Oppel,

Q. M. Phung, K. Pierloot, F. Plasser, M. Reiher, A. M. Sand, I. Schapiro, P. Sharma, C. J. Stein, L. K. Sørensen, D. G. Truhlar, M. Ugandi, L. Ungur, A. Valentini, S. Vancoillie, V. Veryazov, O. Weser, T. A. Wesołowski, P.-O. Widmark, S. Wouters, A. Zech, J. P. Zobel, R. Lindh, *J. Chem. Theory Comput.* **2019**, *15*, 5925–5964.

[63] P. Å. Malmqvist, A. Rendell, B. O. Roos, *J. Phys. Chem.* **1990**, *94*, 5477–5482.

[64] P. Å. Malmqvist, K. Pierloot, A. R. M. Shahi, C. J. Cramer, L. Gagliardi, *J. Chem. Phys.* **2008**, *128*, 204109.

[65] V. Sauri, L. Serrano-Andrés, A. R. M. Shahi, G. L, S. Vancoillie, K. Pierloot, *J. Chem. Theory Comput.* **2011**, *7*, 153–168.

[66] H. Köppel, W. Domcke, L. S. Cederbaum, *Adv. Chem. Phys.* **1984**, *57*, 59.

[67] T. J. Lee, D. J. Fox, H. F. Schaefer III, *J. Chem. Phys.* **1984**, *81*, 356.

[68] G. A. Worth, L. S. Cederbaum, *Annu. Rev. Phys. Chem.* **2004**, *55*, 127–58.

[69] Q. Lu, *ACS Omega* **2022**, *7*, 44078–44084.

[70] G. A. Worth, K. Giri, G. W. Richings, I. Burghardt, M. H. Beck, A. Jäckle, H.-D. Meyer, The Quantics Package Version2.0. See http://www.chem.ucl.ac.uk/quantics, University College London, U.K., **2020**.

[71] G. A. Worth, *Comput. Phys. Commun.* **2020**, *248*, 107040.

[72] S. Saddique, G. A. Worth, *Chem. Phys.* **2006**, *329*, 99–108.

[73] M. P. Taylor, G. A. Worth, *Chem. Phys.* **2018**, *515*, 719–727.

[74] M. H. Beck, A. Jäckle, G. A. Worth, H.-D. Meyer, *Phys. Rep.* **2000**, *324*, 1–105.

[75] A. Van Haeften, C. Ash, G. A. Worth, *J. Chem. Phys.* **2023**, To be submitted.

[76] A. Raab, I. Burghardt, H.-D. Meyer, *J. Chem. Phys.* **1999**, *111*, 8759–8772.

[77] O. Vendrell, H.-D. Meyer, *J. Chem. Phys.* **2011**, *134*, 44135.

[78] L. A. Curtiss, P. C. Redfern, K. Raghavachari, *J. Chem. Phys.* **2007**, *126*, 084108.

[79] M. J. Frisch, G. W. Trucks, H. B. Schlegel, G. E. Scuseria, M. A. Robb, J. R. Cheeseman, G. Scalmani, V. Barone, B. Mennucci, G. A. Petersson, H. Nakatsuji, M. Caricato, X. Li, H. P. Hratchian, A. F. Izmaylov, J. Bloino, G. Zheng, J. L. Sonnenberg, M. Hada, M. Ehara, K. Toyota, R. Fukuda, J. Hasegawa, M. Ishida, T. Nakajima, Y. Honda, O. Kitao, H. Nakai, T. Vreven, J. A. Montgomery Jr., J. E. Peralta, F. Ogliaro, M. Bearpark, J. J. Heyd, E. Brothers, K. N. Kudin, V. N. Staroverov, R. Kobayashi, J. Normand, K. Raghavachari, A. Rendell, J. C. Burant, S. S. Iyengar, J. Tomasi, M. Cossi, N. Rega, J. M. Millam, M. Klene, J. E. Knox, J. B. Cross, V. Bakken, C. Adamo, J. Jaramillo, R. Gomperts, R. E. Stratmann, O. Yazyev, A. J. Austin, R. Cammi, C. Pomelli, J. W. Ochterski, R. L. Martin, K. Morokuma, V. G. Zakrzewski, G. A. Voth, P. Salvador, J. J. Dannenberg, S. Dapprich, A. D. Daniels, Ö. Farkas, J. B. Foresman, J. V. Ortiz, J. Cioslowski, D. J. Fox, *Gaussian 16, Revision B.01*, Gaussian, Inc., Wallingford CT, **2016**.

[80] H. B. Schlegel, *J. Comp. Chem.* **1982**, *3*, 214–218.

[81] B. Sztáray, A. Bodi, T. Baer, *J. Mass. Spectrom.* **2010**, *45*, 1233–1245.

[82] M. Mladenović, M. Elhiyani, M. Lewerenzc, *J. Chem. Phys.* **2009**, *131*, 034302.

[83] A. Naindoubaa, C. Nkema, Y. Ajilib, K. Hammamib, N. Gotouma, L. C. Owono Owonoa, *Chem. Phys. Lett.* **2015**, *636*, 67–71.

[84] J. E. Reutt, L. S. Wang, Y. T. Lee, D. A. Shirley, *J. Chem. Phys.* **1986**, *85*, 6928–6939.

[85] J. W. Rabalais, T. P. Debies, J. L. Berkosky, J.-T. J. Huang, F. O. Ellison, *J. Chem. Phys.* **1974**, *61*, 516–528.

[86] B. Ruscic, D. H. Bross, Active Thermochemical Tables (ATcT) values based on ver. 1.122r of the Thermochemical Network (2021); available at ATcT.anl.gov.

[87] B. Ruscic, R. E. Pinzon, G. von Laszewski, D. Kodeboyina, A. Burcat, D. Leahy, D. Montoy, A. F. Wagner, *J. Phys.: Conference Series* **2005**, *16*, 561.

[88] A. Kramida, Yu. Ralchenko, J. Reader, and NIST ASD Team, NIST Atomic Spectra Database (ver. 5.9), [Online]. Available: https://physics.nist.gov/asd [2022, August 31]. National Institute of Standards and Technology, Gaithersburg, MD. **2021**.

[89] A. Jiménez-Escobar, B. M. Giuliano, G. M. Muñoz Caro, J. Cernicharo, N. Marcelino, *Astrophys. J.* **2014**, *788*, 19.

[90] R. Wilmes, M. Winnewisser, *J. Labelled Compd. Radiopharm.* **1993**, *33*, 157–159.

[91] C. Wentrup, *Angew. Chemie Int. Ed.* **2017**, *56*, 14808–14835.

[92] J. V. Ortiz, *J. Quantum Chem.* **2005**, *105*, 803–808.

[93] M. Wormit, D. R. Rehn, P. H. P. Harbach, J. Wenzel, C. M. Krauter, E. Epifanovsky, A. Dreuw, *Mol. Phys.* **2014**, *112*, 774.

[94] P. H. P. Harbach, M. Wormit, A. Dreuw, *J. Chem. Phys.* **2014**, *141*, 064113.

[95] Y. Shao et al, *Mol. Phys.* **2015**, *113*, 184–215.

[96] J. F. Stanton, J. Gauss, *J. Chem. Phys.* **1994**, *101*, 8938.

CHAPTER 4

Auger electron spectroscopy of fulminic acid, HCNO: An experimental and theoretical study

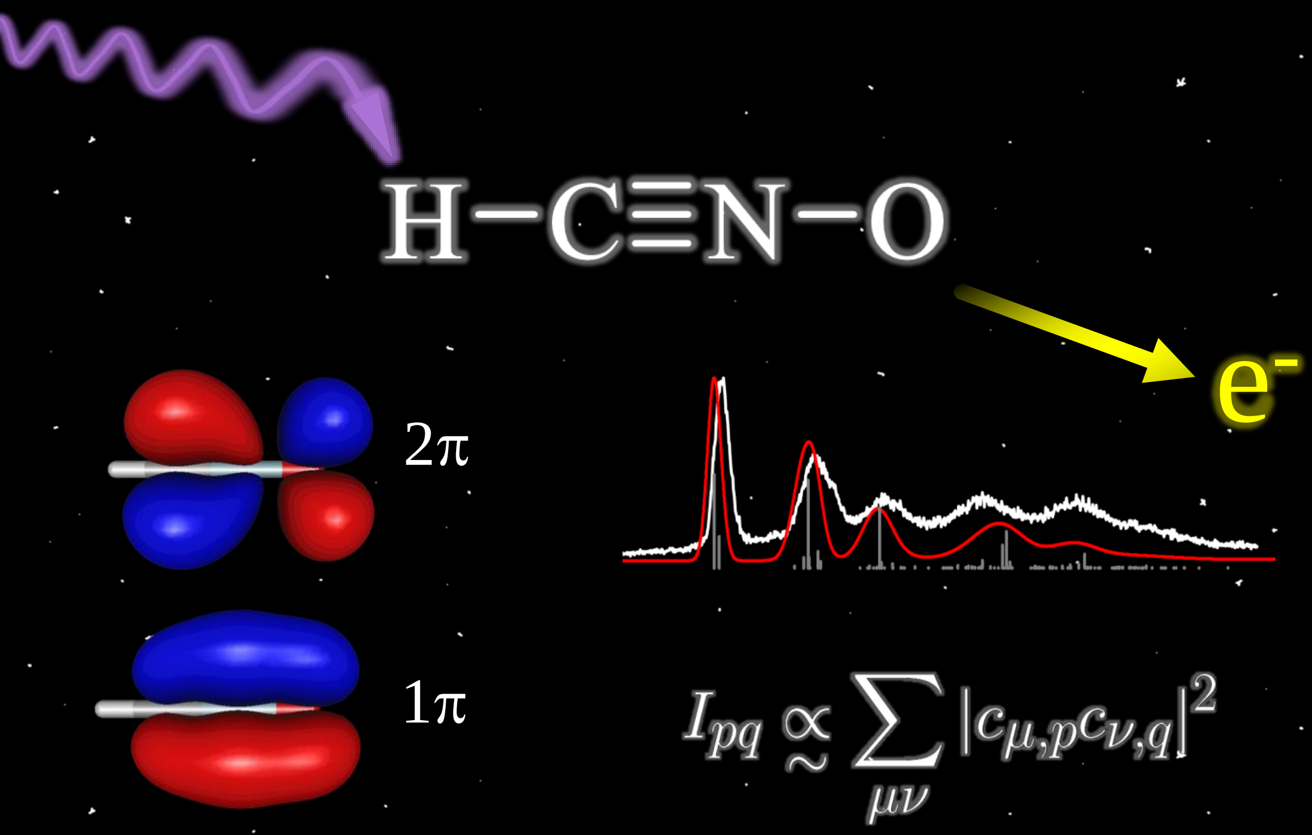

This chapter is reproduced and partly adapted from

Phys. Chem. Chem. Phys., 2022, 24, 15217-15229
Marius Gerlach, Tobias Preitschopf, Emil Karaev,
Heidy M. Quitián-Lara, Dennis Mayer, John Bozek,
Ingo Fischer and Reinhold F. Fink

with permission of the Royal Society of Chemistry.

Abstract

HCNO is a molecule of considerable astrochemical interest as a precursor to prebiotic molecules. It is synthesized by preparative pyrolysis and is unstable at room temperature. Here, we investigate its spectroscopy in the soft X-ray regime at the C 1s, N 1s and O 1s edges. All 1s ionization energies are reported and X-ray absorption spectra reveal the transitions from the 1s to the π^* state. Resonant and normal Auger electron spectra for the decay of the core hole states are recorded in a hemispherical analyzer. An assignment of the experimental spectra is provided with the aid of theoretical counterparts. The latter are using a valence configuration interaction representation of the intermediate and final state energies and wavefunctions, the one-center approximation for transition rates and band shapes according to the moment theory. The computed spectra are in very good agreement with the experimental data and most of the relevant bands are assigned. Additionally, we present a simple approach to estimate relative Auger transition rates on the basis of a minimal basis representation of the molecular orbitals. We demonstrate that this provides a qualitatively good and reliable estimate for several signals in the normal and resonant Auger electron spectra which have significantly different intensities in the decay of the three core holes.

4.1 Introduction

Fulminic acid, HCNO, has an illustrious history.[1,2] It was first prepared by Edward Howard in 1800 by combining ethanol, nitric oxide and mercury oxide. A white crystalline substance formed, which upon addition of sulfuric acid detonated. Howard called the compound "a new fulminating mercury" and described the compound to have a "saline taste".[3] Today we know that the substance Howard discovered was the highly explosive mercury fulminate $Hg(CNO)_2$. In 1899, Ley and Kissel first proposed the structures CNO^- and HCNO for the fulminate salt and fulminic acid.[4] This was supported by the observations of the 1,3-dipolar addition of fulminic acid to unsaturated systems by Huisgen in 1961.[5] The first spectroscopic evidence was presented in the form of a gas phase IR spectrum of isolated fulminic acid.[6] Fulminic acid has now been investigated with numerous spectroscopic methods, such as IR-spectroscopy[6–10], rotational spectroscopy[10,11] and photoelectron spectroscopy.[12,13] Additionally, Feng *et al.* studied the reaction kinetics with OH[14] and the photodissociation of HCNO at 248 nm and 193 nm.[15,16] In contrast, no studies in the X-ray regime have been reported yet. Because HCNO consists of only 4 atoms and 22 electrons it has also been attractive for theoretical chemists early on. This is best evidenced by Paulings calculation of the free energy of the [H, N, C, O] system already in 1926.[17] He concluded that the correct structure should be HCNO and not HONC as previously thought.[18] Since then numerous high level theoretical studies have been published.[19–22]

Fulminic acid also has significant astrochemical relevance as a precursor to prebiotic molecules. The first astrophysical identification of HCNO was made through observations using the 3 mm band of the IRAM 30m radio telescope. It was observed towards the dark molecular clouds B1, L1544, and L183, and in the low-mass pre-stellar object L1527.[23] Isocyanic acid, HNCO, was also detected and the abundance ratio HNCO/HCNO was determined to be between 40 and 70.[23] Currently, HCNO has been identified in numerous sources that illustrate the different chemical stages of a solar-type star, such as L1157-mm, L1157-B1, NGC 1333 IRAS4A, as well as the dense core L483.[24–26] In cold clouds and low-mass star formation objects, the most accepted gas-phase formation pathway for HCNO is the neutral-neutral reaction involving methylene (CH_2) and nitric oxide (NO).[23] However, given the different temperature gradients and regimes present in these objects, other HCNO formation processes should also be considered, including chemical reactions on the surface of grains.[27] HCNO and its isomers isocyanic acid (HNCO), cyanic acid (HOCN), and isofulminic acid (HONC) form a tetrad of species collectively known as CHON.[28] In planetary atmospheres, these molecules are expected to be formed by UV interaction with molecules such as CH_4, CO, and N_2. Indeed, CHON isomers are of great prebiotic importance as they participate in reaction chains that lead to complex organic molecules of astrochemical and astrobiological interests.[29]

Our group already investigated the Auger electron spectroscopy (based on the Auger-Meitner effect[30]) of the isomer isocyanic acid, HNCO, and compared the spectra with computations to rationalise the observed transitions.[31] Furthermore, the photofragmentation of HNCO upon soft X-ray excitation was studied.[32,33] By investigating the Auger electron spectroscopy of its isomer fulminic acid, we intend to better understand the effects of atom connectivity on the Auger-Meitner effect in molecules. Note that only a few reactive molecules have been investigated in the soft X-ray regime. For example, Auger spectra have been reported for HS[34], while X-ray absorption spectra (XAS) were recorded for allyl, C_3H_5[35] and methyl, CH_3.[36]

4.2 Methods

4.2.1 Experimental

The experiments were conducted at the soft X-ray beamline PLEIADES[37] of Synchrotron SOLEIL. Fulminic acid was prepared according to the procedure by Wentrup *et al.*[38] The precursor 3-phenyl-4-oximino-isoxazol-5(4H)-one was heated to around 100°C and sublimated under high vacuum, provided by a turbopump. The gaseous precursor entered a 40 cm long quartz glass tube with an inner diameter of 3 cm. This tube was heated to 460 °C by a Carbolite EVA12/300B tube furnace. The resulting products HCNO, CO_2 and benzonitrile were collected in a liquid nitrogen cooled trap. Impurities like CO_2 and minor isocyanic acid contributions were removed by the forepump vacuum at $-50\,^\circ$C (ethanol/dry ice bath) due to their higher vapour pressure. During the experiments the fulminic acid sample was kept at $-40\,^\circ$C and entered the experimental chamber through an effusive inlet. Benzonitrile contamination was unproblematic as its vapor pressure is insignificant at $-40\,^\circ$C. In the experimental chamber the sample crossed the linearly polarized soft X-ray radiation produced by an Apple II HU80 permanent magnet undulator, which was monochromatized using a 600 lines mm^{-1} grating. The light was oriented at the magic angle of 54.7° with respect to the electron analyzer to eliminate angular dependence effects of the electron emission. Auger electrons were measured by a VG Sciencta R4000 hemispherical analyzer using an entrance slit size of 0.3 mm at a pass energy of 50 eV, leading to a spectral resolution of 37.5 meV. X-ray absorption spectra (XAS/NEXAFS) were recorded by scanning the photon energy and recording the total ion yield. It was measured with a channeltron biased with −2 kV on the front of its 25 mm diameter cone. The sample is introduced from an effusive needle and intersects the photon beam about 5 mm in front of the channeltron. The 2 kV field of the channeltron is assumed to collect all ions produced regardless of their kinetic energy. Photon energy and electron kinetic energy were calibrated using the literature spectra of CO_2, N_2[39] and HNCO.[31]

4.2.2 Theoretical Details

Theoretical Auger electron spectra were obtained with the *wavels* program package.[40–45] The approach implemented there has been applied successfully to molecular K-LL,[31,46,47] $L_{2,3}$-$M_{1,2,3}M_{1,2,3}$,[48–50] and $M_{4,5}$-$N_{1,2,3}N_{1,2,3}$[51] Auger electron spectra and we refer to these articles for further details. Briefly, the molecular structure and vibrational frequencies of the molecule were calculated at the B3LYP[52]/def2-TZVPP[53] level with Turbomole[54] providing C–H, C–N, and N–O distances of 106.05 pm, 115.59 pm, and 119.88 pm, respectively, for the linear HCNO molecule. The molecular orbitals (MOs) used to represent the core-hole and final states were Hartree-Fock orbitals as determined with a cc-pVTZ basis set[55] and virtual valence-type orbitals obtained with the procedure described in Ref. [45]. The latter generates orbitals complementing the occupied MOs to the orbital space of the atomic valence orbitals (1s for hydrogen and 1s, 2s, and 2p for C, N, and O). These virtual valence MOs allow to represent static correlation and charge fluctuations within the molecule with the configuration interaction (CI) approach employed in this work. The orbitals are shown in Figure 4.1 and the MO-coefficients providing their optimal representation in terms of the atomic valence orbitals are given in Tab. 4.1. The table shows also the overlap of the molecular orbitals as evaluated in the quantum chemical calculation with those in the minimal basis representation, $\langle\psi_p|\psi_p^{MB}\rangle$, as well as the squared sums of the MO coefficients, $\sum_\mu c_{\mu,p}^2$ [here and in the following p/q count MOs, while μ and ν represent atomic orbitals (AOs)]. As the atomic orbitals are overlapping, an orbital can be characterized as bonding, non-bonding, and antibonding, respectively, if this number is clearly smaller, about equal, or much larger than one.

Accordingly, the 4-6σ and 1π orbitals are bonding, the 7σ and 2π orbitals are non-bonding and the others are antibonding.

Auger transition rates were evaluated with the one-center approximation[44,56–58] which approximates the continuum wavefunctions of the Auger electrons by their atomic counterparts. Furthermore, Auger decay rates are determined by only considering electrons in the minimal basis expansion (here Tab. 4.1) of the atomic valence orbitals of the core-hole atom. This means the required Auger transition integrals are only needed for atomic Auger transitions which are readily available.[59–62] In the present work the values from the compilation of Chelkowska and Larkins[62] were employed. As described there, the Auger transition rate (in atomic units, *a.u.*) for the transition from the initial state i to the final state f is obtained from the Fermi-Wentzel "golden rule"[63] expression

$$I_f = 2\pi|\langle\Psi_i|\hat{H}|\Psi_f\rangle|^2, \tag{4.1}$$

where Ψ_i and Ψ_f are the respective wavefunctions which are assumed to be orthogonal and $\hat{H}$ is the molecular electronic Hamiltonian. In our approach the matrix element in eq. (4.1) is evaluated for the CI wavefunctions described above.

Note that the final states in our calculations are always linear combinations of several configurations. Nevertheless, it is common to designate these states with their leading configuration (i.e. the configuration with the largest weight). For important features in Auger electron spectra such an assignment is generally reasonable as there is only a single leading configuration. This allows to relate intensities to the MO expansion coefficients of the involved valence orbitals at the core hole atom. Thus, we approximate the core hole wavefunctions with the Hartree-Fock Slater determinant, Φ, with a hole in the core-orbital ψ_c and designate it as Φ_c.[56,64,65] The present K-LL-type normal Auger electron spectra are known to be dominated by decay to singlet final states.[64,66] These final state wavefunctions are represented with configurations having two holes in the valence orbitals ψ_p and ψ_q as well as an electron in the outgoing continuum channel ϵ_{lm}. l and m are the angular momentum and magnetic quantum numbers of the channel. We designate the final state configuration as $\Phi_{pq}^{\epsilon_{lm}}$ where the holes shall be coupled to a singlet. Further details and the treatment of other final state configurations

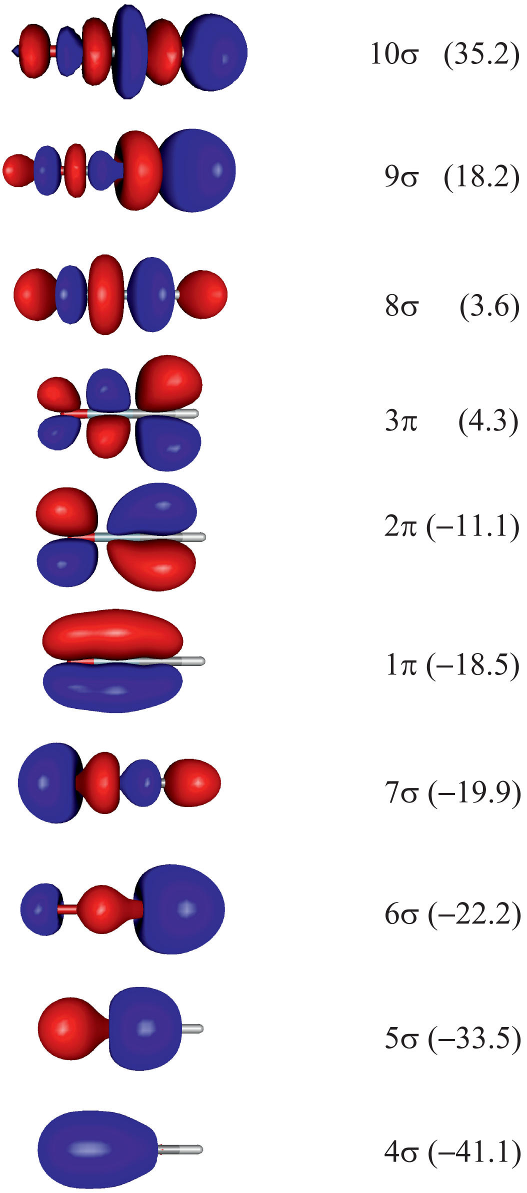

Figure 4.1: Orbitals of the HCNO molecule which were used for calculating the Auger electron spectra. Note that the H-atom points to the right. See text for details for the determination of the orbitals. Orbital energies in eV are given in brackets.

Table 4.1: Minimal basis representation of the valence molecular orbitals (MOs) of the HCNO molecule with the atomic orbitals (AOs). For the degenerate π-orbitals only the component in x-direction is shown. The orbital energies, ϵ, are the expectation values of the molecular orbitals with the ground state Fock operator. The overlap between the molecular orbital and its representation in the indicated minimal basis, $\langle\psi_p|\psi_p^{MB}\rangle$, provides a measure for the error introduced when the molecular orbitals are represented in the minimal basis. Significant coefficients with absolute value above 0.3 are given as bold numbers.

MO (p)	4σ	5σ	6σ	7σ	1π	2π	3π	8σ	9σ	10σ
ϵ (eV)	−41.14	−33.45	−22.24	−19.88	−18.49	−11.06	4.31	3.63	18.19	35.16
$\langle\psi_p\|\psi_p^{MB}\rangle$	0.985	0.986	0.976	0.985	0.993	0.989	0.990	0.980	0.980	0.980
$\sum_\mu c_{\mu,p}^2$	0.60	0.65	0.69	1.12	0.70	1.04	1.73	3.79	4.54	7.18
AO (μ)	$c_{\mu,p}$									
H $1s$	0.01	0.08	**0.32**	−0.10	0.00	0.00	0.00	**−0.43**	**1.23**	**0.97**
C $2s$	0.09	0.25	**0.48**	−0.07	0.00	0.00	0.00	**0.82**	**−1.29**	**0.67**
C $2p_\pi$	0.00	0.00	0.00	0.00	0.26	**−0.58**	**0.86**	0.00	0.00	0.00
C $2p_\sigma$	−0.06	−0.20	**0.47**	−0.29	0.00	0.00	0.00	−0.29	**−0.42**	**−1.67**
N $2s$	**0.46**	**0.40**	−0.18	−0.24	0.00	0.00	0.00	**−1.30**	−0.18	**−1.06**
N $2p_\pi$	0.00	0.00	0.00	0.00	**0.62**	−0.27	**−0.88**	0.00	0.00	0.00
N $2p_\sigma$	−0.12	**0.49**	0.00	**0.45**	0.00	0.00	0.00	0.29	**0.79**	**−1.24**
O $2s$	**0.58**	**−0.37**	0.27	**0.65**	0.00	0.00	0.00	**0.58**	**0.47**	**−0.44**
O $2p_\pi$	0.00	0.00	0.00	0.00	**0.50**	**0.79**	**0.45**	0.00	0.00	0.00
O $2p_\sigma$	0.19	−0.02	−0.17	**−0.58**	0.00	0.00	0.00	**0.84**	**0.51**	−0.29

and of resonant Auger decay has been described in Refs.[44,56,64,65]. For the case discussed above, the Auger transition rate becomes

$$I_{pq} = (1+\delta_{pq})^{-1}\pi \sum_{lm} \left|\langle pq|c\epsilon_{lm}\rangle + \langle qp|c\epsilon_{lm}\rangle\right|^2 , \tag{4.2}$$

where

$$\langle pq|c\epsilon_{lm}\rangle = \left\langle \psi_p(1)\psi_q(2) \left| \frac{1}{r_{12}} \right| \psi_c(1)\psi_{\epsilon_{lm}}(2) \right\rangle \tag{4.3}$$

is a two-electron integral in Dirac notation.

Plugging in the molecular orbitals as linear combination of atomic orbitals (MO-LCAO) representation of the molecular orbitals (MOs) in terms of the minimal basis, $\psi_p = \sum_\mu c_{\mu p}\chi_\mu$ with the MO expansion coefficients, $c_{\mu,p}$, provides

$$I_{pq} = (1+\delta_{pq})^{-1}\pi \sum_{lm} \left| \sum_{\mu\nu} \left(\langle \mu\nu|c\epsilon_{lm}\rangle + \langle \nu\mu|c\epsilon_{lm}\rangle\right) \cdot c_{\mu,p}c_{\nu,q} \right|^2 . \tag{4.4}$$

Due to the atomic symmetry of the wavefunctions, the ϵ_{lm} involve s, p, and d channels for the outgoing electron from the 1s core hole and the 2s or 2p valence holes. For *K*-*LL*-type Auger decay it is known that these Auger transition integrals are rather independent of the atomic orbitals (AOs) χ_μ and χ_ν.[67] Furthermore, most of the channels are decoupled due to symmetry or due to largely different energies of the resulting final states. Thus, the summed two electron integrals in eq. (4.4) are roughly identical for all $\mu - \nu$ combinations and the relative Auger transition rates can be approximated by the squared MO expansion coefficients

$$I_{pq} \underset{\sim}{\propto} \sum_{\mu\nu} |c_{\mu,p}c_{\nu,q}|^2. \tag{4.5}$$

A similar approximation was used before by Tarantelli *et al.*[68] in the context of a two hole localization analysis of the Auger final states. In the following we shall combine this idea with the minimal basis expansion of the MOs (Tab. 4.1) to explain intensity patterns of the molecular Auger electron spectra of the HCNO molecule.

Electronic wavefunctions of the states contributing to the Auger processes were determined with the CI approach. For the core-hole (final) states a CI space consisting of all configurations with up to 3 (2) electrons in the virtual orbitals (3π and 8-10σ) and the corresponding number of electrons in the core- and valence orbitals was used. As demonstrated in previous applications,[31,47,51] such CI wavefunctions generally provide an appropriate representation of the essential electronic states out of the very large (actually infinite) number of possible final states that can be reached in the Auger decay. Similarly, the energetic order of the states is generally reasonable, but absolute energies may deviate from the experimental ones by several eV. We therefore modified the energy scale of the theoretical spectra, as proposed in Ref. [31] A better estimate for the energy differences between the ground state and the lowest final states was obtained with the multi-configuration coupled electron pair approach[43] (MCCEPA) and the cc-pwCVQZ[69] basis using complete active space self-consistent field (CASSCF) reference wavefunctions with all π-orbitals in the active space. For the resonant Auger electron spectra, the obtained vertical single ionization potential of 10.64 eV was set as the lowest (vertical) final state energy. For normal Auger decay we obtained 30.56 eV for the vertical ionization energy of the lowest doubly ionized state, $^1\Sigma^-$ ($2\pi^{-2}$), however, as the decay to this final state is symmetry forbidden, we used the vertical binding energy of the first excited state ($^1\Delta$) at 31.54 eV to calibrate the theoretical normal Auger electron spectra. Furthermore, the range of final states was squeezed by a factor of 0.85 which corrects the tendency of the CI approach to overestimate energies of higher excited states.[31] Note that this computational energy scale is independent from experiment.

The multi-dimensional moment theory[45,70,71] was used to estimate the band shapes related to the final electronic states reached in the Auger electron spectra. In this approximation the signals that are due to the Auger decay into the vibrational levels of a single final electronic state are represented by a Gaussian distribution. The area under the Gaussian is set to the Auger transition rate. In order to approximate the band shape which is due to the first-order vibrational dynamics of the decay process, the width and the center of the Gaussian is adapted as described in Refs.[70,71] Note that only totally symmetric vibrations are considered at this level of theory, i.e. within these simulations the $C_{\infty v}$-symmetric HCNO molecule retains a linear structure.

4.3 Results

4.3.1 Normal Auger Spectroscopy

Figure 4.2 shows the normal Auger electron spectra (AES) at the a) carbon, b) nitrogen and c) oxygen edge recorded at photon energies of 400, 440 and 560 eV. To allow for a comparison of spectra of different core-holes, the Auger electron yield is shown as a function of the binding energy E_b which is defined as the difference between the 1s ionization energy $E(1s)$ and the kinetic energy of the Auger electrons E_{kin}

$$E_B = E(1s) - E_{kin} \tag{4.6}$$

The binding energy can be thought of as the energy of the doubly ionized final state with respect to the neutral ground state after the Auger electron is ejected. The 1s ionization energies were determined by recording the X-ray photoelectron spectra (XPS), which are shown in the appendix, Figure A4.1 - A4.3. The 1s ionization energies at the three edges are 292.9 eV for C 1s and 410.5 and 539.6 eV for N 1s and O 1s, respectively. Figure 4.2 also shows the stick spectra in gray which were obtained by theory and in red the fully simulated spectra.

Following the formalism that Moddeman *et al.*'s applied to the CO_2 Auger spectra,[39] we can divide the Auger electron spectra into two regions. At low binding energies ($<$ 50 eV) only weakly bound outer-valence orbitals are involved (K-WW), while transitions up to 70 eV have vacancies in one weakly bound outer valence orbital and in one strongly bound inner valence orbital (K-SW). Transitions at higher binding energies would be called K-SS, but were not measured in the present work. These transitions are often broad and difficult to characterize due to the mixing of a multitude of electronic configurations. According to the orbital energies in Table 4.1 the HCNO molecule is a bit unusual. The 2π orbital

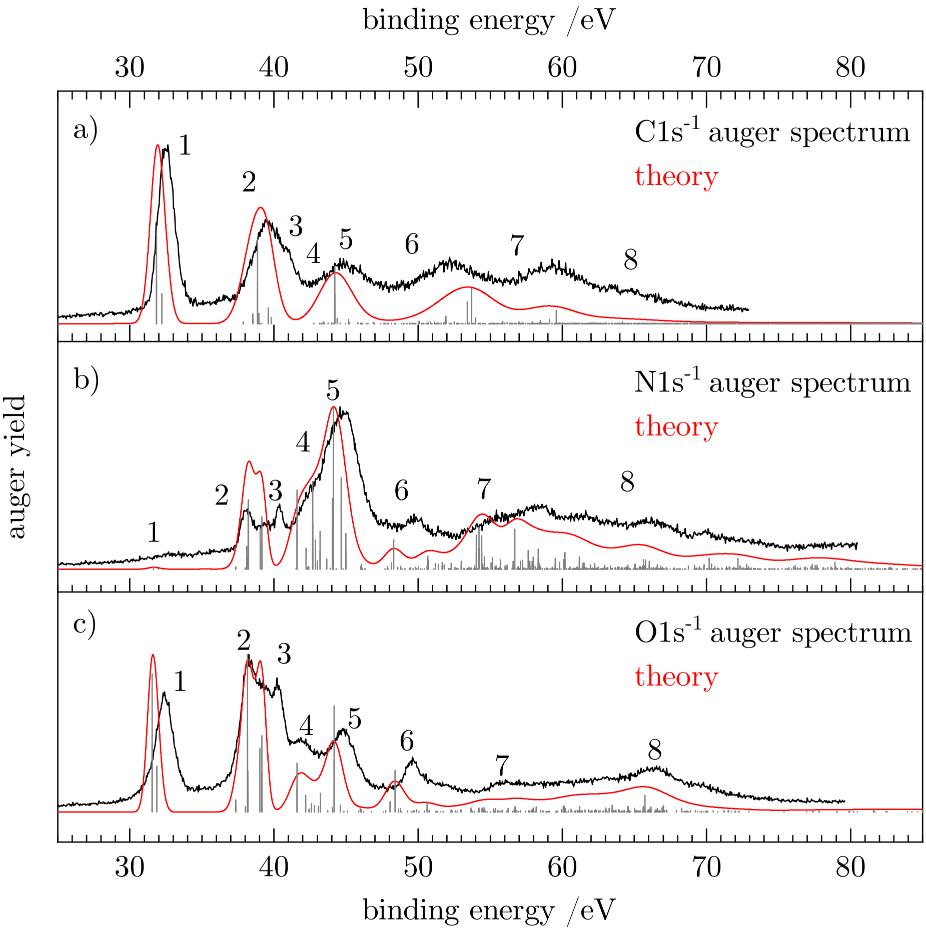

Figure 4.2: Normal Auger electron spectra at the a) carbon, b) nitrogen and c) oxygen edge, shown in black. The kinetic energy of the Auger electrons was converted to binding energy by subtracting it from the 1s ionization energies determined through XPS measurements (see appendix at the end of the chapter). The grey stick spectrum shows the energies and intensities of the individual transitions. The energy positions include shifts due to the moment theory which provides the theoretical spectrum given with the red lines.

($E_b = 11\,\mathrm{eV}$) is well separated from the next group 1π, 7σ and 6σ ($E_b \approx 20\,\mathrm{eV}$). The two lowest orbitals have much higher binding energies of about 40 eV. Additionally, only two molecular orbitals have significant contributions of the carbon AOs. These are the nonbonding 2π MO and the 6σ orbital which represents essentially the C–H bond. Thus, the electronic structure of HCNO is a bit special and at least for the case of the C1s spectra the general arguments of Moddemann *et al.*[39] may only apply to a limited extent here.

The assignment of the experimental features, the calculated partial intensities, the vertical ionization potentials as well as the signal widths and positions according to the moment method are collected in Tab. 4.2 and Tab. 4.3. The signals in the AES can be assigned as follows. The Auger decay from the ${}^2\Sigma^+$ core hole states to the ${}^3\Sigma^-$ ground state of the dication is symmetry forbidden, as coupling of any single electron Auger channel to the Σ^- final state cannot provide the Σ^+ symmetry representation of the core-hole states. Thus, the signal with the lowest binding energy is due to the ${}^1\Delta$ and ${}^1\Sigma^+$ states with ($2\pi^{-2}$) occupation appearing at about 32 eV binding energy. In all spectra the energy difference of these final states amounts to 0.3–0.4 eV, which is within the observed bandwidth. Thus, this feature (as also the other ones in the AES), contains several final states which are not resolved. Note that the assignments presented in the following provide only the dominant character of the electronic states that give rise to the observed signals. The features at lowest binding energy are labelled with 1 in Figure 4.2 and give rise to the prominent signals for C and O1s decay spectra. The intensity of these transitions can be explained with the large absolute value of the MO coefficients of the $2p_\pi$-AOs at these atoms. For the nitrogen atom this value ($c_{N2p_\pi,2\pi} = -0.27$) is more than a factor of two smaller than for C (-0.58) and O (0.79). As this decay generates both holes in $2p_\pi$ AOs, according to eq. (4.5) the relative decay rate is proportional to the fourth power of these coefficients which means that the decay ratios to feature 1 starting from the C1s:N1s:O1s core-hole states should be about 20:1:73. This corresponds well to the experimental spectra where feature 1 is dominant in the C1s and O1s spectra, while it is hardly visible in the N1s AES.

At binding energies between 38 and 40 eV (feature 2) several ${}^1\Pi$ states with the occupations ($7\sigma^{-1}2\pi^{-1}$) and ($6\sigma^{-1}2\pi^{-1}$) as well as ${}^1\Delta$ and ${}^1\Sigma^+$ ($1\pi^{-1}2\pi^{-1}$)

Table 4.2: Assignment of the most intense features in the normal Auger electron spectra (AES) of the C, N, and O $1s$ core-hole states of fulminic acid. Vertical double ionization energies E_{vert}, the centers of the Gaussians, E, and their full widths at half maximum, W, as evaluated with the moment theory are given in eV. Intensities, I, are (partial) lifetime energy widths in meV, i.e. the total intensity represents the Auger contribution to the full width at half maximum of the photoelectron spectrum (or Auger spectrum, respectively). Labels (lab.) refer to Figure 4.2.

			C1s^{-1} decay				N1s^{-1} decay				O1s^{-1} decay			
term	occupation	E_{vert}	I	W	E	lab.	I	W	E	lab.	I	W	E	lab.
$^3\Sigma^-$	$(2\pi^{-2})$	30.84	0.0	1.04	31.13		0.0	0.84	30.93		0.0	0.74	30.83	
$^1\Delta$	$(2\pi^{-2})$	31.54	14.3	1.13	31.85	1	0.1	0.93	31.64	1	22.3	0.82	31.54	1
$^1\Sigma^+$	$(2\pi^{-2})$	31.89	4.8	1.17	32.22	1	0.0	0.95	31.99	1	7.4	0.84	31.88	1
$^3\Pi$	$(7\sigma^{-1}2\pi^{-1})$	37.43	0.3	1.33	37.85		0.1	0.74	37.34		2.0	0.74	37.34	2
$^3\Pi$	$(6\sigma^{-1}2\pi^{-1})$	38.19	1.6	1.87	38.54	2	0.1	1.55	37.99		0.9	1.56	38.03	2
$^1\Delta$	$(1\pi^{-1}2\pi^{-1})$	38.21	3.2	1.89	38.93	2	8.2	0.96	38.20	2	25.4	0.88	38.16	2
$^1\Pi$	$(7\sigma^{-1}2\pi^{-1})$	38.36	13.5	2.03	38.86	2	1.4	1.56	38.12	2	6.6	1.58	38.18	2
$^1\Sigma^+$	$(1\pi^{-1}2\pi^{-1})$	39.07	1.0	1.91	39.80	2	2.5	0.94	39.05	2	10.3	0.87	39.02	2
$^1\Pi$	$(6\sigma^{-1}2\pi^{-1})$	39.24	2.5	1.24	39.61	3	3.1	0.75	39.17	3	12.3	0.75	39.17	3
$^1\Delta$	$(2\pi^{-3}3\pi^{1})$	41.69	0.1	2.79	42.75		4.8	1.43	41.59	4	7.9	1.39	41.59	4
$^1\Sigma^+$	$(2\pi^{-3}3\pi^{1})$	42.28	0.1	2.74	43.33		1.3	1.45	42.23	4	2.7	1.40	42.20	4
$^1\Delta$	$(1\pi^{-1}2\pi^{-2}3\pi^{1})$	42.66	0.1	2.91	43.75		5.3	1.74	42.68	4	1.4	1.66	42.59	4
$^1\Sigma^+$	$(1\pi^{-1}2\pi^{-2}3\pi^{1})$	42.87	0.0	2.94	43.98		1.8	1.72	42.87	4	1.1	1.64	42.80	
$^1\Pi$	$(6\sigma^{-1}1\pi^{-1})$	43.46	9.2	2.57	44.23	5	2.3	1.89	43.20	4	3.0	1.88	43.23	5
$^1\Delta$	$(1\pi^{-2})$	44.12	0.2	2.86	45.20		9.7	1.68	44.12	5	0.7	1.59	44.05	
$^1\Pi$	$(7\sigma^{-1}1\pi^{-1})$	44.30	0.6	2.55	45.18		4.2	1.35	44.06	5	17.1	1.36	44.18	5
$^1\Sigma^+$	$(1\pi^{-2})$	44.71	0.2	2.87	45.81		5.5	1.57	44.66	5	1.1	1.51	44.62	5
$^1\Delta$	$(1\pi^{-1}2\pi^{-2}3\pi^{1})$	44.91	0.1	2.98	46.01		2.1	1.92	44.97	5	0.1	1.82	44.85	

Table 4.3: Continuation of Tab. 4.2. The total intensity at the bottom correponds to the sum of both tables.

			$C1s^{-1}$ decay				$N1s^{-1}$ decay				$O1s^{-1}$ decay			
term	occupation	E_{vert}	I	W	E	lab.	I	W	E	lab.	I	W	E	lab.
$^1\Sigma^+$	$(1\pi^{-1}2\pi^{-2}3\pi^1)$	48.11	0.0	3.00	49.24		0.4	1.81	48.13		1.7	1.73	48.04	6
$^1\Sigma^+$	$(7\sigma^{-2})$	48.51	0.0	2.78	49.50		1.8	1.44	48.31	6	6.7	1.43	48.39	6
$^1\Pi$	$(5\sigma^{-1}2\pi^{-1})$	50.81	1.2	2.99	51.93	6	0.2	1.69	50.62		1.6	1.67	50.63	6
$^1\Sigma^+$	$(6\sigma^{-2})$	52.29	3.5	3.91	53.41	6	0.3	3.14	51.82		0.0	3.13	51.91	
$^1\Sigma^+$	$(6\sigma^{-2})$	52.63	5.6	3.72	53.72	6	0.0	2.93	52.18		0.0	2.92	52.27	
$^1\Pi$	$(7\sigma^{-1}1\pi^{-1}2\pi^{-1}3\pi^1)$	54.43	0.0	3.38	55.69		2.5	2.05	54.21	7	0.6	2.03	54.22	7
$^1\Pi$	$(6\sigma^{-1}7\sigma^{-1}2\pi^{-1}8\sigma^1)$	54.54	0.0	3.85	55.77		2.0	2.82	54.04	7	0.4	2.82	54.18	7
$^1\Pi$	$(6\sigma^{-1}1\pi^{-1}2\pi^{-1}3\pi^1)$	54.67	0.1	3.57	55.98		2.0	2.23	54.41	7	0.7	2.21	54.43	7
$^1\Sigma^+$	$(5\sigma^{-1}7\sigma^{-1})$	56.91	0.3	2.73	57.91		2.4	1.62	56.71	7	0.9	1.61	56.72	7
$^1\Sigma^+$	$(6\sigma^{-1}7\sigma^{-1}1\pi^{-1}3\pi^1)$	57.89	0.7	3.38	59.12		1.1	2.10	57.63		0.2	2.09	57.65	7
$^1\Pi$	$(2\pi^{-4}3\pi^1 9\sigma^1)$	58.40	0.1	4.35	60.01		1.2	2.87	58.32		0.8	2.81	58.20	7
$^1\Sigma^+$	$(5\sigma^{-1}6\sigma^{-1})$	58.48	2.1	3.34	59.58	7	0.2	2.35	58.13		0.0	2.35	58.19	
$^1\Pi$	$(1\pi^{-1}2\pi^{-3}3\pi^1 9\sigma^1)$	60.43	0.1	4.72	62.20		1.0	3.01	60.16	7	1.0	2.99	60.14	
$^1\Sigma^+$	$(4\sigma^{-1}7\sigma^{-1})$	66.04	0.0	4.85	67.87		0.5	2.84	65.64	8	2.7	2.83	65.74	8
total intensity			80.6				119.2				206.3			

states are reached. While as usual for *K-LL* Auger spectra[56,68] most intensity is due to these singlet final states, in the C and O 1s spectra decay to two $^3\Pi$ final states has notable intensity in these region. This can be explained with the relatively large 2s and 2p MO coefficients in the 6σ and 7σ orbitals at these atoms. In the minimal-basis one-center approach used here, normal *K-LL* Auger decay leading to a triplet final state requires that the projection of the double hole state in the molecular orbital representation gives rise to a significant fraction of $2p$-$2s$ hole pairs. A decay to a triplet state with two holes in 2p orbitals is symmetry forbidden and as the 2s orbital is non-degenerate, it is not possible to generate a triplet state with two holes in this orbital. However, the triplet states never contribute more than about 10 % to the intensity of any feature in the AES of the core holes.

We assign feature 3 to the $^1\Pi$ $(6\sigma^{-1}2\pi^{-1})$ state, noting that the energy of this final state seems to be underestimated by about 1 eV with our theoretical approach. The feature may be also assigned to the $^1\Sigma^+$ $(1\pi^{-1}2\pi^{-1})$ state, but the energetic order and the intensities of these states in our calculations as well as the similarity of this $^1\Sigma^+$ state with the $^1\Delta$ state with the same occupation support the former assignment. There is clear agreement between the experimental and theoretical spectra for N and O1s decay. Both show feature 3 as a distinct peak in the spectrum at about 40 eV binding energy. In the C1s spectrum this feature is weaker and only notable as a shoulder in the experimental spectrum.

At higher binding energies the N and O1s hole states decay mostly into similar final states. The C1s hole state leads to different final states as large absolute values of the MO coefficients of the carbon atom are only found at the 2π and 7σ orbitals. Accordingly, final states with at least one hole in these orbitals give rise to strong signals. The clearly notable features 5, 6, and 7 in the C1s^{-1} decay correspond mostly to $^1\Pi$ $(6\sigma^{-1}1\pi^{-1})$, $^1\Sigma^+$ $(6\sigma^{-2})$, and $^1\Sigma^+$ $(5\sigma^{-1}6\sigma^{-1})$ final states. In the N and O1s decay these final states do not play a significant role. For example, feature 4 which is absent in the C1s Auger spectrum but visible as a shoulder on the N1s decay and as a small but distinct peak in the O1s spectrum is preferentially due to the decay into $^1\Delta$ final states at about 41-43 eV binding energy. For O1s decay feature 5 is due to the $^1\Pi$ $(7\sigma^{-1}1\pi^{-1})$ final state while for N1s decay this additional intensity is mostly decay to $(1\pi^{-2})$ states. Feature

6 corresponds to the $^1\Sigma^+$ ($7\sigma^{-2}$) state and feature 7 to several $^1\Pi$ states as well as the $^1\Sigma^+$ ($5\sigma^{-1}6\sigma^{-1}$) state. Finally, the nitrogen and oxygen Auger electron spectra show both a broad signal at 65 eV (feature 8) which can be assigned to the $^1\Sigma^+$ ($4\sigma^{-1}7\sigma^{-1}$) state.

A comparison of the intense features in the spectra shows that final state configurations with large absolute values of the MO coefficients at the respective core hole atom correspond to intense features in the Auger spectrum. This is particularly notable for the ($2\pi^{-2}$), ($1\pi^{-1}2\pi^{-1}$), and ($1\pi^{-2}$) configurations giving rise to features 1, 2, and 5. Their intensity decreases in that order for C1s decay as the carbon AO coefficient of the 2π orbital (-0.58) is larger than that one of the 1π orbital (0.26). The ratio of the $2\pi/1\pi$ MO coefficients at the oxygen is 1.6 which is smaller than the corresponding value for the carbon atom (2.3). This explains the relatively small intensity of feature 5 in the O1s AES where feature 2 is about equally intense as 1. The latter is due to admixture of other states in feature 2 and due to configuration mixing. For the nitrogen atom the absolute value of the $2\pi/1\pi$ ratio is 0.4. Correspondingly, in the N1s Auger spectra the intensity of features 1, 2, and 5 increases in that order.

4.3.2 NEXAFS

NEXAFS (near-edge x-ray absorption fine structure) spectra were recorded by scanning the photon energy and monitoring the total ion yield. The spectrum contains electronic transitions from the 1s orbitals to unoccupied orbitals. Figure 4.3(a-c) show the NEXAFS at the carbon, nitrogen and oxygen edge, respectively. The carbon NEXAFS [Figure 4.3a)] exhibits one intense band at 286.6 eV. It corresponds to the $\pi^* \leftarrow 1s$ transition into the 3π LUMO (lowest unoccupied molecular orbital). Furthermore, a progression is visible with three members at 290.26, 290.46 and 290.62 eV. The average spacing corresponds to 0.18 eV or about 1400 cm^{-1}, which is on the order of a vibrational transition. Additional weak bands appear at 288.8 and 291.6 eV. These weaker transitions correspond most likely to transitions into Rydberg states. At the N-edge [Fig 4.3b)] the intense $3\pi \leftarrow 1s$ transition is observed at 403.6 eV. A band with a clearly discernible vibrational progression appears around 400.83 eV and is assigned to a small N_2 contamination (grey star).[72] Several weak bands are also observed at 399.8, 407.1

and 408.6 eV . A similar picture is encountered at the O 1s edge, with an intense band observed at 534.0, and two weaker ones at 535.62 and 537.06 eV. Another small feature at 530.8 eV originates from O_2 (grey star).[73]

The transitions visible in the NEXAFS spectrum were employed to record resonant Auger spectra (RAES). The energies at which resonant Auger spectra were recorded are marked with red crosses in Figure 4.3. At the carbon edge, the crosses

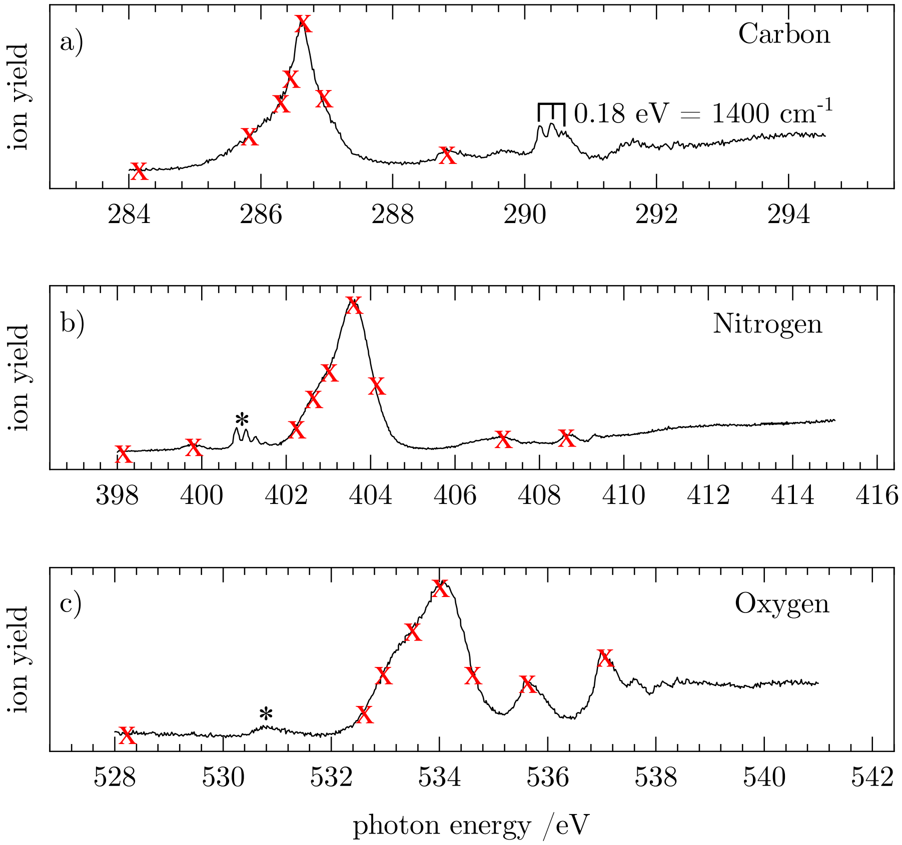

Figure 4.3: NEXAFS spectra at the a) carbon, b) nitrogen and c) oxygen edge. The red crosses indicate at which photon energies resonant Auger electron spectra were recorded. At 290.26 eV, 290.46 eV and 290.62 eV three crosses were omitted for clarity. The grey asterisks indicate contaminations of N_2 and O_2, respectively.

at 290.26 eV, 290.46 eV and 290.62 eV were omitted to avoid congestion in the figure. Off-resonance spectra were recorded at energies below the first resonance. They correspond to direct photoelectron spectra.

4.3.3 Resonant Auger

After exciting a 1s electron into an unoccupied orbital, the molecule can electronically relax via a resonant Auger-Meitner process. Like in the non-resonant case, a valence electron fills the hole in the 1s orbital and the excess energy is removed by ejecting another valence electron. Here, two processes can be distinguished. When the initially excited electron participates in the decay, a participator Auger decay results and the final states are similar to those obtained by valence photoelectron spectroscopy. In contrast, when the initially excited electron is not involved, the decay is referred to as a spectator process. The final states of these processes resemble those in the normal Auger spectra, see below.

Experimental Results

Figure 4.4 shows the resonant Auger electron spectra (RAES) which were obtained by exciting the intense $3\pi \leftarrow 1s$ transition. Traces a), c) and e) represent the off resonant spectra, while traces b), d) and f) show the spectra on the band maximum. Binding energies were calculated from the difference of the photon energy and the Auger electron kinetic energy. RAES recorded on the low- and high-energy side of the 3π state have a similar appearance and are shown in the appendix. Only at the N 1s edge subtle differences are seen. The additional band at around 8 eV in trace a) is due to ionization by the second harmonic.

In the spectrum recorded at the carbon edge (Figure 4.4b)) three intense bands at 10.85, 16.85 and 17.85 eV are observed as well as two broader ones at 20.7 and 24.9 eV. Comparison to the off resonant spectrum 4.4a) shows resonance enhancement in particular for the transitions at 16.9, 20.7 and 24.9 eV. The red line depicts the simulation which is in good agreement with the experimental spectrum.

The RAES recorded on the most intense peak in the N-NEXAFS is shown in Figure 4.4 d). In addition, the off-resonant measurement at 398.1 eV is included

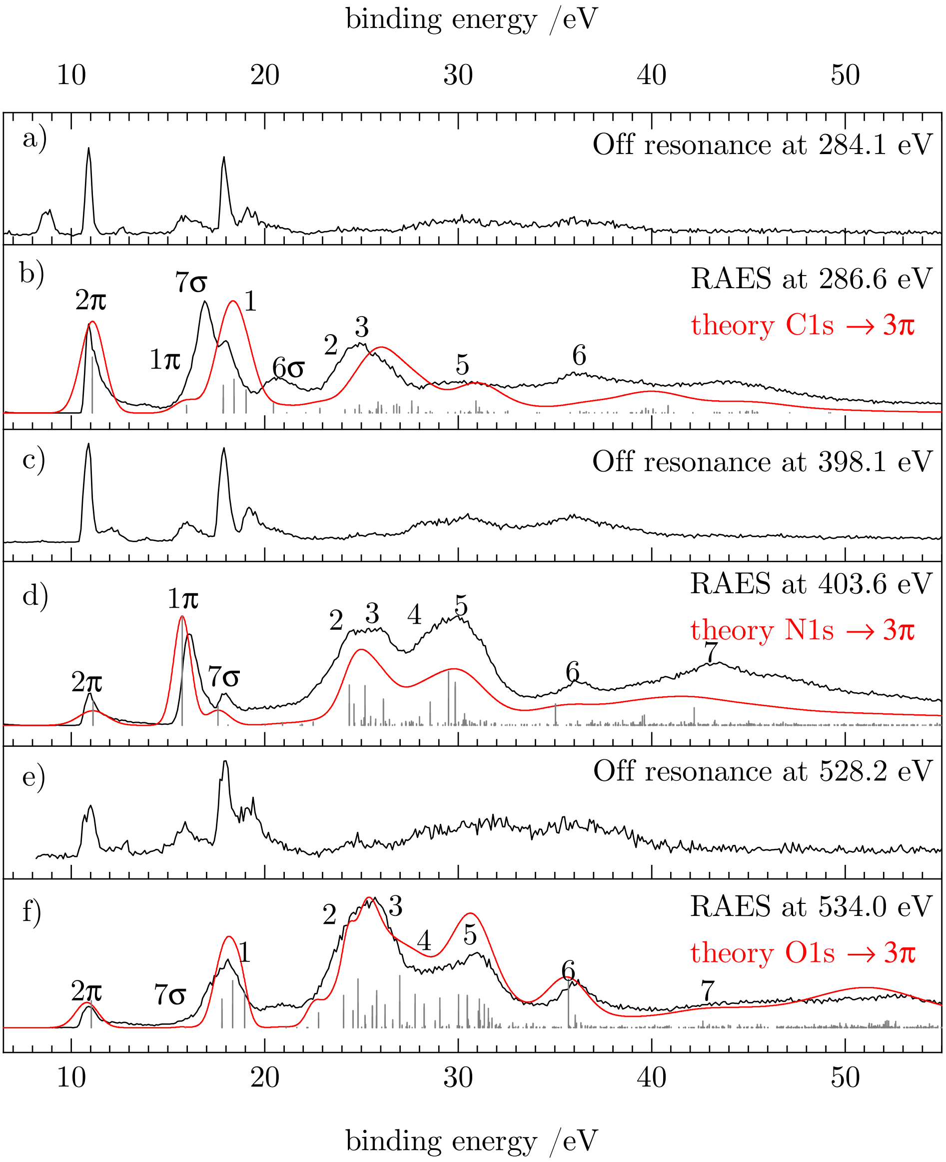

Figure 4.4: Resonant Auger electron spectra at the b) carbon d) nitrogen and f) oxygen edge, as well as the corresponding off resonant measurements at each edge (a), c) and e). The computed spectra are shown in red and the contributions of individual final states are represented as grey sticks.

in trace c). By resonantly exciting HCNO, the peak at 16.1 eV and the two broad bands at 25 and 29.1 eV are enhanced, similar to what was observed at the C-edge. By scanning the excitation energy along the absorption band, the 7σ band (see below for assignment) decreases in relative intensity, see appendix. On the Figure 4.4 traces e) and f) finally show the off-resonance spectrum and the RAES when scanning over the most intense band in the O-NEXAFS. Comparison shows that the peaks at binding energies at 17, 24 and 30 eV are enhanced. RAES recorded at the other positions indicated in Figure 4.3 are given in the appendix, Figure A4.7 - A4.9.

4.3.4 Assignment

In order to assign the observed spectral features, we compare the experimental and theoretical RAES in Figure 4.4 b), d) and f) with the off-resonance photoelectron spectra show in Figure 4.4 a), c) and e) and the most intense features in the theoretical spectra collected in Tab. 4.4 and Tab. 4.5. As expected the RAES show spectator transitions at ≈15 eV lower binding energy than corresponding signals in the AES (Figure 4.2). Participator transitions are seen as additional features at the energies of the signals in the photoelectron spectra, however, with different intensities. We note that the differentiation between participator and spectator states is not strict as the final states are actually mixtures of participator and spectator configurations.[74] However, for qualitative considerations it is generally a good approximation to assume that states are dominated by a single configuration which can then also be used to designate the respective state (see above).

The assignment of the participator states is easily possible with the off-resonant spectra presented in traces a), c) and e) of Figugres 4.4), and the orbitals shown in Figure 4.1 and Tab. 4.1. In the following these states will be designated as 2π, 1π, 7σ, and 6σ for the $\tilde{X}\ {}^2\Pi$ ($2\pi^{-1}$), $\tilde{A}\ {}^2\Pi$ ($1\pi^{-1}$), $\tilde{B}\ {}^2\Sigma^+$ ($7\sigma^{-1}$), and $\tilde{C}\ {}^2\Sigma^+$ ($6\sigma^{-1}$) states, respectively. In the off-resonant spectra sharp signals are observed for the participator states which differ from the ground state configuration by the essentially nonbonding 2π and 7σ orbitals. On the other hand, the 1π and 6σ signals are broadened due to the vibrational excitations associated with the

Table 4.4: Assignment of the most intense features in the resonant Auger electron spectra (RAES) of the C, N, and O $1s$-3π excited states of fulminic acid. Vertical double ionization energies E_{vert}, the centers and widths of the Gaussians according to the moment theory, E and W (eV) are given in eV. Intensities, I, are (partial) lifetime energy widths in meV, i.e. the total intensity represents the Auger contribution to the full width at half maximum of the photoelectron spectrum (or Auger spectrum, respectively). Labels (lab.) refer to Figure 4.4.

			$\mathrm{C1s}^{-1}$ decay				$\mathrm{N1s}^{-1}$ decay				$\mathrm{O1s}^{-1}$ decay			
term	occupation	E_{vert}	I	W	E	lab.	I	W	E	lab.	I	W	E	lab.
$^2\Pi$	$(2\pi^{-1})$	10.64	15.1	1.04	11.10	2π	3.3	1.43	11.13	2π	4.3	1.33	11.05	2π
$^2\Pi$	$(1\pi^{-1})$	15.82	2.1	1.04	15.97	1π	14.6	0.29	15.74	1π	0.1	0.55	15.92	1π
$^2\Sigma^+$	$(7\sigma^{-1})$	17.31	0.9	1.34	17.84	7σ	2.6	0.92	17.60	7σ	0.9	1.48	17.79	7σ
$^2\Pi$	$(2\pi^{-2}3\pi^1)$	17.91	7.5	1.08	17.86	1	0.0	1.28	18.11		3.7	0.85	17.79	1
$^2\Phi$	$(2\pi^{-2}3\pi^1)$	18.48	9.1	1.10	18.42	1	0.0	1.30	18.68	1	7.5	0.88	18.35	1
$^2\Pi$	$(2\pi^{-2}3\pi^1)$	19.12	6.3	1.09	19.04	1	0.0	1.22	19.27	1	5.5	0.84	18.97	1
$^2\Sigma^+$	$(\mathbf{6}\sigma^{-1})$	19.23	2.8	3.01	20.46	6σ	0.0	2.63	20.02	6σ	0.0	2.50	19.88	6σ
$^2\Pi$	$(2\pi^{-2}3\pi^1)$	22.89	1.3	1.39	22.85	2	0.5	1.16	22.51	2	2.4	0.90	22.79	2
$^2\Pi$	$(1\pi^{-1}2\pi^{-1}3\pi^1)$	24.60	0.9	1.68	24.15	2	5.4	1.62	24.38	2	5.1	1.69	24.08	2
$^2\Sigma^+$	$(7\sigma^{-1}2\pi^{-1}3\pi^1)$	24.69	1.0	1.15	24.67	2	2.8	0.78	24.61	2	2.7	0.58	24.56	2
$^2\Phi$	$(1\pi^{-1}2\pi^{-1}3\pi^1)$	25.37	2.2	1.76	24.90	2	5.3	1.70	25.18		7.7	1.80	24.83	2
$^2\Delta$	$(7\sigma^{-1}2\pi^{-1}3\pi^1)$	25.58	3.0	1.74	25.87	3	1.2	0.98	25.48		3.4	0.94	25.57	3
$^2\Sigma^-$	$(7\sigma^{-1}2\pi^{-1}3\pi^1)$	25.80	2.1	1.60	26.04	3	0.8	0.89	25.74		1.9	0.82	25.78	3
$^2\Sigma^+$	$(6\sigma^{-1}2\pi^{-1}3\pi^1)$	25.91	2.0	3.10	26.67	3	0.3	2.00	25.73		0.1	2.05	26.05	
$^2\Pi$	$(1\pi^{-1}2\pi^{-1}3\pi^1)$	26.35	1.6	1.81	25.87	3	3.5	1.74	26.13	3	5.9	1.86	25.79	3
$^2\Delta$	$(6\sigma^{-1}2\pi^{-1}3\pi^1)$	26.49	1.7	1.99	26.96	3	0.8	1.04	26.45		1.3	1.15	26.62	3
$^2\Sigma^+$	$(1\pi^{-1}2\pi^{-1}8\sigma^1)$	26.49	2.4	2.87	26.83	3	0.2	2.34	26.00		0.1	2.13	26.27	
$^2\Pi$	$(2\pi^{-3}3\pi^2)$	26.86	0.0	1.92	26.29		0.2	2.05	26.29		3.7	2.03	26.23	3

Table 4.5: Continuation of Tab. 4.2. The total intensity at the bottom corresponds to the sum of both tables.

			C1s^{-1} decay				N1s^{-1} decay				O1s^{-1} decay			
term	occupation	E_{vert}	I	W	E	lab.	I	W	E	lab.	I	W	E	lab.
$^2\Delta$	$(6\sigma^{-1}2\pi^{-1}3\pi^1)$	26.99	3.3	2.40	27.60	3	0.3	1.46	27.09		0.4	1.47	27.10	
$^2\Sigma^-$	$(6\sigma^{-1}2\pi^{-1}3\pi^1)$	27.37	1.8	2.37	27.94	3	0.3	1.38	27.32		0.3	1.44	27.48	
$^2\Phi$	$(2\pi^{-3}3\pi^2)$	27.63	0.0	1.92	27.05		0.1	2.03	27.09		8.3	2.04	26.99	3
$^2\Pi$	$(2\pi^{-3}3\pi^2)$	28.42	0.1	1.95	27.86		0.2	2.08	27.85		5.3	2.05	27.78	4
$^2\Pi$	$(1\pi^{-1}2\pi^{-1}3\pi^1)$	28.59	0.1	2.30	28.36		0.4	2.77	27.68		3.7	2.07	28.25	4
$^2\Pi$	$(1\pi^{-2}3\pi^1)$	29.61	0.0	2.38	29.08		3.1	3.14	28.55	4	4.7	2.40	29.06	4
$^2\Phi$	$(1\pi^{-2}3\pi^1)$	30.34	0.1	2.73	30.39		7.2	2.84	29.51	4	5.3	2.28	30.02	4
$^2\Delta$	$(6\sigma^{-1}1\pi^{-1}3\pi^1)$	30.70	3.3	2.36	30.92	5	0.5	1.89	30.26		1.4	1.68	30.51	4
$^2\Sigma^-$	$(6\sigma^{-1}1\pi^{-1}3\pi^1)$	30.75	1.5	2.76	31.10	5	0.2	2.22	30.26		0.3	1.99	30.59	
$^2\Pi$	$(1\pi^{-2}3\pi^1)$	31.05	0.1	2.64	30.52		5.8	3.55	29.85	5	5.1	2.69	30.47	4
$^2\Sigma^+$	$(6\sigma^{-1}1\pi^{-1}3\pi^1)$	31.18	0.5	2.45	31.51		0.4	1.95	30.71		1.2	1.70	31.14	
$^2\Delta$	$(7\sigma^{-1}1\pi^{-1}3\pi^1)$	31.47	0.2	2.62	31.24		0.7	3.25	30.41		4.6	2.42	31.10	5
$^2\Sigma^+$	$(7\sigma^{-1}2\pi^{-2}3\pi^2)$	31.56	0.3	2.06	31.18		0.2	2.37	30.79		2.7	1.98	31.05	5
$^2\Sigma^-$	$(7\sigma^{-1}1\pi^{-1}3\pi^1)$	31.74	0.1	2.87	31.56		0.6	3.56	30.60		3.7	2.65	31.36	5
$^2\Delta$	$(6\sigma^{-1}1\pi^{-1}3\pi^1)$	31.94	0.2	2.42	31.86		0.7	2.60	31.15		3.0	2.07	31.58	5
$^2\Pi$	$(7\sigma^{-2}3\pi^1)$	36.03	0.1	2.46	35.79		2.9	3.05	35.03	6	7.7	2.24	35.71	6
$^2\Delta$	$(5\sigma^{-1}2\pi^{-1}3\pi^1)$	36.64	0.5	2.33	36.30		0.2	2.63	35.83		1.7	2.28	36.06	6
$^2\Pi$	$(6\sigma^{-1}7\sigma^{-1}2\pi^{-1}3\pi^2)$	40.20	2.0	3.61	40.86	6	0.1	2.67	39.91		0.1	2.64	40.03	
$^2\Pi$	$(5\sigma^{-1}7\sigma^{-1}3\pi^1)$	43.23	0.0	2.83	42.99		2.4	3.31	42.20	7	1.1	2.72	42.65	
total intensity			106.3				138.4				212.3			

emission of an electron of these bonding orbitals. Note that the Renner-Teller splitting in the degenerate $^2\Pi$ states[75,76] was neglected in the computations.

The relative intensity of the σ participator states as compared to the π counterparts increases with photon energy. This is readily explained by the different photoelectron cross sections of the $2s$ and $2p$ atomic orbitals on the atoms in the molecule and their contributions to the respective orbitals.[77,78] Without going into details, we mention that the minimal basis expansion of the molecular orbitals (Table 4.1) provide a simple access to the populations of the atomic orbitals. The same coefficients provide also a straightforward explanation of the intensity patterns observed for the participator states. While the participator states are not well resolved from the intense spectator structures in the C1s-3π resonant Auger electron spectra, we can state that for both spectra, the 2π signal is stronger than the 1π one and an opposite intensity ratio is found for the N1s-3π decay. According to the considerations given above, these intensities should be proportional to the square of the $2p_\pi$ coefficients of the respective molecular orbital at the core hole atom. For the C and N atom this ratio $(c_{2p_\pi,2\pi}/c_{2p_\pi,1\pi})^2$ amounts to 5.0 and 0.19, respectively, which is a good estimate for the intensity ratio of the 2π and 1π signals in the carbon and nitrogen resonant Auger electron spectra. For the nitrogen spectra the 7σ feature is well observed, while the 6σ one cannot be detected in the experimental spectra and its intensity is predicted to be negligible (0.006 meV) as compared to the other transitions.

As expected, the resonant Auger electron spectra show spectator features strongly resembling the signals observed in the normal Auger decay for the same core hole. However, details are less pronounced in the resonant spectra than in the nonresonant ones. For example the RAES-features at about 22-28 eV labelled 2 and 3 are hardly resolved in the experimental spectra, while distinct features can be observed in the corresponding AES-spectra at 37 and 40 eV. A similar behaviour is found for features 4 and 5. We note that broadening of spectator features was already recognized by Carol and Thomas in O1s Auger spectra of CO, CO_2, and OCS.[79]

The broader shape of the RAES is due to an additional splitting of several final states by the spectator electron in the 3π orbital. In the following, we discuss and explain this point for feature 1: In the AES it is due to transitions into the

$^1\Delta$ and $^1\Sigma^+$ states with $(2\pi^{-2})$ occupation and vertical binding energies of 31.54 and 31.89 eV. Additionally, the $^3\Sigma^-$ ground state of the dication has the same occupation. Coupling the spectator electron in the 3π orbital to these states leads to the configurations that represent the final states of the RAES. In particular, the $^1\Delta$ $(2\pi^{-2})$ AES-state gives rise to a $^2\Phi$ and a $^2\Pi$ configuration in the RAES, the $^3\Sigma^-$ state splits into a $^4\Pi$ and a $^2\Pi$, while coupling an electron in the 3π orbital to the $^1\Sigma^+$ AES-state generates only a single $^2\Pi$ configuration. Thus, the $(2\pi^{-2}3\pi)$ occupation gives rise to one $^4\Pi$, one $^2\Phi$ and three $^2\Pi$ configurations. While the Auger transition to the quartet state out of the singlet core-excited state is spin forbidden, the $^2\Pi$ states couple via the Hamiltonian and give rise to three final states in the RAES with calculated vertical binding energies of 17.91, 19.12, and 22.89 eV. The $^2\Phi$ state is obtained at 18.48 eV. In the AES the $(2\pi^{-2})$ states give rise to two final states at a vertical binding energy of 31.54 and 31.89 eV. Thus, coupling of the “spectating” electron to the AES final states divides intensity found in a very narrow energy range in the AES to features spread over a much larger range in the corresponding RAES spectra.

Otherwise the spectator parts of the RAES are rather similar to the AES, albeit with a ≈15 eV shift to lower binding energies due to the additional electron in the 3π orbital. For that reason we do not discuss a detailed assignment of these features but refer to the corresponding consideration in the AES part of this publication.

4.4 Discussion

One of the most interesting features in the present work is the very good agreement between theory and experiment for both, normal and resonant Auger spectra. Band positions and intensities are well represented by the computations. The bands at low binding energies can be unambiguously assigned to specific final states and their intensities are rationalized by the orbital coefficients of the relevant orbitals at the ionization site. All AES are dominated by bands with at least one hole in a weakly bound valence orbital.

Figure 4.5 depicts a comparison between the normal and resonant Auger spectra of HCNO. When the RAES are shifted by 15 eV, AES and RAES have a similar appearance in the spectator region. This resemblance has been observed before, for example in CO.[80] While spectator Auger decay produces 2h1p (two hole, one particle) final states, normal Auger decay leads to 2h states. In a simplified picture, the spectator electron has only a small impact on the electronic structure, which leads to a similar appearance of AES and RAES. However, the presence

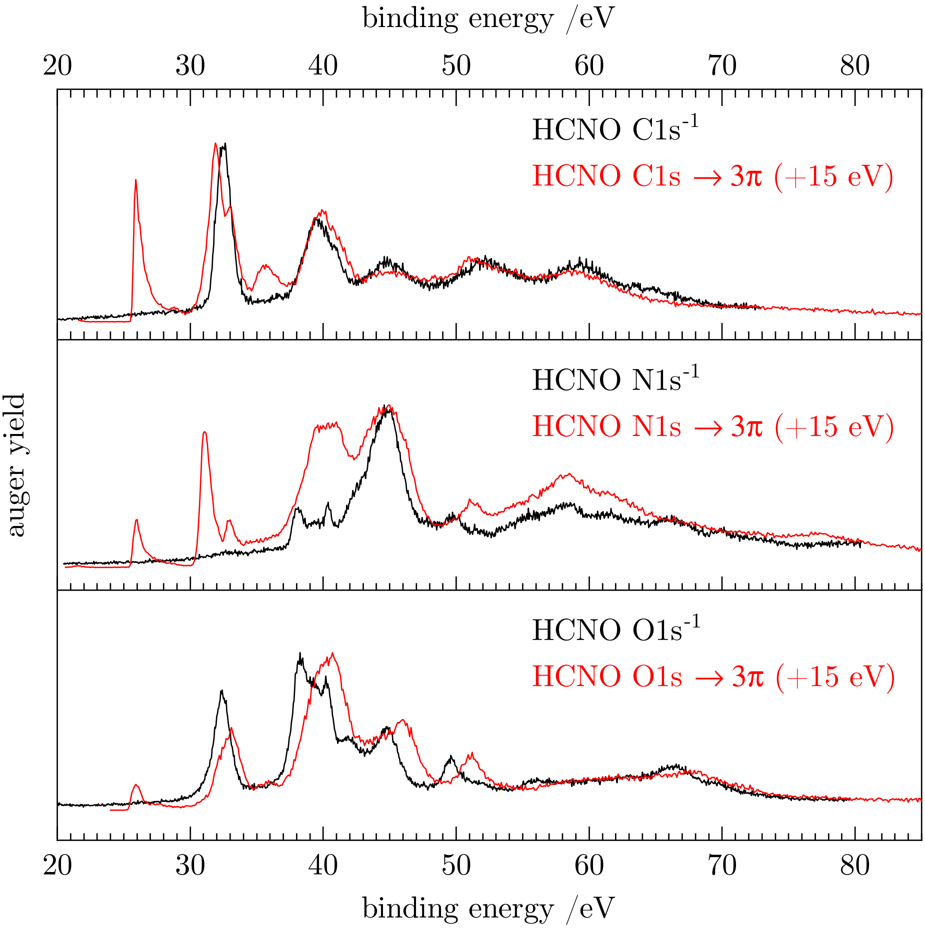

Figure 4.5: Comparison of the normal (black) and resonant (red) Auger spectra of fulminic acid. The resonant spectra were each shifted by 15 eV to higher binding energy.

of a spectator electron leads to a screening effect on the emitted Auger electron and thus to a shift of the RAES bands to higher kinetic energies compared with normal Auger decay, which is 15 eV in the case HCNO. As discussed above, the spectator electron couples to the valence holes leading to additional splitting in the RAES and subsequent bluring of some of the finer features seen in the AES (see e.g. the signals at 37-41 eV binding energy in the N1s and O1s spectra).

It is illustrative to compare the spectra of HCNO with the previously recorded ones of HNCO.[31] This can give information on the influence of nuclear charge versus nuclear site/bonding situation in the two related molecules. Differences in binding energies measured by XPS have often been rationalized (at least qualitatively) using the "equivalent core" or "Z+1" model.[81,82] Here, the shift in the binding energy for an atom in different molecules is estimated by a thermochemical cycle. This cycle is based on the assumption that for a valence electron a core hole in an atom with nuclear charge Z is equivalent to an atom with a nuclear charge Z+1. This allows to estimate ΔE_B, the difference in the C 1s binding energies in HNCO and HCNO from tabulated thermochemical data. HCNO and HNCO with a C 1s core hole would both resemble $HNNO^+$ from the point of view of a valence electron. In the "equivalent core" model, ΔE_B is then equivalent to the heat of reaction $\Delta_r H$ for the hypothetical process given by

$$\mathrm{HNNO^+ + HNCO \rightarrow HCNO + HNNO^+}, \qquad (4.7)$$

where the hypothetical $HNNO^+$ cancels on both sides. For $\Delta_r H$ we obtain 2.97 eV, using data from the active thermochemical tables.[83] From Figure A4.1 a C 1s ionization energy of 292.9 eV is determined, while for HNCO a value of 295.9 eV was reported.[31], i.e. ΔE_B=3.0 eV, in excellent agreement with the equivalent core model. Unfortunately, thermochemical formation enthalpies for several species resulting from the N 1s and O 1s core holes are not available.

Figures 4.6 and 4.7 show a comparison of the normal and resonant Auger spectra of fulminic acid and isocyanic acid. HNCO spectra were taken from Ref. [31]. Both molecules have the same number of electrons, so a comparison should give insight into the influence of atom connectivity on the Auger spectra. Note that the N 1s spectra of HNCO are compared to the C 1s spectra of HCNO and vice versa. Thus, we compare sites in the two molecules rather than atoms. This is based on the assumption that the site should influence the appearance of the Auger spectra, i.e. the band structure, more strongly than the nuclear charge. In fact, Figure 4.6 a) shows that the AES of the atoms next to the hydrogen atom (C 1s in HCNO and N 1s in HNCO) are quite similar, apart from a slightly different

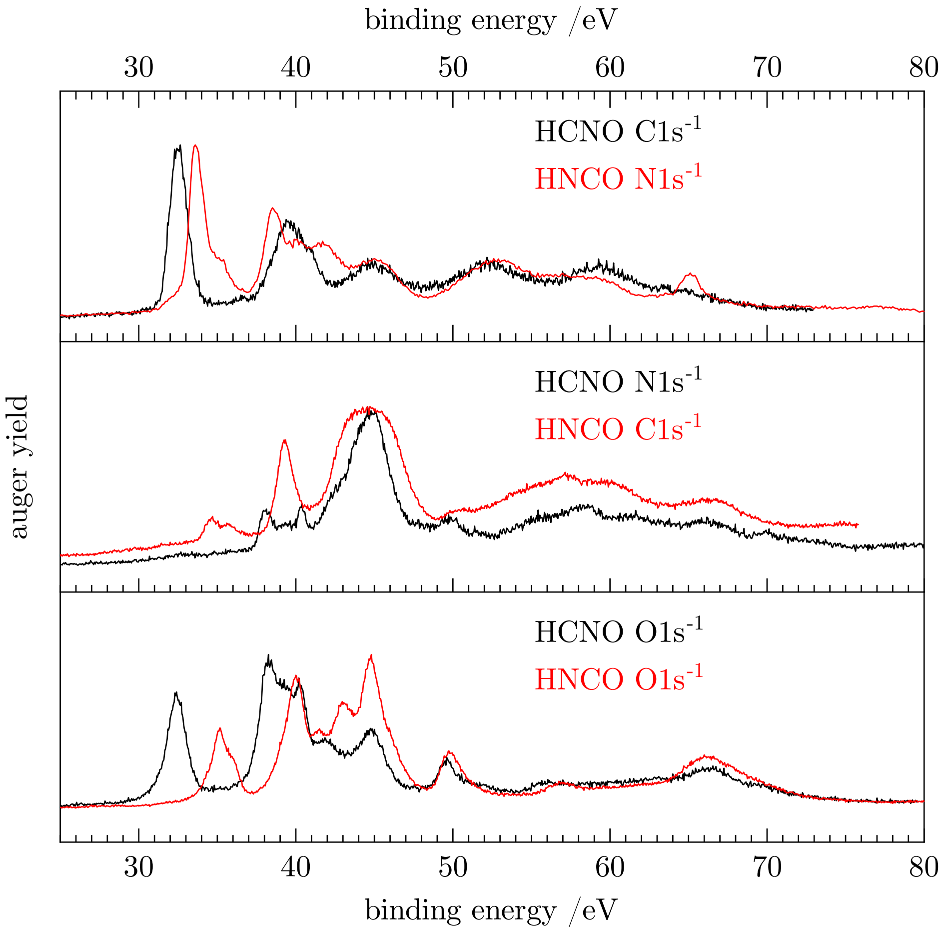

Figure 4.6: Comparison of the normal Auger spectra of fulminic acid (black) and isocyanic acid (red). The spectra of isocyanic acid are taken from Ref. [31]. Spectra are compared according to their position in the molecule, i.e. carbon to nitrogen and oxygen to oxygen.

binding energy. However, symmetry is different in both molecules, while HCNO is linear, HNCO is bent. In HCNO the H-X-Y- angle is 180°, whereas in HNCO this angle is around 128°.[84] Therefore the degeneracy of the π orbitals is lifted in HNCO. As a consequence, several final states of similar energy overlap in HNCO, resulting in broader bands and additional features. However, both spectra are

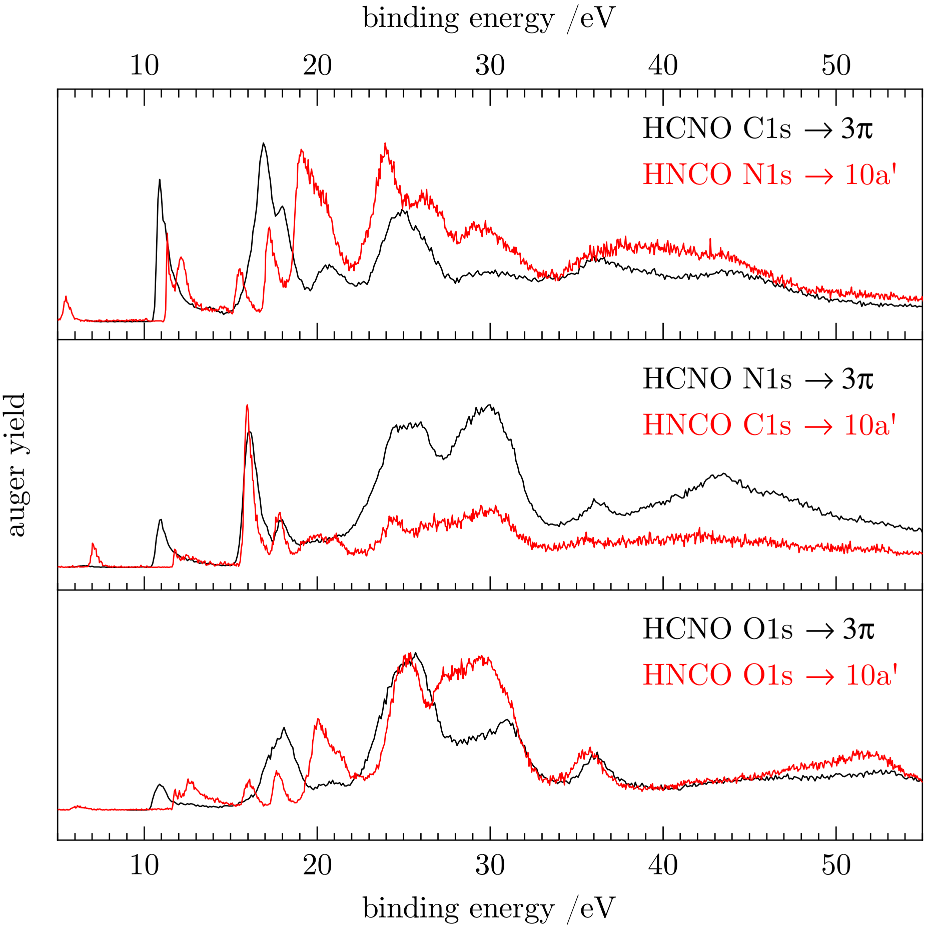

Figure 4.7: Comparison of the resonant Auger spectra of fulminic acid (black) and isocyanic acid (red). The spectra of isocyanic acid are taken from Ref. [31]. Spectra are compared according to their position in the molecule, i.e. carbon to nitrogen and oxygen to oxygen.

dominated by the band at lowest binding energies (band 1 in Figure 4.2), assigned to the ($2\pi^{-2}$) hole state in HCNO. In HNCO it corresponds to two final states, ($2a"^{-2}$) and ($2a"^{-1}$)($9a'^{-1}$).[31] In trace b) the N 1s edge of HCNO is compared with the C 1s edge of HNCO. While band 1 is absent in the N 1s AES of HCNO, it is observable in the C 1s AES of HNCO, but only with low intensity. This low intensity was also explained by the small orbital coefficients at the carbon atom, leading to a nodal plane in the molecular orbital. Interestingly, a similarly low intensity of the first band was also observed in the AES of the central N atom in N_2O.[85] Finally for the O-atoms, the AES also show a similar shape, but different intensities. In both molecules, band 1 appears with reasonable intensity, but is weaker than band 2.

In Figure 4.7 the RAES obtained upon the 1s → LUMO transition of the two molecules are compared. The latter corresponds to a transition into the 3π orbital of fulminic acid and the $10a'$ orbital of isocyanic acid. Again, the RAES spectra at the three sites are compared. Note that the peaks at very low binding energy (<6 eV) in the HNCO spectra originate from core ionization by second-harmonic light. It is evident that the RAES of HCNO and HNCO differ more strongly than the AES, in particular below 20 eV binding energy. Here, the lifting of degeneracy in HNCO leads to a larger number of final states and additional transitions in HNCO. At higher binding energies, the spectra become more similar, in particular at the O 1s edge. However, the participators states become particularly intense upon N 1s excitation in both molecules, thus, it seems that nuclear charge is more important in RAES than in AES

4.5 Conclusions

We conducted an extensive spectroscopic study of the inner-shell levels of fulminic acid, HCNO in the soft X-ray regime, employing synchrotron radiation provided by the PLEIADES beamline at Synchrotron SOLEIL. HCNO is a reactive molecule that was synthesized by preparative pyrolysis. For 1s ionization, IEs of 292.9 eV (C 1s), 410.5 eV (N 1s) and 539.6 eV (O 1s) were determined by XPS. X-ray absorption spectra at all three edges are dominated by an intense band assigned to the $\pi^* \leftarrow 1s$ transition into the 3π LUMO. In addition, several smaller bands are visible, assigned to transitions into Rydberg states. Normal and resonant Auger spectra are reported, with assignments based on computations.

The one-center approximation provides a simple and reliable representation of the Auger spectra of HCNO. We have shown that the underlying data – the expansion of the molecular orbitals in terms of a minimal basis – provides a simple interpretation for the observed intensity patterns in the spectra. The normal Auger spectra (AES) at the C 1s and O 1s show a well separated intense band at 32.5 eV binding energy, which is assigned to the $^1\Delta$ state with a double hole in the ($2\pi^{-2}$) HOMO and corresponds to the double ionization energy of HCNO to its first excited state. Computations indicate additional smaller contributions from the $^1\Sigma^+$ state. This band is almost absent in the N 1s AES, which can be explained by the small orbital coefficients at the nitrogen atom. The resonant Auger spectra (RAES) obtained upon excitation of the $\pi^* \leftarrow 1s$ transition show well-resolved bands originating from participator states at low binding energies. Above 20 eV, the RAES are dominated by spectator states. In the N 1s and O 1s RAES their intensity is higher than the one of the participator states. Only minor changes were observed in the RAES, when the excitation energy was scanned over the $\pi^* \leftarrow 1s$ transition. A comparison between the normal Auger spectra of HCNO and the previously investigated HNCO shows that the spectra recorded at the central heavy atom (N 1s in HCNO and C 1s in HNCO) and at the atom connected to hydrogen show a similar appearance. This indicates that the molecular site is more important than the nuclear charge.

This work indicates that intensities for the Auger decay follow common rules that can be used to obtain insight into the related electronic structure properties. While similar approaches have been proposed previously,[64,66,68,86] it seems that a consistent formulation of such approximations is not yet available. For that reason, we plan to elaborate the models proposed here in subsequent work and to identify the area in which they are valid.

Appendix

X-Ray photoelectron spectra

To determine the 1s ionization energies, X-ray photoelectron spectra (XPES) were recorded at all three edges (A4.1, A4.2 and A4.3). In those spectra the binding energy of the electrons were determined by subtracting the experimentally determined kinetic energy from the photon energy.

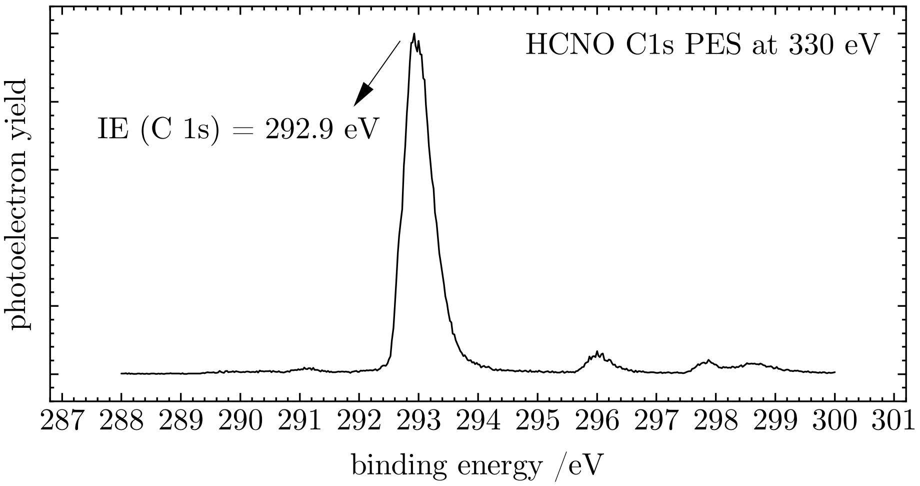

Figure A4.1: C 1s photoelectron spectrum of HCNO. An ionisation energy of 292.9 eV is determined. Contaminations from CO_2 and HNCO are visible at 297.8[87] and 295.9 eV.[31]

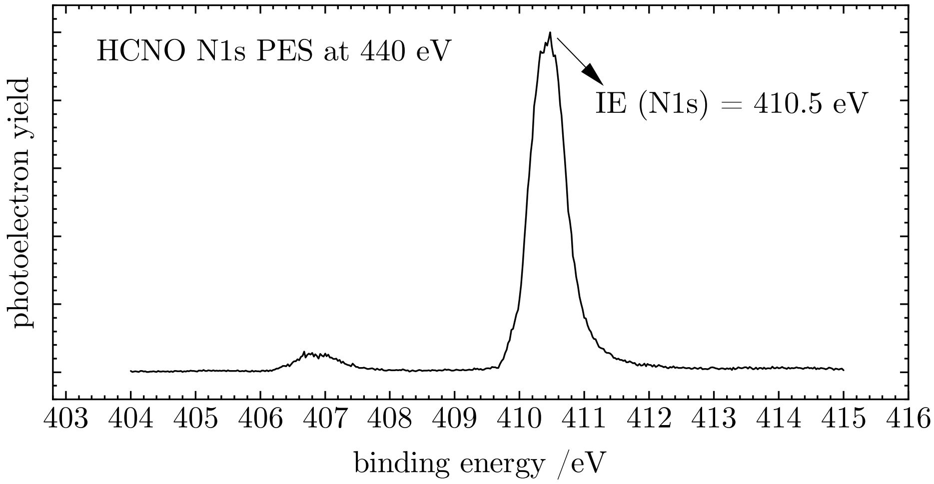

Figure A4.2: N 1s photelectron spectrum of HCNO. An ionisation energy of 410.5 eV is determined. Contaminations due to HCN from the synthesis are visible at 406.9 eV.[88]

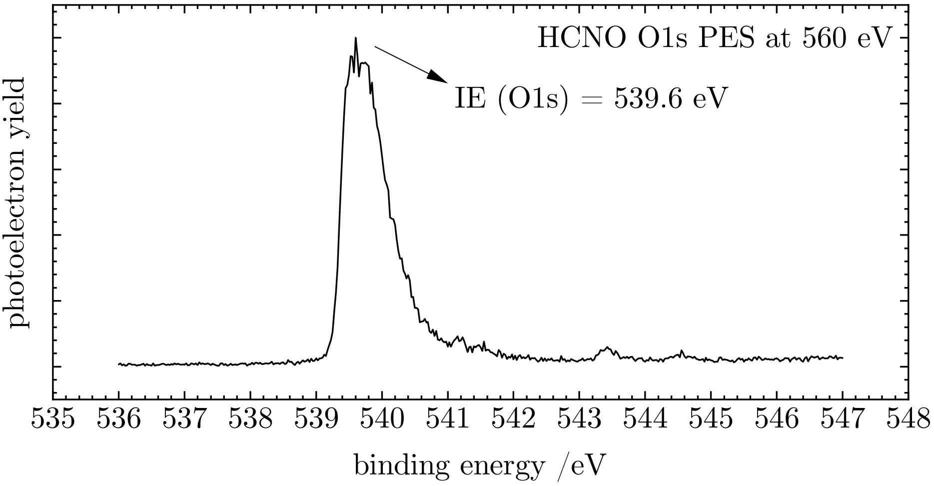

Figure A4.3: O 1s photelectron spectrum of HCNO. An ionisation energy of 539.6 eV is determined. Contaminations from CO_2 and O_2 are visible at 541.2 and 543.4 eV.[89]

Comparison of HCNO Auger electron spectra to those of HNCO, CO_2 and N_2

In this section, we compare our normal Auger elecron spectra (AES) to known spectra of HNCO, N_2 and CO_2. The spectra of CO_2 and N_2 were recorded for calibration purposes during the beamtime. The spectra of Isocyanic acid were taken from Holzmeier *et al.*.[31]

Normal Auger electron spectra

Note that the electron kinetic energy is chosen for comparison.

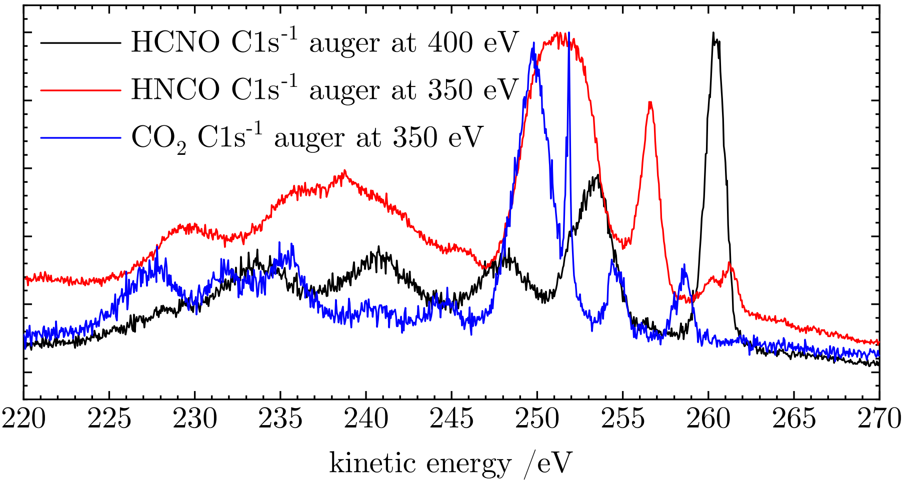

Figure A4.4: Comparison of normal Auger electron spectra (AES) at the carbon K-edge of HCNO (black), HNCO (red),[31] and CO_2 (blue). The spectra show that a contamination from HNCO or CO_2 can be ruled out.

.

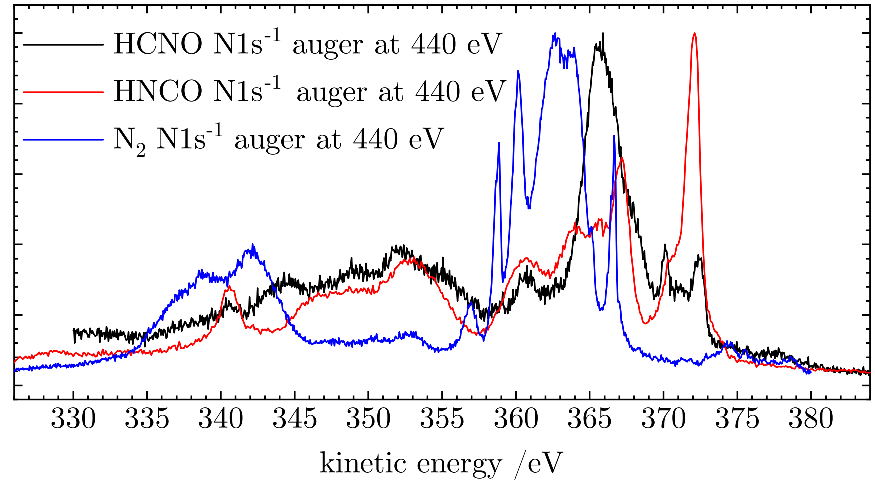

Figure A4.5: Comparison of AES at the nitrogen K-edge of HCNO (black), HNCO (red),[31] and N_2 (blue). Again, a contamination can be ruled out.

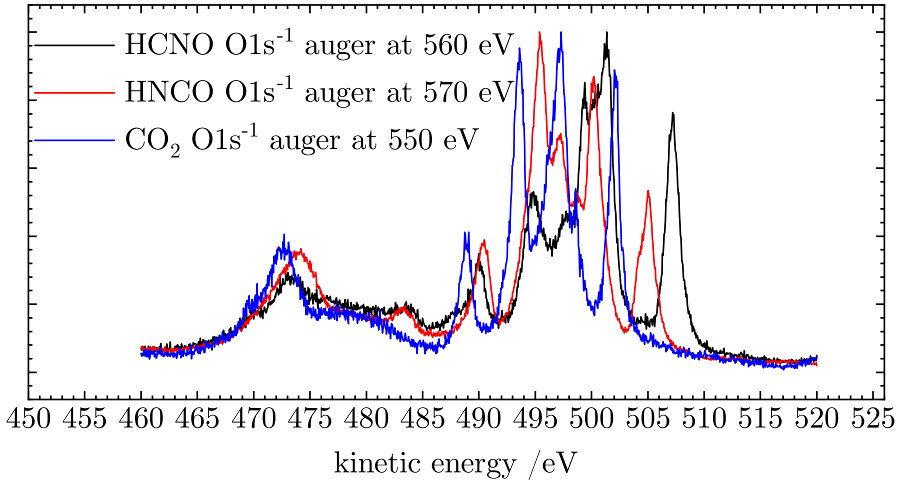

Figure A4.6: Comparison of AES at the oxygen K-edge of HCNO (black), HNCO (red),[31] and CO_2 (blue). The spectra show that a contamination from CO_2 can be ruled out.

Additional resonant Auger electron spectra

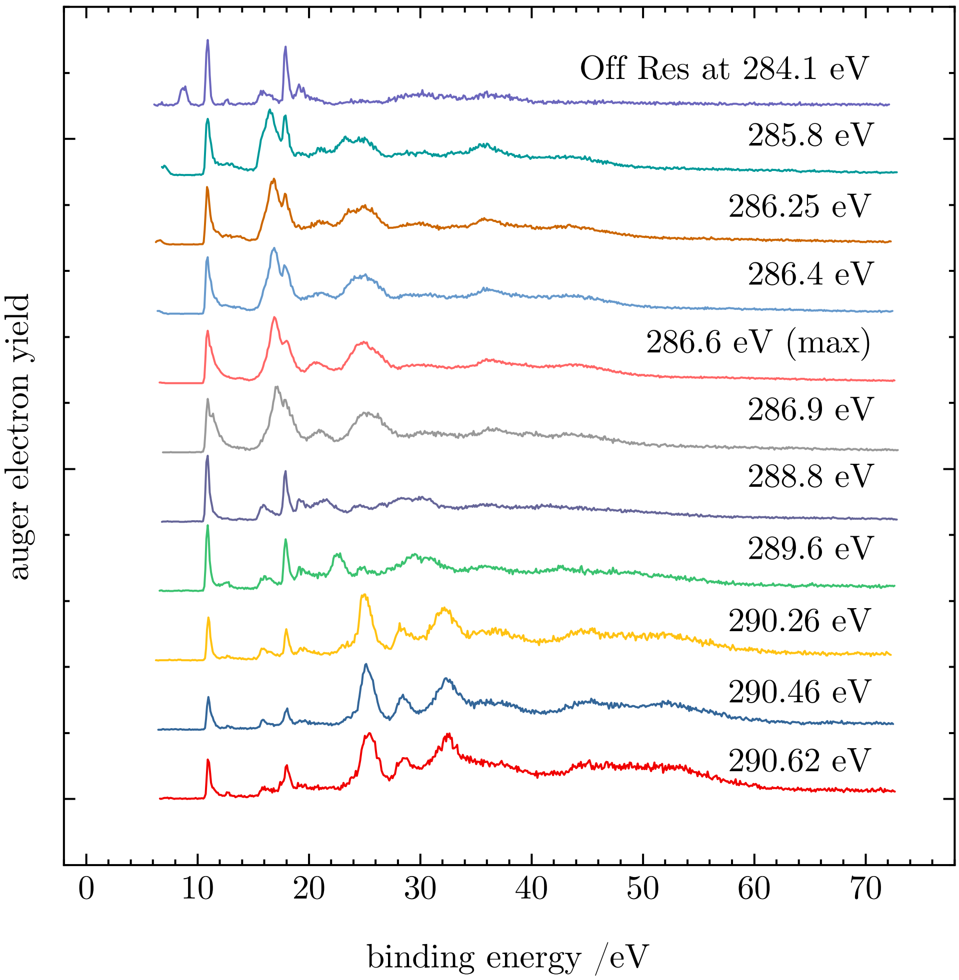

Figure A4.7: Resonant Auger electron spectra (RAES) at the carbon edge. The top trace shows the off-resonant spectrum. The additional peak at 8 eV is due to the second harmonic of the synchrotron light ionizing the C1s electron. The other traces show the RAES recorded on the various absorption bands.

Figure A4.7 shows the resonant Auger electron spectra (RAES) at the C 1s edge upon all excitation energies indicated in the NEXAFS spectra (Figure 4.3 a) in the main paper). The top trace shows the off-resonant photoelectron spectrum

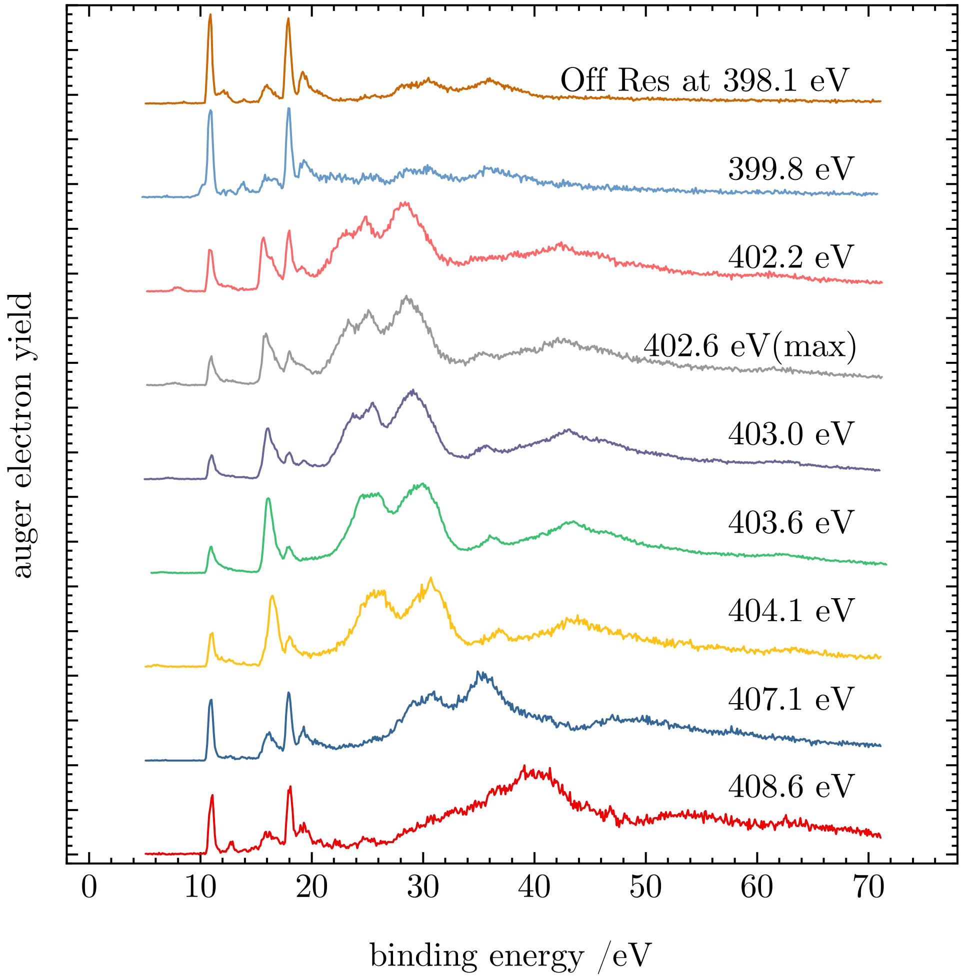

Figure A4.8: Resonant Auger electron spectra (RAES) at the nitrogen edge. The top trace shows the off-resonant excitation at 389.1 eV, the traces below show RAES recorded at the excitation energies marked in Figure 4.3 b) in the main paper.

obtained at 284.1 eV. The additional peak at 8 eV is created by the second harmonic of the synchrotron light ionizing the C1s electron. The next five traces show the RAES recorded on the $3\pi^* \leftarrow 1s$ band. The spectra have a similar appearance, demonstrating the absence of vibrational effects. The weak bands at 288.8 eV and 289.6 eV show only small resonance enhancement. The bottom three

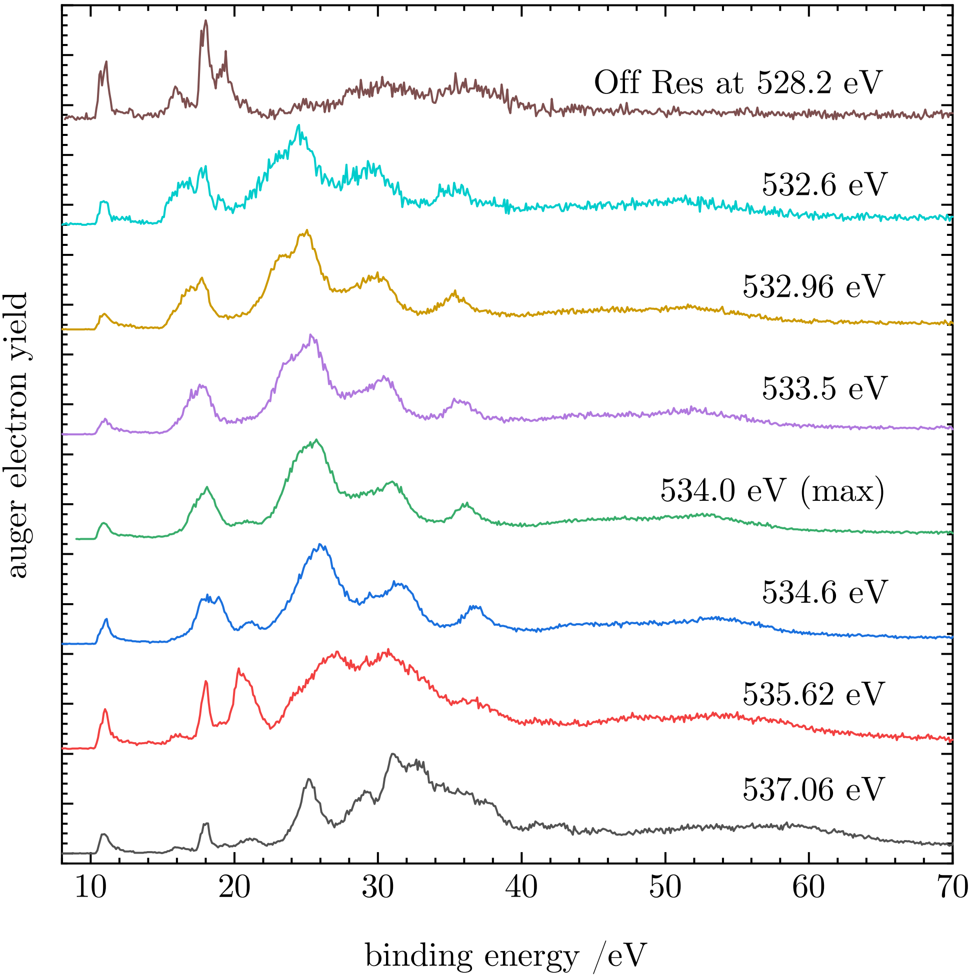

Figure A4.9: Resonant Auger electron spectra at the oxygen 1s edge with the off-resonant spectrum at 528.2 eV in the top trace. The traces below show RAES recorded at the excitation energies marked in Figure 4.3 c) in the main paper.

spectra show the RAES obtained upon exciting the band that shows a vibrational progression in the NEXAFS spectrum, presumably a Rydberg state. They exhibit a massive enhancement of participator states at binding energies between 24 eV and 34 eV, but only a weak enhancement of the low energy spectator states. However, the RAES recorded on the various vibrational bands are very similar.

Figure A4.8 shows the RAES at the N 1s edge upon all excitation energies indicated in the NEXAFS spectra (Figure 4.3 b) in the main paper). The top trace shows the off-resonant photoelectron spectrum. The RAES recorded on the $3\pi^*$ excitation show small, but recognisable differences. With increasing energy the resonant enhancement of the 7σ signal at 18 eV binding energy decreases, compared to the 1π signal (see Tables 4.4 and 4.5 in the main paper for detailed description of the states). The weak Rydberg states at 407.1 eV and 408.6 eV show a strong enhancement of spectator states at high binding energies.

Finally, Figure A4.9 shows the RAES at the O 1s edge upon all excitation energies indicated in the NEXAFS spectra (Figure 4.3 c) in the main paper). The spectra recorded on the $3\pi^*$ band between 532.6 eV and 534.6 eV are very similar. Like in the C 1s and N 1s case, excitation of Rydberg states leads to strong enhancement of high binding energy spectator states. At an excitation energy of 535.62 eV (possibly excitation to a 3s Rydberg state) an intense band appears at a binding energy of around 21 eV, most likely due to a spectator state. As the computed RAES are based on the $3\pi^*$ excitation, it is difficult to draw reasonable conclusions on the character of the state.

References

[1] F. Kurzer, *J. Chem. Educ.* **2000**, *77*, 851.

[2] C. Wentrup, *Angew. Chem. Int. Ed.* **2019**, *58*, 14800–14808.

[3] E. Howard, *Philos. Trans. R. Soc.* **1800**, *90*, 204–238.

[4] H. Ley, H. Kissel, *Ber. Dtsch. Chem. Ges.* **1899**, *32*, 1357–1368.

[5] R. Huisgen, *Proc. Chem. Soc.* **1961**, 357–396.

[6] W. Beck, K. Feldl, *Angew. Chem.* **1966**, *78*, 746–746.

[7] B. P. Winnewisser, M. Winnewisser, *J. Mol. Spectrosc.* **1969**, *29*, 505–507.

[8] W. Beck, P. Swoboda, K. Feldl, R. S. Tobias, *Chem. Ber.* **1971**, *104*, 533–543.

[9] B. P. Winnewisser, P. Jensen, *J. Mol. Spectrosc.* **1983**, *101*, 408–421.

[10] B. P. Winnewisser, M. Winnewisser, G. Wagner, J. Preusser, *J. Mol. Spectrosc.* **1990**, *142*, 29–56.

[11] M. Winnewisser, H. K. Bodenseh, *Z. Naturforsch. A* **1967**, *22*, 1724.

[12] J. Bastide, J. P. Maier, *Chem. Phys.* **1976**, *12*, 177–190.

[13] T. Pasinszki, N. Kishimoto, K. Ohno, *J. Phys. Chem. A* **1999**, *103*, 6746–6756.

[14] W. Feng, J. P. Meyer, J. F. Hershberger, *J. Phys. Chem. A* **2006**, *110*, 4458–4464.

[15] W. Feng, J. F. Hershberger, *J. Phys. Chem. A* **2014**, *118*, 829–837.

[16] W. Feng, J. F. Hershberger, *Chem. Phys.* **2016**, *472*, 18–23.

[17] L. Pauling, S. B. Hendricks, *J. Am. Chem. Soc.* **1926**, *48*, 641–651.

[18] J. U. Nef, *Justus Liebigs Ann. Chem.* **1894**, *280*, 291–342.

[19] J. Koput, B. P. Winnewisser, M. Winnewisser, *Chem. Phys. Lett.* **1996**, *255*, 357–362.

[20] A. Luna, A. M. Mebel, K. Morokuma, *J. Chem. Phys.* **1996**, *105*, 3187–3205.

[21] M. S. Schuurman, S. R. Muir, W. D. Allen, H. F. S. III, *J. Chem. Phys.* **2004**, *120*, 11586–11599.

[22] M. Mladenović, M. Lewerenz, *Chem. Phys.* **2008**, *343*, 129–140.

[23] N. Marcelino, J. Cernicharo, B. Tercero, E. Roueff, *Astrophys. J.* **2009**, *690*, L27–L30.

[24] E. Mendoza, B. Lefloch, A. López-Sepulcre, C. Ceccarelli, C. Codella, H. M. Boechat-Roberty, R. Bachiller, *Mon. Not. R. Astron. Soc.* **2014**, *445*, 151–161.

[25] B. Lefloch, R. Bachiller, C. Ceccarelli, J. Cernicharo, C. Codella, A. Fuente, C. Kahane, A. López-Sepulcre, M. Tafalla, C. Vastel, E. Caux, M. González-García, E. Bianchi, A. Gómez-Ruiz, J. Holdship, E. Mendoza, J. Ospina-Zamudio, L. Podio, D. Quénard, E. Roueff, N. Sakai, S. Viti, S. Yamamoto, K. Yoshida, C. Favre, T. Monfredini, H. M. Quitián-Lara, N. Marcelino, H. M. Boechat-Roberty, S. Cabrit, *Mon. Not. R. Astron Soc.* **2018**, *477*, 4792–4809.

[26] N. Marcelino, M. Agúndez, J. Cernicharo, E. Roueff, M. Tafalla, *Astron. Astrophys.* **2018**, *612*, L10.

[27] D. H. Quan, E. Herbst, Y. Osamura, E. Roueff, *Astrophys. J.* **2010**, *725*, 2101–2109.

[28] M. Lattelais, F. Pauzat, Y. Ellinger, C. Ceccarelli, *Astrophys. J.* **2009**, *696*, L133–L136.

[29] J. A. Sebree, M. C. Roach, E. R. Shipley, C. He, S. M. Hörst, *Astrophys. J.* **2018**, *865*, 133.

[30] D. Matsakis, A. Coster, B. Laster, R. Sime, *Phys. Today* **2019**, *72*, 10–11.

[31] F. Holzmeier, T. J. A. Wolf, C. Gienger, I. Wagner, J. Bozek, S. Nandi, C. Nicolas, I. Fischer, M. Gühr, R. F. Fink, *J. Chem. Phys.* **2018**, *149*, 034308.

[32] M. Gerlach, F. Fantuzzi, L. Wohlfart, K. Kopp, B. Engels, J. Bozek, C. Nicolas, D. Mayer, M. Gühr, F. Holzmeier, I. Fischer, *J. Chem. Phys.* **2021**, *154*, 114302.

[33] J. H. D. Eland, R. J. Squibb, A. J. Sterling, M. Wallner, A. H. Roos, J. Andersson, V. Axelsson, E. Johansson, A. Teichter, S. Stranges, B. Brunetti, J. M. Dyke, F. Duarte, R. Feifel, *Sci. Rep.* **2020**, *10*, 2288.

[34] A. deBrito, S. Svensson, S. Osborne, A. Ausmees, A. Kivimaki, O. Sairanen, E. Nommiste, H. Aksela, L. Saethre, *J. Chem. Phys.* **1997**, *106*, 18–23.

[35] M. Alagia, E. Bodo, P. Decleva, S. Falcinelli, A. Ponzi, R. Richter, S. Stranges, *Phys. Chem. Chem. Phys.* **2013**, *15*, 1310–1318.

[36] U. Ekström, V. Carravetta, M. Alagia, M. Lavollée, R. Richter, C. Bolcato, S. Stranges, *J. Chem. Phys.* **2008**, *128*, 044302.

[37] Pleiades, `https://www.synchrotron-soleil.fr/fr/lignes-de-lumiere/pleiades` (visited on 09/16/2019, 15:43).

[38] C. Wentrup, B. Gerecht, H. Briehl, *Angew. Chem. Int. Ed.* **1979**, *18*, 467–468.

[39] W. E. Moddeman, T. A. Carlson, M. O. Krause, B. P. Pullen, W. E. Bull, G. K. Schweitzer, *J. Chem. Phys.* **1971**, *55*, 2317–2336.

[40] V. Staemmler, R. Jaquet, *Theor. Chim. Acta* **1981**, *59*, 487–500.

[41] J. Wasilewski, *Int. J. Quantum Chem.* **1989**, *36*, 503–524.

[42] U. Meier, V. Staemmler, *Theor. Chim. Acta* **1989**, *76*, 95–111.

[43] R. Fink, V. Staemmler, *Theor. Chim. Acta* **1993**, *87*, 129–45.

[44] R. Fink, *J. Electron Spectrosc. Relat. Phenom.* **1995**, *76*, 295–300.

[45] R. F. Fink, S. L. Sorensen, A. Naves de Brito, A. Ausmees, S. Svensson, *J. Chem. Phys.* **2000**, *112*, 6666–6677.

[46] R. Fink, *J. Chem. Phys.* **1997**, *106*, 4038–4052.

[47] A. Rüdel, U. Hergenhahn, K. Maier, E. E. Rennie, O. Kugeler, J. Viefhaus, P. Lin, R. R. Lucchese, A. M. Bradshaw, *New J. Phys.* **2005**, *7*, 189.

[48] R. F. Fink, M. Kivilompolo, H. Aksela, S. Aksela, *Phys. Rev. A* **1998**, *58*, 1988.

[49] A. Machado Bueno, A. Naves de Brito, R. F. Fink, M. Bassler, O. Bjorneholm, F. Burmeister, R. Feifel, C. Miron, S. L. Sorensen, H. Wang, S. Svensson, *Phys. Rev. A* **2003**, *67*, 022714-1–7.

[50] J. H. D. Eland, R. F. Fink, P. Linusson, L. Hedin, S. Plogmaker, R. Feifel, *Phys. Chem. Chem. Phys.* **2011**, *13*, 18428–18435.

[51] J. Palaudoux, T. Kaneyasu, L. Andric, S. Carniato, G. Gamblin, F. Penent, Y. Hikosaka, E. Shigemasa, K. Ito, S. Fritzsche, E. Kukk, S. Sheinerman, R. F. Fink, P. Lablanquie, R. Püttner, *Phys. Rev. A* **2018**, *98*, 043406.

[52] A. D. Becke, *J. Chem. Phys.* **1993**, *98*, 5648–5652.

[53] F. Weigend, R. Ahlrichs, *Phys. Chem. Chem. Phys.* **2005**, *7*, 3297–3305.

[54] F. Furche, R. Ahlrichs, C. Hättig, W. Klopper, M. Sierka, F. Weigend, *WIREs Comput Mol Sci* **2014**, *4*, 91–100.

[55] T. H. Dunning, Jr., *J. Chem. Phys.* **1989**, *90*, 1007–1023.

[56] H. Siegbahn, L. Asplund, P. Kelfve, *Chem. Phys. Lett.* **1975**, *35*, 330–335.

[57] H. Ågren, S. Svensson, U. Wahlgren, *Chem. Phys. Lett.* **1975**, *35*, 336–344.

[58] C.-M. Liegener, *Chem. Phys. Lett.* **1982**, *90*, 188–92.

[59] E. J. Mc Guire, *Phys. Rev.* **1969**, *185*, 1.

[60] D. Walters, C. Bhalla, *At. Data Nucl. Data Tab.* **1971**, *3*, 301–315.

[61] M. H. Chen, F. P. Larkins, B. Crasemann, *At. Data Nucl. Data Tables* **1990**, *45*, 1–205.

[62] E. Z. Chelkowska, F. P. Larkins, *At. Data Nucl. Data Tab.* **1991**, *49*, 121–206.

[63] G. Wentzel, *Z. Physik* **1927**, *43*, 524.

[64] H. Ågren, *J. Chem. Phys.* **1981**, *75*, 1267–83.

[65] H.-J. Freund, C.-M. Liegener, *Chem. Phys. Lett.* **1987**, *134*, 70–5.

[66] T. X. Carroll, T. D. Thomas, *J. Chem. Phys.* **1992**, *97*, 894–9.

[67] R. W. Shaw, Jr., T. D. Thomas, *Phys. Rev. A* **1975**, *11*, 1491–7.

[68] F. Tarantelli, A. Sgamellotti, L. S. Cederbaum, *J. Chem. Phys.* **1991**, *94*, 523–32.

[69] K. A. Peterson, T. H. Dunning, *J. Chem. Phys.* **2002**, *117*, 10548–10560.

[70] L. S. Cederbaum, P. Campos, F. Tarantelli, A. Sgamellotti, *J. Chem. Phys.* **1991**, *95*, 6634–6644.

[71] L. S. Cederbaum, F. Tarantelli, *J. Chem. Phys.* **1993**, *99*, 5871.

[72] C. T. Chen, Y. Ma, F. Sette, *Phys. Rev. A* **1989**, *40*, 6737–6740.

[73] J. Stöhr in *NEXAFS Spectroscopy*, Springer Series in Surface Sciences, Springer-Verlag Berlin Heidelberg 1992, **1992**, Chapter 4, p. 105.

[74] M. N. Piancastelli, R. F. Fink, R. Feifel, M. Bässler, S. L. Sorensen, C. Miron, H. Wang, I. Hjelte, O. Björneholm, A. Ausmees, S. Svensson, P. Salek, F. K. Gel'mukhanov, H. Ågren, *J. Phys. B* **2000**, *33*, 1819–1826.

[75] E. Kukk, J. D. Bozek, N. Berrah, *Phys. Rev. A* **2000**, *62*, 032708.

[76] E. Antonsson, M. Patanen, C. Nicolas, S. Benkoula, J. J. Neville, V. L. Sukhorukov, J. D. Bozek, P. V. Demekhin, C. Miron, *Phys. Rev. A* **2015**, *92*, 042506.

[77] U. Gelius, *Phys. Scripta* **1974**, *9*, 133–147.

[78] D. P. Chong, *Can. J. Chem.* **1985**, *63*, 2007–2011.

[79] T. X. Carroll, T. D. Thomas, *J. Chem. Phys.* **1989**, *90*, 3479–3483.

[80] L. Ungier, T. D. Thomas, *J. Chem. Phys.* **1985**, *82*, 3146–3151.

[81] W. L. Jolly, D. N. Hendrickson, *J. Am. Chem. Soc.* **1970**, *92*, 1863–18716.

[82] P. S. Bagus, C. Sousa, F. Illas, *Phys. Chem. Chem. Phys.* **2020**, *22*, 22617–22626.

[83] B. Ruscic, R. E. Pinzon, G. von Laszewski, D. Kodeboyina, A. Burcat, D. Leahy, D. Montoy, A. F. Wagner, *J. Phys: Conf. Ser.* **2005**, *16*, 561–570.

[84] K. Yamada, *J. Mol. Spectrosc.* **1980**, *79*, 323–344.

[85] P. Bolognesi, M. Coreno, L. Avaldi, L. Storchi, F. Tarantelli, *J. Chem. Phys.* **2006**, *125*, 054306.

[86] R. H. Temperton, W. Quevedo, R. Seidel, J. Uhlig, J. Schnadt, P. Persson, *Phys. Rev. Research* **2021**, *3*, 033030.

[87] V. Myrseth, J. D. Bozek, E. Kukk, L. J. Sæthre, T. D. Thomas, *J. Electron Spectros. Relat. Phenomena* **2002**, *122*, 57–63.

[88] A. P. Hitchcock, C. E. Brion, *Chem. Phys.* **1979**, *37*, 319–331.

[89] P. Wang, T. X. Carroll, T. D. Thomas, L. J. Sæthre, K. J. Børve, *J. Electron Spectros. Relat. Phenomena* **2021**, *251*, 147103.

CHAPTER 5

X-ray induced fragmentation of fulminic acid, HCNO

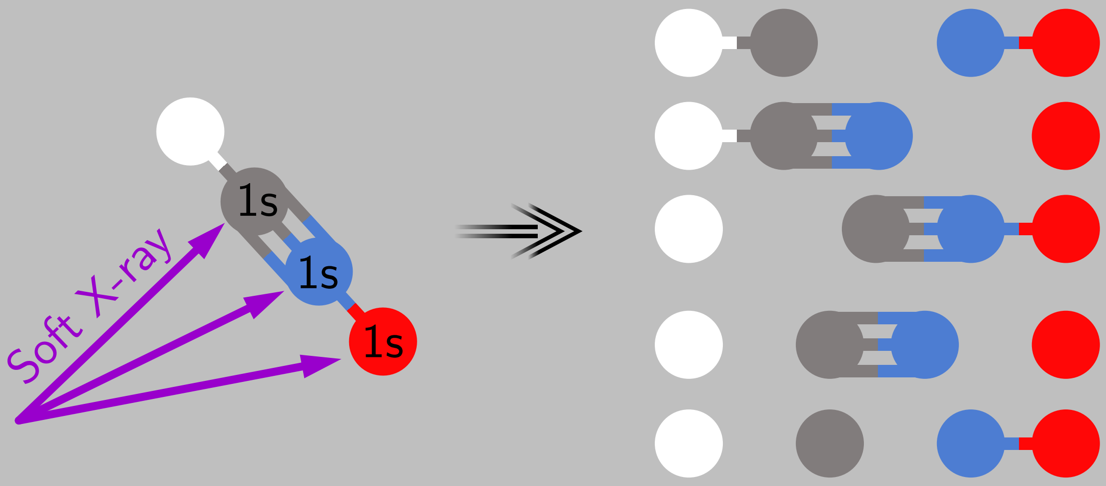

This chapter is an adapted version of a submitted manuscript.

J. Chem. Phys.
Marius Gerlach, Dorothee Schaffner, Tobias Preitschopf, Emil Karaev, Fabian Holzmeier, John Bozek and Ingo Fischer

5.1 Abstract

The fragmentation of fulminic acid, HCNO, after excitation and ionization of core electrons was investigated using Auger-electron-photoion coincidence spectroscopy. A considerable degree of site-selectivity is observed. Ionization of the carbon and oxygen 1s electron leads to around 70% CH^+ + NO^+, while ionization at the central N-atom produces only 37% CH^+ + NO^+, but preferentially forms O^+ + HCN^+ and O^+ + CN^+. The mass-selected Auger-electron spectra show that these fragments are associated with higher binding energy final states. Furthermore, ionization of the C 1s electron leads to a higher propensity for C-H bond fission compared to O 1s ionization. Following resonant Auger-Meitner decay after 1s → 3π excitation, eleven different ionic products are formed. At the C K-edge the parent ion $HCNO^+$ is significantly more stable compared to the other two edges, which we also attribute to the higher contribution of final states with low binding energies in the C 1s resonant Auger electron spectra.

5.2 Introduction

HCNO, fulminic acid, was observed in interstellar space in 2009 by Marcelino *et al.*.[1] Since then it has been detected in numerous objects, like molecular clouds, protostars, the low-mass star-forming region L1527 and many more.[2–4] Fulminic acid is part of the CHON tetrad of isomers, which also include cyanic acid, HOCN, isofulminic acid, HONC and isocyanic acid, HNCO.[5–7] The spectroscopy of these molecules is to a large part motivated by their composition of the four basic elements essential to organic life, which make up over 99% of the biomass on earth.[8] Therefore, these species are assumed to play a role as precursors to prebiotic molecules in space.[9–12]

Interstellar X-ray radiation can be emitted by several different sources, such as binary stars[13] and galaxy clusters[14,15] or even our own sun.[16] In addition, so called supersoft X-ray sources with effective blackbody temperatures of 20 to 100 eV are an important class of bright X-ray sources.[17,18] As of 2005, more than a 100 such sources could be identified in external galaxies, the Magellanic Clouds and our own galaxy.[19] The light from these sources can induce ionization and possibly dissociation. Identification of the possible fragments may be of interest for astrochemical models. Previously, we recorded the normal and resonant (RAES) Auger electron spectra of fulminic acid and analyzed them using high-level calculations (Chapter 4 of this thesis).[20] We also reported the dissociative photoionization of HCNO upon interaction with photons up to 15 eV and recorded a vibrationally resolved photoelectron spectrum up to 22 eV binding energy (Chapter 3 of this thesis).[21] HCNO has also been investigated previously using IR-spectroscopy[22–26], rotational spectroscopy[26,27] and photoelectron spectroscopy.[28,29] More recently, the reaction kinetics with OH[30], CN[31,32], NCO[33] and O[34] and the photodissociation of HCNO at 248 nm and 193 nm were investigated.[35,36] In the present paper we elucidate the fragmentation of HCNO following core excitation or ionization via soft X-ray radiation. The work will be contrasted with prior work on the most stable isomer isocyanic acid, HNCO. A higher degree of site-selectivity was observed here for HCNO with, for example, a higher preponderance of N-H bond fission with N 1s ionization than for O 1s ionization. We also observed the formation of NO^+ and HCO^+, which requires rearrangement on the ionic potential energy surface after Auger decay. Computations provided conclusive mechanisms for these reactions.[37] A comparison between HNCO and HCNO will highlight the role of the site of the excitation and therefore its nearest neighbors on the X-ray induced fragmentation.

Normal Auger-Meitner processes occur after 1s ionization via soft X-ray radiation and lead to doubly charged final states, while resonant excitation of 1s electrons to unoccupied molecular orbitals (MO) leads to singly charged ions. Both cations and dications can have enough internal energy to fragment. The focus of our study is on the possible site selectivity, i.e. whether the site of the initial ionization or excitation influences the branching ratios of the various product channels.The catalog of molecules investigated for site-selectivity is still rather limited. Small molecules have been studied such as O_2,[38] O_3,[39,40] CO_2,[41] OCS,[42] H_2O,[43] H_2CO,[44], ClNO,[45], HNCO,[37] SF_6[46] as well as some organic molecules.[47–52] Halogenated organic molecules[53–61] and halogenated organosilicon compounds[62,63] have also been studied for site selective effects. Furthermore, amide bond containing molecules and small amino acids like cystein,[64] serine,[65] N-methylacetamide,[66] N-methylfluoracetamide[67] and several further amides[68,69] have been of interest.

In the ozone molecule O_3 for example Mocellin *et al.*[40] found that ionizing one of the 1s electrons of the terminal oxygens resulted in enhanced $O_2^+ + O^+$ formation compared to the ionization of the central oxygen 1s electron. The authors tentatively explained this difference by the different Auger-Meitner decay rates after the respective 1s ionizations. Similar effects could also be observed following Br or Cl ionization of CH_2BrCl.[57,58] Dissociation was enhanced at the ionization site, i.e. after Br 3d ionization Br^+ was observed preferentially, while Cl 2p ionization leads to an increase in the Cl^+ signal. The authors proposed that due to the localized nature of the Auger-Meitner process, the involved valence orbitals are preferentially those that are highly localized at the ionization site. Depopulation of these orbitals may lead to the weakening and subsequent cleavage of the surrounding bonds.[58]

5.3 Experimental and Computational Methods

The experiments were carried out at the soft X-ray beamline PLÉIADES at Synchrotron SOLEIL.[70] Fulminic acid samples were prepared via the preparative pyrolysis of 3-phenyl-4-oximino-isoxazol-5(4H)-one according to the procedure by Wentrup *et al.*.[71] A detailed description of this synthesis is provided in a previous study of HCNO.[21] The vapor of the sample, kept at −45°C, was introduced effusively into the experimental chamber. Under these conditions the sample was stable for around 6 hours. Its purity was determined by recording X-ray absorption (NEXAFS) spectra in intervals of 1-2 hours and comparing them to the literature spectra of fulminic acid[20], isocyanic acid,[72] carbon dioxide and nitrogen.[73]

An Apple II HU80 permanent magnet undulator provides the soft X-ray radiation, which is monochromatized by a 600 lines per mm grating. The light then entered the EPICEA setup,[74] which combines a double toroidal electron analyzer (DTA) and a 3D focusing ion TOF spectrometer. The DTA collects electrons that are emitted at an angle of 54.7 ±3°relative to the horizontally polarized light. Before entering the DTA the electrons are retarded to a pass energy E_p of 250 eV.

The pass energy determines both the range of energies of the detected electrons (~12% of E_p) as well as their energy resolution (~1% of E_p).[75] Typically, the center of the electron energy range was chosen to be 40 eV below the 1s ionization energy for normal Auger electrons and 20 eV below the 1s → 3π (LUMO) excitation energy for resonant Auger electrons, respectively. Electrons exiting the DTA are recorded by a position-sensitive delay-line anode detector (PSD).[76] For the relation between the distance of the electron from the center of the PSD, r, and its kinetic energy E_k the empirical formula by Liu *et al.* was used:[77]

$$E_k = E_0 + a(r - r_0) + b(1/r - 1/r_0). \tag{5.1}$$

Here, r_0 is the radial position of the electrons with kinetic energy E_0. The dispersive coefficients a and b were determined using calibration measurement of the well-known $3\mathrm{d}_{3/2}$ and $3d_{5/2}$ lines of Kr at 95.05 eV and 93.80 eV.[78] In the present case we determined a = -0.05607 and b = 8628.4 Note that since in all measurements the electron are retarded to the same pass energy E_p of 250 eV, we can use the same coefficients a and b at all three edges.

After an electron is detected, a pulsed field extracts all ions out of the interaction region towards a hexagonal delay line ion detector. The ion's position on the detector and time of flight are recorded. Ions detected in this manner are in coincidence with the electron that triggered the extraction. In order to simulate false coincidences the extraction is also triggered randomly at a rate of around 100 starts per second. The total amount of starts was held at a maximum of 250 per second to reduce false coincidences. The contribution of false coincidences was calculated and removed according to the literature,[79] additional details are provided in the appendix at the end of the chapter, Figure A5.1. Mass-selected Auger electron spectra are generated by extracting all electrons that are in coincidence with an ion in a given mass range. In order to produce Auger electron spectra in coincidence with ion pairs, signals are selected from the photoion-photoion-coincidence (PIPICO) maps.

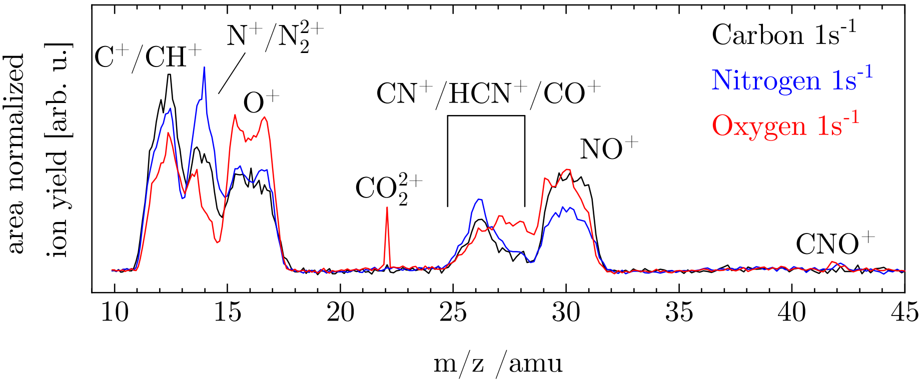

Figure 5.1: Time-of-flight mass spectra (TOF-MS) of the ions produced after 1s ionization at the three different sites. The black curve was measured after C 1s ionization and blue and red curves correspond to the ionization of N 1s and O 1s. The spectra are normalized so that the total area at all three edges is equal. The signal at $m/z = 22.0$ is due to a CO_2 contamination, while the sharp feature at $m/z = 14$ originates from residual N_2 in the chamber.

5.4 Results

5.4.1 Normal Auger-Meitner processes

Figure 5.1 shows the time-of-flight mass spectra (TOF-MS) of the ions formed after the ionization of the C, N and O 1s electrons in HCNO. The black curve corresponds to the ionization of the carbon 1s electron, while the blue and red curves represent N 1s and O 1s ionization. In all three spectra broad peaks are present, due to the high kinetic energy that is released when dications fragment into two ions. We detect a weak signal at m/z 42, the fast H^+ fragment cannot be detected due to noise created by the pulsed extraction field. The structure of m/z 42 is ambiguous and assigned to either CNO^+, or NCO^+. Note that no parent dication (m/z 21.5) signal is produced, whereas a considerable $HNCO^{2+}$ signal was observed for isocyanic acid.[37] Evidently, the fulminic acid dication is unstable and rapidly fragments before it can be detected. At m/z 30 we observe a broad signal of NO^+. Contributions by HCO^+ (m/z 29) and HNO^+ (m/z 31) can be ruled out using the photoion-photoion coincidence (PIPICO) maps (*vide* *infra*, Figure 5.2). The NO^+ signal is weakest after N1s ionization and most intense at the oxygen K-edge. At around m/z = 26 another broad signal is detected comprising the cations CN^+, HCN^+ and CO^+. The signal at m/z 22 originates from CO_2^{2+}, which is a contamination from either the synthesis or the background. CO_2 may also produce CO^+, C^+ and O^+ signals. To quantify these contributions we recorded spectra at the same photon energies using pure CO_2 which are included in the appendix (Figure A5.2). Below m/z 20 three broad peaks are observed, which correspond to the atomic ions C^+, N^+ and O^+, as well as CH^+. A sharp peak at m/z 14, is due to the stable dication N_2^{2+}, which most likely also originates from background gas. As with carbon dioxide, we recorded spectra of pure nitrogen at the relevant photon energies to correct for these contributions, shown also in Figure A5.2.

The photoion-photoion coincidence (PIPICO) maps show which ion pairs originate from the same dissociation event and may reveal signals that are obscured in the TOF-MS. Figure 5.2 shows the PIPICO maps at the three edges. These spectra consist of stripes, each corresponding to a specific product pair. The signal shape is due to the kinetic energy that is released in the fragmentation. Since the product ions are propelled in opposite directions, the time of flight of one ion will decrease while the time of flight of partner ion is increased by the same amount. In time of flight units these signals have a slope of roughly -1.[80] The maps show similar ion pairs at all three edges, but with different intensities. The most intense channels are $CH^+ + NO^+$, $C^+ + NO^+$, $O^+ + HCN^+$ and $O^+ + CN^+$. Weak signals of the ion pairs $C^+ + O^+$ and $C^+ + N^+$ are also observed. Additionally, contaminations by carbon dioxide, nitrogen and oxygen produce the signals $O^+ + CO^+$, $N^+ + N^+$ and $O^+ + O^+$. At all three edges the $CH^+ + NO^+$ pair is the dominant product. Furthermore, the PIPICO map confirms that the signal at m/z = 26 in the TOF-MS indeed contains overlapping signals of CN^+, HCN^+ and occasionally CO^+ from carbon dioxide contamination. To quantify the different intensities we calculated branching ratios by integrating the signals and dividing them by the total signal. These branching ratios are summarized in Table 5.1. The value for NCO^+ was obtained from the TOF-MS. Since contributions of ion pairs are compared, contributions from CO_2 fragmentations are easily removed. The $C^+ + O^+$ and $C^+ + N^+$ pairs were omitted due to their low signal. The CH^+

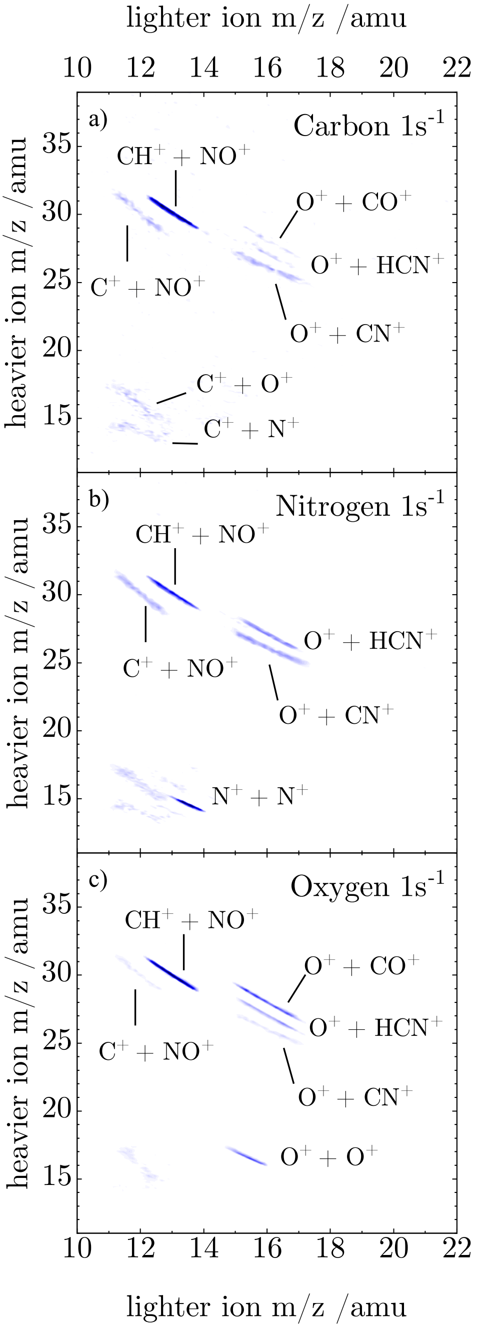

Figure 5.2: Photoion-photoion coincidence maps after a) carbon , b) nitrogen (b)) and c) oxygen 1s ionization. While the CH^+ + NO^+ channel dominates at the carbon and oxygen K-edge, the N 1s map shows intensities for the various frgamentation channels that are more evenly distributed. The ion pairs CO^+ + O^+ and N^+ + N^+ are due to contaminations from carbon dioxide and nitrogen.

Table 5.1: Summary of the branching ratios after ionization of the carbon, nitrogen and oxygen 1s electrons. The relative intensities were determined from the PIPICO maps (ion pairs) or mass spectra (single ions) and normalized so that the sum of all channels amounts to 100%. Each branching ratio is associated with an error of around ±10%.

Channel	Carbon [%]	Nitrogen [%]	Oxygen [%]
$CH^+ + NO^+$	66	37	72
$C^+ + NO^+$	12	18	6
$O^+ + HCN^+$	5	21	14
$O^+ + CN^+$	17	23	7
CNO^+/NCO^+ $(+H^+)$	Not detected	1	1

+ NO^+ pair is most abundant at all three edges, but is twice as intense at the C- and O K-edge with 66% and 72% compared to only 37% at the N K-edge. On the other hand, at the N K-edge the $O^+ + HCN^+$ and $O^+ + CN^+$ are amplified and in general the branching ratios are more evenly distributed. CNO^+/NCO^+ play only a minor role at all three edges. In general, the branching ratios after C1s and O1s ionization are similar to each other and strongly differ from the branching ratios after N1s ionization.

Mass-selected Auger electron spectra (ms-AES) may help to explain these differences and are depicted in Figure 5.3. Here we show the mass-selected AES (ms-AES) after O1s and N1s ionization. The ms-AES after C 1s ionization is shown in the appendix as it is quite similar to the ms-AES at the oxygen K-edge (Figure A5.3). The traces a) and c) show a comparison between total Auger electron spectra measured in the present work in black and a better resolved spectrum measured recently with a SCIENTA hemispherical analyzer in red.[20] Agreement between the spectra is good, differences are caused by the lower resolution and possible detection efficiency variations along the energy scale of the DTA. Trace a) shows the Auger electron spectrum after oxygen 1s ionization. Although the spectrum has been analyzed in detail,[20] we would like to reiterate the most important assignments. The signal at a binding energy of 31 eV corresponds to the $^1\Delta$ and $^1\Sigma^+$ states of the dication, which are $2\pi^{-2}$ (HOMO) two-hole states. The most intense feature of the O 1s AES is the double peak feature from 38 to 41 eV.

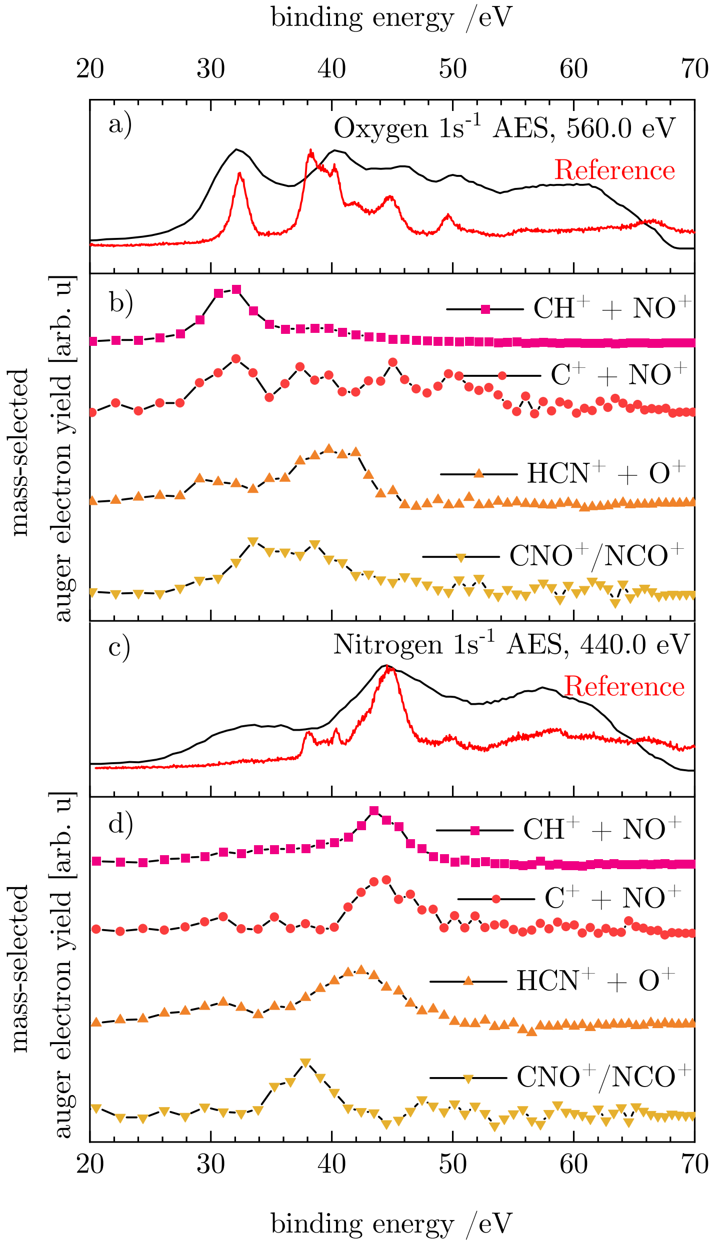

Figure 5.3: Mass-selected Auger electron spectra of all relevant ion pairs as well as CNO^+/NCO^+ at the oxygen and the nitrogen K-edge. The top traces shows in black the measured total Auger electron spectrum and in red the same spectrum measured using a SCIENTA hemispherical analyzer.[20] False coincidences in the mass-selected spectra were reduced with the literature known procedures.[79]

These final states correspond to states derived from $1\pi^{-1}2\pi^{-1}$ and $6\sigma^{-1}2\pi^{-1}$ configurations that give rise to $^1\Delta$, $^1\Sigma^+$ and $^1\Pi$ states. This double peak feature cannot be resolved in our current measurements and is slightly shifted to higher binding energies, but can still be assigned unambiguously. The high-resolution nitrogen AES (c), red) only has weak signal at 31 eV, due to a small overlap between the nitrogen 1s orbital and the 2π molecular orbital that is involved in that transition.[20] The double peak feature from 38 to 41 eV is also relatively weak. The most intense band is located at around 45 eV and correspond to a $^1\Delta$ final state with $1\pi^{-2}$ configuration. In contrast to the reference spectrum, the N 1s AES measured in this work shows significant signal between 30 and 40 eV, possibly due to the mentioned variations in the detection efficiency .

Traces b) and d) show the mass-selected Auger electron spectra of the most important fragment ion pairs $CH^+ + NO^+$, $C^+ + NO^+$ and $HCN^+ + O^+$ as well as the CNO^+/NCO^+ ions. At the oxygen K-edge (b)) the $CH^+ + NO^+$ pair is predominately formed in coincidence with Auger electrons of around 31 eV, i.e. in coincidence with $2\pi^{-2}$ two hole states. In contrast, this product channel is small at the nitrogen K-edge. In addition a smaller signal appears at 39 eV. The $C^+ + NO^+$ pair also forms at excess energies of 31 eV, but its signal stays constant up to around 50 eV and is formed in coincidence with a range of dicationic states. A small amount of $HCN^+ + O^+$ is also formed at 31 eV, but the signal maximizes at 40 eV, and falls to zero around 45 eV. It is thus coincident with the $1\pi^{-1}2\pi^{-1}$ and the $6\sigma^{-1}2\pi^{-1}$ configurations. The signal of CNO^+/NCO^+ is visibly shifted relative to the $CH^+ + NO^+$ pair with a maximum at 34 eV and significant signal up to 45 eV. At the nitrogen K-edge these spectra have significantly different appearances. $CH^+ + NO^+$ and $C^+ + NO^+$ are shifted to higher binding energies of 45 eV, while the maximum of $HCN^+ + O^+$ is at 42 eV. The CNO^+/NCO^+ signal reaches its maximum at 39 eV. Using the heats of formation tabulated in the Active Thermchemical Tables (ATcT)[81], we calculated heats of reaction $\Delta_r H(0K)$ for the processes from the neutral HCNO to these ion pairs, which are given in Table 5.2. We note that the adiabatic double ionization energy of HCNO is 32.5 eV.[20] Since four out of the five channels are below 32.5 eV, they are exergonic relative to $HCNO^{2+}$ and thus explain why no signal of the dication is apparent.

Table 5.2: $\Delta_r H(0K)$ for the reaction HCNO → Products. The values (given in eV) are based on the $\Delta_f H(0K)$ heats of formation of the fragments, as provided by the Active Thermochemical Tables (ATcT).[81]

	Products	$\Delta_r H(0K)$ /eV
	$CH^+ + NO^+$	25.2
	$C^+ + NO^+ + H$	29.3
HCNO ⟶	$O^+ + HCN^+$	29.3
	$O^+ + CN^+ + H$	35.1
	CNO^+ ($+H^+$)	29.7

The different branching ratios between the N K-edge and the other two edges are associated with the intensity distributions of the final states in the normal Auger electron spectra. The small overlap between the N 1s and the 2π MO leads to low contributions of low binding energy states to the N 1s AES spectrum. The $CH^+ + NO^+$ product is therefore less intense upon N 1s ionization. In contrast, most Auger transitions produce a parent dication with at least 8 eV relative to the adiabatic double ionization energy of 32.5 eV.[20] At this energy, the $CH^+ + NO^+$ is unstable and further fragments to C^+ and H. At the oxygen K-edge the CH^+ and NO^+ ions are predominately formed in coincidence with electrons that correspond to low binding energies, thus they remain stable and can be detected. Product formation seems to be mostly governed by the excess energy available in the Auger final state. We assume that at all edges molecules deactivate after ionization by a fast internal conversion to the dicationic ground state and fragment from there. There are, however, some observations that do not fit this thermodynamic argument. As visible in Figure 5.3, at the nitrogen K-edge a pronounced $CH^+ + NO^+$ signal appears in coincidence with Auger electrons at a $E_B \approx 43$ eV. At the oxygen K-edge, this contribution is very small. This implies the presence of a dissociative final state that is specifically populated upon N1s ionization that preferentially produces $CH^+ + NO^+$. At 42.68 eV, $^1\Delta$ and $^1\Sigma^+$ final states with an orbital occupation of $1\pi^{-1}2\pi^{-1}3\pi^1$ contribute only weakly to the AES features at the O K-edge, but significantly at the N K-edge. The 3π is an anti-bonding orbital, with nodal planes at the C-N and the N-O bond. Population of these final states might lead to the destabilization of the C-N bond and more pronounced fragmentation to CH^+ + NO^+ and C^+ + NO^+ at the N K-edge.

Comparing the branching ratios at the C K-edge and the O K-edge in more detail, some smaller differences can be seen. Adding the branching ratios of CH^+ + NO^+ and C^+ + NO^+ yields the same value of 78% at both edges. This implies that the C-N bond fission is equally likely at both edges and that the differences are due to different ratios for C-H bond fission. The C-H bond is less stable after C 1s ionization, i.e. after ionizing the atomic site close to the bond. The same trend is observed, when inspecting the O^+ + HCN^+ and O^+ + CN^+ branching ratios. This confirms that ionization at a particular site also weakens the adjacent bond, an effect that has been observed before.[58,62,66] Thus direct dissociation appears as well in HCNO.

5.4.2 Resonant Auger-Meitner processes

Excitation of a core electron to an unoccupied orbital leads to a highly excited neutral molecule, which can also relax *via* an Auger-Meitner process, producing an Auger electron and a singly charged cation.

Figure 5.4 shows the time-of-flight mass spectra following the resonant $1s \rightarrow 3\pi$ excitation at each edge. The photon energies of 286.6, 403.6 and 534.0 eV for C 1s, N 1s and O 1s excitation respectively were chosen based on the previously reported x-ray absorption spectra of HCNO.[20] A comparison with mass spectra recorded at off-resonant photon energies is given in the appendix in Figure A5.4. The most pronounced difference between the three spectra is the strong $HCNO^+$ molecular ion signal at the carbon K-edge.

Compared to the TOF-MS spectra after 1s ionization (Figure 5.1), the ions have less kinetic energy and hence the peaks are narrower after resonant excitation. At m/z 43 and 42 the parent cation $HCNO^+$ and the Δm=-1 fragment are observed. Again, the structure of the signal at m/z 42 is ambiguous. While CNO^+ is the product of a simple C-H bond cleavage, isomerization to NCO^+ has been identified at 14 eV.[21] In the region between m/z = 25 and 32 two distinct peaks are visible corresponding to m/z = 26 (CN^+) and m/z = 30 (NO^+). On the low-mass side of the NO^+ peak a shoulder is observed, which might be due to HCO^+, a fragment also formed after dissociative photoionization.[21] Generation of this fragment also requires an isomerization and has been attributed to a branched structure in previous work.[37] To show whether HCO^+ is covered by the broad NO^+ signal, we can use the coincidence information and plot TOF-MS in coincidence with resonant Auger electrons with different binding energy ranges. These spectra are shown in the appendix (see Figure A5.5). Mass peaks coincident with low binding energy Auger electrons are sharper and do not cover neighboring signals. In the spectrum corresponding to binding energies of 13.6 to 20.4 eV, HCO^+ is unambiguously observed. A signal at m/z 27, corresponding to HCN^+, is present at both the C and N K-edge, which might originate from a HCN contamination in the synthesis. However, the N1s $\rightarrow \pi^*$ (LUMO) transition of HCN lies at 399.7 eV, well below the photon energy used here.[82] In contrast, the C1s $\rightarrow \pi^*$ (LUMO) transition of HCN at 286.4 eV overlaps with the C1s $\rightarrow 3\pi$ transition of HCNO,[82] but the branching ratios for HCN^+ and CN^+ formation (Table 5.3) are smaller

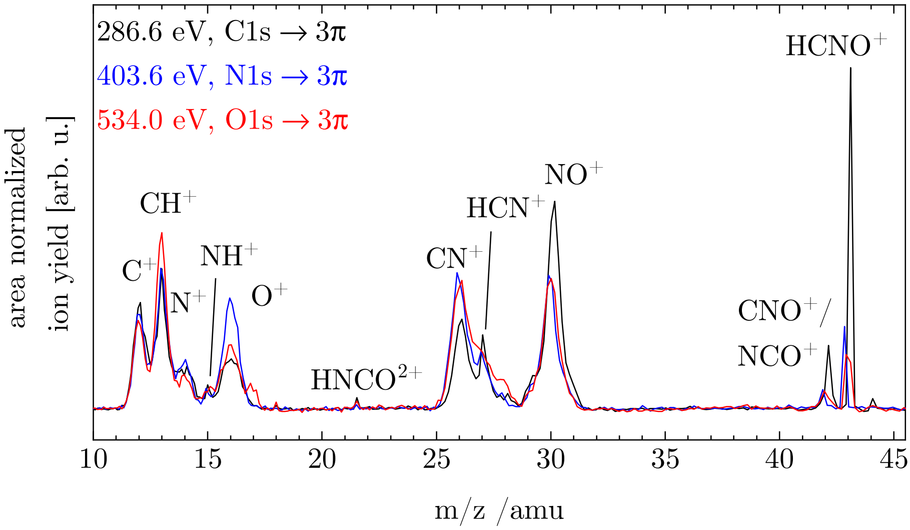

Figure 5.4: Time-of-Flight mass spectra after the resonant excitation of the carbon (black), nitrogen (blue) and oxygen (red) 1s electron into the 3π LUMO. The spectra are normalized so that the total area at all three edges is equal.

at the C K-edge and the mass-selected RAES shows no contribution of molecular HCN. Therefore we rule out signal contributions from a HCN contaminations.

At m/z = 28 small amounts of CO^+ appear. As in the NAES experiments, the contributions from N_2 and CO_2 were determined from the pure samples, as shown in Figures A5.6 to A5.8 in the appendix. The branching rations given in Table 5.3 are corrected for CO_2 and N_2 fragmentation. In the lower mass region five peaks are observed, C^+, CH^+, N^+, NH^+, and O^+. In the spectrum after O 1s excitation (red trace) small amounts of OH^+ are apparent, likely caused by residual water. However, contributions are small.

Table 5.3: Summary of the branching ratios observed after 1s → 3π excitation at the carbon, nitrogen and oxygen K-edge. The relative intensities were determined from the TOF-MS (Figure 5.4). Integrals of overlapping masses were determined by fitting Gauss functions. The branching ratios at the C and O K-edge were corrected for the contribution of carbon dioxide by using the TOF-MS of pure CO_2 shown in the appendix (Figures A5.6 to A5.8). The values are each associated with an error of around ±10%.

Channel	Carbon [%]	Nitrogen [%]	Oxygen [%]
$HCNO^+$	11	3	4
CNO^+/NCO^+	3	1	2
NO^+	27	19	21
HCO^+	3	1	1
CO^+	<1	<1	<1
HCN^+	5	8	11
CN^+	11	19	18
$HNCO^{2+}$	1	1	1
O^+	8	16	8
NH^+	<1	1	2
N^+	8	6	6
CH^+	10	15	18
C^+	12	10	9

Of note is also the small ion signal at m/z = 21.5, which corresponds to the doubly charged parent ion $HCNO^{2+}$. It is not observed after 1s ionization, therefore we want to consider reasons for its appearance upon resonant excitation. As contaminations from the HNCO isomer in the sample can be excluded based on the X-ray absorption and XPS spectra, two possible mechanisms can explain the presence of the dication in the resonant spectrum concomitant with its absence upon direct ionization. First, the resonant excitation and subsequent Auger decay might populate for example the $^3\Sigma^-$ $(2\pi^{-2})$ two-hole final state that is not allowed in a normal decay. If this dicationic state is stable towards fragmentation, this could explain the observed $HCNO^{2+}$ signal. The second possibility is a rearrangement of the $HCNO^+$ to $HNCO^+$ after the resonant Auger-Meitner process, followed by ejection of a second electron. In fact, the isomerization of $HCNO^+$ to $HNCO^+$ has been observed in the vacuum ultraviolet (VUV) and is associated with an energy reduction of 2.22 eV.[21] PIPICO maps of the resonant Auger experiments shown in the appendix (Figure A5.9) yield signals that confirm the existence of dicationic reaction channels upon resonant excitation. Mostly CH^+ + NO^+ and a smaller amount of HCN^+ + O^+ ion pairs are present. This suggests that the singly charged species formed after the resonant Auger decay eject another electron and generate $HCNO^{2+}$ which subsequently fragments.

All branching ratios are summarized in Table 5.3. Overlapping signals were disentangled by deconvoluting the peaks using Gauss functions. Contributions of CO_2 were reduced using the spectra measured of pure CO_2 (appendix, Figures A5.6 to A5.8). At all edges, NO^+ and CN^+ are most abundant, however the relative intensities vary. For example, NO^+ formation is most pronounced at the carbon K-edge. In contrast to HNCO, NO^+ formation does not require a structural rearrangement. Its strong appearance thus marks a difference in the X-ray induced chemistry of the two isomers. As noted above, $HCNO^+$ is significantly more stable upon resonant C1s excitation. Here it contributes around 11% to the total signal, while at the other two edges it contributes only about 3%. O^+ on the other hand appears particularly intense at the nitrogen K-edge.

To rationalize these differences we will again use the coincidence information to extract mass-selected resonant Auger electron spectra (Figure 5.5) at the carbon and oxygen K-edge. The results at the nitrogen K-edge are similar to those

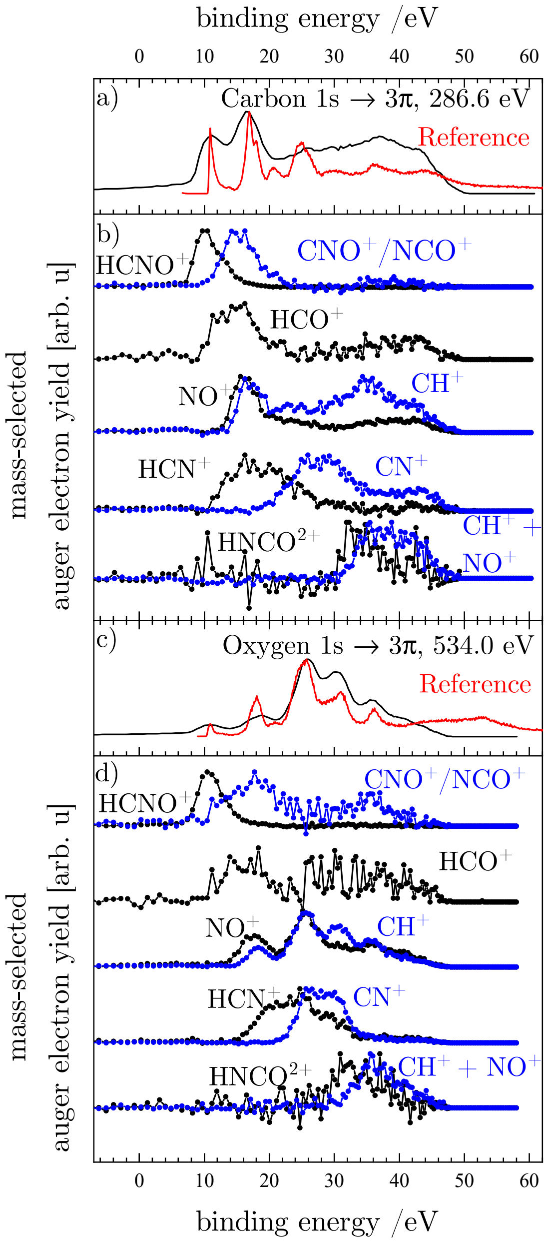

Figure 5.5: Mass-selected resonant Auger electron spectra after C1s → 3π and N1s → 3π excitation. The top trace shows a comparison of the measured spectrum (black) and a highly resolved spectrum measured with a hemispherical analyzer.[20] False coincidences were reduced using the procedures given in the literature.[79]

at the O K-edge and are therefore only shown in the appendix (Figure A5.10). The traces a) and c) show a comparison of the measured RAES with a previous reference spectrum.[20] The final states can be classified by two different categories. In a participator process, the initially excited electron participates in the Auger-Meitner decay, and a one-hole (1h) state is produced. Alternatively, in a spectator process the initially excited electron does not participate and two hole one particle (2h1p) final states are produced.

The previously reported RAES[20] in Figure 5.5 are well reproduced, although again with lower resolution. Thus the bands can be assigned based on the previous work. After C1s → 3π excitation, two broad signals are present at around 11 eV and 17 eV. The first is assigned to the $^2\Pi$ ground state of $HCNO^+$ with $(2\pi^{-1})$ occupation, formally a participator final state. An ionization energy of 10.83 eV was determined.[21,28] Only formation of $HCNO^+$ is associated with the transition into the ground state of the monocation. Two further valence excited states, a $^2\Pi$ $(1\pi^{-1})$ and $^2\Sigma^+$ $(7\sigma^{-1})$ contribute to the second band. However, we would like to emphasize that assigning single configurations to these states is a significant simplification, because they are of a multi-configuration character.[21] In addition, $^2\Phi$ and $^2\Pi$ spectator states with $2\pi^{-1}3\pi^1$ occupation contribute to this band. Two fragments are connected to the second band, CNO^+ or NCO^+ and HCO^+. According to theory,[83] as well as our previous study on the valence photoionisation,[21] the lowest energy pathway for dissociative photoionisation proceeds via fragmentation to HCO^+ + ^4N with an experimental appearance energy of 13.0 eV.[21] Indeed, HCO^+ is the fragment that appears at the lowest binding energies. Its signal is centered at roughly 14.0 eV in agreement with our study of the dissociative photoionisation of HCNO.[21] The band corresponding to m/z 42 appears at slightly higher E_B with a maximum between 14 and 15 eV. This matches the appearance energy of 13.5 eV for NCO^+ + H, but is lower than the computed limit of 16.11 eV for CNO^+ + H. Therefore we conclude that the band is due to NCO^+ rather than CNO^+. Both HCN^+ and NO^+ appear almost simultaneously with NCO^+, but extend to higher E_B. Note that a thermodynamic onset of 14.57 eV was computed for appearance of NO^+. At higher binding energies, bands become diffuse and cannot be separated anymore, so not even approximate assignments to final states are possible. CH^+ also shows a second maximum at higher energies. The CN^+ signal rises concomitantly with the decrease of HCN^+, implying that CN^+ is formed by dissociation of HCN^+. Additionally we show the signals for m/z 21.5 and for the ion pair CH^+ + NO^+. The dication signal rises sharply at around 30.0 eV and maximizes at 32 eV in agreement with the adiabatic double ionization energy of HCNO of 32.5 eV.

At the oxygen K-edge five bands can be distinguished. The two low-energy bands are assigned to the same final states as in the carbon case, but show lower intensity. The most intense band at E_B=25 eV is assigned to transitions into several spectator final states, $^2\Phi$ and $^2\Pi$, all with the occupation $1\pi^{-1}2\pi^{-1}3\pi^1$. Traces b) and d) show the resonant Auger electron spectra of selected masses. Spectra in coincidence to the atomic fragments C^+, N^+ and O^+ are shown in the appendix, Figures A5.10 and A5.11. Although some of the fragment ion bands are broader than at the carbon K-edge the difference might partially be due to the lower signal/noise ratio. However, a slight shift of the NO^+ and HCN^+ fragments to higher E_B values is observable, indicating that different final states contribute to the fragmentation. CH^+ + NO^+ also rises at slightly higher E_B relative to $HNCO^{2+}$.

Again, we propose the different probabilities to form specific final states at the three edges to cause the differences in the branching ratios . The C1s → 3π RAES spectrum (Figure 5.5 a)) has most of its intensity in the region of low binding energies up to 20 eV. In contrast, this region is relatively weak at the oxygen K-edge (Figure 5.5 c)) and most intensity lies at binding energies upwards of 20 eV. As a result fragments like CH^+ and CN^+ appear with higher intensity at the O K-edge, because they are associated with final states of higher E_B, while $HCNO^+$ and NCO^+ dominate at the C K-edge and are associated with low E_B final states of the monocation. This agrees well with the order of the heats of reaction given in Table 5.4 and the observed signals are in general consistent with $\Delta_r H(0K)$. This confirms that the fragmentation patterns depends on the excess energy and that the thermodynamic argument is valid here.

Further support is provided by the TOF-MS (Figure 5.6, red) that is obtained after exciting the C1s electron into a higher electronic state, possibly of Rydberg character.[20] The RAES after this resonant excitation at 290.3 eV is given in the appendix (Figure A5.12).[20] It has most of its intensity above 25 eV binding

Table 5.4: Enthalpies of the reaction HCNO → Products. The values (given in eV) are based on the enthalpy of formation at 0K $\Delta_f H^\circ(0K)$ of the fragments provided by the Active Thermochemical Tables (ATcT).[81] The ground state multiplicities are taken from Luna *et al.*.[83]

	Products	$\Delta_r H(0K)$ /eV
	$^1HCO^+ + ^4N$	11.68
	$^3NCO^+ + ^2H$	13.54
	$^1NO^+ + ^2CH$	14.57
HCNO →	$^2HNC^+ + ^3O$	14.79
	$^2HCN^+ + ^3O$	15.73
	$^1CH^+ + ^2NO$	15.95
	$^3CNO^+ + ^2H$	16.11
	$^3CN^+ + ^3O + ^2H$	21.5

energy and is dominated by transitions into spectator final states. In the TOF-MS, after excitation with 290.26 eV significantly less $HCNO^+$, NO^+ and HCN^+ are detected, whereas the signals of O^+ and N^+ increase. Thus more fragmentation takes place upon excitation to higher electronic states..

5.5 Conclusion

In this work, the fragmentation of fulminic acid following 1s ionization and excitation at all three edges has been analyzed. After 1s ionization we observe CNO^+/NCO^+ as well as the ion pairs $CH^+ + NO^+$, $C^+ + NO^+$, $O^+ + HCN^+$ and $O^+ + CN^+$. The parent dication $HCNO^{2+}$ is not observed. Significant site-selectivity is evident: C 1s and O 1s ionization lead primarily to $CH^+ + NO^+$, whereas N 1s ionization produces less $CH^+ + NO^+$, but more of the other three channels. This difference is due to the the small overlap between the N 1s orbital and the HOMO of HCNO, which leads to a more pronounced formation of low binding energy final states upon C 1s and O 1s ionization. These states do not possess enough internal energy to dissociate beyond the $CH^+ + NO^+$ pair. However, the dependence of the $CH^+ + NO^+$ pair on the electron binding energy at the nitrogen K-edge might be influenced by dicationic states at higher binding

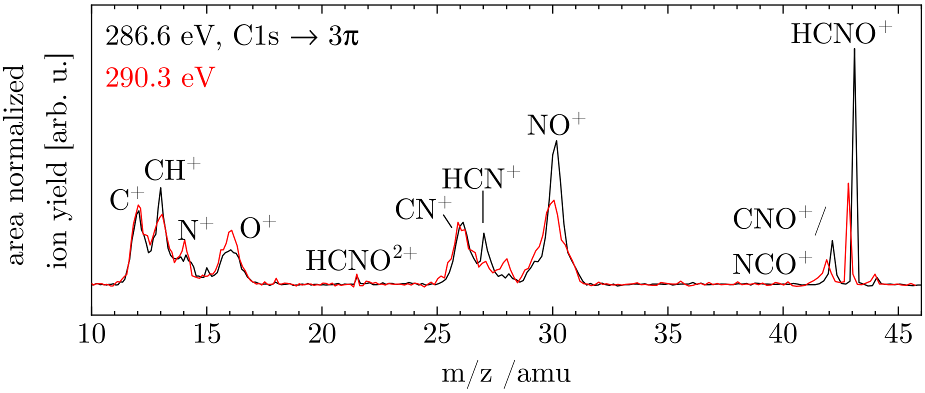

Figure 5.6: TOF-MS after the C1s excitation into to different unoccupied valence orbitals. The spectrum given as a black line corresponds to excitation into the 3π state given in Figure 5.4, while the spectrum given as a red line corresponds to excitation into a Rydberg state.[20]

energies that preferentially produce CH$^+$ + NO$^+$. We also observe slight differences between the C K-edge and the O K-edge. The second most intense ion pair is C$^+$ + NO$^+$, while O$^+$ + HCN$^+$ dominates after O1s ionization. This suggests that the bonds close to the ionized atomic center are weakened, i.e. the C-H bond and the O-N bond, thus direct dissociation is present as well. Fragmentation after resonant 1s excitation lead to a variety of ionic products. At all three edges, NO$^+$ is the most abundant product with around 20% at the N K-edge and the O K-edge and 27% at the C K-edge. We also observe a signal corresponding to the doubly charged parent ion at $m/z = 21.5$, which is absent in the non-resonant case. Its appearance can be rationalized either by the population of resonant Auger final states that are not accessed in a normal Auger process, or by an isomerization to the more stable isomer HNCO^{2+}. In the resonant case, the C 1s excitation leads to different branching ratios compared to the other two edges. In particular, the parent cation HCNO$^+$ is more stable after C 1s excitation. Again, we suggest that this is caused by the different probabilities for accessing different final states in the resonant Auger process, which leads to different internal energy distributions. Since the C1s → 3π RAES has significant contribution of final states with lower binding energy, the parent cation remains stable and can be detected. This

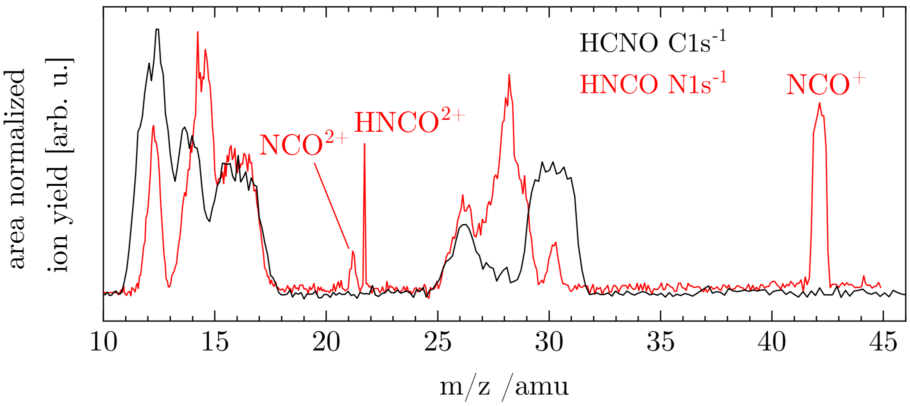

Figure 5.7: TOF-MS after ionizing the C1s electron in HCNO (black) and the N1s electron in HNCO (red), which is taken from Ref. [37].

thermodynamic picture is consistent with the products heat of reaction, which agree well with the observed mass-selected signals.

A relevant aspect of this work is a comparison of the differences and similarities in the fragmentation pattern between HCNO and the HNCO isomer investigated previously. This allows the influence of nuclear charge, nuclear site and bonding situation in the two related molecules on the fragmentation pattern to be investigated. Figure 5.7 shows a comparison of the TOF-MS after ionizing the 1s electron of the atom connected to the hydrogen, i.e. C 1s in the case of HCNO and N 1s in the case of HNCO. Thus we compare the nuclear site or bonding situation rather than the nuclear charge. Some of the observed differences between HNCO and HCNO are simply related to the atom connectivity: Whereas in HCNO fragments like NO^+ and CH^+ appear with high intensity, NH^+ and CO^+ dominate in HNCO. A major difference concerns the the parent ions and the m/z = 42 fragment, CNO^+/NCO^+. In the present work on HCNO, the normal Auger electron/photoion coincidence spectra show no parent dication $HCNO^{2+}$ and very little m/z = 42. In contrast, the HNCO experiment revealed a strong NCO^+ signal (branching ratio around 16%),a small amount of $HNCO^{2+}$ (1-3%) and even some NCO^{2+} (1-2%) in coincidence with normal Auger electrons. This is in line with the higher stability of $HNCO^{2+}$ In contrast, Figure A5.13 in the appendix compares the spectra obtained at the oxygen K-edge in coincidence with

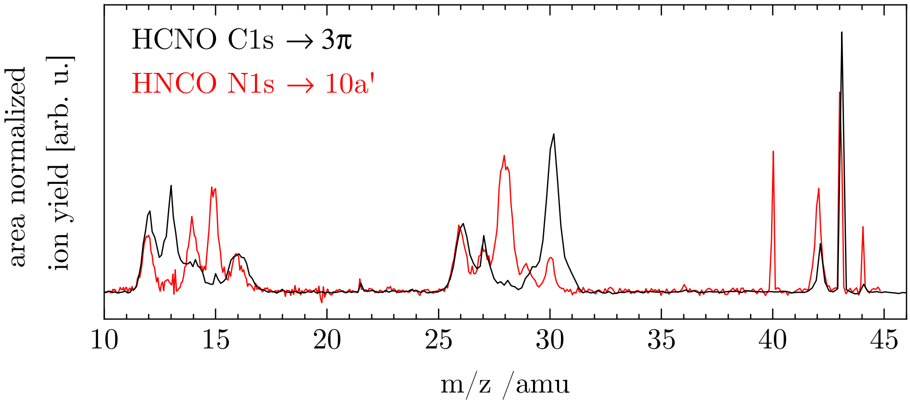

Figure 5.8: TOF-MS after C1s → 3π excitation in HCNO (black) and N 1s → 10a' excitation HNCO (red), which is taken from Ref. [37]. Note that the signal m/z 40 originates from residual Ar.

normal Auger electrons in both molecules. Here both, charge and site are equivalent. Apart from the mass signals related to the different connectivity in both molecules, a slightly larger NCO^+ signal in HNCO compared to HCNO apears to be the major difference.

Figure 5.8 shows the mass spectra recorded in coincidence with resonant Auger electrons. Note that in the nonlinear HNCO the degenerate 3π LUMO is split into a 10a' and a 3a" MO. The propensity of NO^+ and CH^+ in HCNO versus CO^+ and NH^+ in HNCO is rapidly rationalized by the different connectivities. Formation of the molecular ion hardly differs in the two molecules, branching ratios are 11 % for $HCNO^+$ and 8 % for $HNCO^+$. Thus in the case of resonant excitation, the differences between the two molecules are less pronounced than in direct ionization.

Appendix

Additional Experimental Details

Auger electron kinetic energy calibration

The Auger electron kinetic energy is determined using the empirical formula by Liu *et al.*:[77]

$$E_k = E_p + a(r - r_p) + b(1/r - 1/r_0). \tag{5.2}$$

In this equation, E_p is the pass energy and r_p is the position of those electrons with their kinetic energy equal to the pass energy. a and b are dispersive coefficients. These parameters were determined through a calibration on the $3d_{3/2}$ and $3d_{5/2}$ lines of Krypton.[78].

Treatment of false coincidences

This section provides some details about how the present spectra are corrected for false coincidences. The procedures are based on those published by Prümper and Ueda.[79]

Total time-of-flight mass spectra

The comparison of the total TOF-MS of the electron events and random events provides information on the contribution by the false coincidences. Figure A5.1 shows an example recorded after resonant O1s → 3π excitation. Here, the random events are already scaled. The scaling was determined by integrating both signals in the region of m/z = 32 to m/z = 40, since in this region no true signal can be present from the sample. Eq (2) then determines the scaling factor SC:

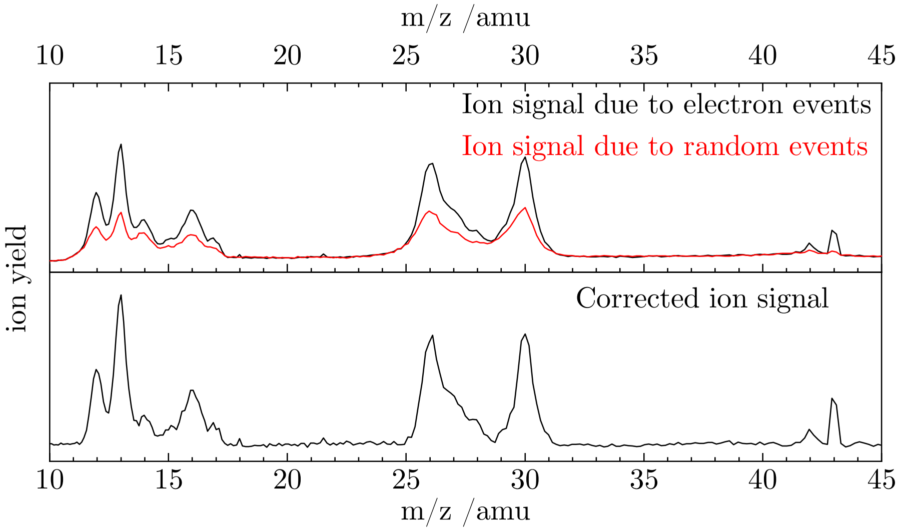

Figure A5.1: Demonstration of the false coincidence simulation using random shots. The spectra shown are after HCNO O1s → 3π excitation.

$$SC = \frac{\sum\limits_{m/z=32}^{m/z=40} Ion, et}{\sum\limits_{m/z=32}^{m/z=40} Ion, rt} \tag{5.3}$$

Here, *rt* indicates the ions detected upon a random trigger, while *et* indicates ions detected following an electron detection.

Mass-selected Auger electron spectra

The ms-AES where only one ion is selected are corrected by appropriately scaling the total Auger electron spectrum, henceforth called AES_{total}. To extract mass-selected spectra we define a tof region of interest called TOF. We quantify the contribution of the false coincidences FC by counting both the random events and the electron events in this region and computing the ratio:

$$FC,I(tof) = \frac{\sum\limits_{tof} Ion,rt \cdot SC}{\sum\limits_{tof} Ion,et} \tag{5.4}$$

This tells us the how large the contribution of the false coincidence signal is. Finally, to subtract the false coincidence background in a mass-selected spectrum, we used a scaled version of the total Auger electron spectrum. This is valid, since false coincidences are produced by the ion being in coincidence with a random electron. The statistical contribution of the Auger electrons is equal to the measured Auger electron spectrum without coincidence filtering.

To obtain the correction factor *BES,I(tof)*, the total AES is normalized to the mass-selected AES and multiplied by $FC, I(tof)$ and subtracted to yield the true Auger electron spectrum in coincidence to *tof* $TES, I(tof)$.

$$BES,I(tof) = \frac{AES_{total}}{\sum\limits_{E_{kin}=0}^{\infty} AES_{total}} \sum_{E_{kin}=0}^{\infty} [MS\text{-}AES(tof)] \cdot FC,I(tof) \tag{5.5}$$

$$TES,I(tof) = MS\text{-}AES(tof) - BES,I(tof) \tag{5.6}$$

Photoion-photoion-coincidence maps

Here, the correction is according to according to Equation 6 given by Prümper and Ueda. Occasionally the background was scaled to better fit the observed spectrum, at mots around 10% difference were found.

Ionpair-selected Auger electron spectra

The ionpair-selected spectra were corrected according to the equations 11 and 17 given in the paper by Prümper and Ueda.[79]

Additonal experimental Results

Normal Auger

Figure A5.3 shows the mass-selected normal Auger electron spectra after C1s ionization recorded at 330 eV. The spectra are similar to those recorded after O1s ionization.

To quantify the contributions of CO_2 and N_2 contaminations in our spectra, spectra of pure CO_2 and N_2 were recorded at the same photon energies, shown in Figure A5.2. Since the branching ratios determined in the main paper used the ion pair signals in the PIPICO map, these results are free from any contaminations.

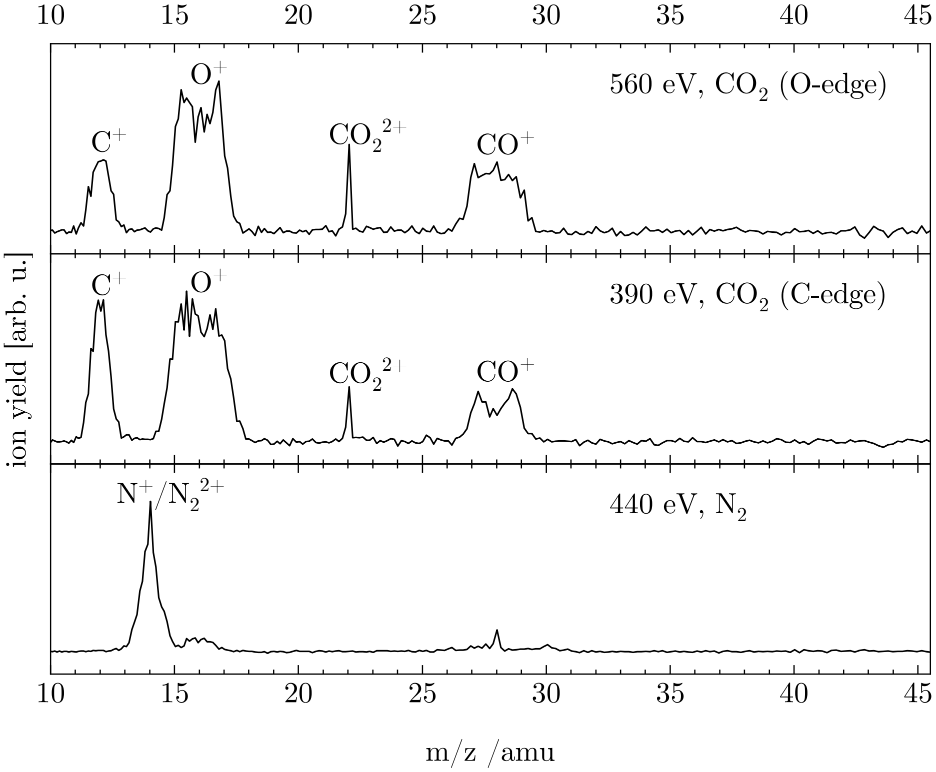

Figure A5.2: TOF-MS of CO_2 and N_2 at the photon energies employed for Fulminic Acid. The spectra were employed for background correction.

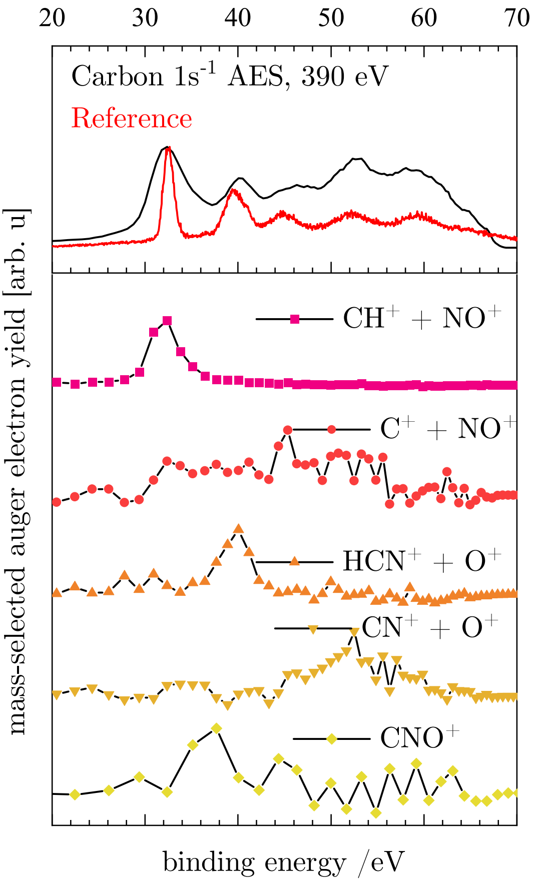

Figure A5.3: Mass-selected normal Auger electron spectra after C1s ionization. The top trace shows in black the total Auger spectrum and in red the reference spectrum from ref.[20].

Resonant Auger

Figure A5.4 depicts the comparison of TOF-MS measured at resonance with off-resonant spectra at all three edges.

Figures A5.6, A5.7, A5.8 show the TOF-MS of pure CO_2 and N_2 after resonant 1s excitation.

Figure A5.9 shows the PIPICO maps recorded after resonant 1s excitation at all three edges. Figure A5.10 shows the mass-selected RAES recorded after N1s $\rightarrow 3\pi$ excitation, while Figure A5.11 shows the mass-selected RAES of the atomic fragments after O1s and C1s excitation.

Figure A5.12 depicts a comparison of the recorded RAES and the previously reported spectra of two C1s excitations.

Figure A5.13 compares the TOF-MS recorded after O1s ionization of fulminic acid and isocyanic acid.[37]

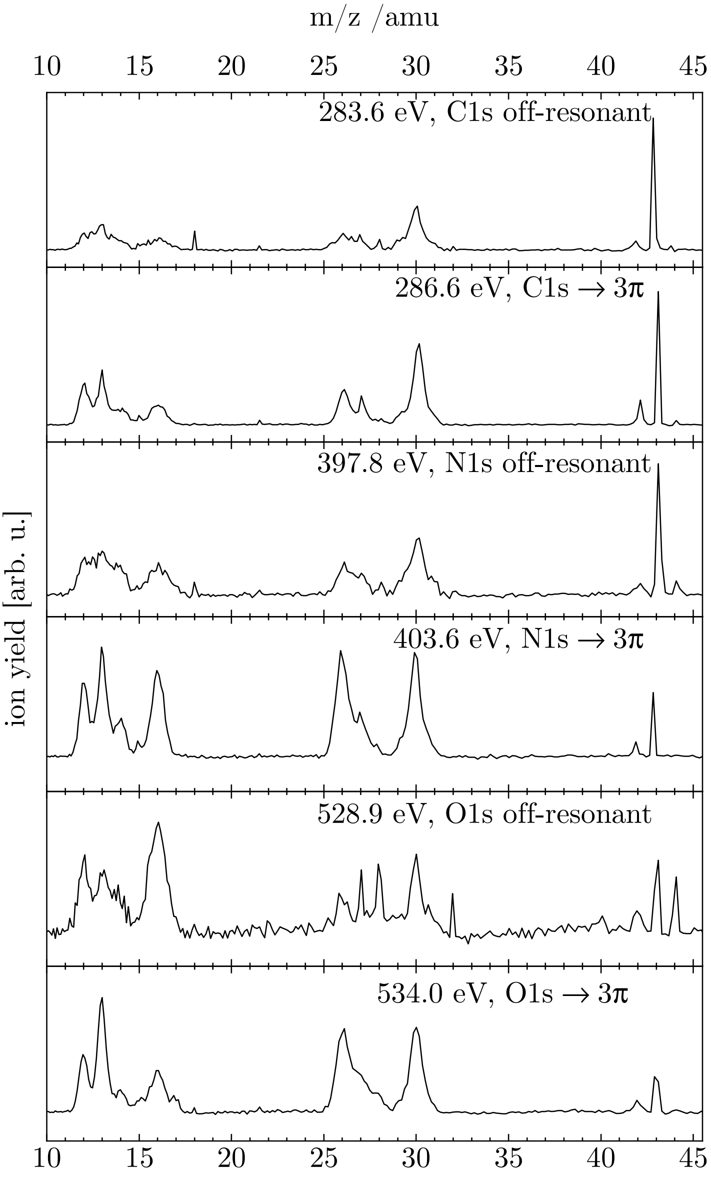

Figure A5.4: Comparison of the TOF-MS after resonant 1s excitation to the off-resonant spectra.

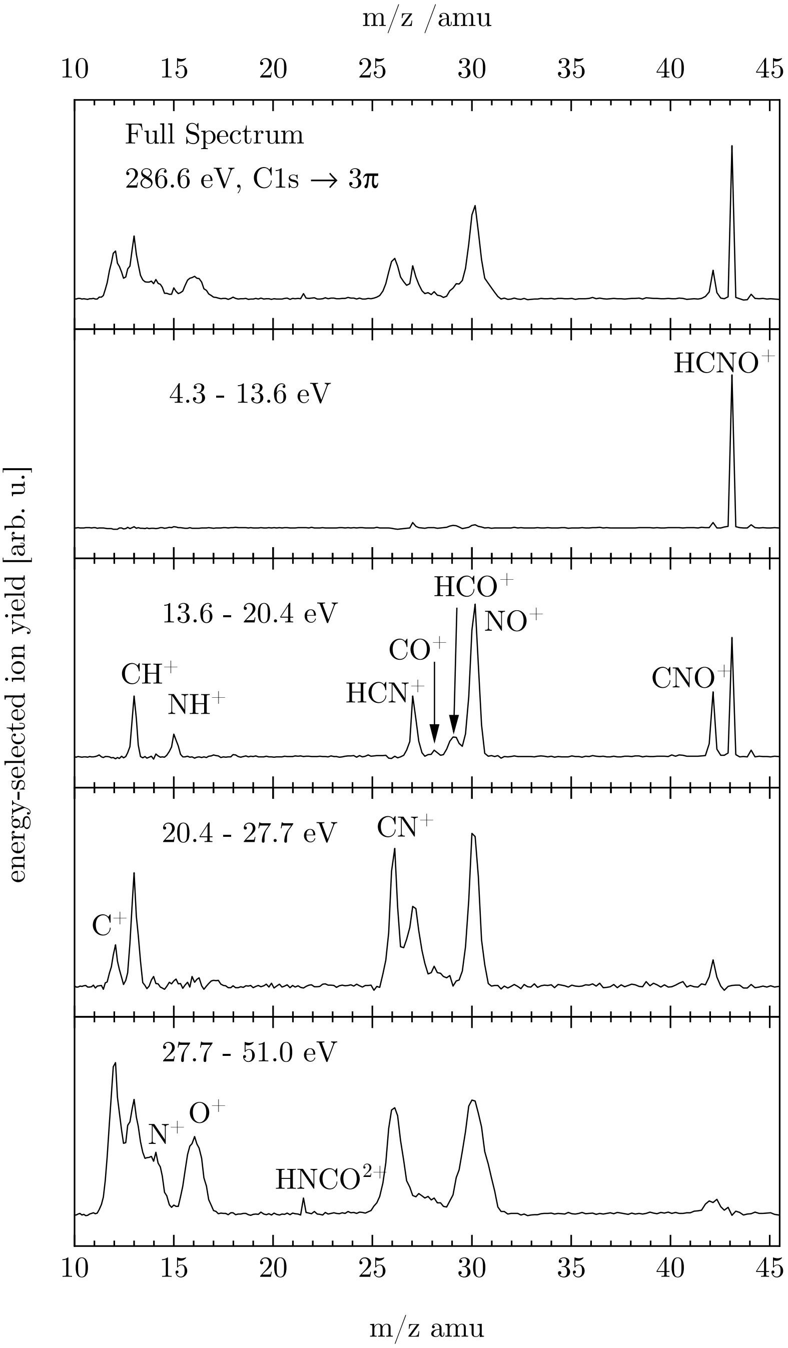

Figure A5.5: Energy-selected TOF-MS after resonant C1s excitation. The top trace shows the total spectrum, while the other spectra are in coincidence with the indicated energy range.

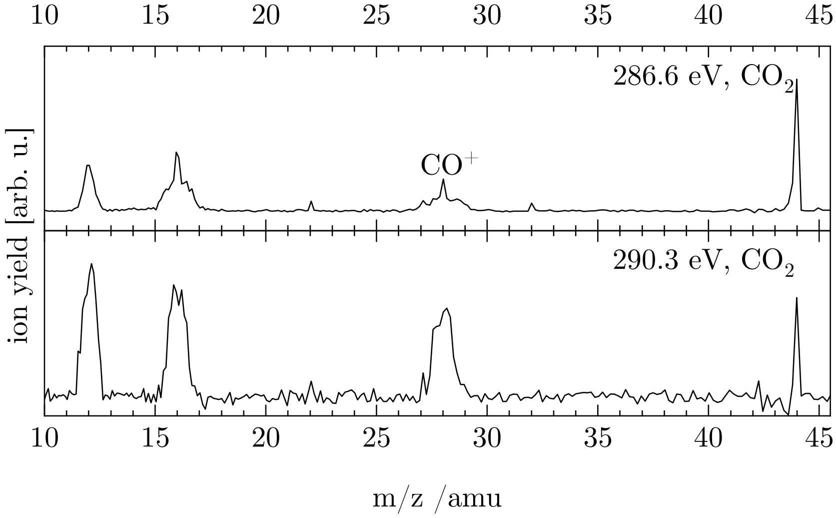

Figure A5.6: Measurements of pure CO_2 at photon energies used to resonantly excite the C1s electron of Fulminic Acid.

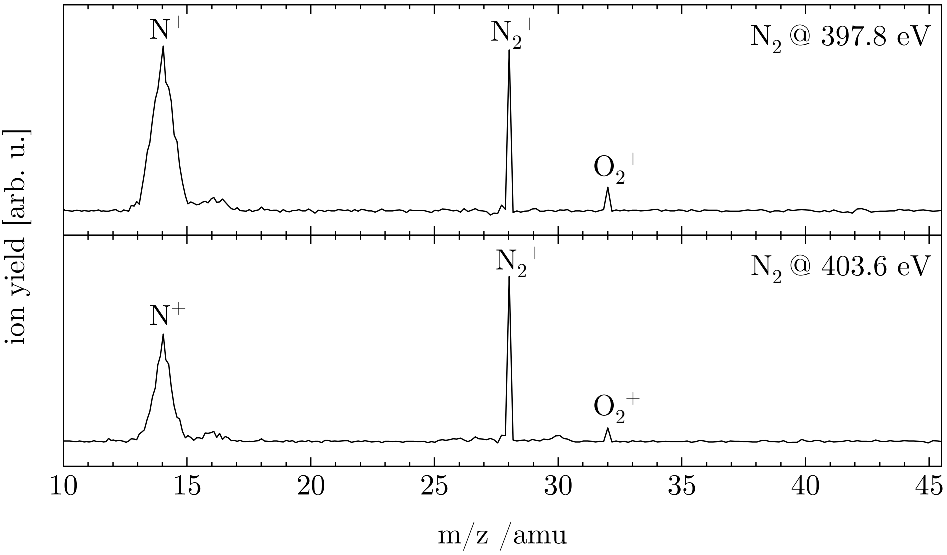

Figure A5.7: Measurements of pure N_2 at photon energies that were used to resonantly excite the N1s electron of Fulminic Acid.

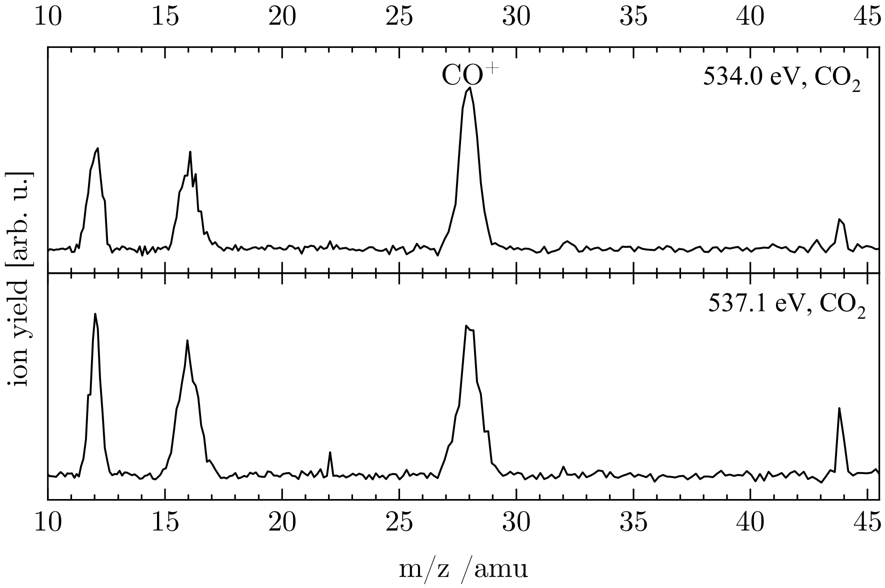

Figure A5.8: Measurements of pure CO_2 at photon energies that were used to resonantly excite the O1s electron of Fulminic Acid.

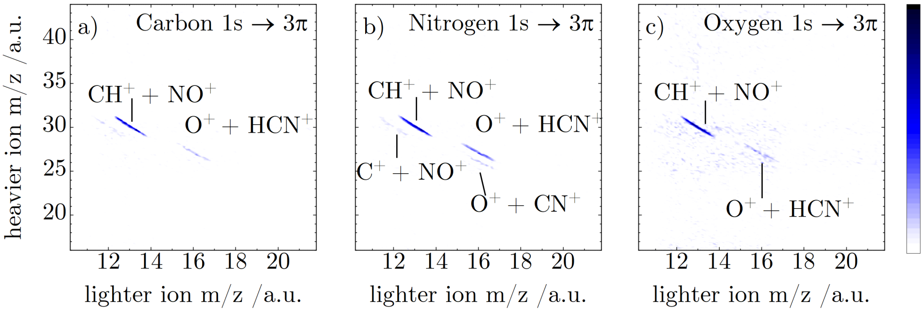

Figure A5.9: PIPICO maps measured after resonant 1s excitation at all three edges.

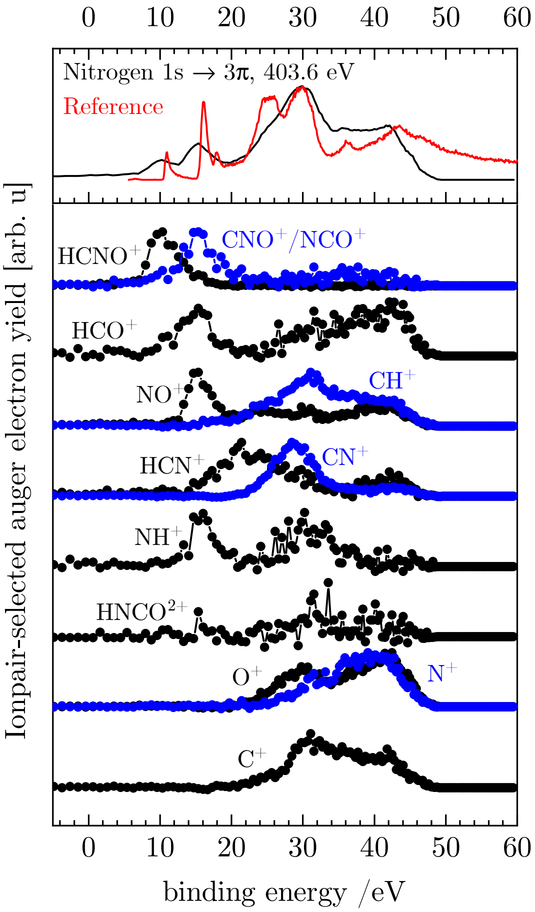

Figure A5.10: Mass-selected resonant auger electron spectra after N1s → 3π excitation. The top trace shows a comparison between the measured total RAES (black) and the reference spectrum from the literature.[20]

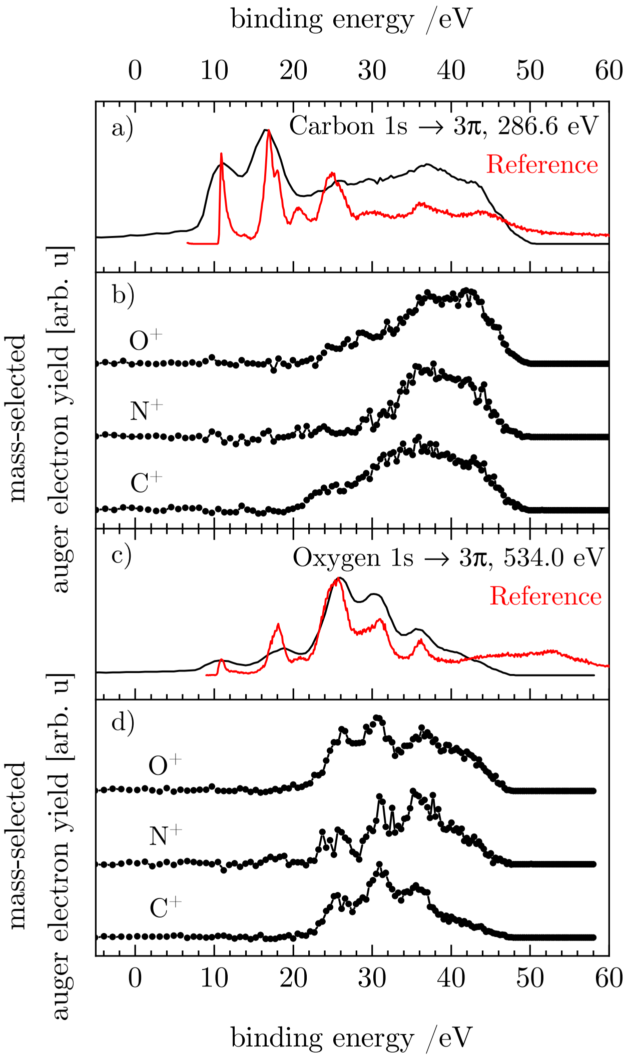

Figure A5.11: Mass-selected of the atomic fragments resonant auger electron spectra after C1s and O1s → 3π excitation. The top trace shows a comparison between the measured total RAES (black) and the reference spectrum from the literature.[20]

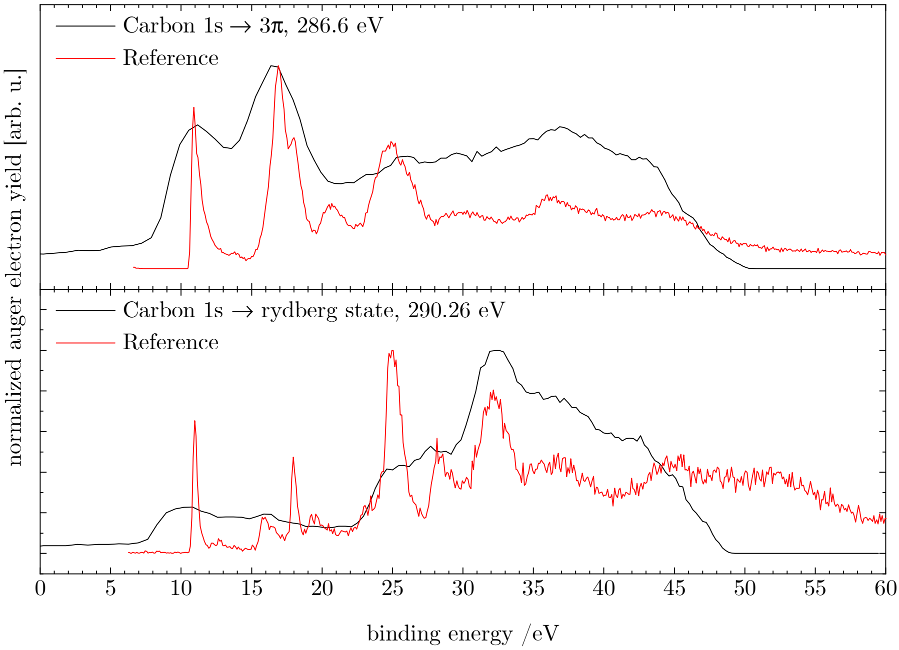

Figure A5.12: Comparison of the C1s RAES measured at 286.6 and 290.26 eV. The black curves are the spectra measured in this work and the red curves were measured using a hemispherical analyzer.[20]

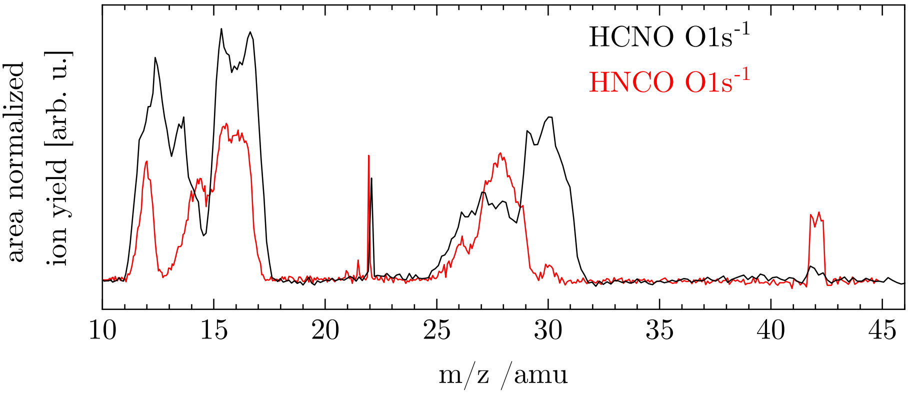

Figure A5.13: TOF-MS after ionizing the O 1s electron in HCNO (black) and HNCO (red), which is taken from Ref. [37].

References

[1] N. Marcelino, J. Cernicharo, B. Tercero, E. Roueff, *Astrophys. J.* **2009**, *690*, L27–L30.

[2] E. Mendoza, B. Lefloch, A. López-Sepulcre, C. Ceccarelli, C. Codella, H. M. Boechat-Roberty, R. Bachiller, *Mon. Not. R. Astron. Soc.* **2014**, *445*, 151–161.

[3] B. Lefloch, R. Bachiller, C. Ceccarelli, J. Cernicharo, C. Codella, A. Fuente, C. Kahane, A. López-Sepulcre, M. Tafalla, C. Vastel, E. Caux, M. González-García, E. Bianchi, A. Gómez-Ruiz, J. Holdship, E. Mendoza, J. Ospina-Zamudio, L. Podio, D. Quénard, E. Roueff, N. Sakai, S. Viti, S. Yamamoto, K. Yoshida, C. Favre, T. Monfredini, H. M. Quitián-Lara, N. Marcelino, H. M. Boechat-Roberty, S. Cabrit, *Mon. Not. R. Astron Soc.* **2018**, *477*, 4792–4809.

[4] N. Marcelino, M. Agúndez, J. Cernicharo, E. Roueff, M. Tafalla, *Astron. Astrophys.* **2018**, *612*, L10.

[5] N. Marcelino, S. Brünken, J. Cernicharo, D. Quan, E. Roueff, E. Herbst, P. Thaddeus, *Astron. Astrophys.* **2010**, *516*, A105.

[6] J. H. Teles, G. Maier, B. Andes Hess Jr, L. J. Schaad, M. Winnewisser, B. P. Winnewisser, *Chem. Ber.* **1989**, *122*, 753–766.

[7] M. Mladenović, M. Lewerenz, *Chem. Phys.* **2008**, *343*, 129–140.

[8] S. V. Vassilev, D. Baxter, L. K. Andersen, C. G. Vassileva, *Fuel* **2010**, *89*, 913–933.

[9] M. Ferus, V. Laitl, A. Knizek, P. Kubelík, J. Sponer, J. Kára, J. E. Sponer, B. Lefloch, G. Cassone, S. Civiš, *Astron. Astrophys.* **2018**, *616*, A150.

[10] M. Ferus, R. Michalčíková, V. Shestivská, J. Šponer, J. E. Šponer, S. Civiš, *J. Phys. Chem. A* **2014**, *118*, 719–736.

[11] J. A. Sebree, M. C. Roach, E. R. Shipley, C. He, S. M. Hörst, *Astrophys. J.* **2018**, *865*, 133.

[12] P. Gorai, B. Bhat, M. Sil, S. K. Mondal, R. Ghosh, S. K. Chakrabarti, A. Das, *Astrophys. J.* **2020**, *895*, 86.

[13] C. Tan, *J. Phys.: Conf. Ser.* **2021**, *2012*, 012119.

[14] W. Tucker, P. Blanco, S. Rappoport, L. David, D. Fabricant, E. E. Falco, W. Forman, A. Dressler, M. Ramella, *Astrophys. J.* **1998**, *496*, L5.

[15] D. Clowe, M. Bradač, A. H. Gonzalez, M. Markevitch, S. W. Randall, C. Jones, D. Zaritsky, *Astrophys. J.* **2006**, *648*, L109.

[16] P. Morrison, *Annu. Rev. Astron. Astrophys.* **1967**, *5*, 325–350.

[17] J. Trümper, G. Hasinger, B. Aschenbach, H. Bräuninger, U. G. Briel, W. Burkert, H. Fink, E. Pfeffermann, W. Pietsch, P. Predehl, J. H. M. M. Schmitt, W. Voges, U. Zimmermann, K. Beuermann, *Nature* **1991**, *349*, 579–583.

[18] P. Kahabka, E. P. J. van den Heuvel, *Annu. Rev. Astron. Astrophys.* **1997**, *35*, 69–100.

[19] P. Kahabka, *Adv. Space Res.* **2006**, *38*, 2836–2839.

[20] M. Gerlach, T. Preitschopf, E. Karaev, H. M. Quitián-Lara, D. Mayer, J. Bozek, I. Fischer, R. F. Fink, *Phys. Chem. Chem. Phys.* **2022**, *24*, 15217–15229.

[21] M. Gerlach, B. Mant, T. Preitschopf, E. Karaev, D. Mayer, H. M. Quitián-Lara, P. Hemberger, J. Bozek, G. Worth, I. Fischer, *J. Chem. Phys.* **2023**, *158*, 134303.

[22] W. Beck, K. Feldl, *Angew. Chem.* **1966**, *78*, 746–746.

[23] B. P. Winnewisser, M. Winnewisser, *J. Mol. Spectrosc.* **1969**, *29*, 505–507.

[24] W. Beck, P. Swoboda, K. Feldl, R. S. Tobias, *Chem. Ber.* **1971**, *104*, 533–543.

[25] B. P. Winnewisser, P. Jensen, *J. Mol. Spectrosc.* **1983**, *101*, 408–421.

[26] B. P. Winnewisser, M. Winnewisser, G. Wagner, J. Preusser, *J. Mol. Spectrosc.* **1990**, *142*, 29–56.

[27] M. Winnewisser, H. K. Bodenseh, *Z. Naturforsch. A* **1967**, *22*, 1724.

[28] J. Bastide, J. P. Maier, *Chem. Phys.* **1976**, *12*, 177–190.

[29] T. Pasinszki, N. Kishimoto, K. Ohno, *J. Phys. Chem. A* **1999**, *103*, 6746–6756.

[30] W. Feng, J. P. Meyer, J. F. Hershberger, *J. Phys. Chem. A* **2006**, *110*, 4458–4464.

[31] W. Feng, J. F. Hershberger, *J. Phys. Chem. A* **2006**, *110*, 12184–12190.

[32] W. Feng, J. F. Hershberger, *J. Phys. Chem. A* **2012**, *116*, 10285–10292.

[33] W. Feng, J. F. Hershberger, *J. Phys. Chem. A* **2007**, *111*, 3831–3835.

[34] W. Feng, J. F. Hershberger, *J. Phys. Chem. A* **2007**, *111*, 10654–10659.

[35] W. Feng, J. F. Hershberger, *J. Phys. Chem. A* **2014**, *118*, 829–837.

[36] W. Feng, J. F. Hershberger, *Chem. Phys.* **2016**, *472*, 18–23.

[37] M. Gerlach, F. Fantuzzi, L. Wohlfart, K. Kopp, B. Engels, J. Bozek, C. Nicolas, D. Mayer, M. Gühr, F. Holzmeier, I. Fischer, *J. Chem. Phys.* **2021**, *154*, 114302.

[38] X.-J. Liu, C. Nicolas, M. Patanen, C. Miron, *Sci. Rep.* **2017**, *7*, 2898.

[39] A. Naves de Brito, S. Sundin, R. Marinho, I. Hjelte, G. Fraguas, T. Gejo, N. Kosugi, S. Sorensen, O. Björneholm, *Chem. Phys. Lett.* **2000**, *328*, 177–187.

[40] A. Mocellin, K. Wiesner, S. L. Sorensen, C. Miron, K. L. Guen, D. Céolin, M. Simon, P. Morin, A. B. Machado, O. Björneholm, A. N. de Brito, *Chem. Phys. Lett.* **2007**, *435*, 214–218.

[41] P. Morin, M. Simon, C. Miron, N. Leclercq, E. Kukk, J. D. Bozek, N. Berrah, *Phys. Rev. A* **2000**, *61*, 050701.

[42] P. Erman, A. Karawajczyk, E. Rachlew, M. Stankiewicz, K. Y. Franzén, *J. Chem. Phys.* **1997**, *107*, 10827–10828.

[43] A. Naves de Brito, R. Feifel, A. Mocellin, A. B. Machado, S. Sundin, I. Hjelte, S. L. Sorensen, O. Björneholm, *Chem. Phys. Lett.* **1999**, *309*, 377–385.

[44] H. M. Boechat-Roberty, S. Pilling, A. C. F. Santos, *Astron. Astrophys.* **2005**, *438*, 915–922.

[45] P. Salen, L. Schio, R. Richter, M. Alagia, S. Stranges, V. Zhaunerchyk, *J. Chem. Phys.* **2018**, *149*, 164305.

[46] G. Prümper, Y. Tamenori, A. De Fanis, U. Hergenhahn, M. Kitajima, M. Hoshino, H. Tanaka, K. Ueda, *J. Phys. B At. Mol. Opt. Phys.* **2005**, *38*, 1.

[47] J. Eland, P. Linusson, M. Mucke, R. Feifel, *Chem. Phys. Lett.* **2012**, *548*, 90–94.

[48] H. M. Boechat-Roberty, R. Neves, S. Pilling, A. F. Lago, G. G. B. De Souza, *Mon. Not. R. Astron. Soc.* **2009**, *394*, 810–817.

[49] R. B. Bernini, L. H. Coutinho, C. V. Nunez, R. B. de Castilho, G. G. B. de Souza, *J. Electron Spectrosc. Relat. Phenom.* **2015**, *202*, 107–111.

[50] E. Kukk, D. T. Ha, Y. Wang, D. G. Piekarski, S. Diaz-Tendero, K. Kooser, E. Itälä, H. Levola, M. Alcamí, E. Rachlew, F. Martín, *Phys. Rev. A* **2015**, *91*, 043417.

[51] S. Zagorodskikh, J. H. D. Eland, V. Zhaunerchyk, M. Mucke, R. J. Squibb, P. Linusson, R. Feifel, *J. Chem. Phys.* **2016**, *145*, 124302.

[52] F. Fantuzzi, S. Pilling, A. C. F. Santos, L. Baptista, A. B. Rocha, H. M. Boechat-Roberty, *Mon. Not. R. Astron. Soc.* **2011**, *417*, 2631–2641.

[53] H. C. Schmelz, C. Reynaud, M. Simon, I. Nenner, *J. Chem. Phys.* **1994**, 3742–3749.

[54] L. Inhester, B. Oostenrijk, M. Patanen, E. Kokkonen, S. H. Southworth, C. H. Bostedt, O. Travnikova, T. Marchenko, S.-K. Son, R. Santra, M. Simon, L. Young, S. L. Sorensen, *J. Phys. Chem. Lett.* **2018**, *9*, 1156–1163.

[55] H. Fukuzawa, G. Prümper, X. Liu, E. Kukk, R. Sankari, M. Hoshino, H. Tanaka, Y. Tamenori, K. Ueda, *Chem. Phys. Lett.* **2007**, *436*, 51–56.

[56] X. J. Liu, G. Prümper, E. Kukk, R. Sankari, M. Hoshino, C. Makochekanwa, M. Kitajima, H. Tanaka, H. Yoshida, Y. Tamenori, K. Ueda, *Phys. Rev. A* **2005**, *72*, 042704.

[57] K. Le Guen, M. Ahmad, D. Céolin, P. Lablanquie, C. Miron, F. Penent, P. Morin, M. Simon, *J. Chem. Phys.* **2005**, *123*, 084302.

[58] C. Miron, M. Simon, N. Leclercq, D. L. Hansen, P. Morin, *Phys. Rev. Lett.* **1998**, *81*, 4104–4107.

[59] H. Levola, E. Itälä, K. Schlesier, K. Kooser, S. Laine, J. Laksman, D. T. Ha, E. Rachlew, M. Tarkanovskaja, K. Tanzer, E. Kukk, *Phys. Rev. A* **2015**, *92*, 063409.

[60] P. Bolognesi, J. A. Kettunen, A. Cartoni, R. Richter, S. Tosic, S. Maclot, P. Rousseau, R. Delaunay, L. Avaldi, *Phys. Chem. Chem. Phys.* **2015**, *17*, 24063–24069.

[61] E. Itälä, D. Ha, K. Kooser, M. Huels, E. Rachlew, E. Nõmmiste, U. Joost, E. Kukk, *J. Electron Spectros. Relat. Phenomena* **2011**, *184*, 119–124.

[62] S. Nagaoka, G. Prümper, H. Fukuzawa, M. Hino, M. Takemoto, Y. Tamenori, J. Harries, I. H. Suzuki, O. Takahashi, K. Okada, K. Tabayashi, X.-J. Liu, T. Lischke, K. Ueda, *Phys. Rev. A* **2007**, *75*, 020502.

[63] S.-i. Nagaoka, H. Fukuzawa, G. Prümper, M. Takemoto, O. Takahashi, K. Yamaguchi, T. Kakiuchi, K. Tabayashi, I. H. Suzuki, J. R. Harries, Y. Tamenori, K. Ueda, *J. Phys. Chem. A* **2011**, *115*, 8822–8831.

[64] J. Laksman, K. Kooser, H. Levola, E. Itälä, D. T. Ha, E. Rachlew, E. Kukk, *J. Phys. Chem. B* **2014**, *118*, 11688–11695.

[65] E. Itälä, H. Levola, D. T. Ha, K. Kooser, E. Rachlew, E. Kukk, *J. Phys. Chem. A* **2016**, *120*, 5419–5426.

[66] Y.-S. Lin, C.-C. Tsai, H.-R. Lin, T.-L. Hsieh, J.-L. Chen, W.-P. Hu, C.-K. Ni, C.-L. Liu, *J. Phys. Chem. A* **2015**, *119*, 6195–6202.

[67] P. Salén, L. Schio, R. Richter, M. Alagia, S. Stranges, V. Zhaunerchyk, *Phys. Rev. A* **2020**, *102*, 032817.

[68] P. Salen, V. Yatsyna, L. Schio, R. Feifel, R. Richter, M. Alagia, S. Stranges, V. Zhaunerchyk, *J. Chem. Phys.* **2016**, *144*.

[69] Y.-J. Chiang, W.-C. Huang, C.-K. Ni, C.-L. Liu, C.-C. Tsai, W.-P. Hu, *AIP Adv.* **2019**, *9*, 085023.

[70] Pleiades, `https://www.synchrotron-soleil.fr/fr/lignes-de-lumiere/pleiades` (visited on 09/16/2019, 15:43).

[71] C. Wentrup, B. Gerecht, H. Briehl, *Angew. Chem. Int. Ed.* **1979**, *18*, 467–468.

[72] F. Holzmeier, T. J. A. Wolf, C. Gienger, I. Wagner, J. Bozek, S. Nandi, C. Nicolas, I. Fischer, M. Gühr, R. F. Fink, *J. Chem. Phys.* **2018**, *149*, 034308.

[73] W. E. Moddeman, T. A. Carlson, M. O. Krause, B. P. Pullen, W. E. Bull, G. K. Schweitzer, *J. Chem. Phys.* **1971**, *55*, 2317–2336.

[74] X.-J. Liu, C. Nicolas, E. Robert, C. Miron, *J. Phys. Conf. Ser.* **2014**, *488*, 142005.

[75] K. Le Guen, D. Céolin, R. Guillemin, C. Miron, N. Leclercq, M. Bougeard, M. Simon, P. Morin, A. Mocellin, F. Burmeister, A. Naves de Brito, S. L. Sorensen, *Rev. Sci. Instrum.* **2002**, *73*, 3885–3894.

[76] C. Miron, M. Simon, N. Leclercq, P. Morin, *Rev. Sci. Instrum.* **1997**, *68*, 3728–3737.

[77] X.-J. Liu, C. Nicolas, C. Miron, *Rev. Sci. Instrum.* **2013**, *84*, 033105.

[78] G. Johansson, J. Hedman, A. Berndtsson, M. Klasson, R. Nilsson, *J. Electron Spectrosc. Relat. Phenom.* **1973**, *2*, 295–317.

[79] G. Prümper, K. Ueda, *Nucl. Instrum. Meth. A* **2007**, *574*, 350–362.

[80] J. H. D. Eland, *Laser Chem.* **1991**, *11*, 259–263.

[81] B. Ruscic, D. H. Bross, Active Thermochemical Tables (ATcT) values based on ver. 1.122r of the Thermochemical Network (2021); available at ATcT.anl.gov.

[82] A. P. Hitchcock, C. E. Brion, *Chem. Phys.* **1979**, *37*, 319–331.

[83] A. Luna, A. M. Mebel, K. Morokuma, *J. Chem. Phys.* **1996**, *105*, 3187–3205.

CHAPTER 6

Summary and Outlook

Since its discovery in 1800 by Edward Howard,[1] fulminic acid, HCNO, was used by chemists as a model molecule to elucidate a variety of chemical questions. Based on experiments conducted on HCNO and isocyanic acid, HNCO, and their salts, Berzelius proposed the idea of isomerism, i.e. that chemical properties are not just based on the elemental composition, but also on their chemical structure.[2] Linus Pauling conducted theoretical calculations to aid in the determination of the molecular structure[3] and Beck and Feldl used infrared spectroscopy to provide the final proof for the structure.[4] In this thesis, we wanted to examine the complex processes, that occur due to the interaction with VUV- and soft X-ray radiation. Also, the data obtained by these measurements can help to explain the fate of fulminic acid in interstellar space.

The first challenge of this thesis was to find a reliable and safe synthetic route for fulminic acid, HCNO, in order to conduct experiments at different synchrotron radiation facilities. Fulminic acid was then investigated using photoelectron spectroscopy, Auger electron spectroscopy as well as electron-ion-coincidence techniques. The small size of HCNO enables high-level computations and detailed analysis. This analysis may improve the understanding of the underlying processes, such as for example the Auger-Meitner process.

Chapter 3 of this thesis presents the photoelectron spectroscopy and dissociative photoionization of fulminic acid. We recorded photoelectron spectra, which were better resolved than the previous spectrum by Bastide *et al.*.[5] We observed four bands, three of which showed well resolved vibrational structure. Wavepacket dynamics simulations were conducted of the Renner-Teller split cationic ground state. Using these calculations, Renner-Teller parameters of 0.48 for the HCN bending mode and 0.41 for the CNO bending mode were computed, indicating an intermediate coupling strength. The simulations also provided tentative assignment of the vibrations of the cationic ground state. We also examined the dissociative photoionization of HCNO. Up to 15.3 eV four fragmentation products, HCO^+, NCO^+, NO^+ and NH^+ are formed. For the fragments HCO^+ and NCO^+ we modeled the dissociation rates and confirmed the mechanisms calculated in the literature.[6] The mechanism to form HCO^+ proceeds *via* a switch from the doublet to the quartet potential energy surface. The formation of NCO^+ requires first the isomerization to the isocyanic acid cation $HNCO^+$ with a barrier of 2.7 eV. Since the cations can be precursors for the neutral molecule,[7] this isomerization mechanism may be important in their interstellar chemistry. This could help to explain the relative abundance of the CHNO isomers in interstellar space, which is so far not well understood.[8,9]

Chapter 4 covers the Auger electron spectroscopy of fulminic acid. 1s ionization and excitation and the subsequent Auger-Meitner processes at all atomic sites in the molecule were measured. Through X-ray photoelectron spectroscopy we determined the carbon, nitrogen, and oxygen 1s ionization energies of 292.9 eV, 410.5 eV and 539.6 eV. The normal Auger electron spectra were then recorded and an adiabatic double ionization energy of 32.5 eV was found. Simulations based on the one-center approximation agreed very well with the experiment and provided an intuitive interpretation of the intensity differences between the three edges. We found that the intensity of a transition is proportional to the contribution of the atomic orbitals to the valence orbitals, which explained the low intensity of the $2\pi^{-2}$ final states at the N-edge. The 2π orbital of HCNO exhibits a nodal plane at the nitrogen atom leading to a small overlap of this orbital and the N1s orbital. This results in a low transition probability compared to the other two edges. The near-edge X-ray absorption fine structure (NEXAFS) spectra showed one intense peak at all edges. This was assigned to the $1s \rightarrow 3\pi$ transition. In addition, some smaller signals were tentatively assigned to excitation into Rydberg orbitals. Resonant Auger electron spectra were then recorded at over twenty photon energies at all edges. The measured spectra again displayed excellent agreement with the simulated spectra. Comparing these spectra to the Auger electron spectra of isocyanic acid, HNCO, showed that the chemical and electronic environment of the atom in the molecule is more relevant for the Auger-Meitner process than the nuclear charge.

The resonant auger electron spectrum contains both participator and spectator final states (see Section 2.4). Participator final states are equivalent to those produced by single photon ionization, while spectator states are analogous to the two-hole final states produced by normal Auger-Meitner processes. Thus, the resonant Auger electron spectra can be seen as the sum of the photoelectron spectrum and the normal Auger electron spectra. This comparison has worked before for isocyanic acid, HNCO.[10] The comparison for fulminic acid is shown

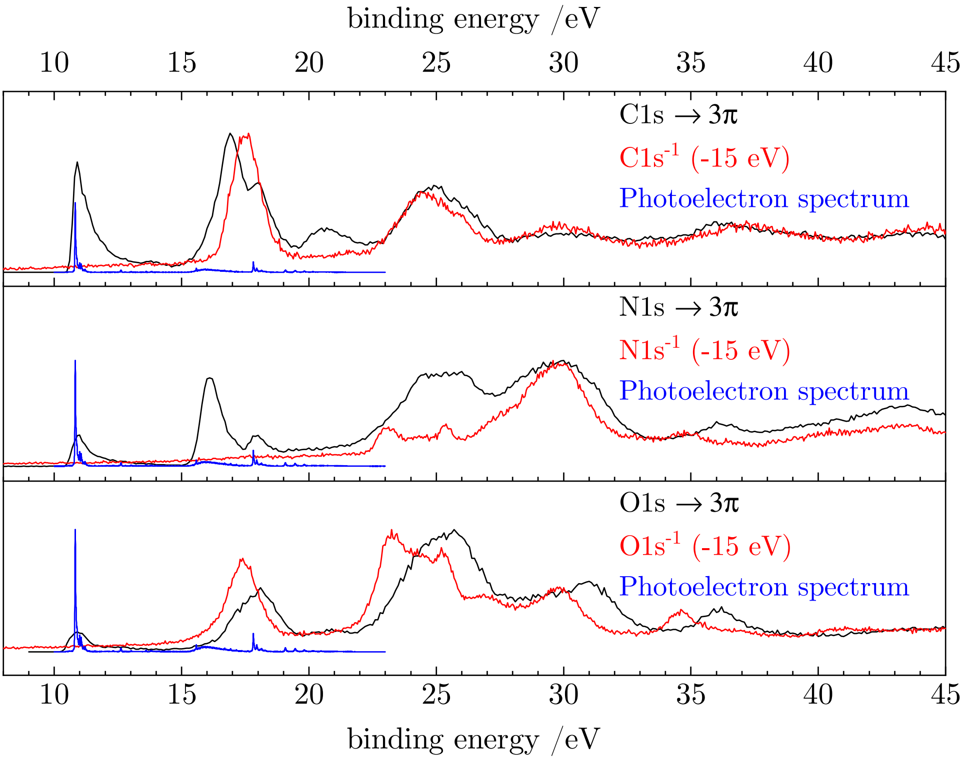

Figure 6.1: Comparison of the resonant Auger electron spectra (black) of fulminic acid, the normal Auger electron spectra (red) and the photoelectron spectrum (blue). The normal auger electron spectra are shifted by −15 eV to better show the parallels between the spectra.

in Figure 6.1, where all spectra are taken from this thesis. At the C-edge and the O-edge the first peak in the RAES is described well by the photoelectron spectrum, while the next signals are also present in the normal Auger electron spectrum, showing that spectator final states already overlap with the participator signals. At the N-edge we observe a different behavior. Here the next two peaks are only present in the photoelectron spectrum and the RAES, but not in the AES. This corroborates our assignment of these peaks in the N1s $\rightarrow 3\pi$ RAES to the $1\pi^{-1}$ and the $7\sigma^{-1}$ states. In addition, this also confirms the calculations that were conducted for the simulation of the photoelectron spectrum. In this region from 15 to 20 eV a large number of excited cationic states overlap impeding the simulation of the photoelectron spectrum.

Chapter 5 shows the Auger-electron-photoion-coincidence spectra using the EPICEA setup at the PLÉIADES beamline of the Synchrotron SOLEIL. The goal was to study the fragmentation of the cations and dications after an Auger-Meitner process. After the normal Auger-Meitner process the products are CH^+ + NO^+, C^+ + NO^+, HCN^+ + O^+, CN^+ + O^+ and trace amounts of CNO^+. The CH^+ + NO^+ pair is most abundant at all three edges. The branching ratios after N1s ionization differ significantly compared to O1s and C1s ionization. We explain these differences by the contribution of high binding energy final states at the N-edge as shown in Chapter 4. This results in more fragmentation at the N-edge. No $HCNO^{2+}$ is observed indicating that the $HCNO^{2+}$ dication fragments before it can be detected. The branching ratios after C1s and O1s ionization also exhibit minor differences. At the C-edge the adjacent C-H bond fragments more than after O1s ionization. Following resonant 1s excitation, many products are detected. $HCNO^+$ is significantly more stable after C1s excitation compared to O1s or N1s excitation. As shown in Chapter 4 the most intense signals in the C1s RAES are at low binding energies, most likely leading to the observed stability of the parent ion. We also observe a signal of m/z = 21.5, formally corresponding to the doubly charged parent ion, which was unstable after 1s ionization. Possibly, the resonant excitation leads to a stable dicationic final state, which is not allowed after normal Auger-Meitner decay. Comparing the results of HCNO to our study on the X-ray induced fragmentation of isocyanic acid, HNCO, revealed some significant differences after 1s ionization.[11] We observed signals of

$HNCO^{2+}$, NCO^{+} and some NCO^{2+} showing that the $HNCO^{2+}$ ion is more stable compared to $HCNO^{2+}$. As pointed out above, ionization of the C1s and O1s lead to destabilization of the adjacent bond. The same was observed for HNCO, where N1s ionization weakened the N-H bond and lead to the formation of N^{+} + CO^{+} and neutral H.

This thesis shows that the developed synthesis is suitable for synchrotron beamtimes. The measurements provide a comprehensive picture of the electronic structure of fulminic acid in the cationic and dicationic state. Its small size allowed a detailed analysis of the underlying processes, leading to more intuitive understanding of the Auger-Meitner process. The wavepacket dynamics simulations on the other hand showed that the cationic electronic states and in particular the Renner-Teller distorted states pose a significant challenge to quantum chemical theory. $HCNO^{+}$ could serve as a benchmark for new theoretical models describing the vibrational structure of Renner-Teller distorted states. The fragmentation after Auger-Meitner processes showed significant site-selectivity. This could be tentatively explained using a thermodynamic argument.

We showed that fragmentation following interaction with either VUV- or soft X-ray radiation is an essential part of the chemistry of the produced ions. Ionization using VUV-radiation leads to the formation of unexpected daughter ions like HCO^{+} and NCO^{+}, while X-ray radiation leaves at most only 10% of absorbing molecules intact in the case of resonant excitation and completely destroys the molecule in case of ionization. After determining the ionization cross sections of HCNO, the branching ratios presented should be included in astrochemical models, possibly explaining the relatively low abundance of HCNO in interstellar space. Our photoelectron spectroscopy study showed that more experiments have to be conducted in order to understand the vibrational structure of $HCNO^{+}$. Vibrational action spectroscopy could be the tool of choice, using an ion trap setup such as the FELion endstation at the FELIX laboratory in Nijmegen, The Netherlands.[12] There, ions are produced by an electron impact source and guided into a 22-pole ion trap. A quadrupole mass filter enables control over the ion mass, which enter the trap. Infrared radiation is provided by the FELIX free electron laser yielding radiation from 66-3600 cm^{-1}. In the ion trap, the ions can be cooled to as low as 4K and form complexes with noble gas tags like He. The infrared radiation is scanned and whenever vibrational excitation occurs, the weakly bound He-cation complex dissociates, leading to a change in the mass-to-charge ratio. By measuring this change, infrared spectra of cations can be recorded. This experiment should provide more insights about the vibrational structure of $HCNO^+$, but may also be conducted on the closely related molecules isocyanic acid, HNCO, and isothiocyanic acid, HNCS. Like fulminic acid these molecules have been detected in interstellar space,[13,14] but information on the cationic species is limited to photoelectron spectroscopy studies.[15,16] The measurement of the infrared spectra of astrochemical molecules has become particularly relevant with the launch of the James-Webb Space Telescope in 2021. It is the largest optical telescope in space and features high-resolution and high-sensitivity instruments allowing it to conduct infrared astronomy of distant astrophysical objects. Spectroscopic data of the ions of these molecules may lead to new insights about their formation and destruction in the interstellar environment.

References

[1] E. Howard, *Philos. Trans. R. Soc.* **1800**, *90*, 204–238.

[2] J. J. Berzelius, *Jahresberichte über die Fortschritte der Physischen Wissenschaften* **1832**, *11*, 44–48.

[3] L. Pauling, S. B. Hendricks, *J. Am. Chem. Soc.* **1926**, *48*, 641–651.

[4] W. Beck, K. Feldl, *Angew. Chem.* **1966**, *78*, 746–746.

[5] J. Bastide, J. P. Maier, *Chem. Phys.* **1976**, *12*, 177–190.

[6] A. Luna, A. M. Mebel, K. Morokuma, *J. Chem. Phys.* **1996**, *105*, 3187–3205.

[7] D. H. Quan, E. Herbst, Y. Osamura, E. Roueff, *Astrophys. J.* **2010**, *725*, 2101–2109.

[8] N. Marcelino, S. Brünken, J. Cernicharo, D. Quan, E. Roueff, E. Herbst, P. Thaddeus, *Astron. Astrophys.* **2010**, *516*, A105.

[9] A. Jiménez-Escobar, B. M. Giuliano, G. M. Muñoz Caro, J. Cernicharo, N. Marcelino, *Astrophys. J.* **2014**, *788*, 19.

[10] F. Holzmeier, T. J. A. Wolf, C. Gienger, I. Wagner, J. Bozek, S. Nandi, C. Nicolas, I. Fischer, M. Gühr, R. F. Fink, *J. Chem. Phys.* **2018**, *149*, 034308.

[11] M. Gerlach, F. Fantuzzi, L. Wohlfart, K. Kopp, B. Engels, J. Bozek, C. Nicolas, D. Mayer, M. Gühr, F. Holzmeier, I. Fischer, *J. Chem. Phys.* **2021**, *154*, 114302.

[12] P. Jusko, S. Brünken, O. Asvany, S. Thorwirth, A. Stoffels, L. van der Meer, G. Berden, B. Redlich, J. Oomens, S. Schlemmer, *Faraday Discuss.* **2019**, *217*, 172–202.

[13] L. E. Snyder, D. Buhl, *Astrophys. J.* **1972**, *177*, 619.

[14] M. A. Frerking, R. A. Linke, P. Thaddeus, *Astrophys. J.* **1979**, *234*, L143–L145.

[15] F. Holzmeier, M. Lang, I. Fischer, X. Tang, B. Cunha de Miranda, C. Romanzin, C. Alcaraz, P. Hemberger, *J. Chem. Phys.* **2015**, *142*, 184306.

[16] J. H. D. Eland, W. C. Price, D. W. Turner, *Philos. Trans. R. Soc. A* **1970**, *268*, 87–96.

KAPITEL 7

Zusammenfassung und Ausblick

Seit der Entdeckung der Fulminsäure, HCNO, durch Edward Howard in 1800,[1] wurde diese von Chemikern als Modellmolekül verwendet, um verschiedenste chemische Fragen zu beantworten. Basierend auf Experimenten an HCNO und der Isocyansäure, HNCO, und deren Salzen, schlug Berzelius erstmals das Konzept der Isomerie vor. Es besagte, dass die chemischen Eigenschaften nicht nur von der elementaren Zusammensetzung, sondern auch von der chemischen Struktur abhängen.[2] Linus Pauling führte quantenchemische Rechnungen durch, um die Struktur der Fulminsäure aufzuklären,[3] dann nutzen Beck und Feldl Infrarot-Spektroskopie, um den finalen Beweis für die Struktur zu liefern.[4] In dieser Dissertation wollten wir die komplexen Prozesse untersuchen, die nach der Interaktion mit VUV- und weicher Röntgenstrahlung stattfinden. Außerdem könnten die Messdaten dabei helfen, die Chemie der Fulminsäure im interstellaren Raum besser zu erklären.

Die erste Aufgabe dieser Arbeit war es, eine verlässliche und sichere Syntheseroute für die Fulminsäure, HCNO, zu finden. Mit dieser Methode konnten dann Experimente an mehreren Einrichtungen für Synchrotronstrahlung durchgeführt werden. Die Fulminsäure wurde mit Photoelektronenspektroskopie, Augerelektronenspektroskopie und Elektron-Ion-Koinzidenz Methoden untersucht. Die geringe Größe des HCNOs erlaubt auch quantenchemische Rechnungen auf hohem Niveau. Diese Analyse könnte dann auch ein besseres Verständnis der vorliegenden Prozesse ermöglichen.

Kapitel 3 präsentiert die Photoelektronenspektroskopie und dissoziative Photoionisation der Fulminsäure. Die aufgenommenen Photoelektronenspektren weisen eine bessere Auflösung auf als die vorherigen Spektren von Bastide *et al.*.[5]

Wir beobachteten vier Banden, von denen drei gut aufgelöste Schwingungsstruktur zeigten. Um die Spektren zu analysieren, wurde die Dynamik eines Wellenpakets im Renner-Teller aufgespaltenen kationischen Grundzustand simuliert. Aus diesen Rechnungen wurden Renner-Teller Parameter von jeweils 0.48 und 0.41 für die HCN Biegeschwingung und die CNO Biegeschwingung erhalten. Das deutet auf eine mittelstarke Kopplung zwischen den Zuständen hin. Die Simulationen erlaubten außerdem eine vorläufige Zuordnung der Schwingungen des Kations im elektronischen Grundzustand. Des Weiteren untersuchten wir die dissoziative Photoionisation von HCNO. Bis 15.3 eV werden vier Fragmentierungsprodukte, HCO^+, NCO^+, NO^+ und NH^+ gebildet. Für die Produkte HCO^+ und NCO^+ modellierten wir die Dissoziationsraten und konnten die gerechneten Mechanismen aus der Literatur bestätigen.[6] Der Bildungsmechanismus von HCO^+ verläuft über einen Wechsel von der Dublett zur Quartettoberfläche. Die Bildung von NCO^+ benötigt zunächst die Umlagerung zum Kation der Isocyansäure, $HNCO^+$ mit einer Barriere von 2.7 eV. Da angenommen wird, dass im interstellaren Medium die neutralen Moleküle aus den Kationen gebildet werden,[7] könnten diese Mechanismen auch astrochemische Bedeutung haben. Dies könnte zum Beispiel die relative Häufigkeit der CHNO Isomere erklären, welche bislang nicht komplett verstanden ist.[8,9]

Kapitel 4 zeigt die Augerelektronenspektroskopie der Fulminsäure. 1s Ionisierungs- sowie Anregungsenergien und die darauffolgenden Auger-Meitner Prozesse wurden vermessen. Durch Röntgenphotoelektronenspektroskopie bestimmten wir Kohlenstoff, Stickstoff und Sauerstoff 1s Ionisierungsenergien von 292.9 eV, 410.5 eV und 539.6 eV. Die normalen Augerelektronenspektren wurden aufgenommen und daraus eine adiabatische Doppelionisierungsenergie von 32.5 eV bestimmt. Simulationen basierend auf der *one-center*-Näherung stimmten sehr gut mit dem Experiment überein und erlaubte eine intuitive Interpretation der Unterschiede zwischen den drei Kanten. Wir konnten feststellen, dass die Intensität der Übergänge proportional zum Beitrag der jeweiligen Atomorbitale zu den Valenzorbitalen ist. Dies erklärte die niedrige Intensität der $2\pi^{-2}$ Endzustände an der N-Kante. Das 2π Orbital des HCNO besitzt eine Knotenfläche an dem Stickstoffatom, was zu einer niedrigen Übergangswahrscheinlichkeit führt. Die *near-edge X-ray absorption fine structure* (NEXAFS)-Spektren zeigten jeweils ein intensives Signal an allen drei Kanten. Dies wurde dem 1s → 3π Übergang zugeordnet. Zusätzlich wurden schwächere Signale gemessen, welche vorläufig der Anregung in Rydbergorbitale zugeordnet wurden. Resonante Augerelektronenspektren wurden dann bei über zwanzig verschiedenen Photonenenergien an allen drei Kanten aufgenommen. Diese Spektren stimmten wieder sehr gut mit den simulierten Spektren überein. Durch einen Vergleich zu den Augerelektronenspektren der Isocyansäure, HNCO, konnten wir zeigen, dass die chemische und elektrische Umgebung relevant ist für den Auger-Meitner Prozess und nicht die atomare Ladung.

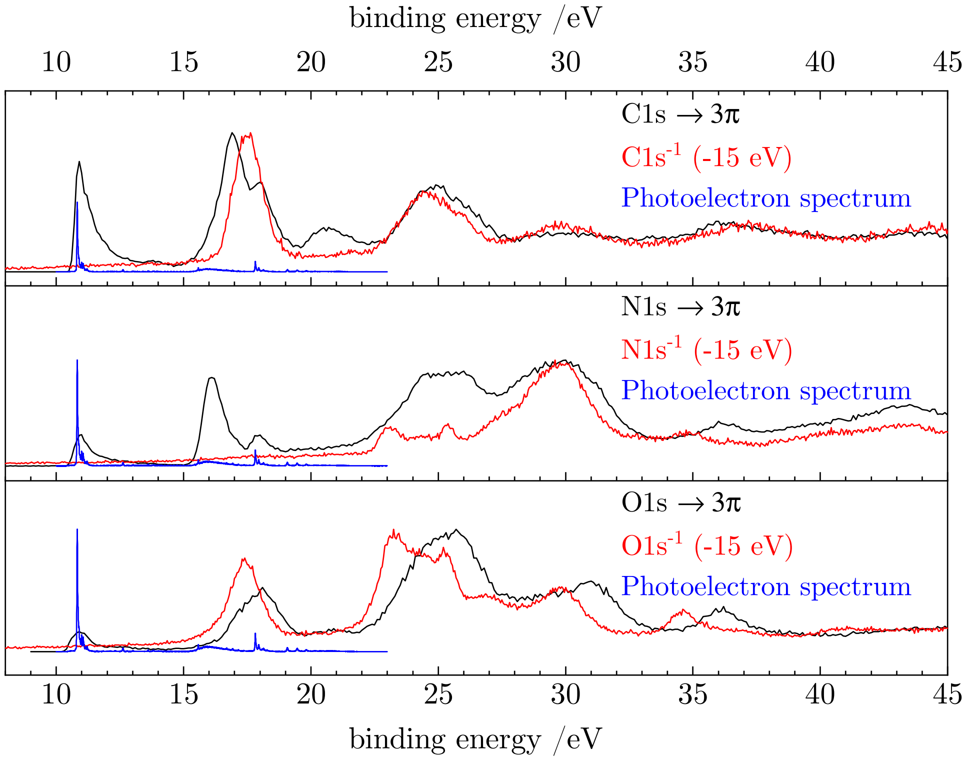

Abbildung 7.1: Vergleich der resonanten Augerelektronenspektren (schwarz), der normalen Augerelektronenspektren (rot) und des Photoelektronenspektrum (blau). Das normale Augerelektronenspektrum ist um −15 eV verschoben, um die Paralellen der Spektrum zu zeigen.

Die resonanten Augerelektronenspektren beinhalten sogenannte *Participator*- und *Spectator*-Endzustände (siehe Abschnitt 2.4). *Participator*-Endzustände sind äquivalent zu den durch Ein-Photon-Ionisation erzeugten Endzuständen, während *Spectator*-Endzustände analog zu den Zwei-Loch Endzuständen der normalen Augerelektronenspektroskopie sind. Dementsprechend lässt sich das resonante Augerelektronenspektrum als Summe des Photoelektronenspektrum und des normalen Augerelektronenspektrums ansehen. Dieser Zusammenhang konnte gut für die Isocyansäure gezeigt werden.[10] Abbildung 7.1 zeigt diesen Vergleich bei HCNO, wobei alle gezeigten Spektren aus dieser Dissertation stammen. An der C- und an der O-Kante ist das erste Signal des RAES noch gut durch das Photoelektronenspektrum beschrieben, während die nächsten Signale auch im normalen Augerelektronenspektrum präsent sind. Das zeigt, dass in diesem Bereich *Participator*- und *Spectator*-Endzustände bereits überlagern. An der N-Kante wird ein anderes Verhalten beobachtet. Hier sind die nächsten zwei Signale nur im Photoelektronenspektrum und im RAES sichtbar, aber nicht im AES. Das unterstützt unsere Zuweisung dieses Signales im N1s $\rightarrow 3\pi$ zu den $1\pi^{-1}$ und $7\sigma^{-1}$ Endzuständen. Außerdem bestätigt dies die Rechnungen, welche im Zuge der Simulation des Photoelektronenspektrums gemacht wurden. In der Region von 15 bis 20 eV überlagern viele angeregte Zustände des Kations, was eine Simulation dieser Spektren erschwert.

Kapitel 5 umfasst die Augerelektronen-Photoionen-Koinzidenzspektren, welche mit dem EPICEA Aufbau der PLÉIADES Strahllinie des Synchrotron SOLEIL aufgenommen wurden. Das Ziel war es, die Fragmentierung der Kationen und Dikationen nach dem Auger-Meitner Prozess zu messen. Die Produkte nach dem normalen Auger-Meitner Zerfall sind $CH^+ + NO^+$, $C^+ + NO^+$, $HCN^+ + O^+$, $CN^+ + O^+$ und eine geringe Menge CNO^+. Das $CH^+ + NO^+$ Paar ist das häufigste Produkt an allen drei Kanten. Die Zerfallsverhältnisse nach N1s Ionisierung unterscheiden sich stark zu der O1s und C1s Ionisierung. Wir erklären diesen Unterschied durch den Beitrag von Endzuständen an der N-Kante mit hoher Bindungsenergie (siehe auch Kapitel 4). Das führt zu mehr Fragmentierung an der N-Kante. Es wurde kein $HCNO^{2+}$ beobachtet, was darauf hindeutet, dass das Dikation fragmentiert, bevor es detektiert werden kann. Die Zerfallsverhältnisse nach O1s und C1s Ionisierung unterscheiden sich ebenfalls leicht. An der C-Kante fragmentierte die anliegende C-H-Bindung vermehrt im Vergleich zur O-Kante. Nach resonanter 1s Anregung wurden viele verschiedene Produkte gemessen. $HCNO^+$ selbst ist im Vergleich zur O1s oder N1s Anregung deutlich stabiler nach C1s Anregung. Wie in Kapitel 4 gezeigt wurde, liegen die intensivsten Signale im C1s RAES bei niedrigen Bindungsenergien. Dies führt wahrscheinlich zur höheren Stabilität des Mutterions. Wir beobachteten außerdem ein Signal bei $m/z = 21.5$, was formell zum doppelt geladenen Mutterion gehört, welches nach 1s Ionisierung instabil ist. Möglicherweise führt die resonante Anregung zu einem stabilen dikationischen Endzustand, welcher durch den normalen Auger-Meitner Zerfall aufgrund von Auswahlregeln nicht erreichbar ist. Der Vergleich dieser Ergebnisse mit unserer Studie an der durch Röntgenstrahlen induzierten Fragmentierung von Isocyansäure, HNCO, zeigte einige deutliche Unterschiede.[11] Hier wurden $HNCO^{2+}$, NCO^+ und Spuren NCO^{2+} gemessen, $HNCO^{2+}$ ist also im Gegensatz zu $HCNO^{2+}$ stabiler. Auch bei der Isocyansäure konnten wir beobachten, dass N1s Ionisierung zur Destabilisierung der anliegenden N-H-Bindung.

Diese Arbeit zeigt, dass die entwickelte Synthese der Fulminsäure für Messzeiten geeignet ist. Die Messungen liefern umfassende Informationen über die elektronische Struktur der Fulminsäure im kationischen und dikationischen Zustand. Die geringe Größe ermöglichte eine detaillierte Analyse der vorliegenden Prozesse, was zu einem intuitiveren Verständnis des Auger-Meitner Prozesses führte. Die Simulation der Wellenpaketdynamik zeigte wiederum, dass die kationischen elektronischen Zustände und insbesondere die Renner-Teller verzerrten Zustände eine Herausforderung für die quantenchemische Theorie darstellen. $HCNO^+$ könnte als Testmolekül für die theoretische Beschreibung der Schwingungsstruktur von Renner-Teller verzerrten Zuständen fungieren. Die Fragmentierung nach Auger-Meitner Zerfall zeigte starke Selektivität dafür, an welchem Atom ionisiert bzw. angeregt wird. Dies konnte vorläufig durch ein thermodynamisches Argument erklärt werden.

Die Fragmentierung nach Interaktion mit VUV- und weicher Röntgenstrahlung ist also ein essenzieller Teil der Chemie der produzierten Ionen. Die Ionisierung mit VUV-Strahlung führt zur Bildung unerwarteter Produkte, wie HCO^+ und NCO^+. Röntgenstrahlung lässt höchstens 10% der absorbierenden Moleküle intakt, während Ionisierung zur Zerstörung des Moleküls führt. Eine Bestimmung der Absorptionsquerschnitte würde es dann ermöglichen, die Zerfallsverhältnisse in astrochemischen Modellen zu berücksichtigen und so möglicherweise auch die geringe Menge von HCNO im interstellaren Raum erklären. Unsere Studie der Photoelektronenspektren hat gezeigt, dass weitere Experimente nötig sind, um die Schwingungsstruktur des $HCNO^+$ zu verstehen. Hier könnte *vibrational action spectroscopy* die richtige Methode sein. Diese ist möglich mit der Ionenfalle der FELion Strahllinie des FELIX Laboratory in Nijmegen, Niederlande.[12] Ionen werden dort mittels einer Elektronenstoßquelle produziert und anschließend in die 22-Pol Ionenfalle geleitet. Ein Quadrupol Massenfilter ermöglicht Kontrolle darüber, welche Ionen in die Falle gelangen. Die Infrarotstrahlung von 66 bis 3600 cm^{-1} wird durch einen Freien-Elektronen-Laser erzeugt. In der Ionenfalle können die Ionen auf bis zu 4K abgekühlt werden und dann schwach gebundene Komplexe mit einem Edelgas, beispielsweise He, bilden. Die IR-Strahlung wird durchgestimmt und führt bei Schwingungsanregung zum Zerfall dieser Komplexe. Diese Änderung des Masse-zu-Ladungs-Verhältnisses abhängig von der IR-Strahlung stellt das IR-Spektrum des freien Kations dar. Dieses Experiment sollte weitere Informationen über die Schwingungsstruktur des $HCNO^+$ liefern, kann aber auch an verwandten Molekülen wie HNCO und der Isothiocyansäure, HNCS, durchgeführt werden. Diese Moleküle wurden, wie auch HCNO, bereits im interstellaren Raum detektiert,[13,14] allerdings sind die Informationen über die Kationen auf Photoelektronenspektren beschränkt.[15,16] Die Messung der IR-Spektren von astrochemischen Molekülen ist durch den Start des James-Webb Space Telescopes im Jahr 2021 besonders wichtig geworden. Spektroskopische Daten über die Kationen dieser Moleküle könnten dann zu neuen Erkenntnissen hinsichtlich der Bildung und Zerstörung dieser Moleküle im interstellaren Medium führen.

References

[1] E. Howard, *Philos. Trans. R. Soc.* **1800**, *90*, 204–238.

[2] J. J. Berzelius, *Jahresberichte über die Fortschritte der Physischen Wissenschaften* **1832**, *11*, 44–48.

[3] L. Pauling, S. B. Hendricks, *J. Am. Chem. Soc.* **1926**, *48*, 641–651.

[4] W. Beck, K. Feldl, *Angew. Chem.* **1966**, *78*, 746–746.

[5] J. Bastide, J. P. Maier, *Chem. Phys.* **1976**, *12*, 177–190.

[6] A. Luna, A. M. Mebel, K. Morokuma, *J. Chem. Phys.* **1996**, *105*, 3187–3205.

[7] D. H. Quan, E. Herbst, Y. Osamura, E. Roueff, *Astrophys. J.* **2010**, *725*, 2101–2109.

[8] N. Marcelino, S. Brünken, J. Cernicharo, D. Quan, E. Roueff, E. Herbst, P. Thaddeus, *Astron. Astrophys.* **2010**, *516*, A105.

[9] A. Jiménez-Escobar, B. M. Giuliano, G. M. Muñoz Caro, J. Cernicharo, N. Marcelino, *Astrophys. J.* **2014**, *788*, 19.

[10] F. Holzmeier, T. J. A. Wolf, C. Gienger, I. Wagner, J. Bozek, S. Nandi, C. Nicolas, I. Fischer, M. Gühr, R. F. Fink, *J. Chem. Phys.* **2018**, *149*, 034308.

[11] M. Gerlach, F. Fantuzzi, L. Wohlfart, K. Kopp, B. Engels, J. Bozek, C. Nicolas, D. Mayer, M. Gühr, F. Holzmeier, I. Fischer, *J. Chem. Phys.* **2021**, *154*, 114302.

[12] P. Jusko, S. Brünken, O. Asvany, S. Thorwirth, A. Stoffels, L. van der Meer, G. Berden, B. Redlich, J. Oomens, S. Schlemmer, *Faraday Discuss.* **2019**, *217*, 172–202.

[13] L. E. Snyder, D. Buhl, *Astrophys. J.* **1972**, *177*, 619.

[14] M. A. Frerking, R. A. Linke, P. Thaddeus, *Astrophys. J.* **1979**, *234*, L143–L145.

[15] F. Holzmeier, M. Lang, I. Fischer, X. Tang, B. Cunha de Miranda, C. Romanzin, C. Alcaraz, P. Hemberger, *J. Chem. Phys.* **2015**, *142*, 184306.

[16] J. H. D. Eland, W. C. Price, D. W. Turner, *Philos. Trans. R. Soc. A* **1970**, *268*, 87–96.

CHAPTER 8

Erklärungen zu Autorenschaften

Erklärung zur Autorenschaft

Photoelectron spectroscopy and dissociative photoionization of fulminic acid, HCNO
Marius Gerlach, Barry Mant, Tobias Preitschopf, Emil Karaev, Dennis Mayer, Heidy M. Quitián-Lara, Patrick Hemberger, John Bozek, Graham Worth
Ingo Fischer
J. Chem. Phys. **2023**, *158*, 134303.

Detaillierte Darstellung der Anteile an der Veröffentlichung (in %)
Angabe Autoren/innen (ggf. Haupt- / Ko- / korrespondierende/r Autor/in) mit Vorname Nachname (Initialen)

Autor	**M. Gerlach**	**B. Mant**	**T. Preitschopf**	**E. Karaev**	**D. Mayer**	**H. Quitián-Lara**	**P. Hemberger**	**J. Bozek**	**G. Worth**	**I. Fischer**	**∑ in Prozent**
Synthesis of fulminic acid	80%		10%	10%							100%
Measurement of photoelectron spectra	30%		10%	10%	10%	10%		20%		10%	100%
Measurement of dissotiative photoionisation	50%			30%			20%				100%
Analysis of raw data	90%						10%				100%
Computations	30%	40%							30%		100%
Conception of the publication	50%	20%							10%	20%	100%
Writing the publication	40%	40%								20%	100%
Correcting the manuscript	20%	20%					20%		20%	20%	100%
Coordination of the publication										100%	100%
Summe	43%	13%	2%	6%	1%	1%	6%	2%	7%	19%	100%

Erklärung zur Autorenschaft

Auger electron spectroscopy of fulminic acid, HCNO: an experimental and theoretical study
Marius Gerlach, Tobias Preitschopf, Emil Karaev, Heidy M. Quitián-Lara, Dennis Mayer, John Bozek, Ingo Fischer, Reinhold F. Fink
Phys. Chem. Chem. Phys. **2022**, *24*, 15217-15229.

Detaillierte Darstellung der Anteile an der Veröffentlichung (in %)
Angabe Autoren/innen (ggf. Haupt- / Ko- / korrespondierende/r Autor/in) mit Vorname Nachname (Initialen)

Autor	**M. Gerlach**	**T. Preitschopf**	**E. Karaev**	**H. Quitián-Lara**	**D. Mayer**	**J. Bozek**	**I. Fischer**	**R. Fink**	**∑ in Prozent**
Synthesis of fulminic acid	80%	10%	10%						100%
AES & RAES measurements	14%	14%	14%	14%	14%	14%	14%		100%
Analysis of raw data	100%								100%
Discussion of experimental results	50%						50%		100%
Computations								100%	100%
Conception of the publication	50%						25%	25%	100%
Writing the publication	50%						25%	25%	100%
Correcting the manuscript	33%						33%	33%	100%
Coordination of the publication							100%		100%
Summe	42%	3%	3%	2%	2%	2%	26%	20%	100%

Erklärung zur Autorenschaft

X-ray induced fragmentation of fulminic acid, HCNO
Marius Gerlach, Dorothee Schaffner, Tobias Preitschopf, Emil Karaev, John Bozek, Fabian Holzmeier, Ingo Fischer
Submitted to *J. Chem. Phys.*

Detaillierte Darstellung der Anteile an der Veröffentlichung (in %)
Angabe Autoren/innen (ggf. Haupt- / Ko- / korrespondierende/r Autor/in) mit Vorname Nachname (Initialen)

Autor	**M. Gerlach**	**D. Schaffner**	**T. Preitschopf**	**E. Karaev**	**J. Bozek**	**F. Holzmeier**	**I. Fischer**	**∑ in Prozent**
Synthesis of fulminic acid	80%		10%	10%				100%
Measurement of AEPICO spectra	20%	20%			20%	20%	20%	100%
Data analysis	60%	40%						100%
								100%
								100%
Conception of the publication	50%	25%					25%	100%
Writing the publication	50%	25%					25%	100%
Correcting the manuscript	33%	33%					33%	100%
Coordination of the publication							100%	100%
Summe	42%	20%	1%	1%	3%	3%	29%	100%

CHAPTER 9

Danksagung

Ich möchte zunächst ganz herzlich meinem Doktorvater *Prof. Ingo Fischer* danken. Eigentlich begann deine Betreuung ja schon mit meiner Bachelorarbeit und setzte sich mit einem Forschungspraktikum sowie einem Auslandspraktikum an der Swiss Light Source fort. Mit der Masterarbeit über die Fragmentierung der Isocyansäure nach Auger-Meitner Prozessen gabst du mir ein äußerst anspruchsvolles Projekt mit vielen Unbekannten. Für dieses Vertrauen danke ich dir. Auch während der Doktorarbeit hast du mir viel Freiheit gelassen, eigenständig zu arbeiten und hast mir die Teilnahme an vielen Strahlzeiten und internationalen Konferenzen ermöglicht. Der Umgang war stets locker und sorgte zudem für eine sehr angenehme Atmosphäre in der Gruppe.

Mein äußerster Dank gilt auch *Dr. Patrick Hemberger* der VUV beamline der Swiss Light Source. Auch die Zusammenarbeit mit dir geht über die Doktorarbeit hinaus und begann mit einem Auslandspraktikum in Villigen. Seitdem warst du immer eine unterstützende Kraft und hattest stets Zeit, jede meiner Fragen zu beantworten. Die vielzähligen Kooperationen mit dir waren immer spannend. Ich möchte hier auch *Jana Hemberger* danken, welche die wunderschöne Illustration auf der Titelseite dieser Arbeit gemalt hat. Zudem möchte ich mich auch bei *Dr. András Bödi* bedanken für die Unterstützung bei den Messzeiten und bei der Auswertung der Messdaten.

I would also like to thank the team of the PLÉIADES Beamline of the SOLEIL Synchrotron. I extend my thanks to *Dr. John Bozek* who supported us during our beamtimes always providing excellent insight and a keen sense for what is actually interesting to measure. With your guidance we achieved two highly efficient and productive beamtimes. I would also like to thank *Dr. Christophe Nicolas*, *Dr.*

Emmanuel Robert and *Dr. Aleksandar Milosavljevic* for their support and their helpful discussions of the EPICEA data.

Ich möchte mich auch ganz herzlich bei (fast *Dr.*) *Tobias Preitschopf* bedanken. In dir hatte ich ab dem ersten Tag einen Freund, mit dem ich quatschen, Witze machen und auch über die ernsteren Dinge des Lebens reden konnte. Vielen Dank dafür. Du hast stets 100% für den Arbeitskreis gegeben und hast immer jede auch noch so nervige Aufgabe übernommen. Ich werde unsere gemeinsame Zeit sehr vermissen.

Bedanken möchte ich mich auch bei meinen Messkumpanen, dem Synchrotron Team, *Dorothee Schaffner* und *Emil Karaev*. Emil, bei uns beiden hat es ab dem ersten Moment einfach funktioniert und die Zusammenarbeit war stets top. Doro, ich weiß, dass ich das Auger-Thema in mehr als fähige Händen übergebe. Außerdem danke ich dir vielmals für die top Arbeit bei der Auswertung der EPICEA Daten der Fulminsäure.

Ich bedanke mich auch bei den weiteren Gruppenmitgliedern des AKF *Klaus Hofmann*, *Lukas Faschingbauer*, *Lilith Wohlfart*, *Jonas Fackelmayer*, *Floriane Sturm* und *Christian Matthaei* für die wunderschöne Zeit mit vielen lustigen Aktionen. Es hat mir sehr viel Spaß gemacht, jeden Tag mit euch zusammenzuarbeiten und ich werde euch alle sehr vermissen. Hier möchte ich außerdem *Katharina Theil*, *Sophie Monninger* und *Karina Kopp* danken für ihre großartige Unterstützung im Zuge von Bachelorarbeiten bzw. Forschungspraktika.

Mein Dank gilt auch unserem Kooperationspartner *Prof. Reinhold Fink* der Universität Tübingen. Die Zusammenarbeit an den Augerspektren der Fulminsäure war sehr ertragreich und hat uns ein besseres Verständnis über die Auger-Meitner Prozesse ermöglicht.

I also want to thank *Prof. Graham Worth* and *Dr. Barry Mant* for their cooperation regarding the photoelectron spectrum of HCNO, which in the end turned out to be much more difficult than originally expected.

Dankbar bin ich auch *Dr. Fabian Holzmeier*. Vielen Dank für die Unterstützung während der Messzeiten, aber auch für die Unterstützung und Diskussionen am Anfang meiner Doktorarbeit, wo du mir viele Fragen beantworten konntest. Außerdem danke ich dir für die Möglichkeit, bei einer Messzeit am Sincrotrone Trieste teilzunehmen und einen, wenn auch kleinen Einblick, in die Welt der Lithographie zu erhalten.

Auch *Dr. Dennis Mayer* möchte ich ganz herzlich danken für die Unterstützung bei den Messzeiten, wo du stets hilfsbereit die Nachtschichten übernommen hast. An dieser Stelle möchte ich auch *Prof. Markus Gühr* danken, für die Zusammenarbeit an der HNCO Fragmentierung.

Thanks also to *Dr. Felipe Fantuzzi* and *Dr. Heidy Quitián-Lara*. *Felipe*, I thank you for your cooperation on the HNCO project and your support. *Heidy*, I would like to thank you for your support during our beamtimes and for providing your astrochemical point-of-view.

Ich bedanke mich auch bei *Prof. Anke Krüger* und ihrer Gruppe für die Bereitstellung von Equipment für die Synthese der Fulminsäure.

Bedanken möchte ich mich auch bei den bereits promovierten Arbeitskollegen *Dr. Engelbert Reusch*, *Dr. Marco Flock*, *Dr. Domenik Schleier* und *Dr. Florian Hirsch* für die tolle Aufnahme in den Arbeitskreis und natürlich auch die vielen Lektionen, die mich auf das *echte* Leben vorbereitet haben.

Ich möchte mich auch bei den Mitarbeitern unserer Werkstatt *Wolfgang Liebler*, *Katharina Wittmann*, *Ralf Kohrmann* und *Markus Keller* sowie unserem Elektriker *Uwe Reus* bedanken. Vielen Dank für euren tatkräftigen Einsatz.

Großer Dank gilt auch meinen Freunden aus dem Studium *Felix Full*, *Jonas Rauch* und *Martin Luff*. Nur langsam wird mir klar, dass jetzt 8 Jahre Studium an der Uni Würzburg zu Ende gehen. Ich blicke zurück auf eine sehr schöne Zeit, in der ich viel gelernt habe. Vielen Dank dafür.

Ich möchte auch meiner Freundin *Julia Frenzel* danken. Danke, dass du mich so toll unterstützt und mich auch in schwierigen Phasen immer unterstützt hast. Zwar habe ich mich immer auf Messzeiten gefreut, allerdings war ich dann auch glücklich, wenn sie vorbei waren und ich dich wieder sehen konnte.

Zu guter Letzt bedanke ich mich auch ganz herzlich bei meinen Eltern *Dr. Uwe Gerlach* und *Dr. Doris Gerlach* und meinem Bruder *Adrian Gerlach*. Vielen Dank für den starken Zusammenhalt und die großartige Unterstützung.